Vol. 45 No. 1 (2024)

ARCHIVES OF THERMODYNAMICS

ISSN: 1231-0956
ISSN: 2083-6023 (Online)

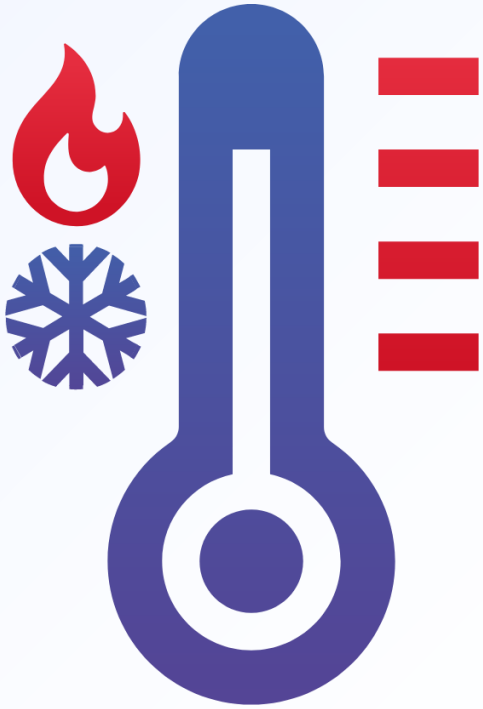

Co-published by

Institute of Fluid Flow Machinery
Polish Academy of Sciences

Committee on Thermodynamics and Combustion
Polish Academy of Sciences

WYDAWNICTWO IMP PAN

Aims and Scope

The aim of the quarterly journal Archives of Thermodynamics (AoT) is to disseminate knowledge between scientists and engineers worldwide and to provide a forum for original research conducted in the field of thermodynamics, heat transfer, fluid flow, combustion and energy conversion in various aspects of thermal sciences, mechanical and power engineering. Besides original research papers, review articles are also welcome.

The journal scope of interest encompasses in particular, but is not limited to:

- Classical and extended non-equilibrium thermodynamics
- Thermodynamic analysis including exergy
- Thermodynamics of heating and cooling
- Thermodynamics of nuclear power generation
- Thermodynamics in defense engineering
- Advances in thermodynamics
- Experimental, theoretical and numerical heat transfer
- Thermal and energy system analysis
- Renewable energy sources including solar energy
- Secondary fuels and fuel conversion
- Heat and momentum transfer in multiphase flows
- Nanofluids
- Energy transition
- Advanced energy carriers
- Energy storage and efficiency
- Energy in buildings
- Hydrogen energy
- Combustion and emissions
- Turbomachinery
- Thermal and energy system analysis
- Integrated energy systems
- Distributed energy generation
- Thermal incineration of wastes
- Waste heat recovery

Vol. 45 No. 1 (2024)

ARCHIVES OF THERMODYNAMICS

ISSN: 1231-0956
ISSN: 2083-6023 (Online)

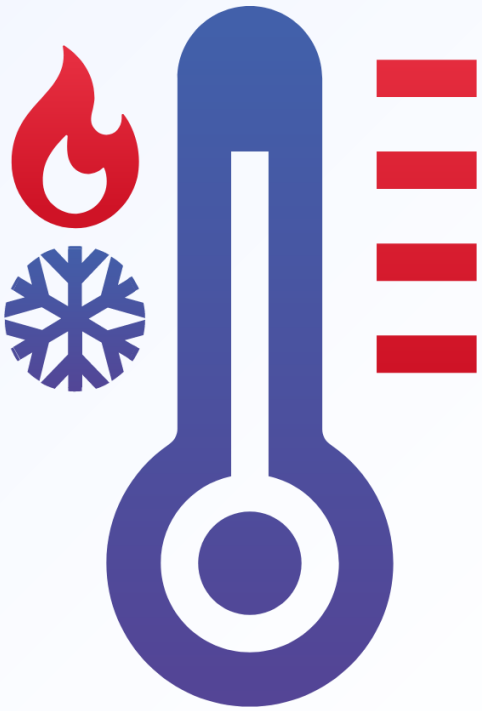

Co-published by

Institute of Fluid Flow Machinery
Polish Academy of Sciences

Committee on Thermodynamics and Combustion
Polish Academy of Sciences

WYDAWNICTWO IMP PAN

Editorial Office
IMP PAN Publishers
Institute of Fluid Flow Machinery, Fiszera 14, 80-231 Gdańsk, Poland,
Phone: (+48) 58-341-12-71 int. 230, e-mail: redakcja(at)imp.gda(.)pl
https://www.imp.gda.pl/archives-of-thermodynamics/
Journals PAS – Electronic Library Polish Academy of Sciences
https://journals.pan.pl/ather

Subscription outside Poland
From 2024, Archives of Thermodynamics appear only in electronic version as an open access journal. However, printed archive volumes or issues are still available. The price of a full volume outside Poland is **120 EUR**. The price of a single issue is **30 EUR**. Archived volumes or issues are available on request. Orders should be sent directly to IMP PAN Publishers:
Institute of Fluid-Flow Machinery,
Fiszera 14, 80-231 Gdansk, Poland,
e-mail: redakcja(at)imp.gda.pl or jfrk(at)imp.gda(.)pl or jrybka(at)imp.gda(.)pl.
Payments should be transferred to the bank account of IMP PAN:
IBAN 28 1130 1121 0006 5498 9520 0011 at Bank Gospodarstwa Krajowego; Code SWIFT: GOSKPLPW.

Prenumerata w Polsce
Od 2024, czasopismo ukazuje się tylko w formie elektronicznej otwartej. Osiągalne są jednak wydania papierowe archiwalne. Cena pojedynczego numeru wynosi **50 PLN**. Cena rocznika **200 PLN**. Zamówienia z określeniem numeru (rocznika), nazwiskiem i adresem odbiorcy należy kierować bezpośrednio do Wydawcy:
Instytut Maszyn Przepływowych PAN
ul. Fiszera 14, 80-231 Gdańsk,
e-mail: redakcja(at)imp.gda(.)pl lub jfrk(at)imp.gda(.)pl lub jrybka(at)imp.gda(.)pl.
Wpłaty prosimy kierować na konto Instytutu Maszyn Przepływowych PAN:
nr 28 1130 1121 0006 5498 9520 0011 w Banku Gospodarstwa Krajowego.

Articles in Archives of Thermodynamics are abstracted and indexed within:
Applied Mechanics Reviews • Arianta • Baidu Scholar • BazTech • Cabell's Directory • Celdes • Chemical Abstracts Service (CAS) – CAplus • CNKI Scholar (China National Knowledge Infrastucture) • CNPIEC • EBSCO (relevant databases) • EBSCO Discovery Service • Elsevier – SCOPUS • ESCI (Emerging Sources Citation Index) • Genamics JournalSeek • Google Scholar • Inspec • Index Copernicus • J-Gate • Journal TOCs • Naviga (Softweco) • Paperbase • Pirabase • POL-index • Polymer Library •Primo Central (ExLibris) • ProQuest (relevant databases) • ReadCube • Referativnyi Zhurnal (VINITI) • SCImago (SJR) • Summon (Serials Solutions/ProQuest) • TDOne (TDNet) • TEMA Technik und Management • Ulrich's Periodicals Directory/ulrichsweb • WorldCat (OCLC)

ISSN 1231-0956
ISSN 2083-6023 (Online)

Publication funding of this journal is provided by resources of the Polish Academy of Sciences and the Institute of Fluid Flow Machinery

Contents

Co-published by
Institute of Fluid-Flow Machinery
Polish Academy of Sciences
Committee on Thermodynamics and Combustion
Polish Academy of Sciences

http://www.imp.gda.pl/archives-of-thermodynamics/

A holistic approach to the total energy and cost for carbon capture and sequestration

Efstathios E. Michaelides[a]

[a]Department of Engineering, Texas Christian University, Fort Worth, TX, 76129, USA, e-mail: e.michaelides@tcu.edu

Received: 14.09.2023; revised: 12.01.2024; accepted: 15.01.2024

Abstract

Carbon capture and sequestration from a stationary source comprises four distinct engineering processes: separation of CO_2 from the other flue gases, compression, transportation, and injection into the chosen storage site. An analysis of the thermodynamic and transport properties of CO_2 shows that dissolving this gas in seawater at depths more than 600 m is, most likely, an optimal long-term storage method; and that for transportation, the CO_2 must be in the denser supercritical state at pressures higher than 7.377 MPa. The separation, compression, transportation, and injection processes require significant energy expenditures, which are determined in this paper using realistic equipment efficiencies, for the cases of two currently in operation coal power plants in Texas. The computations show that the total energy requirements for carbon removal and sequestration are substantial, close to one-third of the energy currently generated by the two power plants. The cost analysis shows that two parameters – the unit cost of the pipeline and the discount factor of the corporation – have a very significant effect on the annualized cost of the CCS process. Doubling the unit cost of the pipeline increases the total annualized cost of the entire CCS project by 36% and increasing the discount rate from 5% to 15% increases this annualized cost by 32%.

Keywords: Carbon capture; Carbon sequestration; Minimum work; CO_2 removal; Cost of carbon sequestration.

Vol. 45(2024), No. 1, 5–16; doi: 10.24425/ather.2024.150433

Cite this manuscript as: Michaelides, E.E. (2024). A holistic approach to the total energy and cost for carbon capture and sequestration. *Archives of Thermodynamics*, 45(1), 5–16.

1. Introduction

Carbon capture and storage (CCS) is considered one of the ways to reduce the global carbon dioxide atmospheric emissions by safely storing this greenhouse gas. CCS entails a series of processes that include a) separation of the CO_2 gas from the combustion effluent mixture; b) compression to achieve a dense state for transportation; c) transportation of the gas in a dense phase to the storage facility; and d) long-term storage, monitoring and prevention of CO_2 from entering the atmosphere.

Major point sources, for which CCS is proposed, include fossil fuel power plants (coal as well as gas-fired); cement production factories; and syngas production plants. These stationary, large point sources accounted for 49% of the total global CO_2 emissions in 2020 [1]. The capture and sequestration of a large fraction of these emissions will result in a substantial decrease of the CO_2 accumulation in the atmosphere. The transportation sector (the exhausts of moving vehicles), which contributes to 27% of the global CO_2 emissions, is not targeted for CCS be-

Nomenclature

D – diameter, m
f – friction factor
g – gravitational acceleration, m^2/s
h – enthalpy, kJ/kg
L – length scale, m
P – pressure, kPa
Re – Reynolds number, $= Dv\rho/\mu$
T – temperature, K
t – time, s
V – velocity, m/s
w – specific work, kJ/kg
W – power, kW

Greek symbols

η – efficiency
μ – dynamic viscosity, Pa·s
ρ – density, kg/m^3

Subscripts and Superscripts

0 – (sub) environment condition
0 – (sup) ideal, reversible
a – air
g – gas
n – time step number
sep – separation
T – terminal
w – water

cause emissions from this sector are diffuse, and capture is not practical in vehicles in motion.

An early Intergovernmental Panel for Climate Change (IPCC) report [2] suggested as candidate locations for CO_2 storage tight geological formations – oil and gas fields, un-minable coal beds, and deep saline aquifers – and offshore, deep ocean storage, where the CO_2 is injected at a substantial depth into the seawater. Another suggestion is industrial fixation of this greenhouse gas into solid inorganic carbonates accompanied by local disposal [2, 3]. However, this method requires very large amounts of other chemicals and very high additional energy for the mining and transportation of the chemicals to the disposal sites. For example, the calcination and sequestration of one ton of CO_2 requires 1.27 tons of CaO, or 1.68 tons of $Ca(OH)_2$ to be mined and transported to the source of CO_2.

Several chemical separation processes have been developed for the removal of CO_2 from the combustion products mixture. Among the chemical processes for large-scale CO_2 capture, separation with ammonia and amines appears to be the most promising. Rao and Rubin [4] devised methods to improve the capture efficiency with amines. Valenti et al. [5] performed a detailed study on the chemical separation and capture of CO_2 using chilled ammonia. An analytical/numerical study using ammonia by Bonalumi et al. [6] includes some of the economic aspects and estimated that CO_2 separation using ammonia will cause significant electricity generation costs, close to $124/MWh – three to four times higher than the wholesale electricity price in most States of the USA.

Separation of CO_2 with amine absorption and subsequent regeneration of the amine has received a great deal of attention. Weiland et al. proposed the use of a solution of monoethanolamine (MEA) and methyldiethanolamine (MDEA) for the separation of CO_2 from the other gases [7]. Aqueous MEA and piperazine as CO_2 removal solvents, were extensively studied by Aliyon et al. [8]. Carapellucci et al. [9] also considered the MEA capture in the retrofitting of a coal-fired power plant with a molten carbonate fuel cell, which concentrates the CO_2 gas in its anode and simplifies its capture. Other amine solutions were studied by several researchers, including Rochelle et al. [10] and Li et al. [11]. The latter included calculations of the energy requirements for the CO_2 separation and capture using several amine-based solvents. Among the studies on the chemical separation methods, Furcasa et al. advocated the use of the carbonate mineral *trona* (trisodium hydrogendicarbonate dihydrate) as the main sorbent feedstock source [12]. A comparison of the environmental and ecological impacts using ammonia and amines for CO_2 capture as well as life-cycle assessments were conducted by Strube et al. [13], who concluded that such impacts are significantly less in the long run if amines are used.

Several studies considered the performance of chemical separation methods of CO_2 from the combustion effluents within the framework of specific power plants. Lee et al. [14], considered the CO_2 capture in a 300 MW Integrated Gas Combined Cycle (IGCC) using MDEA and a *Solexol* chemical processes. Their exergy analysis pointed ways to improve the separation processes, which have very low exergetic efficiency. Other separation studies with IGCC cycles that considered chemical separation methods are those by Kunze et al. [15] who used methanol as the chemical agent for capture; Arabkhalaj et al. [16] who compared the effects of two coal types (low-ash and high-ash) in the gas separation process; and the analytical, thermos-economics study by Rosner et al. [17]. An exergo-environmental analysis of CO_2 removal by chemicals including the regeneration process by Petrakopoulou et al. highlighted the environmental advantages of the chemical processes, but also showed the substantial amount of heat input at relatively high temperatures, for the regeneration of the chemicals [18]. A recent review article by Akinola et al. [19] summarizes absorbent materials for the post-combustion capture of CO_2 and details the molecular simulation processes that characterize the absorption of this gas.

A second category of separation methods for CO_2 removal from the flue gases is mechanical separation methods, using primarily membranes. Zhang et al. [20] determined that the selectivity of current-technology membranes is in the range of 70–90% and that high amounts of energy need to be expended for the flue gas pressurization – a significant constraint for the membrane separation technology. In order to supplement the energy consumed by the separation processes, Li et al. [2] suggested that a solar-assisted cycle be used for the capture of CO_2, while Carapellucci et al. [22] suggested a biomass-assisted process. A review of the solar-assisted coal cycles by Saghafifar

and Sabra [23] advised that solar systems composed of large solar collectors be used to supply the high-temperature heat for the chemical separation, in order to avoid the deterioration in the power plant's efficiency. This would entail additional capital cost and exergy dissipation emanating from the conversion of the solar irradiance to heat [24].

A number of recent studies examined the application of CCS technology in specific industries that are heavily dependent on fossil fuels. The removal of CO_2 enables these energy-intensive industries to operate in their traditional ways, while contributing to the mitigation of Global Climate Change. Among these, Paltsev et al. performed a computational study on CCS in "hard to abate sectors" of industry that include cement, chemicals, and the steel industries [25]. Lee et al., used a hybrid economic model to examine the application of CCS in the steel industry [26]. Al Baradi et al. conducted a review of the CO_2 shipping methods in order to extend the carbon abatement to countries and industries where CCS is not feasible, because of their geographic location [27].

In order to answer the question of the minimum equivalent mechanical work required for the separation of CO_2 from other gases (in this case the atmosphere or flue gases), Michaelides [28] used the classical concept of reversible semipermeable membranes – a concept readily used in Thermodynamics – and determined the minimum work required for the separation, regardless of the separation method (chemical, electrochemical, mechanical, etc.). This minimum work is the benchmark of the separation processes and helps define realistic efficiencies for these processes.

After separation, the CO_2 gas must be compressed and transported to the storage sites, which are located at long distances from the generation/capture sites. To minimize pressure losses, compression to supercritical states is recommended. This mode of transportation was examined by Zai et al. [29], who also calculated the water requirements for the pressurization and transportation as well as some commercial uses of the captured CO_2. Geological studies on the storage of CO_2, primarily appraise the suitability of geological formations for the long-term sequestration of CO_2 at supercritical conditions, as for example, in the Utsira formation [30] off the coast of Norway; in several sites considered in Japan [31]; in the pilot-study in the Frio location in Texas [32]; and in the deep sea [33]. Regarding deep ocean sequestration, Caldeira and Wicket [34] warned about the environmental risks of hydrate formation and ocean acidification resulting from the disposal of large CO_2 quantities; and in another study [35] about the possible exchange of this gas between the ocean and the atmosphere.

While CCS entails several technological processes, most of the studies on CCS only consider one aspect of these processes, primarily the separation of this greenhouse gas. This paper contributes to the body of knowledge by presenting a holistic energy analysis of the entire CCS sequence of processes. Some of the novel parts of this paper include: the separation and capture efficiencies, based on the minimum work benchmark; the power for the compression and transportation of CO_2 in real-size pipelines; the analysis of the injection depth and the determination of the maximum size of bubbles for the injection of the CO_2 in the ocean. Based on the thermodynamic properties and the volume of the produced CO_2, the paper shows that deep ocean injection is a realistic storage location for the long run. The energy and power requirements of all the CCS processes are analyzed and the effect of the CCS on the power generated by two power plants currently in operation is determined. In addition to the energy requirements, this study presents the monetary cost for the entire CCS using realistic parameters from two coal power plants, currently in operation. This economic analysis shows the effects of the entire CCS process on the net electric power generated by the power plants, their overall efficiency, and the cost of electricity generated. In summary, this study offers a holistic view of the energy and monetary requirements for CCS to become a realistic solution to the global climate change.

2. Relevant properties of CO_2

2.1. Thermodynamic properties

At ambient conditions (0.1 MPa and 300 K) CO_2 is a gas, usually modelled as an ideal gas. The critical temperature of CO_2 is 304.13 K (31.0°C) and its critical pressure is 7.377 MPa, which implies that CO_2 may turn to the dense supercritical state at ambient temperatures. The dense states of this material (liquid or supercritical) are essential for its transportation, where pressure losses must be kept low. Fig. 1 depicts the T,s diagram of CO_2, with data obtained from [36]. Four isobars at 6, 8, 10 and 12 MPa are depicted in the figure.

While it is possible to transport CO_2 in the liquid state at lower than critical pressures, when the ambient temperature

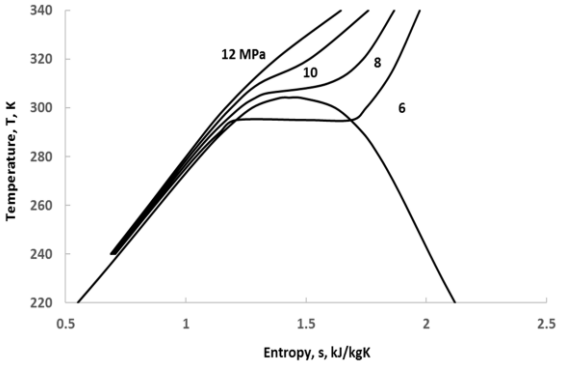

Fig. 1. T,s diagram of carbon dioxide with four isobars around the critical point.

rises (e.g. on summer days) vapour bubbles are formed in the pipeline, the flow becomes two-phase flow, the average velocity increases, and the pressure loss significantly rises. In addition, the risk for pipeline erosion increases. Because of this, the long-distance CO_2 transportation is always recommended at supercritical pressures.

An important consideration for the long-distance transportation of all fluids is the minimization of frictional power dissipation, which is proportional to the third power of the transport velocity, V. This is achieved in practice with wider pipelines and high densities of the transported fluid. Fig. 2 shows the density

of carbon dioxide as a function of the local pressure for four isotherms (at 273 K, 290 K, 300 K and 310 K). Because the CO_2 pipelines are typically buried underground, at depths more than 1 m, extreme air temperatures are avoided, and the four temperatures represent pipeline conditions for all seasons. The four isotherms show that at supercritical pressures – in particular, above 10 MPa – the transported fluid is at sufficiently high densities, which result in lower velocities and friction dissipation. This is the practice in most existing CO_2 pipelines (e.g., for enhanced oil recovery applications) where the fluid typically enters at pressures higher than 10 MPa [37].

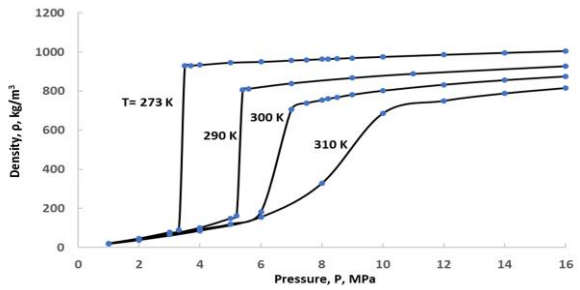

Fig. 2. Pressure density diagram with four isotherms for carbon dioxide.

2.2. Transport and storage properties

As it happens with all the substances in the vicinity of their critical points, the dynamic viscosity of CO_2 significantly varies with temperature and pressure. At any temperature close to the critical point, the dynamic viscosity of any substance is bound to be between the viscosity of the liquid and the viscosity of the vapor. At the typical transportation conditions $273 < T < 310$ K, $8 < P < 14$ MPa, the dynamic viscosity of CO_2 is in the range $10 \times 10^{-6} < \mu < 18 \times 10^{-6}$ Pa·s [38, 39]. It is of interest that the viscosity of CO_2 at these conditions is significantly lower than that of liquid water.

The CO_2 readily dissolves in water as well as in saline water. The solubility of CO_2 in water at 20 °C and 1 bar is 1.69 kg/m^3, and this value becomes significantly higher at higher pressures [40]. An interesting property of the saline water–CO_2 solution is that its density is slightly higher than that of saline water. For example, the seawater density at 4 MPa and 276.15 K increases from 1 031 kg/m^3 to 1 048 kg/m^3 at 6% CO_2 by mass as determined by Song et al. [41]. This characteristic is helpful for CO_2 sequestration, because the heavier solution of seawater–CO_2 sinks and settles at the bottom of the ocean instead of rising to the surface, where the CO_2 may escape into the atmosphere. The timescale of dissolved CO_2 in seawater is on the order of 500 years [42].

3. Mechanical work for CO_2 capture

Classical thermodynamics proves that the minimum work for the separation of CO_2 from a mixture of other gases is achieved with reversible semipermeable membranes [28]. When the CO_2 is separated from the mixture, its partial pressure increases from P_i to P_0=1 atm and the ideal (minimum) specific work w^0_{sep} for the separation is:

$$w^0_{sep} = T_0 R \ln\left(\frac{P_i}{P_0}\right) \approx T_0 R \ln(x_i), \quad (1)$$

where T_0 is the temperature at which separation occurs, typically the ambient; and R is the gas constant of CO_2, 0.189 kJ/kgK. Since CO_2 behaves as an ideal gas at low pressures the ratio of the pressures, P_i/P_0, is equal to the molar fraction of the gas, x_i, in the original mixture. Because $x_i < 1$, $w^0_{sep} < 0$ signifying that mechanical work needs to be spent for the separation of a gas from a mixture of other gases. The ideal separation work is 107 kJ/kg when the volume concentration of CO_2 is 0.15 – the typical concentration of flue gases – and becomes higher at lower concentrations. Eq. (1) also proves that the work for the separation of CO_2 from the flue gas mixture of a stationary CO_2 source (power plant, cement factory, etc. where $x_i \approx 0.15$) would be 3.5 times lower than the work to remove this gas from the atmosphere (where $x_i \approx 0.0004$). Such considerations favour the separation and removal of CO_2 at the point sources where its concentration is significantly higher than in the atmosphere.

Reversible semipermeable membranes that would efficiently separate the CO_2 from a gaseous mixture have not been developed. The practical methods for CO_2 separation are characterized by an efficiency, defined as the ratio of the ideal specific work from Eq. (1) to the actual specific work spent for the separation:

$$\eta_{sep} = \frac{w^0_{sep}}{w_{act}}, \quad (2)$$

at the current state of technology, the separation efficiencies are rather low, when compared to the minimum work benchmark of Eq. (1). Actual mechanical membranes that operate in several stages at high pressures, have rather low selectivity and their efficiency is below 10% [20]. Liquefaction and separation of CO_2 entails the pressurization of the entire original gaseous mixture and subsequent throttling for the removal of CO_2 droplets, and its efficiencies are in the range of 5−8% [24]. Chemical methods for the separation, e.g. using ammonia or amines, entail mechanical (parasitic) work for the flow of the gas and the chemicals as well as heat at a relatively high temperature, 81−115 °C. When the equivalent work of the heat is added to the parasitic work, the efficiencies of the chemical methods are in the range of 8−13% [43, 16, 5]. This is in line with the observations in the original IPCC report [2] and by Davison [44] that the CO_2 capture alone reduces the overall efficiency of a power plant by 6−11% points and that, depending on the type of power plant, 11−25% more fuel is required for the capture process per MWh of electricity generated. If the parasitic mechanical work is minimized or eliminated – e.g., using gravitational rather than mechanical separation of the CO_2-rich amines with phase-change solvents [45] – the efficiency of the separation process may slightly improve to be in the range of 15−20%.

4. Mechanical work for compression and transportation

It is observed in the T,s diagram of Fig. 1 that, at relatively low pressures and ambient temperatures, CO_2 exists as a two-phase mixture. Two-phase flow is avoided in long-distance pipelines because of two detrimental effects:

a) the low density of the vapour dramatically increases the local velocity and the power dissipation, sometimes leading to pipeline chocking (critical flow) [46], and
b) vapour bubbles and slugs cause vibrations that damage the pipelines.

The liquefaction and transportation of CO_2 at low temperatures in the liquid phase presents significant technological difficulties and batch transportation by trucks or railways is very expensive. Such considerations leave pipeline transportation in the supercritical state as the only mode for the long-distance transportation of CO_2. The existing CO_2 pipelines for enhanced oil recovery and smaller pilot pipelines, which extend to more than 2 500 km in the USA, follow this practice too [2, 37]. Before transportation in these pipelines, chemical scrubbers remove the small amounts of hydrogen sulfide, and sulfur oxides as well as the traces of other corrosive materials that were not separated from the CO_2 stream. If such corrosive materials are not removed, the interior of the pipelines must be covered by a corrosion-resistant lining.

While the theory of elementary thermodynamics proves that isothermal compression is the optimum method of pressurization, such processes entail heat transfer and are extremely slow to be used for practical applications. Instead, industrial compressors (which ideally operate isentropically) with intercoolers, in two to four compression stages pressurize the gas. The actual power required for the compressors in a multistage compression unit is:

$$\dot{W}_{pr}^{act} = \dot{m}\left(\frac{1}{\eta_{C1}}\Delta h_{s1} + \frac{1}{\eta_{C2}}\Delta h_{s2} + \frac{1}{\eta_{C3}}\Delta h_{s3} + \ldots\right), \qquad (3)$$

where Δh_{si} and η_{Ci} represent the isentropic enthalpy difference and the corresponding isentropic efficiency of each compressor and the sum is extended to the number of stages. The efficiency of large industrial compressors is in the range of 75−85%. The small parasitic power for the operation of the intercoolers may be incorporated in the efficiencies η_{Ci}.

The mechanical energy equation for the transportation of a fluid from point 1 to point 2 in a pipeline is [47]:

$$P_1 + \rho g z_1 + \frac{1}{2}\rho V_1^2 + \frac{|\dot{W}_{tr}^0|\rho}{\dot{m}} = P_2 + \rho g z_2 + \frac{1}{2}\rho V_2^2 + \frac{1}{2}\rho V_{av}^2\left(f\frac{L}{D} + \sum K_{ml}\right), \qquad (4)$$

where V_{av} is the average velocity of the fluid in the pipeline; P is the static pressure; ρ is the density of the fluid; g is the gravitational constant; $\dot{W}_{tr}^0$ is the pumping power needed for the transportation; $\dot{m}$ is the mass flow rate of the fluid; D is the diameter of the pipe; f is the friction factor of the pipe; L is the pipeline length between points 1 and 2; and K_{ml} represents the so-called "minor losses" in the pipeline that include elbows, other bends, safety valves, etc. The last term essentially represents the energy dissipation in the pipeline and becomes the dominant term in long-distance transportation, where the length is on the order of 100−1 000 km. In most of the existing CO_2 pipelines, the initial gas compression (in the range of 10−15 MPa) at the starting point of the pipeline is sufficient to overcome the dissipation during transportation, and for the gas to arrive at point 2 at supercritical pressure and low density. In this case, $\dot{W}_{tr}^0 = 0$. If this is not the case, intermediate compression stations must be built from an intermediate point i to point 2, to supply additional power. The actual power needed for the transportation of any fluid in the segment 1–2 of a pipeline becomes [47]:

$$\dot{W}_{act}^{tr} = \frac{\pi}{8}D^2\rho V_{av}^3\left(f\frac{L}{D} + \sum K_{ml} + 2g\frac{z_2 - z_1}{V_{av}^2}\right), \qquad (5)$$

4.1. Effect of temperature

The ambient temperature significantly affects the density of a fluid in the vicinity of the critical point. The effect of ambient temperature on pipelines is shown in Fig. 3, which depicts the pressure loss and power dissipation for a horizontal pipeline carrying 300 kg/s (approximately the average mass flow rate generated in a 620 MW power plant) of CO_2, for a length of 500 km. The two pipelines considered for this transportation are schedule-30 steel pipes with nominal diameters of 24 inch (ID = 581 mm) and 30-inch (ID = 730 mm). Schedule 30 corresponds to steel pipelines with sufficient thickness (0.562" or 14.3 mm and 0.625" or 15.9 mm) to withstand the high internal pressure of the supercritical fluid. Such pipelines have sufficient peripheral area for the heat generated from the frictional power dissipation to be transferred to the surroundings. As a result, they operate isothermally and constant CO_2 temperature was assumed along the length of the pipeline, as specified in the ordinate of the figure. The pressure drop and power dissipation due to friction were calculated for a horizontal pipeline with zero minor losses using Eqs. (4) and (5) and a finite difference numerical scheme with segments of 5 km length. It is observed in Fig. 3 that, when the ambient temperature rises above 308 K (35°C), both the dissipated power and the pressure drop increase substantially. To keep the pressure drop and the dissipation within the design conditions, the currently operating CO_2 pipelines in Texas are buried in the ground, at depths of at least 1 m, where the annual temperature variability is limited [2].

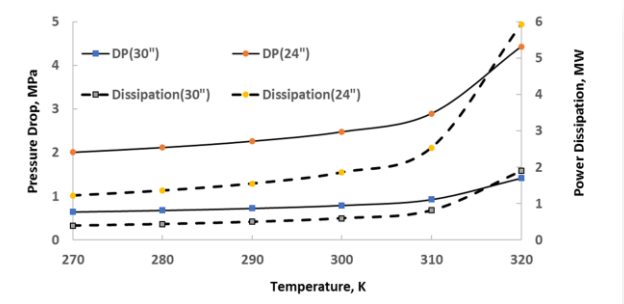

Fig. 3. Pressure drop and power dissipation in two pipelines carrying 300 kg/s of CO_2 for 500 km.

5. Storage locations – injection in oceans

Although the science of CO_2 capture and transportation has offered quantitative results and conclusions that may be followed with certainty, there are several non-technical and legal issues that will need to be resolved before many additional permits are issued for the large-scale and long-term storage of this gas. Among these issues are:

1. Lack of national and regional legal frameworks for the development of a CCS infrastructure. This includes rights-of-way for the transportation pipelines.
2. The need for significant economic incentives (a national carbon tax or emissions allowances), which are lacking in most countries.
3. The legal custody (stewardship) of the stored CO_2. Who is responsible for any atmospheric leakages of the stored CO_2, and the monitoring of the storage sites?
4. For international conventions and agreements should CCS be treated as a reduction of emissions or as removal from the atmosphere?

With the current emphasis on decarbonization, it is reasonable to assume that these economic and legal issues will be resolved at the national and international levels. Then the selection of storage sites will become of importance. CO_2 storage may take place onshore, in geological formations – coal mines, deep saline aquifers, oil fields, etc. – and offshore.

Regarding inland storage, it must be noted that, for any meaningful impact on the global emissions, the CO_2 volume to be stored is very high and inland storage is hampered by the high temperature of the underground locations. If CO_2 were to be compressed to the supercritical pressure of 12 MPa and stored in underground mines and aquifers where the temperature is close to 50°C, the density of CO_2 would be 587 kg/m^3 [36]. Given that the total global emissions of CO_2 in 2021 amounted to 37.9×10^{12} kg [48], this corresponds to a volume of 64.6×10^9 m^3, or 406.1×10^9 bbl. In the same year, the total global volume of petroleum extraction from all the oil fields was 32.8×10^9 bbl, and this implies that, if all the oil fields in the world were used for CO_2 storage, only 8.1% of the emitted CO_2 could be stored in the depleted oil reservoirs. In the state of Texas, where CO_2 is extensively used for enhanced oil recovery, a single coal power plant (the Martin Lake plant, see section 6) generates enough CO_2 annually to fill 13% of the operational oil wells in the entire State.

A second problem with the onshore storage of CO_2 is that – since supercritical CO_2 is a powerful solvent, its molecule is planar and forms a weak acid with water – in the long run the action of the acid will induce cracks and passages that will allow the gas to escape from onshore geological formations that may have trapped methane (a three-dimensional molecule, which is inert with water) or other hydrocarbons. This was the conclusion of several geological studies on pilot CCS projects: The monitoring of a CO_2 injection facility in Frio, Texas, showed that CO_2 in saline aquifers decreases the brine pH and dissolves iron and carbonate oxyhydroxides. This weakens the surrounding rocks, allows CO_2 to escape via the induced cracks and may mobilize toxic metals and organic compounds, which have a path to migrate into the potable groundwater [32]. Another geological monitoring study in Cranfield, Mississippi revealed that the currently available models and computational tools do not yield sufficiently accurate predictions for the long-term fate and transport of CO_2 in aquatic reservoirs [49]. Given such uncertainties and the risk of catastrophic environmental impacts, it is doubtful that many permits will be issued for the long-term onshore storage of CO_2, including storage in aquifers.

5.1 Deep ocean injection

Offshore storage is different because the CO_2 readily dissolves in seawater and forms a mixture with higher density than the seawater [41]. The heavier CO_2 solution in saline water sinks to the bottom of the ocean, where it resides at very high hydrostatic pressure. In addition to the high pressures at the bottom of the ocean, the prevailing temperature of approximately 4°C reduces the chemical activity of the CO_2 molecules. The already-in-operation CCS facility in Sleipner West (Norway) is an offshore storage facility, where the CO_2 is injected in the sandstone of the Utsira formation (a Miocene era formation) at depths more than 1 000 from the surface of the sea [50]. The seawater and sediment column combine to keep the seawater–CO_2 mixture at high pressure, isolated, and chemically stable. Ozaki et al. [33] envisioned CO_2 disposal in the deep ocean by a fleet of ships in motion and high-pressure injection. The deep ocean sequestration of CO_2 is significantly less risky than onshore storage and is the preferable long-term storage location for the gas [2, 51].

For the CO_2 to dissolve in seawater, it must be injected as small bubbles/droplets and this is achieved with high-pressure atomizers – e.g., orifice, pressure swirl, spinning disk, and rotary atomizers – that will, typically, disperse the CO_2 in small droplets of sizes on the order of mm [52]. To facilitate injection, the transportation pipeline must be divided into multiple branches with small nozzles and atomizers that inject the drops of CO_2 in the ocean. Since the prevailing temperature in deep water is 277 K and the pressure at 600 m is 6.033 MPa, the CO_2 is liquid, and the small drops rise with terminal velocity [53]:

$$V_T = \frac{2(\rho_w - \rho_g) g \alpha^2}{9 \mu_w}, \tag{6}$$

where ρ_w and ρ_g are the densities of the seawater and the liquid CO_2; α is the radius of the drops; and μ_w is the viscosity of the seawater, approximately 0.00167 Ns/m^2. As the liquid droplets rise in the seawater, the CO_2 is slowly dissolved, the droplet size decreases and the terminal velocity decreases. The time scale for the mass transfer process from gaseous CO_2 in the seawater is [53]:

$$\tau_m = \frac{\alpha^2}{D}, \tag{7}$$

where D is the diffusion coefficient of CO_2 in the seawater, 1.6×10^{-9} m^2/s [54, 55]. Therefore, the length scale for the diffusion of the rising CO_2 drops is:

$$L_m = \frac{2(\rho_w - \rho_g) g \alpha^4}{9 \mu_w D}, \tag{8}$$

Figure 4 depicts the diffusion length scale of CO_2 in seawater. As the CO_2 diffuses into the seawater and the drops become smaller, the diffusion length-scale diminishes to a vanishing point, when all the CO_2 has been dissolved. Because of this, a distance of two length scales ($2L_m$) is sufficient for the complete dissolution of this gas in seawater. A glance at Fig. 4 proves that, if the CO_2 is injected at 500–600 m depth all the droplets up to 2.6 mm in size will dissolve before they reach the ocean surface, where the gas may be exchanged with the atmosphere. Because atomizers inject drops with sizes that belong in a statistical distribution (e.g., average size 2 mm with 0.2 mm standard deviation), injection at 600 m is recommended here to ensure that even the drops at the upper tail of the distribution (three standard deviations) have enough residence time in the seawater for complete dissolution of CO_2. The naturally occurring downward advection of the denser CO_2–H_2O mixture ensures the replenishment of the injection zone with seawater of lower CO_2 concentration.

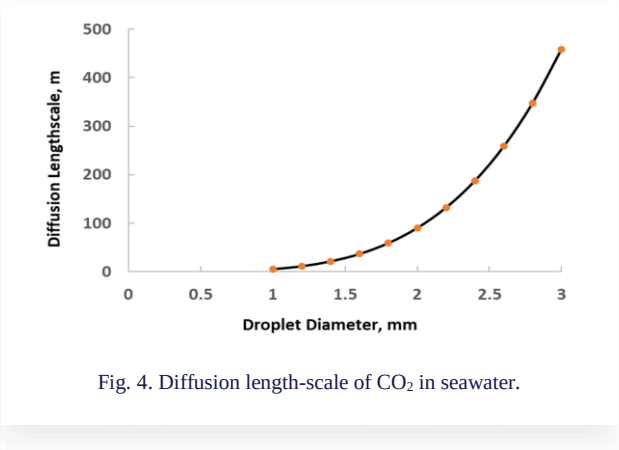

Fig. 4. Diffusion length-scale of CO_2 in seawater.

Alternatively, the CO_2 injection may be accomplished by a fleet of ships [33] that roam the ocean. In order to discharge all the CO_2, in their holds the ships will need to be furnished with compressors that will pressurize the CO_2 and inject it with a pressure higher than 6 MPa.

The monitoring of the CO_2 transportation pipelines and the injection sites is an essential part of the long-term carbon storage problem. Existing CO_2 pipelines in the USA are monitored bi-weekly by helicopters and injection/storage sites need to be continuously monitored by personnel. Such monitoring requires relatively small power consumption, but (because personnel is necessary) adds to the cost of storage. The IPCC report [2] estimates that the cost of monitoring is similar to that of transportation. However, monitoring optimization, – e.g. by partly using remote instrumentation facilities – significantly cuts this part of the CCS cost, as demonstrated in the existing CO_2 pipelines [37].

6. Total power for sequestration – the case of two Texan coal power plants

Calculations were performed for the total power needed for the capture, pressurization, transportation, and injection in the deep ocean of 90% of the yearly-averaged CO_2 emitted by two coal power plants in the ERCOT electrical grid of Texas. The first (case A) is the J. K. Spruce station, which is located outside the city of San Antonio at an elevation 198 m above sea level. The plant is composed of two units with a total power of 1 440 MW and uses subbituminous coal as its principal fuel. In 2021 this power plant generated 7 329 045 MWh and consumed total heat equivalent to 77.853×10^{12} MJ (73 213 439 MMBtu), indicating an average thermal efficiency of 33.89%. The plant emitted approximately 7.138×10^9 kg of CO_2 in the year 2021, or an average of 226.4 kg/s [56]. This power plant is 210 km from the Gulf of Mexico and 255 km from a location where the depth is at least 600 m. The Martin Lake power station in North Texas (case B) is composed of three units with a total rated power of 2 250 MW; it is located at an elevation of 98 m above sea level; and also uses subbituminous coal. In 2021 the Martin Lake power plant generated 13 179 510 MWh and consumed 151.317×10^{12} MJ (150 564 978 MMBtu) of heat with an average efficiency of 29.87%. The plant emitted approximately 14.680×10^9 kg of CO_2 or an average of 465.5 kg/s [57]. This power plant is located 350 km from the coast and 410 km from a location where the depth is at least 600 m. Regarding the transportation distances, it must be noted that the distance of the two power plants from the oil fields in the Permian Basin (for onshore storage) is slightly longer than their distance from the Gulf of Mexico storage sites.

It was stipulated that 90% of the emitted CO_2 – 204 kg/s for case A and 419 kg/s for case B – will be captured and transported to the storage locations. The hydrostatic pressure at 600 m is 6.033 MPa and the temperature is 277 K. As explained in section 4 it was also stipulated that, at the end of the pipeline, the CO_2 will be at supercritical pressure, that is its pressure will be at least 7.377 MPa. This is 1.344 MPa higher than the pressure at 600 m, which implies that the injection equipment will have enough pressure differential to operate. In all cases, common steel pipelines of schedule 30 were chosen for the transportation to withstand the high internal pressure.

Computations were performed to determine the pressure at the power plant that would enable the transportation and injection of CO_2. For the calculations, Eq. (4) was discretized and used in a finite-difference numerical scheme with the properties of CO_2 obtained from [36]. For case A it was determined that either an 18" (ID = 0.435 m) pipeline with initial pressure 14 MPa or a 20" (ID = 0.530 m) pipeline with initial pressure 9.2 MPa are sufficient for the CO_2 transport without an intermediate pressure station. For case B, which generates more CO_2 and is further from the injection region, it was determined that a 30" pipe (ID = 0.730 m) with initial pressure 11.4 MPa or a 28" pipe (ID =0.679 m) with 14.4 MPa initial pressure are sufficient to carry 90% of the emitted CO_2. The final choice of pipeline size will be determined by economic optimization, taking into account the pipeline cost and the cost of additional energy spent for the pressurization of the gas.

Table 1 shows some details for the total power and total annualized energy spent to operate the entire CCS system for the two cases. For the computations, the initial concentration of CO_2 in the flue gases is 15%. The efficiency of the separation process is 15%, slightly higher than the state-of-the-art facilities (12.8%), anticipating improvements following the current research efforts. The efficiency of the dual stage compressors is

82%, including the parasitic power for the intercooler. Based on the total CCS power in column 3, the fourth column shows the annual energy expenditure of the entire CCS system. The fifth column shows the net energy generated by the power plant. And the sixth column shows the yearly averaged thermal efficiency of the plant, when the energy for the CCS system is taken under consideration.

It is observed in Table 1 that the power for the separation (capture) of CO_2 from the flue gases is very significant, higher than that for the pressurization of the gas, even with the rather optimistic efficiency for separation. Also, that the entire CCS operations would consume close to one-third of the annual energy currently generated by the two power plants and that the thermal efficiency of these units drops by about 10 percentage points when the CCS energy is taken into account. This is in line with the range of estimates in [2], which does not include the injection process.

7. Cost of capture, transportation and storage

Viebahn and Chappin [58] conducted a bibliographical study and showed that the technical and research issues for the different processes that make up the CCS account for 69% of all the publications, while only 31% of the publications address the non-technical issues, which include estimates of the cost of the CCS processes, its effect on electricity prices, economic viability, the financing of the CCS projects in market-oriented economies, and political willingness.

Regarding any type of costs, one must always be cognizant of the fact that they are determined by labour and materials prices that rely on demand and supply considerations as well as the type of economy (market, centralized, regulatory, etc.). As a consequence, costs exhibit high variability [59] and, therefore, are laden with high uncertainty. Any economic analysis of the CCS projects is also laden with significantly higher uncertainty than the power and energy analyses of section 6, which are based on engineering principles and the state of technology. This is corroborated by a recent global assessment [60], which concluded that the costs of the onshore CO_2 transport and storage vary between \$4/ton and \$45/ton (variability of a factor of 11!). An assessment of the total CCS cost for five sites in the USA showed a similar range of variability with significantly higher costs – from \$18/ton to \$67/ton with a value as high as \$161/ton for a natural gas fueled power plant [61]. All of the CCS cost studies conclude that, since this is an evolving technology, further analysis with economic models is needed [2, 58, 59, 60, 61].

The principal costs for any CCS system are the pipeline (with the injection system at the end), the separation system, the compression system, and the cost of maintenance and monitoring. The capital cost of a pipeline in the USA market is made up of five separate costs:

1. Materials and Labour;
2. Rights of Way;
3. Trench construction;
4. Professional services (accounting, surveying, legal, etc.);
5. Terrain challenges (more expensive in rugged terrains). Offshore pipelines are almost twice as expensive as onshore pipelines and their construction cost increased by a factor of 4 since 1980 [59].

While the separation and compression capital costs are fairly well known and documented, the pipeline cost data for the USA market show significant variability with the principal variable being the length (in km) and size (in inches) of the pipe [59, 61, 62]. For this reason, the capital cost of the pipeline is treated as a parameter. Based on data from [60] and [62], for large (diameters larger than 10 inches) pipelines, this parameter varies in the range of \$50,000–\$120,000 per km and per inch.

In addition to the capital costs, the following are recurring annual expenses:

1. Monitoring (weekly or biweekly flights with helicopters, continuous instrument monitoring, education, and information of the urban populations near the pipeline, offshore injection region monitoring, etc.);
2. Maintenance and operational costs of the pipeline, the compression equipment, and the separation equipment;
3. The annual cost of the energy, which is generated by the power plants and diverted to the separation and compression systems.

The cost of the first two items is approximately 5% of the capital costs. For the fuel cost in item 3, the recent average cost of fuel (coal) was used – \$2.17 per MMBtu (\$2.07/GJ) [63] – as well as the average annual thermal efficiency of each power plant [56, 57]. This cost is the actual cost of the fuel to the utility corporation and is used here rather than the price of electricity.

A parameter that is crucial in market-oriented economies is the internal discount factor, r, of the pipeline corporations. The discount factor essentially takes into account the *time-value of money* by discounting future cash flows by a factor equal to $(1+r_d)^N$, where N is the year the cash flow is realized by the corporation [64, 65]. The discount rate, r_d, is higher during in-

Table 1. Power for the separation, transportation and injection of CO_2, annual energy consumed for CCS, net annual energy generated and power plant thermal efficiency.

	Separation MW	Transportation, Injection, MW	Total, MW	CCS Energy, GWh	Net Energy, GWh	Plant Efficiency, %
Case A, 18" pipe	162	103	265	2 325.6	5 003.4	24.5
Case A, 20" pipe	162	94	256	2 242.7	5 086.4	24.9
Case B, 28" pipe	333	214	548	4 796.6	8 382.9	19.9
Case B, 30" pipe	333	203	537	4 701.4	8 478.1	20.2

Table 2. Summary of CCS costs, cost per MWh and percentage price increase.

Discount rate, %	5	8	10	12	15
Case A, 18" pipe					
Ann. worth of capital	29 399 816	39 268 686	46 163 900	53 157 069	63 619 923
Additional cost	24 067 352	24 067 352	24 067 352	24 067 352	24 067 352
Cost of fuel for CCS	50 413 323	50 413 323	50 413 323	50 413 323	50 413 323
Cost per MWh	20.8	22.7	24.1	25.5	27.6
Price increase, %	61.1	66.9	70.9	75.0	81.2
Case B, 28" pipe					
Ann. worth of capital	63 958 878	85 428 464	100 428 905	115 642 443	138 404 232
Additional cost	52 358 180	52 358 180	52 358 180	52 358 180	52 358 180
Cost of fuel for CCS	118 910 540	118 910 540	118 910 540	118 910 540	118 910 540
Cost per MWh	28.1	30.6	32.4	34.2	36.9
Price increase, %	82.5	90.1	95.3	100.7	108.7

flationary times and is one of the dominant parameters for the appraisal of all long-term investments [66].

Using a lifetime for the CCS project of 30 years and a discount rate in the range of 5% to 15%, the capital cost for the construction of the entire CCS system was annualized using the annual worth, *AW*, value of the capital cost [67]:

$$AW = PV\left[\frac{r_d(1+r_d)^N}{(1+r_d)^{N+1}-1}\right], \quad (9)$$

where *PV* is the present (initial) cost of the investment and *N* is the lifetime of the project. The costs mentioned above in items 1–3 are added to the annual worth of the project to determine the total annualized cost.

Table 2 summarizes these results for two cases – using an 18" pipeline for the Spruce unit and a 28" pipeline for the Martin Lake unit. The costs in the table pertain to a unit cost for the construction of the pipeline of $70 000 per km and per inch; and 5% for the operations, maintenance, and monitoring cost of the pipeline. The percentage cost increase in the last lines has been calculated using the average selling price per MWh ($34/MWh) in the five-year period 2017–2021. In the absence of any subsidies for CCS, this cost is the minimum amount that will have to be added to the current average price of electricity for the utilities to recoup their investments.

The data of Table 2 are also shown graphically in Fig. 5. It is observed in Table 2 and Fig. 5 that the installation of a CCS unit that would remove 90% of the CO_2 generated in the two power plants would also add significantly to the cost of electricity generation. Changing the corporation discount rate from the low end of 5% to the high end of 15 %, would increase the cost of the entire CCS process by approximately 32% for both power plants. The lower part of the discount rates (5–8%) can only be achieved with government subsidies and loan guarantees – with such guarantees, bonds can be issued by the corporation at low interest. In the absence of loan guarantees or other governmental incentives, the investing corporations will use the upper range of the discount rates (12–15%) because they will have to issue their own bonds at a higher interest rate.

The other parameter that significantly affects the cost of transportation and storage is the unit cost of the pipeline, which is substantially higher in mountainous regions and offshore locations. Figure 6 shows the effect of this parameter on the cost

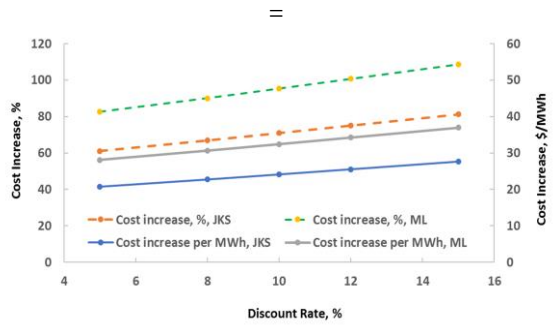

Fig. 5. The cost of carbon capture and storage for two power plants in Texas as a function of the discount rate.

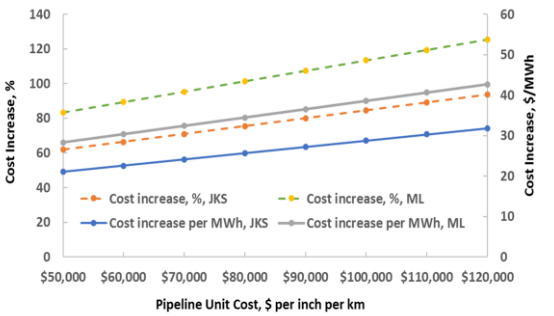

Fig. 6. The cost of carbon capture and storage for two power plants in Texas as a function of the unit cost of the pipeline.

increase as well as the fraction of this cost in relation to the average wholesale price of electricity, $34/MWh. It is observed in the data of Fig. 6 that doubling the unit price of the pipeline (e.g. from $50k to $100k) increases the total cost of the CCS process by 36%.

8. Conclusions

A holistic calculation of the energy required, and the associated cost for CCS entails calculations for four distinct processes: a) separation of CO_2 from the other flue gases; b) compression; c) transportation; and d) injection into the storage site. The separation of this gas from the flue gases requires mechanical work or a combination of high-temperature heat (which corresponds to significant equivalent work) and parasitic work. For the transportation part, the CO_2 should be in the dense supercritical state until it reaches the injection site. This implies that the gas must be compressed to states higher than 7.3 MPa at the expense of significant power. For the injection process, given the properties of this greenhouse gas, its dissolution with seawater at depths more than 600 m is very likely the most promising storage method at present.

Calculations were made for the power and annualized energy requirements as well as for the cost of the entire CCS for two power plants, located in Texas, USA. The CCS process for the Martin Lake unit would consume annually 31% of the total electricity generated by the plant. For the larger Spruce power plant, the CCS process would consume close to 36% of the annually generated electricity. The pipelines for the transportation of the compressed CO_2 to the storage sites, the separation unit, and the compression unit entail significant capital cost. Two parameters, the unit cost of the pipeline and the discount rate, have a significant influence on the total annualized cost of CCS. Doubling the unit prices for the pipeline installation increases by 36% the annual cost of the entire CCS system. Increasing the discount rate from 5% to 15% would increase this annualized cost of CCS by 32%.

Acknowledgements

This research was partly supported by the W.A. (Tex) Moncrief chair in Engineering at Technical Christian University.

References

[1] US-EPA. (2020). *Sources of Greenhouse Gas Emissions*. Report at: https://www.epa.gov/ghgemissions/sources-greenhouse-gas-emissions [accessed in June 2023].

[2] Metz, B., Davidson, O., de Coninck, H.C., Loos, M., & Meyer, L.A. (Eds.). (2007). *IPCC Special Report on Carbon Dioxide Capture and Storage*, Cambridge University Press, Cambridge, UK.

[3] Zevenhoven, R., Fagerlund, J., & Songok, J.K. (2011). CO_2 mineral sequestration: developments toward large-scale application. *GHG: Science and Technology*, 1(1), 48–57. doi: 10.1002/ghg3.7

[4] Rao, A., & Rubin, E. (2006). Identifying cost-effective CO2 control levels for amine-based CO2 capture systems. *Industrial and Engineering Chemistry Research*, 45(8), 2421–2429. doi: 10.1021/ie050603p

[5] Valenti, G., Bonalumi, D., & Macchi, E. (2009). Energy and exergy analyses for the carbon capture with the Chilled Ammonia Process (CAP). *Energy Procedia*, 1(1), 1959–1066. doi: 10.1016/j.egypro.2009.01.140

[6] Bonalumi, D., Lillia, S., & Valenti, G. (2019). Rate-based simulation and techno-economic analysis of coal-fired power plants with aqueous ammonia carbon capture. *Energy Conversion and Management*, 199, 111966. doi: 10.1016/j.enconman.2019.111966

[7] Weiland, R.H., Dingman, J.C., & Cronin, D.B. (1997). Heat Capacity of Aqueous Monoethanolamine, Diethanolamine, Nmethyldiethanolamine, and N-methyldiethanolamine-Based Blends with Carbon Dioxide. *Journal* of *Chemical and Engineering Data*, 42, 1004–1006. doi: 10.1021/je960314v

[8] Aliyon, K., Hajinezhad, A., & Mehrpooya, M. (2019) Energy assessment of coal-fired steam power plant, carbon capture, and carbon liquefaction process chain as a whole. *Energy Conversion and Management*, 199, 111994. doi: 10.1016/j.enconman.2019.111994

[9] Carapellucci, R., Di Battista, D., & Cipollone, R. (2019) The retrofitting of a coal-fired subcritical steam power plant for carbon dioxide capture: A comparison between MCFC-based active systems and conventional MEA. *Energy Conversion and Management*, 194, 124–139. doi: 10.1016/j.enconman.2019.04.077

[10] Rochelle, G., Chen, E., Freeman, S., Van Wagener, D., Xu, Q., & Voice, A. (2011). Aqueous piperazine as the new standard for CO2 capture technology. *Chemical Engineering Journal*, 171(3), 725–733. doi: 10.1016/j.cej.2011.02.011

[11] Li, X., Wang, S., & Chen, C. (2013). Experimental study of energy requirement of CO2 desorption from rich solvent. *Energy Procedia*, 37, 1836–1843. doi: 10.1016/j.egypro.2013.06.063

[12] Furcasa, F.E., Wanawan, P., Chacartegui, R., & Afzal, W. (2020). Sodium carbonate-based post combustion carbon capture utilising trona as main sorbent feed stock. *Energy Conversion and Management*, 208, 112484. doi: 10.1016/j.enconman.2020.112484

[13] Strube, R., Pellegrini, G., & Manfrida, G. (2011). The environmental impact of post-combustion CO2 capture with MEA, with aqueous ammonia, and with an aqueous ammonia–ethanol mixture for a coal-fired power plant. *Energy*, 36, 3763–3770. doi: 10.1016/j.energy.2010.12.060

[14] Lee, W.S., Lee, J.C., Oh, H.T., Baek, S.W., Oh, M., & Lee, C.H. (2017). Performance, economic and exergy analyses of carbon capture processes for a 300 MW class integrated gasification combined cycle power plant. *Energy*, 134, 731–742. 10.1016/j.energy.2017.06.059

[15] Kunze, C., Riedl, K., & Spliethoff, H. (2011). Structured exergy analysis of an integrated gasification combined cycle (IGCC) plant with carbon capture. *Energy*, 36, 1480–1487. doi: 10.1016/j.energy.2011.01.020

[16] Arabkhalaj, A., Ghassemi, H., & Markadeh, R.S. (2016). Thermodynamic evaluation of integrated gasification combined cycle: Comparison between high-ash and low-ash coals. *International Journal of Energy Research*, 40(12), 1638–1651. doi: 10.1002/er.3541

[17] Rosner, F., Qin, C., Rao, A., & Samuelsen S. (2019) Thermoeconomic analyses of concepts for increasing carbon capture in high-methane syngas integrated gasification combined cycle power plants. *Energy Conversion and Management*, 199, 112020. doi: 10.1016/j.enconman.2019.112020

[18] Petrakopoulou, F., Boyano, A., Cabrera, M., & Tsatsaronis, G. (2011). Exergoeconomic and exergoenvironmental analyses of a combined cycle power plant with chemical looping technology.

International Journal of Greenhouse Gas Control, 5(3), 475–482. doi: 10.1016/j.ijggc.2010.06.008

[19] Akinola, T.E., Bonilla Prado, P.L., & Wang, M. (2022). Experimental studies, molecular simulation and process modelling simulation of adsorption-based post-combustion carbon capture for power plants: A state-of-the-art review. *Applied Energy*, 317, 119156. doi: 10.1016/j.apenergy.2022.119156

[20] Zhang, X., He, X., & Gundersen, T. (2013). Post-combustion Carbon Capture with a Gas Separation Membrane: Parametric Study, Capture Cost, and Exergy Analysis. *Energy and Fuels*, 27(8), 3021798. doi: 10.1021/ef3021798

[21] Li, C., Guo, S., Ye, X., & Fu, W. (2019). Performance and thermoeconomics of solar-aided double-reheat coal-fired power systems with carbon capture. *Energy*, 177, 1–15. doi: 10.1016/j.energy.2019.04.058

[22] Carapellucci, R., Giordano, L., & Vaccarelli, M. (2015). Analysis of CO_2 post-combustion capture in coal-fired power plants integrated with renewable energies. *Energy Procedia*, 82, 350–357. doi: 10.1016/j.egypro.2015.11.801

[23] Saghafifar, M., & Gabra, S. (2020). A critical overview of solar assisted carbon capture systems: Is solar always the solution? *International Journal of Greenhouse Gas Control*, 92(10), 102852. doi: 10.1016/j.ijggc.2019.102852

[24] Michaelides, E. E. (2020). *Exergy and the Conversion of Energy.* Cambridge Univ. Press, Cambridge, UK.

[25] Paltsev, S., Morris, J., Kheshgi, H., & Herzog, H. (2021). Hard-to-Abate Sectors: The role of industrial carbon capture and storage (CCS) in emission mitigation. *Applied Energy*, 300, 117322. doi: 10.1016/j.apenergy.2021.117322

[26] Lee, H., Lee, J., & Koo, Y. (2022). Economic impacts of carbon capture and storage on the steel industry–A hybrid energy system model incorporating technological change. *Applied Energy*, 317, 119208. doi: 10.1016/j.apenergy.2022.119208

[27] Al Baroudi, H., Awoyomi, A., Patchigolla, K., Jonnalagadda, K., & Anthony, E.J. (2022). A review of large-scale CO_2 shipping and marine emissions management for carbon capture, utilisation and storage. *Applied Energy*, 287, 116510. doi: 10.1016/j.apenergy.2021.116510

[28] Michaelides, E.E. (2021). Thermodynamic Analysis and Power Requirements of CO_2 Capture, Transportation, and Storage in the Ocean. *Energy*, 230, 120804. doi: 10.1016/j.energy.2021.120804

[29] Zhai, H., Rubin, E.S., & Versteeg, P.L. (2011). Water use at pulverized coal power plants with post-combustion carbon capture and storage. *Environmental Science and Technology*, 45, 2479–2485. doi: 10.1021/es1034443

[30] Korbol, R., & Kaddour, A. (1995). Sleipner West CO_2 disposal: injection of removed CO_2 into the Utsira formation. *Energy Conversion and Management*, 36(6–9), 509–512. doi: 10.1016/0196-8904(95)00055-i

[31] Tanaka, S., Koide, H., & Sasagawa, A. (1995). Possibility of underground CO_2 sequestration in Japan. *Energy Conversion and Management*, 36(6–9), 527–530. doi: 10.1016/0196-8904(95)00059-M

[32] Kharaka, Y.K., Cole, D.R., Hovorka, S.D., Gunter, W.D., Knauss, K.G., & Freifeld B.M. (2006). Gas-water-rock interactions in Frio formation following CO_2 injection: Implications for the storage of greenhouse gases in sedimentary basins. *Geology*, 34(7), 577–580. doi: 10.1130/G22357.1

[33] Ozaki, M., Minamiura, J., Kitajima, Y., Mizokami, S., Takeuchi, K., & Hatakenka, K. (2001). CO_2 ocean sequestration by moving ships. *Journal of Marine Science and Technology*, 6(2), 51–58. doi: 10.1007/s773-001-8375-8

[34] Caldeira, K., & Wickett, M.E. (2003). Anthropogenic carbon and ocean pH. *Nature*, 425, 365–365. doi: 10.1038/425365a

[35] Caldeira, K., & Wickett, M.E. (2005). Ocean model predictions of chemistry changes from carbon dioxide emissions to the atmosphere and ocean. *Journal of Geophysical Research–Oceans*, 110(C9), C09S04. doi: 10.1029/2004JC002671

[36] REFPROP. (2013). *Reference Thermodynamic and Fluid Transport Properties.* National Institute of Standards and Technology, Boulder, Colorado.

[37] Wallace, M., Goudarzi, L., Callahan, K., & Wallace, R. (2015). *A Review of the CO_2 Pipeline Infrastructure in the U.S.* DOE/NETL Report-2014/1681

[38] Philips, P. (1912). The viscosity of carbon dioxide. *Proceedings of the Royal Society*, 87, 48–61.

[39] https://www.engineeringtoolbox.com/carbon-dioxide-dynamic-kinematic-viscosity-temperature-pressure-d_2074.html [accessed Feb. 2, 2023].

[40] Li, Y.H., & Tsui, T.F. (1971). The Solubility of CO_2 in Water and Sea Water. *Journal of Geophysical Research*, 76(18), 4203–4207. doi: 10.1029/JC076i018p04203

[41] Song, Y., Chen, B., Nishio, B., & Akai, B. (2005). The study on density change of carbon dioxide seawater solution at high pressure and low temperature, *Energy*, 30(11–12), 2298–2307. doi: 10.1016/j.energy.2003.10.022

[42] Hamond, H.F., & Fechner-Levy, E.J. (2000). *Chemical Fate and Transport in the Environment.* Academic Press, San Diego.

[43] Karmakar, S., Kolar, A.K. (2013). Thermodynamic analysis of high-ash coal-fired power plant with carbon dioxide capture. *International Journal of Energy Research*; 37(6), 522–34. doi: 10.1002/er.1931

[44] Davison, J.E. (2005). CO_2 capture and storage and the IEA Greenhouse Gas R&D Programme. *Workshop on CO_2 issues*, Middelfart, Denmark.

[45] Nessi, P., Papadopoulos, A., Kazepidis, P., Polichroniadis, A., Nitourou G., Voutetakis, S., & Seferlis, P. (2022). Pilot Scale Assessment of a Novel Phase-change Solvent for Energy Efficient Post-combustion CO_2 Capture, *Journal of Environmental Management*, 317(C), 115489. doi: 10.1016/j.jenvman.2022.115489

[46] Michaelides, E.E., Crowe, C.T., & Schwarzkopf, J.D. (Eds.) (2017). *Multiphase Flow Handbook* (2nd ed.). CRC Press, Boca Raton.

[47] Munson, B. R., Young, D. F., Okiishi, T. H., & Huwbsch, W. W. (2009). *Fundamentals of Fluid Mechanics*. Wiley.

[48] European Commission Report: https://joint-research-centre.ec.europa.eu/jrc-news/global-CO2-emissions-rebound-2021-after-temporary-reduction-during-covid19-lockdown-2022-10-14_en [accessed June 3, 2023].

[49] Hovorka, S.D., Meckel, T.A., & Trevino, R.H. (2013). Monitoring a large-volume injection at Cranfield, Mississippi—Project design and recommendations. *International Journal of Greenhouse Gas Control*, 18, 345–360. doi: 10.1016/j.ijggc.2013.03.021

[50] EIA. (2009). *Sleipner Project – CO_2 Capture and Storage*. EIA Greenhouse Gas R&D Programme Report.

[51] McBride-Wright, M., Maitland, G.C., & Trusler, J.P.M. (2015). Viscosity and Density of Aqueous Solutions of Carbon Dioxide at Temperatures from 274 to 449 K and at Pressures up to 100 MPa. *Journal of Chemical Engineering Data*, 60(1), 171−180. doi: 10.1021/je5009125

[52] Fritching, U., & Li, X.G. (2017). Spray Systems. In *Multiphase Flow Handbook* (2nd ed.). Michaelides, E.E., Crowe, C.T., & Schwarzkopf, J.D. (Eds.). pp. 1059−1090, CRC Press, Boca Raton.

[53] Michaelides, E.E. (2006). *Particles, Bubbles and Drops, Their motion, Heat and Mass Transfer*. World Scientific, New Jersey.

[54] Cadogan, S.P., Maitland, G.C., & Trusler, .J.P.M. (2015). Diffusion Coefficients of CO_2 and N_2 in Water at Temperatures between 298.15 K and 423.15 K at Pressures up to 45 MPa. *Journal of Chemical Engineering Data*, 59(2), 519−525. doi: 10.1021/je401008s

[55] Liu, Q., Endo, H., Fukuda, K., Shibahara, M., & Zhang, P. (2016). Experimental Study on Solution and Diffusion Process of Single Carbon Dioxide Bubble in Seawater. *Mechanical Engineering Journal*, 3(2), 1–9. DOI: 10.1299/mej.16-00269

[56] https://www.eia.gov/electricity/data/browser/#/plant/7097 [accessed in June 2023].

[57] https://www.eia.gov/electricity/data/browser/#/plant/6146 [accessed in June 2023].

[58] Viebahn, P., & Chappin, E.J.L. (2018). Scrutinising the Gap between the Expected and Actual Deployment of Carbon Capture and Storage—A Bibliometric Analysis. *Energies*, 11(9), 2319. DOI: 10.3390/en11092319

[59] Smith, C.E. (2016). Natural gas pipeline profits, construction both up. *Oil and Gas Journal*, September 5.

[60] Smith, E., Morris, J., Kheshgi, H., Teletzke, G., Herzog, H., & Paltsev, S. (2021). The cost of CO_2 transport and storage in global integrated assessment modelling. *International Journal of. Greenhouse Gas Control*, 109(2**),** 103367. doi: 10.1016/j.ijggc.2021.103367

[61] McKaskle, R. (2021). *Screening-Level Cost Estimates for CO_2 Capture and Transportation*. DOE report, DOE- FE0029381−11.

[62] How is the cost per mile determined? https://hanginghco.com/natural-gaspipeline-construction-cost-per-mile/last [accessed in June 2023].

[63] https://www.eia.gov/electricity/data.php [accessed July 10, 2023].

[64] Sullivan, W.G., Wicks, E.M., & Luxhoj, J.T. (2023). *Engineering Economy* (12th ed.). Pearson, New Jersey.

[65] Park, C.S. (2007). *Contemporary Engineering Economics* (4th ed.). Pearson, New Jersey.

[66] Götze, U., Northcott, D., & Schuster, P. (2015). *Investment Appraisal: Methods and Models* (2nd ed.). Springer, Heidelberg.

[67] Michaelides, E. E. (2018). *Energy, the Environment and Sustainability.* CRC Press, Boca Raton.

Co-published by
Institute of Fluid-Flow Machinery
Polish Academy of Sciences
Committee on Thermodynamics and Combustion
Polish Academy of Sciences

http://www.imp.gda.pl/archives-of-thermodynamics/

Simulation and experimental study of the thermal characteristics of a high-speed motorized spindle

Wei Zhang[1,2*], Huaqiao Jiang[2]

[1]China Light Industry Plastic Mold Engineering Technology Research Center, Ningbo Polytechnic, Ningbo 315800, China
[2]Ningbo Shuaitelong Group Co., Ltd, Ningbo 315000, China
*Corresponding author email: zw111150@163.com

Received: 21.07.2023; revised: 13.10.2023; accepted: 20.10.2023

Abstract

Based on the finite element simulation software ANSYS Workbench, this study reports the thermal characteristics of a high-speed motorized spindle. The temperature field distribution and axial thermal deformation of the motorized spindle are then detected on an experimental platform. A comparison between the experimental and simulation results revealed the temperature rise of the motorized spindle during the working process. Under steady-state conditions of the working motorized spindle, the temperatures of the front bearing, rear bearing and stator were determined as 20°C, approximately 30°C and 25°C, respectively. The axial thermal elongation of the motorized spindle is approximately 10 μm.

Keywords: High-speed motorized spindle; Thermal characteristic; Finite element simulation.

Vol. 45(2024), No. 1, 17–22; doi: 10.24425/ather.2024.150434

Cite this manuscript as: Zhang, W., & Jiang, H.Q. (2024). Simulation and experimental study of the thermal characteristics of a high-speed motorized spindle. *Archives of Thermodynamics*. 45(1), 17–22.

1. Introduction

The electric spindle is the core component of high-speed machine tools. A high-speed electric spindle is highly integrated and has a compact internal structure that impedes heat dissipation from the bearings and motors. Consequent thermal deformation of the electric spindle considerably reduces the machining accuracy, production efficiency and service life of the machine tool. As thermal errors can account for up to 70% of the total error of the machine tool [1–3], thermal problems have dominated research on high-speed electric spindles. Zhang et al. studied a coupled model of thermal-flow-structure. The simulation results showed that when the diameter of the cooling channel is 7 mm, a spiral cooling system develops a lower temperature but greater radial thermal deformation than a U-shaped cooling system [4]. Su et al. established a thermal fluid-solid coupling model of a hydrostatic spindle system using the finite volume method. They simulated the heat generation of the heat source and the fluid-solid heat transfer process [5]. Other researchers analyzed the internal friction force and established a friction dynamics model of the bearing [6, 7]. It was found that sliding friction movement between the bearing ball and the rolling element intensifies after increasing the bearing speed and lowering the preload. Chen et al. [8] studied the influence of rotational speed on the temperature field distribution of a high-speed electric spindle. They reported a linear temperature rise of the electric spindle from 6 000 to 10 000 rpm. At speeds exceeding 10 000 rpm, the temperature rise became exponential owing

Nomenclature

d – diameter, m
H – heat flow in the bearings, N·mm
L – length, m
M – friction torque, N·mm
n_z – rotational speed, rpm
N – exponent
Nu – Nusselt number
P – rated power output, W
Pr – Prandtl number
q – heat generation rate, W/m^3
Q – rated heat output, W
Re – Reynolds number
u – velocity, m/s
x, y, z – coordinates, m

Greek symbols

α_1 – convective heat transfer coefficient, W/(m^2·K)
η – efficiency,
λ – thermal conductivity, W/(m·K)
μ – dynamic viscosity, Pa·s

to the intense heat generated by friction between the front and rear bearings. The method of Kumar et al. [9] selects the optimal number of temperature sensors for predicting the thermal deformation at the required prediction accuracy. The model accuracy was 86.72% with two temperature sensors and 85.99% with one temperature sensor. They concluded that a single temperature sensor can sufficiently predict the deflection of the tool centre point with an accuracy compromise of 0.73%.

Applying the finite element method in ANSYS Workbench, the present authors simulate and study the thermal characteristics of an electric spindle. The simulation results are experimentally verified by measuring the temperature field distribution and axial thermal deformation of the electric spindle. This paper reveals the temperature rise during the working process of the electric spindle, along with the temperature field distribution and axial thermal deformation of the electric spindle under thermally stable conditions, providing a reference and guidance for the thermal design of electric spindles.

2. Materials and research methods

2.1. Simulation model and grid division

The structural models of electric spindles in practical engineering applications are commonly complex. Finite element analyses of the original model require a large number of calculations, which are difficult to run and often obtain non-ideal results. To avoid these problems, a reasonable finite element model for a specific problem must be developed before running the finite element analysis. The present study adopts a series of simplified methods for electric spindle modelling. Smooth component surfaces are assumed and the chamfers, fillets, threaded holes, and small protrusions on the original model are assumed to negligibly affect the thermal structure analysis. Factors with low impact on the thermal analysis, such as the broach in the model and the spiral flow channel on the shell, are also neglected. The surfaces of irregular parts, such as the balls in ball bearings, are simplified as circular rings with the dimension of rolling diameter. The proposed dynamic model is developed based on a high-speed end milling spindle (Model: CFV12000) of rated power 7.5 kW with a maximum spindle speed of 12 000 rpm, an installation dimension of 180 mm and a front bearing diameter of 70 mm. A cross-section of the simplified model is shown in Fig. 1. ANSYS includes various meshing methods for three-dimensional geometries, such as Automatic, Tetrahedral, and Sweep Meshing. The present simulation uses the sweeping method for grid division. The results of the grid division are shown in Fig. 1. The grid size is set to 4 mm and the final number of divided nodes is 291 869 with 147 785 units.

The centre spindle and broach bar of the electric spindle are composed of 20CrMnTi, the spacer parts are composed of GB-standard alloy bearing steel (GCr15), and all other parts are composed of 40Cr. 20CrMnTi, GCr15, and 40Cr were added as new materials to the material library of ANSYS Workbench, and their densities, Young's moduli and Poisson's ratio were assigned to the values given in Table 1.

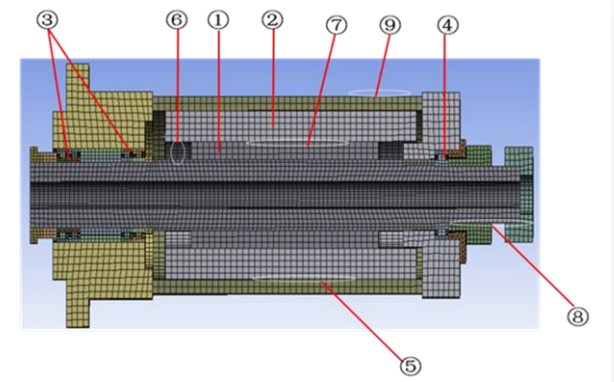

Fig. 1. Cross-section and grid division of the electric spindle model.

2.2. Calculation of thermal boundary conditions

Before analyzing the thermal characteristics of an electric spindle using the finite element method, we must determine the boundary conditions. In the present study, boundary conditions are required only for the heat source and convective heat transfer.

2.2.1. Calculation of heat generation rate of heat source

An electric spindle is heated mainly by losses of the stator and rotor, including magnetic loss, electrical loss and friction loss. The rated heat output Q of a motor is calculated as

Table 1. Properties of the electric spindle materials.

Material	Density (kg/m³)	Elastic modulus (GPa)	Poisson's ratio	Thermal expansion coefficient (K-1)	Specific heat capacity (J/(kg.K))	Thermal conductivity (W/(m.K))
GCr15	7810	219	0.300	1.4e-5	553	40.11
40Cr	7870	211	0.277	1.2e-5	460	34.00
20CrMnTi	7860	212	0.289	1.3e-5	460	44.00
GCr15	7810	219	0.300	1.4e-5	553	40.11

$$Q = P\frac{(1-\eta)}{\eta}, \quad (1)$$

where P is the rated output power of the motor and η is the motor efficiency

The thermal characteristics of the feed system largely depend on the friction heat generated in the rolling bearings, which is mainly caused by friction torque on the bearings and the viscous friction of the lubricants. Palmgren obtained an empirical formula for the friction torque on rolling bearings [10]. The heat flow H in the bearings is the following function of friction torque and speed:

$$H = M \times n_z \times 1.047 \times 10^{-4}, \quad (2)$$

$$M = M_1 + M_v. \quad (3)$$

In this formula, M is the total friction torque on the bearings, (N·mm), n_z is the bearing speed (rpm), and M_1 is the friction loss related to the bearing load which reflects elastic hysteresis and local sliding. M_v is the speed-related fluid power loss in the reaction lubricant.

2.2.2. Calculation of convective heat transfer coefficient

The convective heat transfer coefficient mainly depends on the cooling of the main shaft by circulating cooling oil and the other surface convective coefficients of the main shaft. As the cooling oil flows through a spiral cooling groove, it extracts the heat transferred from the main shaft. The heat is exchanged through the oil–water exchange system and the oil returns to the oil tank for the next cycle. The convective heat transfer coefficient α_1 was calculated using the Nusselt equation [11] under forced convection conditions:

$$\alpha_1 = \frac{\mathrm{Nu}\lambda}{d}, \quad (4)$$

where Nu is the Nusselt number, λ is the thermal conductivity of the fluid and d is the diameter of the conducting cylindrical surface.

In practical applications, the heat transfer through pipes is usually turbulent. The Nusselt number of turbulent heat transfer is calculated using the Dittus–Boelter formula [12] as

$$\mathrm{Nu} = 0.023\mathrm{Re}^{0.8}\mathrm{Pr}^{N}, \quad (5)$$

for Re > 1 000, 0.7 < Pr < 120.

In Eq. (5), Re is the Reynolds number and Pr is the Prandtl number. N = 0.4 when heating the fluid and 0.3 when cooling the fluid. L/d is the ratio of pipe length to pipe diameter during internal convection. By introducing the Nu value to the convective heat transfer formula, we can calculate the forced convective heat transfer coefficient between the coolant and the spindle sleeve.

The convective coefficients on the other surfaces of the axis determine whether the fluid flow is laminar or turbulent [13]. The empirical formula for selecting Nu is based on the flow pattern. The values of Pr and λ depend on the fluid properties. Finally, the convective heat transfer coefficient is calculated using Eq. (4).

Table 2. Calculated heat generation rates and heat transfer coefficients for the main components of the electric spindle.

Fig. 1	Parameter	Calculation results
1	Heat generation rate of motor stator q_d (W/m³)	2.00×10⁵
2	Heat generation rate of motor rotor q_z (W/m³)	4.00×10⁵
3	Heat generation rate of front bearing q_f (W/m³)	4.00×10⁵
4	Heat generation rate of rear bearing q_r (W/m³)	3.00×10⁶
5	Convective heat transfer coefficient between cooling oil and electric spindle α (W/(m²K))	850.00
6	Convective heat transfer coefficient between the rotor end and surrounding air α_{t1} (W/(m²K))	172
7	Coefficient of convective heat transfer between stator and rotor gaps α_{t2} (W/(m²K))	146
8	Convective heat transfer coefficient of other moving surfaces of the spindle α_{t3}(W/(m²K))	180
9	Convective heat transfer coefficient on other stationary surfaces of the main shaft α_{t4} (W/(m²K))	9.70

2.2.3. Calculated heat generation rate and convective heat transfer coefficient of the heat source

The estimates of some components found from empirical formulas may be inaccurate and deviate from the actual values. Therefore, some data were adjusted to fit the actual situation during the simulation. Table 2 lists the adjusted heat generation rates and heat transfer coefficients of the main components, which were loaded into the ANSYS Workbench for analysis.

Typical electric spindles used in practical engineering are complex assemblies of solid components. To ensure heat transfer between these components, the contact area between the entities is automatically created. Heat transfer occurs only between two parts that are initially in contact. The junction surface is set as a bond connection. According to [14], the heat transfer coefficient of each junction surface of a motorized spindle is 3 200 W/(m^2·K).

2.3 Experimental study on the thermal characteristics of three electric spindles

The thermal characteristics of electric spindles must be experimentally determined because finite element simulations inevitably contain numerical errors. Combining experimental methods with finite element analyses can improve the accuracy of thermal characterization of electric spindles. The thermal drift at the end of the spindle and the thermal tilt of the spindle were measured using the 5-point method (sensors installation points x_1, x_2, y_1, y_2, and z in Fig. 2). To measure the temperature field and axial thermal deformation of the electric spindle, this study adopts displacement measurement systems with the appropriate measurement range, resolution, thermal stability and accuracy, along with high-precision capacitive sensors and a thermal-resistance temperature sensor with sufficient resolution and accuracy (LION PT100 with class A accuracy, a measurement error of ±[0.15°C + 0.002|t|] and measurement range of –50°C–500°C). The thermal-resistance temperature sensor was placed in a predrilled hole inside the spindle and the sensors were installed at three positions: the front bearing outer ring, the rear bearing outer ring and the rotor. Data were acquired by a dial indicator that detects the reference movement distance of the electric spindle. The dial indicator should meet the corresponding standards and be provided by relevant suppliers or enterprises. These gauges (accuracy class 0; measurement error ±0.002) were installed on the machine tool as shown in Fig. 2.

The steps for conducting thermal characteristic experiments are as follows: The experimental device was thoroughly cleaned to remove dirt from the device platform, which interferes with the results of the high-accuracy capacitive displacement sensors and inspection rods (resolution 0.06 nm; adjustable bandwidth up to 15 kHz). Next, the inspection instruments and tools were installed in a certain order. All necessary levelling, geometric adjustments and functional inspections of the equipment should be completed prior to the experiment, and the initial experimental conditions must be confirmed and recorded. The initial temperature, front- and rear bearing temperature, stator temperature, and cooling oil flow of the thermal characterization were set to 17.35°C, 18.6°C, 24°C and 24 l/min, respectively. In preparation for the experiments, the machine tool was preheated at 6 000 rpm for five minutes. During the experiments, the speed was increased to 12 000 rpm and continued for approximately two hours while the data were recorded in real time. Recorded were the temperatures of the front and rear bearings, the temperature of the cooling oil, the displacement degree of the sensor and the temperature of the stator. During the first 30 minutes, the experimental data were recorded at half-minute intervals because the temperature of the electric spindle rapidly changed over this period. From 30 minutes to one hour, the overall temperature trend of the electric spindle slowed so the recording period was increased to one minute. After one hour, when the overall temperature of the electric spindle had stabilized, the recording period was further extended to three minutes.

3. Results and analysis

3.1. Simulation results and analysis

3.1.1. Temperature field analysis

Figure 3 shows the simulated temperature field of the electric spindle. The steady-state temperatures of the front bearing, rear bearing, stator and rotor were approximately 20°C, 31°C, 25°C and 35°C, respectively. The temperature field reveals the components with large heat capacity and the key heating areas (rotor and rear bearing). Accurate determination of the heat capacity is crucial for accurate thermal analysis of the motorized spindle. The temperature field analysis of the motorized spindle preliminarily determines the effectiveness of a thermal design and indicates the direction of thermal structure optimization. First, the

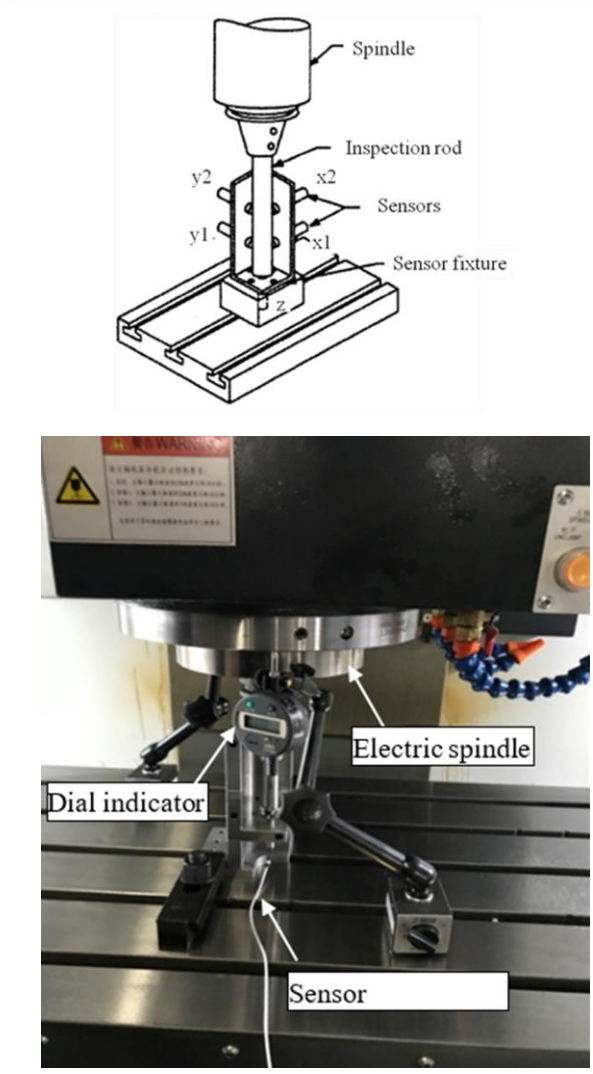

Fig. 2. Schematic diagram (top) and view of the experimental setup (bottom).

key components with large thermal capacity can be optimized to control the heating of the motorized spindle. Second, the heat sources can be symmetrically distributed to prevent thermal tilting and reduce harmful thermal deformation. Third, a thermal equilibrium design of the motorized spindle structure will ensure an evenly distributed temperature field. Finally, the motorized spindle is guided to expand and contract regularly in the desired direction with the desired displacement, laying the foundation of reasonable thermal control.

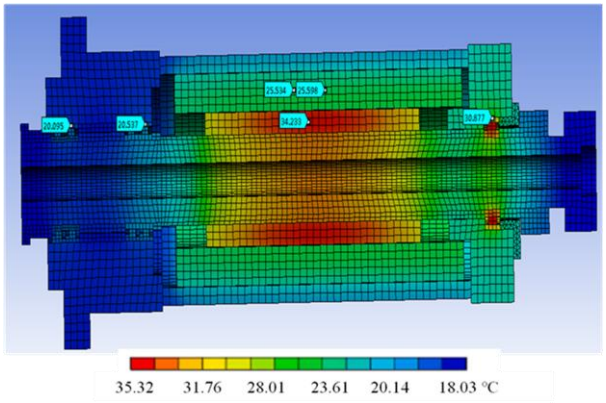

Fig. 3. Calculated temperature field of the electric spindle

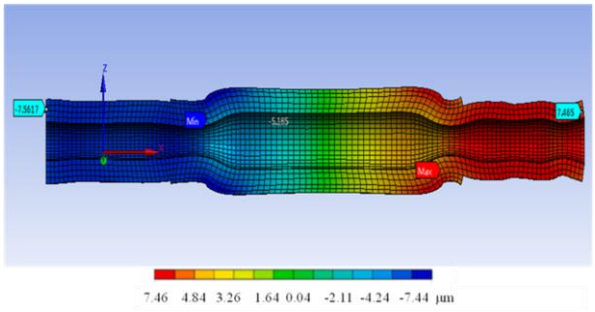

Fig. 4. Calculated axial thermal elongation of the electric spindle.

3.1.2. Thermal deformation analysis

Figure 4 shows the calculated axial thermal elongation of the electric spindle. The maximum thermal elongation appears in the middle of the electric spindle. The front and rear ends are elongated by approximately 7.5 μm. The maximum axial deformation is located at the rear end of the main spindle, because heat is transmitted from the high temperature area to the low temperature area. The final axial deformation will be most obvious at the lowest temperature area because of heat conduction. As the temperature at the rear end of the main shaft is the lowest temperature area of the entire main spindle, the thermal deformation is the largest. When thermally designing an electric spindle, one must first consider the deformation amounts of the most severely deformed components along the axial direction. Therefore, a structural thermal equilibrium design of the key components is necessary for obtaining the overall thermal deformation of the motorized spindle and hence achieving an overall optimized design with a balanced and symmetric structure.

3.2. Experimental results and analysis

3.2.1. Experimentally determined temperature field

Figure 5 plots the time courses of temperatures in different parts of the electric spindle. Between startup and steady-state, the temperatures of the front and rear bearings rose by approximately 1°C (steady-state temperature 20°C) and 10°C (steady-state temperature 28.5°C), respectively. The temperatures of the stator and cooling oil inlet temperature remained nearly constant, stabilizing at 25°C and 17.5°C, respectively. The measured values were very close to the simulation results, in which the approximate steady-state temperatures of the front bearing, rear bearing and stator were 20°C, 31°C and 25°C, respectively. Therefore, the rotor is the main heat source of the motorized spindle during operation. When thermally designing a motorized spindle, ensuring thermal equilibrium of the heat source and designing a reasonably motorized spindle structure are essential.

3.2.2. Experimentally determined thermal deformation

Figure 6 plots the axial thermal elongation of the electric spindle versus time. Here, the axial thermal elongation alone was tested because it substantially influenced the performance of the machining tool. During the experiment, the axial thermal elongation of the electric spindle remained stable at 10.5 μm after 40–60 minutes and slowly decreased as the room temperature

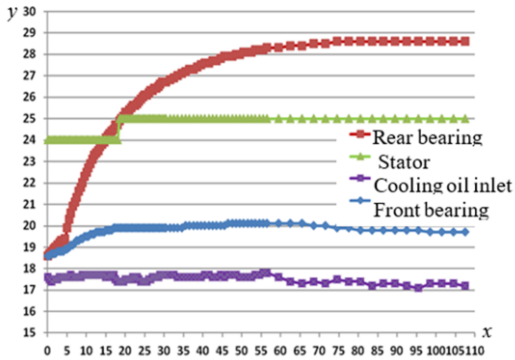

Fig. 5. Measured axial thermal elongation of the electric spindle (*y* coordinate: thermal elongation (um); *x* coordinate: time (min))

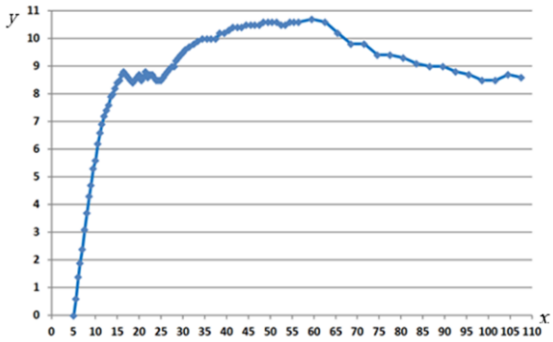

Fig. 6. Measured temperatures of the electric spindle components (*y* coordinate: temperature (°C); *x* coordinate: time (min)).

decreased in the later stages of the experiment. The stable elongation (10.5 μm) was regarded as the maximum thermal elongation of the electric spindle. The simulated thermal elongation of the electric spindle (7.5 μm) agreed with the experimental result within the allowable error range [15, 16]. Therefore, we speculate that the thermal elongation of the electric spindle is between 8 and 10 μm. The impact of the whole thermal elongation must be considered when designing an electric spindle. If the inferred thermal elongation exceeds the requirements, the spindle must be redesigned while considering (1) whether thermal symmetry is required, (2) whether an even temperature field distribution is required, and (3) whether the cooling conditions should be strengthened.

4. Conclusions

This article investigated the thermal characteristics of a high-speed motorized spindle through finite element simulations using the ANSYS Workbench software. First, the thermal characteristics of the electric spindle were simulated and the simulation results were experimentally verified. The results revealed that the temperature rises during the working process of the electric spindle. The temperature field distribution and axial thermal deformation of the electric spindle were determined under thermally stable conditions. The main conclusions are summarized below.

At an initial room temperature and cooling oil-flow rate of 17.35°C and 24 l/min, respectively, the motorized spindle operated at 12 000 rpm. During stable-state operation, the front bearing temperature, rear bearing temperature and stator temperature were approximately 20°C, 30°C and 25°C, respectively. Under axial thermal expansion, the electric spindle was elongated by approximately 10 μm. The experimental and simulation results deviated within the allowable error range. We inferred that the actual thermal elongation of the electric spindle is between 8 and 10 μm. Meanwhile, the main heat sources of the operating electric spindle are the rear bearing and rotor. When designing the electric spindle, one must fully consider the thermal balance of the heat source and the structure of the electric spindle. These results provide a reference and guidance for the thermal design of electric spindles.

Acknowledgement

This work has been funded by the Nature Science Foundation of Ningbo No. 2022J179 and NBPT 2022 national scientific research project cultivation subject No. NZ22GJ002.

References

[1] Hao, J., Li, C.Y., Song, W.J., Yao, Z.H., Miao, H.H., Xu, M.T., et al. (2023). Thermal-mechanical dynamic interaction in high-speed motorized spindle considering nonlinear vibration. *International Journal of Mechanical Sciences*, 240(2), 107959. doi: 10.1016/J.IJMECSCI.2022.107959

[2] Dai, Y., Tao, X.S., Xuan, L.Y., Ou, H., & Wang, G. (2022). Thermal error prediction model of a motorized spindle considering variable preload. *The International Journal of Advanced Manufacturing Technology*, 121(7–8), 4745–4756. doi: 10.1007/S00170-022-09679-Y

[3] Dai, Y., Tao, X.S., Li, Z.L., Zhan, S.Q., Li, Y., & Gao, Y.H. (2022). A Review of Key Technologies for High-Speed Motorized Spindles of CNC Machine Tools. *Machines*, 10(2), 145. doi: 10.3390/MACHINES10020145

[4] Zhang, Y., Wang, L.F., Zhang, Y.D., & Zhang, Y.D. (2021). Design and thermal characteristic analysis of motorized spindle cooling system. *Advances in Mechanical Engineering*, 13(5), 781–802. doi: 10.1177/16878140211020878

[5] Su, H., Lu, L.H., Liang, Y.C., Zhang, Q., Sun, Y. (2014). Thermal analysis of the hydrostatic spindle system by the finite volume element method. *The International Journal of Advanced Manufacturing Technology*, 71(9–12), 1949–1959. doi: 10.1007/s00170-014-5627-8

[6] Sun, X. Y. (2019). *Investigation on Thermal Characteristics and Cooling Method for High-speed Motorized Spindle*. Shanghai Jiaotong University. doi: 10.27307/d.cnki.gsjtu.2019.002077

[7] Su, C., & Chen, W. (2022). An optimized thermal network model to evaluate the thermal behavior on motorized spindle considering lubricating oil and contact factors. *Proceedings of the Institution of Mechanical Engineers, Part C: Journal of Mechanical Engineering Science*, 236(13), 7484–7499. doi: 10.1177/09544062221075171

[8] Zhang, C.X., Chen, L.F., Wang, W.M., & Liu, F.L. (2015). Research on high-speed motorized spindle thermal characteristics: simulation and experiment. *Journal of Beijing University of Chemical Technology (Natural Science Edition)*, 42(6), 90–96. doi: 10.13543/j.cnki.bhxbzr.2015.06.015

[9] Kumar, S., & Srinivasu, D.S. (2022). Optimal number of thermal hotspots selection on motorized milling spindle to predict its thermal deformation. *Materials Today: Proceedings*, 62(6), 3376–3385. doi: 10.1016/J.MATPR.2022.04.267

[10] Sun, S., Qiao, Y., Gao, Z., Wang, J., & Bian, Y. (2023). A thermal error prediction model of the motorized spindles based on AB-HHO-LSSVM. *The International Journal of Advanced Manufacturing Technology*, 127(5–6), 2257–2271. doi: 10.1007/S00170-023-11429-7

[11] Truong, D.S., Kim, B.S., & Ro, S.K. (2021). An analysis of a thermally affected high-speed spindle with angular contact ball bearings. *Tribology International*, 157(5), 106881. doi: 10.1016/J.TRIBOINT.2021.106881

[12] Kumar, B.V., Manikandan, G., & Kanna, P.R. (2021). Enhancement of heat transfer in SAH with polygonal and trapezoidal shape of the rib using CFD. *Energy*, 234(9), 121154. doi: 10.1016/ j.energy.2021.121154

[13] Singh, A., & Singh, D.K. (2021). An investigation on the forced convection heat transfer in the gap of two rotating disks with laminar inflow. *Heat Transfer*, 50(7), 6964–6983. doi: 10.1002/htj.22212

[14] Tang, Y., Jing, X., Li, W., He, Y., & Yao, J.X. (2021). Analysis of influence of different convex structures on cooling effect of rectangular water channel of motorized spindle. *Applied Thermal Engineering*, 198(5), 117478. doi: 10.1002/htj.22212

[15] Jiang, Z.Y., Huang, X.Z., Chang, M.X., Li, C., & Ge, Y. (2021). Thermal error prediction and reliability sensitivity analysis of motorized spindle based on Kriging model. *Engineering Failure Analysis*, 127(9), 105558. doi: 10.1016/J.ENGFAILANAL.2021.105558

[16] Cheng, Y., Zhang, X., Zhang, G., Jiang, W., & Li, B. (2022). Thermal error analysis and modeling for high-speed motorized spindles based on LSTM-CNN. *The International Journal of Advanced Manufacturing Technology*, 121(5/6), 3243–3257. doi: 10.1007/S00170-022-09563-9

Co-published by
Institute of Fluid-Flow Machinery
Polish Academy of Sciences
Committee on Thermodynamics and Combustion
Polish Academy of Sciences

http://www.imp.gda.pl/archives-of-thermodynamics/

Numerical assessment of solar air heater performance having a broken arc and broken S-shaped ribs as roughness

Shivam Haldia[a], Vijay Singh Bisht[a], Prabhakar Bhandari[b*], Lalit Ranakoti[c], Akashdeep Negi[c]

[a]Department of Thermal Engineering, Faculty of Technology, Veer Madho Singh Bhandari Uttarakhand Technical University, Dehradun, Uttarakhand-248007, India
[b]Department of Mechanical Engineering, School of Engineering and Technology, K. R. Mangalam University, Gurgaon, Haryana-122103, India
[c]Department of Mechanical Engineering, Graphic Era Deemed to University, Clement Town, Dehradun, Uttarakhand-248002, India
*Corresponding author email: prabhakar.bhandari40@gmail.com

Received: 23.11.2023; revised: 28.12.2023; accepted: 19.03.2024

Abstract

This research article aims to provide a detailed numerical study of the multifaceted impact of S-shaped and broken arc roughness on solar air heaters. Therefore, a strong comparison was made between the modified heaters and smooth heaters for Reynolds numbers ranging from 2 000–22 000. Also, the impact of two parameters, i.e. pitch and gap was analyzed to optimize the performance of the heater. The gap varies from 0.3 mm to 0.9 mm in both types of ribs with a step size of 0.2 mm. Afterwards, the pitch distance between both types of roughness was varied from 15 mm to 25 mm in the step size of 5 mm. Notably, it has been observed that among all the considered configurations, the gap length of 0.9 mm and pitch length of 25 mm have shown significant improvements in heat transfer characteristics. The specific combination of the gap of 0.9 mm and pitch of 25 mm has demonstrated better heat transfer capabilities at the expense of an increased friction factor. Lastly, the thermal performance factor of the systems was analyzed and reported. It was reported that the pitch length of 25 mm and gap length of 0.9 mm have shown a maximum thermal performance factor value from 2.9 to 3.3, while the pitch length of 25 mm and gap length of 0.3 mm have depicted the lowest thermal performance factor value. In terms of the overall performance, i.e. the thermal performance factor, the combination with a gap of 0.9 mm and pitch of 25 mm has shown the best performance, while a gap of 0.3 mm and pitch of 25 mm has yielded the worst performance.

Keywords: Solar air heater; Thermal performance factor; S-shaped ribs; Broken arc; Numerical study

Vol. 45(2024), No. 1, 23–31; doi: 10.24425/ather.2024.150435

Cite this manuscript as: Haldia, S., Bisht, V.S., Bhandari P., Ranakotic, L., & Negi, A. (2024). Numerical assessment of solar air heater performance having a broken arc and broken S-shaped ribs as roughness. *Archives of Thermodynamics*, 45(1), 23–31.

1. Introduction

The combustion of conventional fuels, including coal, oil, and natural gases releases harmful gases with significant adverse effects on the environment. The limited availability of these conventional fuels has driven towards alternative sustainable and reliable sources, such as solar energy, wind energy, tidal energy, and more. Solar energy has emerged as a leading contender among these alternatives playing a pivotal role in reducing our dependency on conventional fuels by a substantial 40 % over the past few decades [1]. Its application can be seen in various sectors e.g., heating and cooling industries, water desalination, generation of electricity, automobile industries and so on [2–4]. However, harnessing the potential of solar energy always remains a challenge. Adding to this literature, Jani [5] has suggested solar air heaters (SA-heaters) as the best medium for harnessing solar energy in the form of heat.

SA-heaters transfer thermal radiation from the sun to the working fluids i.e., air. However, SA-heaters deal with the inherent drawback of lower thermal efficiency due to the low

Nomenclature

C_p – specific heat, J/(kgK)
f – friction factor
G – gap length in broken arc and broken S-shaped ribs, mm
k – thermal conductivity, W/(mK)
Nu – average Nusselt number
p – pressure, Pa
P – pitch, mm
Pr – Prandtl number
Re – Reynolds number, Re = $Dv\rho/\mu$
T – temperature, K
TPF – thermal performance factor
t – time, s
u, v, w – velocity components, m/s
x, y, z – coordinates

Greek symbols

α – thermal diffusivity, m^2/s
μ – dynamic viscosity, Pa·s
ρ – density, kg/m^3

Subscripts and Superscripts

in – inlet
r – roughened
s – smooth

Abbreviations and Acronyms

TPF – Thermal Performance Factor
SA-heater – Solar Air heater

thermal conductivity of air and reduce heat transfer from the absorber plate to the air. The airflow in SA-heaters is more often in a turbulent regime due to which thin laminar viscous sub-layers are formed near the absorber plate. Therefore, this laminar viscous sublayer can adversely affect the heat transfer rate [6]. To break the laminar viscous layer, various arrangements have been proposed on the absorber plate. Also, the similarity in the working of SA-heaters with various equipment like heat exchangers, car radiators, etc., is often considered by design researchers [7–9]. The use of artificial roughness like baffles, ribs, twisted tapes, dimples, etc., can mitigate the current associated problems [10–13].

A solar air heater with ribs of a square, rectangle, chamfered, circle, semi-circle, and triangle shape was investigated computationally by Chaube et al. [14]. The most effective thermo-hydraulic performance was reported for rectangular ribs. Additionally, it was observed that the data value is precisely predicted by the k-omega SST model, which is the shear stress transport turbulence model. Similarly, W-shaped ribs in upward and downward directions were analyzed by Lanjewar et al. [15]. It was observed that W-downward ribs have better thermo-hydraulic performance compared to W-upward ribs. Apart from this, multiple broken arcs and circular protrusions were used as roughness in a solar air heater in a novel way by Semalty et al. [16]. It was observed that multiple broken arcs and circular protrusions designs significantly enhance the solar air heater thermal performance with the least amount of frictional pressure drop. Furthermore, a numerical analysis was performed, by roughening the absorber plate with 45° Z-shaped baffles [17]. It was reported that a desirable blockage ratio of 0.3 produced optimum performance.

Different shape of tabulators has a significant impact on enhancing the performance of SA-heaters. Therefore, Ghildyal et al. [18] propose three different shaped turbulators i.e., D-shaped, reverse D-shaped and U-shaped for SA-heaters. It was observed that the U-shaped turbulator performs better in terms of overall performance compared to the other two configurations. Singh et al. [19] analyzed the effect of dimple roughness in S-shaped patterns in SA-heaters through computational work. For all arrangements, the dimple dimension of 2.8 mm and relative pitch roughness of 10 at the Reynold number (Re) of 20 000 resulted in the highest thermo hydraulic performance value of 2.15.

Apart from this, nanoparticles play a vital role in the thermal industry for obtaining better heat transfer rates [20]. However, due to their own advantages and disadvantages, hybrid nanofluids came into existence and may offer a tradeoff between them. For instance, Asghar et al. [21] performed a numerical study on the impact of hybrid nanofluid (Al_2O_3-Cu base) over vertical shrinking sheets using partial slip conditions. From this study, the enhancement in heat transfer was observed along with the rise in thermal slip and temperature distribution. Additionally, the influence of various parameters such as the concentration of nanoparticles, viscous dissipation, Biot number, thermal radiation and suction effect were investigated on shrinking surfaces. The study was performed using MATLAB tool using the bvp4c algorithm. During the study significant improvement in heat transfer was observed for hybrid nanofluid, compared to base fluids [22]. Moreover, the paper [23] investigated radiative 2D flow over a horizontal surface. The combined effect of magnetic, suction and velocity slip conditions was analyzed with hybrid nanofluids. The Eckert number was found to be an influential parameter to study. It has been observed that with the rise in the Eckert number, the increased temperature of the hybrid nanofluid resulted in a higher heat transfer rate [24–27].

Based on the literature study, turbulator shapes and hybrid nanofluids can significantly affect the thermo-hydraulic performance of SA-heaters. However, using hybrid nanofluids as a working fluid increases the operating cost of the system. Therefore, introducing roughness on the absorber plate is the most prominent and economical method to trade between cost and performance. However, according to the best knowledge of the authors, S-shaped and broken arc roughness configurations have not been reported as far in the SA-heaters. These configurations are integrated with the smooth absorber plate to disturb the viscous sublayer. Furthermore, a numerical investigation was carried out to analyze the effect of variation in Re number on the fluid flow characteristics, heat transfer, and friction. The present numerical work may show several limitations. Firstly, the existing literature may lack comprehensive studies on the combined impact of broken arc and broken S-shaped ribs, leaving a gap in understanding their synergistic effects on heat transfer and fluid dynamics. Additionally, the numerical models used in these assessments might oversimplify the real-world conditions, neglecting factors such as thermal radiation, material

properties, and ambient conditions. Furthermore, the majority of studies may focus on specific geometric configurations, and a lack of generalization across various parameters could limit the applicability of the findings. The experimental validation of numerical simulations is crucial for the reliability of results, but this aspect may be inadequately addressed in the available research. Overall, there is a need for more comprehensive investigations that consider a broader range of parameters and incorporate experimental validation to enhance the accuracy and applicability of numerical assessments in the context of solar air heater performance with broken arc and broken S-shaped ribs.

2. Numerical methodology

In this section, the numerical methodology carried out for the present study of the SA-heater has been presented. The rectangular air duct design was selected and modified with the broken S and broken arc-shaped ribs with different gaps and pitches. Modified SA-heaters were simulated and later compared with the conventional design model having a smooth absorber. The performance was evaluated by computing different parameters i.e., the average Nusselt number (Nu) and friction factor.

2.1. Geometrical modelling of modified SAH

The solar air heater considered for this study has a rectangular cross-section with dimensions 300 × 25 mm as the width and height. The length of the SA-heater was 2 400 mm. Further, the roughness of S-shaped and broken arc configurations was introduced in the form of ribs over the smooth absorber surface. The hydraulic diameter (D_h) of the present shape is 46.154 mm. Furthermore, Fig. 1 represents the geometrical construction of an SA-heater with a detailed view of the roughness. The total length of the solar air heater was categorized into three zones i.e., (1) entrance section of length 525 mm, (2) roughness section of length 1000 mm, and (3) exit section of length 875 mm. The diagram of the complete SA-heater is shown in Fig. 1. The entrance length is provided to develop the flow for the roughness zone.

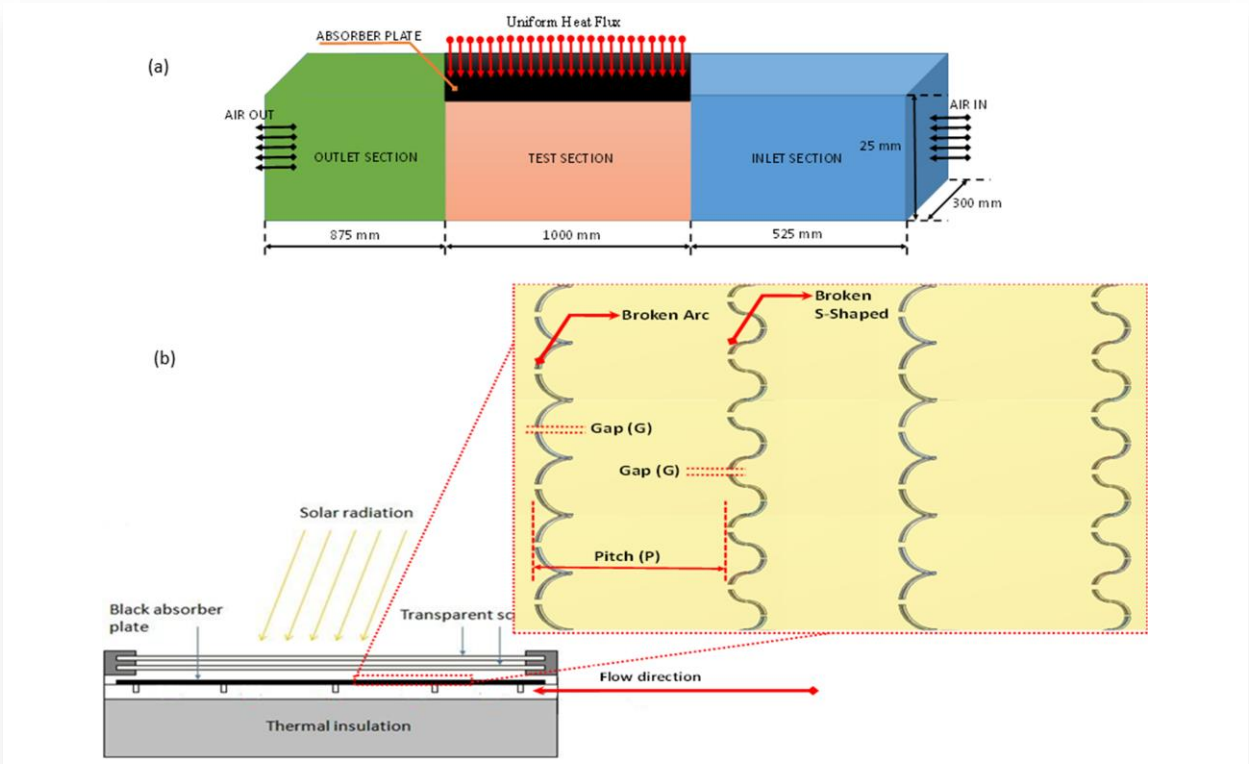

Fig. 1. (a) Schematic diagram of complete SA-heater with sections dimensions; (b) SA-heater cross sectional view with zoomed view of an absorber plate having broken S-shaped and broken arc shaped ribs design.

The roughness of height 1.4 mm was used for different sets of configurations of the SA-heater. In the present work, two different geometrical parameters (gap and pitch) have been varied simultaneously. Firstly, the gap width in the broken arc and broken S-shaped ribs was inserted over the smooth absorber plate. The gap (G) varies from 0.3 mm to 0.9 mm for both rib configurations with a step size of 0.2 mm. Secondly, the pitch distance between both configurations of rib roughness varied from 15 mm to 25 mm with a step size of 5 mm. These parameters were opted for the creation of more reattachment zones in the fluid flow with the roughened surface.

2.2. Governing equations and assumptions

Three important laws, i.e. the conservation of mass (continuity), momentum (N-S) and energy equations are used to govern the problems related to flow. They are expressed by Eqs. (1–5), respectively:

a) **Continuity equation.** The continuity equation is the mathematical statement of the concept of conservation of mass applied to an elemental control volume within a fluid in motion, and it is evaluated by using Eq. (1) [18–19]:

$$\frac{\partial \vec{u}}{\partial x} + \frac{\partial \vec{v}}{\partial y} + \frac{\partial \vec{w}}{\partial z} = 0. \quad (1)$$

This is the mass continuity equation for three-dimensional steady flow.

b) **Momentum equation.** It can be calculated by using Eqs. (2–4) [18–19]:
x–momentum equation:

$$\left(\vec{u}\frac{\partial \vec{u}}{\partial x} + \vec{v}\frac{\partial \vec{u}}{\partial y} + \vec{w}\frac{\partial \vec{u}}{\partial z}\right) = -\frac{1}{\rho}\frac{\partial p}{\partial x} + v\left(\frac{\partial^2 \vec{u}}{\partial x^2} + \frac{\partial^2 \vec{u}}{\partial y^2} + \frac{\partial^2 \vec{u}}{\partial z^2}\right), \quad (2)$$

y–momentum equation:

$$\left(\vec{u}\frac{\partial \vec{v}}{\partial x} + \vec{v}\frac{\partial \vec{v}}{\partial y} + \vec{w}\frac{\partial \vec{v}}{\partial z}\right) = -\frac{1}{\rho}\frac{\partial p}{\partial y} + v\left(\frac{\partial^2 \vec{v}}{\partial x^2} + \frac{\partial^2 \vec{v}}{\partial y^2} + \frac{\partial^2 \vec{v}}{\partial z^2}\right), \quad (3)$$

z–momentum equation:

$$\left(\vec{u}\frac{\partial \vec{w}}{\partial x} + \vec{v}\frac{\partial \vec{w}}{\partial y} + \vec{w}\frac{\partial \vec{w}}{\partial z}\right) = -\frac{1}{\rho}\frac{\partial p}{\partial z} + v\left(\frac{\partial^2 \vec{w}}{\partial x^2} + \frac{\partial^2 \vec{w}}{\partial y^2} + \frac{\partial^2 \vec{w}}{\partial z^2}\right). \quad (4)$$

c) **Energy equation.** If the flow is continuous and incompressible with constant thermal conductivity, there is no compression effect and no heat generation. In this case, no viscous heating is generated and the following equation can be used [18–19, 28]:

$$u\frac{\partial T}{\partial x} + v\frac{\partial T}{\partial y} + w\frac{\partial T}{\partial y} = \alpha\left(\frac{\partial^2 T}{\partial x^2} + \frac{\partial^2 T}{\partial y^2} + \frac{\partial^2 T}{\partial y^2}\right). \quad (5)$$

The turbulence model is the typical *k*–*ε* model. It is the most frequent turbulence model applied in solar air heater applications. The following assumptions were taken into account during numerical simulations of the solar air heater models to simplify the numerical procedure:

(1) The flow must be steady i.e., $\frac{\partial \rho}{\partial t} = 0$.
(2) Variation of the pressure in *y* direction is zero i.e., $\frac{\partial p}{\partial y} = 0$.
(3) The shear force in *y* direction is zero i.e., $\frac{\partial \tau}{\partial y} = 0$.
(4) The body force due to gravity is neglected.
(5) The flow must be incompressible i.e., $\frac{\partial \rho}{\partial x}, \frac{\partial \rho}{\partial y}, \frac{\partial \rho}{\partial z} = 0$.
(6) The flow must be fully developed, while approaching the test section.
(7) The axial heat conduction in the fluid is negligible.
(8) The properties of the air must be constant.

2.3. Boundary conditions and material properties

During the numerical modelling for the study, a constant heat flux (q) of 1200 W/m^2 is applied on the absorber plate. Additionally, the Re number of working fluid, i.e. air is varied from 2 000 – 22 000 with the step size of 4 000. The flow is considered turbulent, having the turbulent kinetic energy intensity of 5%. The temperature of the inlet air (T_{in}) flowing inside the SA-heater channels is 300 K. Aluminium is used as substrate material for the SA-heater. It has great machinability, high thermal conductivity; it is easily available, and economical compared to other materials such as stainless steel (SS). Table 1, tabulates the thermo-physical properties of aluminium and air considered for simulations. It was observed that the variation of properties with respect to temperature is very minimal. So, constant properties were considered during the simulation.

Table 1. Thermo-physical properties categorization of the aluminum and air [19].

Properties	Symbol	Unit	Aluminium	Air
Density	ρ	kg/m^3	2719	1.225
Specific heat	C_p	J/(kgK)	871	1006.4
Thermal conductivity	k	W/(mK)	202.4	0.707
Viscosity	μ	Pa s	---	1.7894e-05

2.4. Mesh generation and grid independence test

Firstly, the geometry was designed, and the model was discretized using different methods. The smooth solar air heater duct does not create much obstruction in mesh generation due to its simplicity and symmetry. In the presence of ribs of different shape, it is necessary to understand flow physics near the roughness. So, fine meshing was created in the vicinity of rib roughness as depicted in Fig. 2.

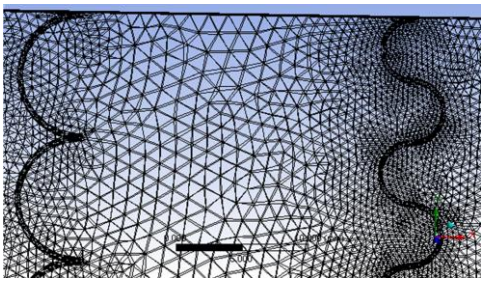

Fig. 2. Meshing of the absorber plate near the ribs.

Using an unstructured grid, the geometry was discretized and an adaptive refinement method was used. When the adaption is employed appropriately, the resulting mesh is most favourable for the flow solution. Further, a grid independence test was performed on the roughened solar air heater to see the influence of grid size. Table 2 highlights the variation of the average Nu number with the number of elements.

Table 2. Grid independence test on the roughened solar air heater.

No. of elements	Average Nu number	% variation
65 932	110.668	14%
130 832	95.170	51.65%
845 671	46.014	2.0%
912 839	46.964	--

It was observed that increasing the cell number beyond 845 671 elements, the variation observed is less than 5%. There-

fore, to avoid waste of the computational resources, the grid of 845 671 elements was proposed for the study.

2.5. Validation of the numerical model

The numerical model was validated by comparing the results with those of the smooth solar air heater. The obtained results were compared with those found from two well-known Eqs. (6) and (7). Firstly, the average Nu number from the present work was compared with that obtained from the Dittus-Boelter equation as in Eq. (6) [29]:

$$\mathrm{Nu} = 0.023 \times \mathrm{Re}^{0.8} \times \mathrm{Pr}^{0.4}, \quad (6)$$

where Re is the Reynolds number and Pr is the Prandtl number. The results are plotted for Re ranging from 2 000–22 000 as presented in Fig. 3. A slight variation of 3–5% is observed between the compared models. Furthermore, another parameter, that is the friction factor *f* was calculated and compared with that of the smooth SA-heater found from the Blasius friction equation as in Eq. (7) [29]:

$$f = 0.0791\mathrm{Re}^{-0.25}. \quad (7)$$

The obtained results for the friction factor are also found to be in good agreement, which validates our numerical model.

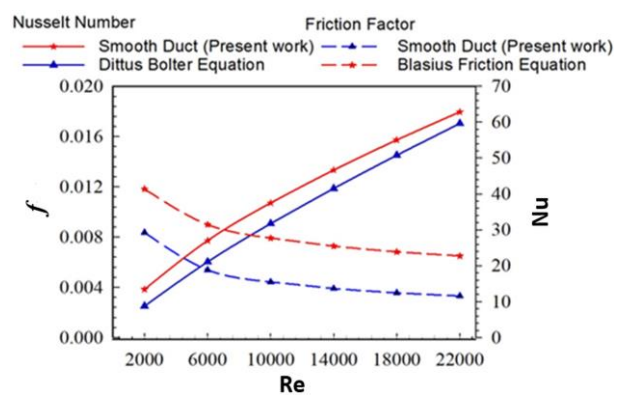

Fig. 3. Validation of the present numerical model of smooth duct based on the previously known empirical correlations.

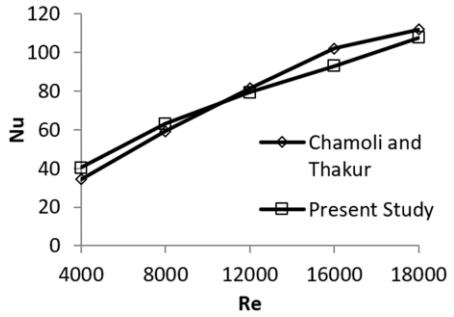

Fig. 4. Validation of present methodology with previous experimental work of Chamoli and Thakur [30].

The validity of the computational model is also established through a rigorous comparison of the Nu number outcomes generated by the current methodology with those obtained through experimental investigations conducted by Chamoli and Thakur [30], as illustrated in Fig. 4. To achieve this, a geometric configuration akin to that employed by Chamoli and Thakur [30] has been replicated and subjected to simulation under identical operating conditions. The assessment reveals an average absolute deviation of 7.86% between the computational and experimental data for the Nu number, affirming the reliability of the computational approach.

3. Results and discussion

The outcome of introducing roughness (broken arc ribs and broken S-shaped ribs) to the absorber surface of the SA-heater is presented in this section. The outcomes of the roughened SA-heaters for variable constructional parameters are presented and compared with smooth SA-heaters. Introducing roughness in SA- heaters stimulates enhanced heat transfer processes with an increase in friction factor coefficient [30]. The influence of varying gaps and pitches on thermal hydraulic performance is evaluated and presented. Additionally, the Re number was varied between 2 000–22 000.

3.1. Effect of geometrical variation on heat transfer characteristics

The Nusselt number is an important parameter for evaluating the heat transfer capabilities of different SA-heater configurations. Figure 5, represents the variation of the average Nu number with the Re number for different SA-heater configurations. The *x*–axis represents the variation of Re while *y*-axis represents the Nu number. During the study, the gap was varied from 0.3 mm to 0.9 mm in Figs. 4 to 5, while the pitch was kept constant for all the cases, i.e. 15–25 mm.

At $G = 0.3$ mm, it is observed that the Nu number increases along with the increase in pitch from 15 mm to 20 mm; further increase of the pitch value decreases the Nu value, irrespective of the Re number. The best performance was reported at the pitch length of 20 mm. The difference in the Nu number for the configurations $P = 15$ mm and $P = 25$ mm is very minimal, while a reasonable amount of increment was observed in the $P = 20$ mm configuration for all Re values. It is interesting to note that the pattern for different pitch lengths changes with an increase in gap length. The earlier pitch of 20 mm has yielded a better performance while for the gap length varying from 0.5 mm to 0.9 mm, the pitch of 25 mm has shown better heat transfer capabilities. Also, the gap between the $P = 20$ mm and $P = 25$ mm kept on increasing from $G = 0.5$ mm to $G = 0.9$ mm as visualized in Fig. 4 (b–d). Among all the configurations considered, the gap length of 0.9 mm and pitch length of 25 mm has shown the best performance.

3.2. Effect of geometrical variation on hydraulic performance

The pressure drop and friction factor are important parameters to be evaluated for the hydraulic performance of SA-heater configurations. In the present work, the friction factor was computed for all configurations. The influence of geometrical parameters and operating parameters on friction factor was depic-

ted in Fig. 6. It is observed that the pitch length of 25 mm has shown the largest value of friction factor, irrespective of gap length and Re number. Further, there is a minimal difference in friction factor observed between P = 20 mm and P = 25 mm, due to very little change in fluid flow characteristics. Also, there appears a significant increase in friction factor for a change in pitch length configuration from 15 mm to 20 mm. Further, the lowest friction factor was observed for the smooth solar air heater duct, which is due to no disturbance in fluid flow across the length of the solar air heater. A sudden drop was observed in all configurations when the Re number changed from 2 000 to 6 000 due to the change in fluid flow from laminar to turbulent.

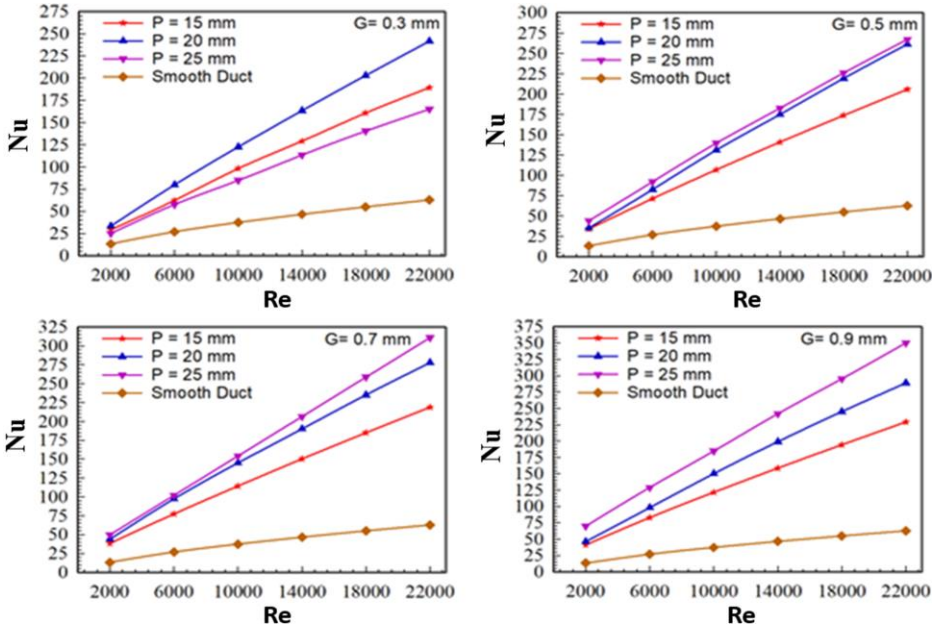

Fig. 5. Effects of varying gap and Re number on Nu number for modified SA-heaters (for G = 0.3 mm, 0.5 mm, 0.7 mm and 0.9 mm).

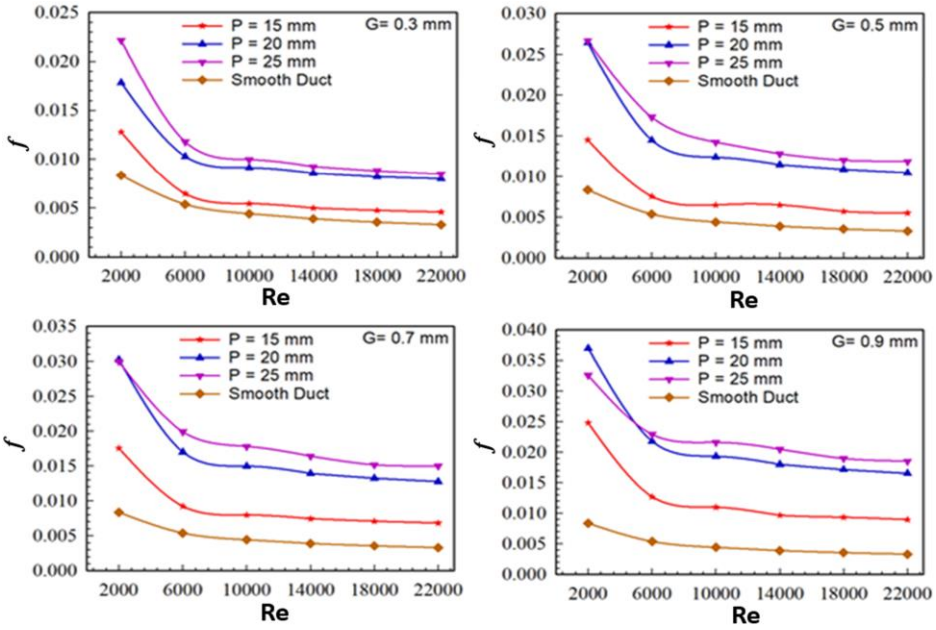

Fig. 6. Variation of f for varying Re number for modified solar air heaters (for G = 0.3 mm, 0.5 mm, 0.7 mm and 0.9 mm).

3.3. Effects of geometrical variations on fluid flow characteristics

The velocity contours were plotted for a constant value of Re number for different configurations. Figure 7 shows velocity contours of SA-heaters for the pitch length of 25 mm having the gap length varying from 0.3 mm to 0.9 mm for the Re number of 22 000. It was observed that for G = 0.3 mm, there is a very large reattachment zone formed around the surface. This reattachment zone kept on decreasing with the increase in gap length. Among all the configurations, that of G = 0.9 mm and P = 25 mm has shown the most favourable fluid flow conditions.

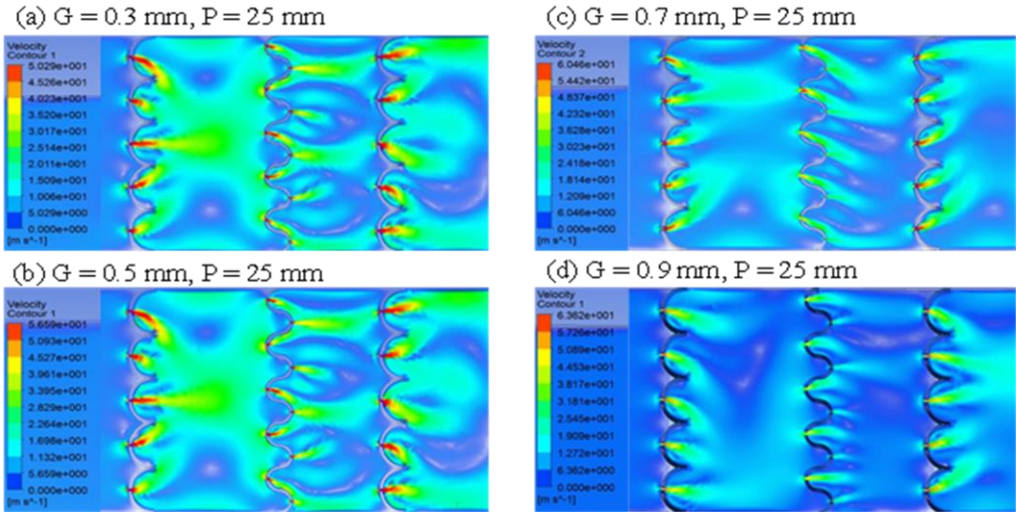

Fig.7. Velocity contours for different configurations of roughened SA-heater: (a) G = 0.3 mm, P = 25 mm; (b) G = 0.5 mm, P = 25 mm; (c) G = 0.7 mm, P = 25 mm; (d) G = 0.9 mm, P = 25 mm.

3.4. Thermo-hydraulic performance

As mentioned, the integration of roughness over the absorber plate in the SA-heaters improves heat transfer capabilities of the SA-heaters. Also, increased values of pressure drop can be observed corresponding to the heat transfer improvement. To identify whether the roughness used yields better heat transfer capability than pressure drop losses, there are various parameters to measure the thermo-hydraulic performance, like the coefficient of performance, thermal performance factor (TPF), efficiency, etc. [32–35]. Figure 8 represents the variation of TPF with Re for the used SA-heater configurations.

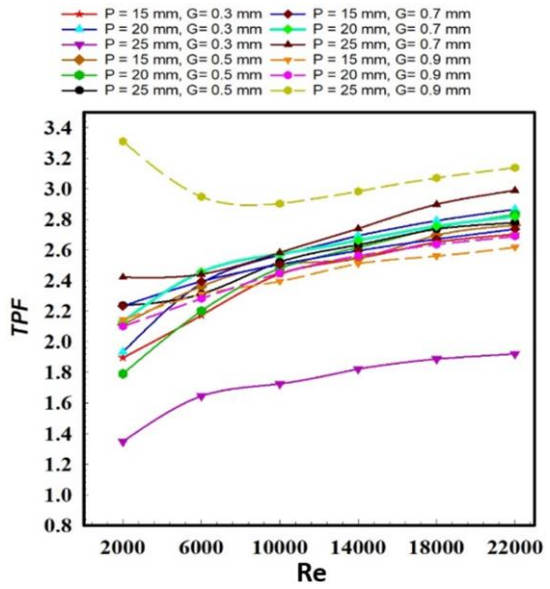

Fig. 8. Variation of thermal performance factor with Reynolds number for roughened SA-heater configurations.

In the present work, TPF is opted to evaluate the design efficiency. TPF was evaluated using Eq. (8). TPF is used often in the literature as it helps researchers comprehend the overall performance of thermal devices

$$TPF = \frac{(\mathrm{Nu}_r/\mathrm{Nu}_s)}{(f_r/f_s)^{\frac{1}{3}}}. \quad (8)$$

It was observed that the pitch length of 25 mm and gap length of 0.9 mm has shown a maximum TPF value from 2.9 to 3.3, while the pitch length of 25 mm and gap length of 0.3 mm has depicted the lowest TPF value, irrespective of the Re number. All other configurations have TPF values ranging between them.

4. Conclusions and scope of future work

In the present article, a numerical study was conducted on the SA-heater modified with ribs of broken S-shape and broken arc shape. Through this research, authors have demonstrated the potential of these specific roughness configurations to enhance heat transfer and improve the overall efficiency of solar air heaters. This work contributes to the advancement of sustainable energy technologies, offering practical solutions that can be implemented to harness solar energy more efficiently in various applications, such as space heating, water heating and industrial processes. The study was performed using the ANSYS Fluent software. During the study, three important parameters (Re number, gap, and pitch) were varied to obtain the best optimum value of each for the improved heat transfer rate. The Re number was varied from 2 000–22 000, while the pitch was varied from 15–25 mm and the gap length was varied from 0.3–0.9 mm. For this study, a constant heat flux of 1 200 W/m^2 was provided to the system. Various contributing parameters such as the Nu number, friction factor and thermal performance factor were evaluated and validated with the smooth surface absorber based SA-heater. On the basis of the study, a few conclusions were made as follows:

1. Among all the configurations considered, the gap length of 0.9 mm and pitch length of 25 mm has shown the best performance and a significant improvement in the Nu number.

2. The pressure drop and friction are important parameters to be evaluated for the hydraulic performance of SA-heater configurations
3. Minimal variations in friction factor were observed between P = 20 mm and P = 25 mm due to very little change in fluid flow characteristics. However, a sudden pressure drop was observed in all configurations when Re changed from 2 000 to 6 000 due to the change in fluid flow from laminar to turbulent.
4. It was observed that the pitch length of 25 mm and gap length of 0.9 mm have shown the maximum thermal performance factor value from 2.9 to 3.3, while the pitch length of 25 mm and gap length of 0.3 mm have depicted the lowest thermal performance factor value.
5. These modifications can be experimentally integrated with the SA-heater device to improve the overall performance of the system.

References

[1] Habib, K., & Wenzel, H. (2014). Exploring rare earths supply constraints for the emerging clean energy technologies and the role of recycling. *Journal of Cleaner Production*, 84, 348–359. doi: 10.1016/j.jclepro.2014.04.035

[2] Kumar, A., Bhandari, P., & Rawat, K. (2021). Numerical Simulation of Solar Air Heater using Paraffin Wax-Aluminum Compound as Phase Changing Material. *Aptisi Transactions on Technopreneurship*, 3(2), 164–170. doi: 10.34306/att.v3i2.199

[3] Varshney, L., Bhandari, P., & Bisht, V.S. (2014). Performance Evaluation of Hybrid Solar Water Heating System Using Wire Screen Packed Solar Air Heater. *International Journal of Engineering Research and Application*, 311–316.

[4] Bhandari, P., Varshney, L., & Bisht, V.S. (2018). Numerical analysis of hybrid solar water heating system using wire screen packed solar air heater. *1st International Conference on New Frontiers in Engineering, Science and Technology*, 1, 415–422, 8–12 January, New Delhi, India.

[5] Jani, D.K.S. (2023). Design and performance analysis of a solar air (SA) heater with phase change material (PCM) heat storage for residential applications. *International Journal of Innovative Research in Engineering and Management*, 10(4), 106–113. doi: 10.55524/ijirem.2023.10.4.13

[6] Bisht, A.S., Bisht, V.S., Bhandari, P., Rawat, K.S., Alam, T., & Blecich, P. (2023). The use of a vortex generator for the efficient cooling of lithium-ion batteries in hybrid electric vehicles. *Processes*, 11, 500. doi: 10.3390/pr11020500

[7] Thapa, R.K., Bisht, V.S., Rawat, K.S., & Bhandari, P. (2022) Computational analysis of automobile radiator roughened with rib roughness. *Journal of Heat and Mass Transfer Research*, 9(2), 209–218. doi: 10.22075/jhmtr.2023.27617.1382

[8] Bhandari, P., Singh, J., Kumar, K., & Ranakoti, L. (2022). A review on active techniques in microchannel heat sink for miniaturisation problem in electronic industry. *Acta Innovations*, 45, 45–54. doi: 10.32933/ActaInnovations.45.4

[9] Singh, B.P., Bisht, V.S., Bhandari, P., & Rawat, K.S. (2021). Thermo-fluidic modelling of a heat exchanger tube with conical shaped insert having protrusion and dimple roughness. *Aptisi Transactions on Technopreneurship*, 3(2), 13–29. doi: 10.34306/att.v3i2.200

[10] Thapa, R.K., Bisht, V.S., Bhandari, P., & Rawat, K.S. (2022). Numerical study of car radiator using dimple roughness and nanofluid. *Archives of Thermodynamics*, 43(3), 125–140. doi: 10.24425/ather.2022.143175

[11] Singh, B.P., Bisht, V.S., & Bhandari, P. (2021). Numerical Study of Heat Exchanger Having Protrusion and Dimple Roughened Conical Ring Inserts. In *Advances in Fluid and Thermal Engineering* (pp. 151–161). Springer Singapore. doi: 10.1007/978-981-16-0159-0_14

[12] Bisht, V.S., Patil, A.K., & Gupta, A. (2018). Review and performance evaluation of roughened solar air heaters. *Renewable and Sustainable Energy Reviews*, 81, 954–977. doi: 10.1016/j.rser.2017.08.036

[13] Alam, T., & Kim, M.H. (2016). Numerical study on thermal hydraulic performance improvement in solar air heater duct with semi ellipse shaped obstacles. *Energy*, 112, 588–598. doi: 10.1016/j.energy.2016.06.105

[14] Chaube, A., Sahoo, P.K., & Solanki, S.C. (2006). Effect of roughness shape on heat transfer and flow friction characteristics of solar air heater with roughened absorber plate. *WIT Transactions on Engineering Sciences*, 53, 43–51. doi: 10.2495/HT060051

[15] Lanjewar, A., Bhagoria, J.L., & Sarviya, R.M. (2011). Experimental study of augmented heat transfer and friction in solar air heater with different orientations of W-rib roughness, *Experimental thermal and fluid science*, 35, 986–995. doi: 10.1016/j.expthermflusci.2011.01.019

[16] Semalty, A., Bisht, V.S., Bhandari, P., Rawat, K., Singh, J., Kumar, K., & Dixit, A.K. (2022). Thermodynamic investigation on solar air heater having roughness as multiple broken arc and circular protrusion. *Materials Today: Proceedings*, 69(2), 181–186. doi: 10.1016/j.matpr.2022.08.336

[17] Bohra, J., Bisht, V.S., Bhandari, P., Rawat, K.S., Singh, J., Kumar, K., & Rawat, B. (2022). Effect of variable blockage height ratio on performance for solar air heater roughened with 45° Z-shaped baffles. *Materials Today: Proceedings*, 69(2), 153–157. doi: 10.1016/j.matpr.2022.08.279

[18] Ghildyal. A., Bisht V.S., Bhandari, P., & Rawat K.S. (2023). Effect of D-shaped, reverse D-shaped and U-shaped turbulators in solar air heater on thermo-hydraulic performance. *Archives of Thermodynamics*, 44(2), 3-20. doi: 10.24425/ather.2023.146556

[19] Singh, J., Bisht, V.S., Bhandari, P., Kumar, K., Singh, J., Alam, T., Dixit, S., Singh, S., & Khusnutdinov, R. (2023). Computational parametric investigation of solar air heater with dimple roughness in S-shaped pattern. *International Journal on Interactive Design and Manufacturing (IJIDeM)*. doi: 10.1007/s12008-023-01392-8

[20] Asghar, A., Lund, L.A., Shah, Z., Vrinceanu, N., Deebani, W., & Shutaywi, M. (2022). Effect of thermal radiation on three-dimensional magnetized rotating flow of a hybrid nanofluid. *Nanomaterials*, 12(9), 1566. doi: 10.3390/nano12091566

[21] Asghar, A., Ying, T.Y., & Zaimi, K. (2022). Two-dimensional mixed convection and radiative Al_2O_3-Cu/H_2O hybrid nanofluid flow over a vertical exponentially shrinking sheet with partial slip conditions. *CFD Letters*, 14(3), 22–38. doi: 10.37934/cfdl.14.3.2238

[22] Asghar, A., Vrinceanu, N., Ying, T.Y., Lund, L.A., Shah, Z., & Tirth, V. (2023). Dual solutions of convective rotating flow of three-dimensional hybrid nanofluid across the linear stretching/shrinking sheet. *Alexandria Engineering Journal*, 75(3), 297–312. doi: 10.1016/j.aej.2023.05.089

[23] Rasool, G., Xinhua, W., Lund, L.A., Yashkun, U., Wakif, A., & Asghar, A. (2023). Dual solutions of unsteady flow of copper-alumina/water based hybrid nanofluid with acute magnetic force and slip condition. *Heliyon*, 9, 22737. doi: 10.1016/j.heliyon.2023.e22737

[24] Teh, Y. Y., & Ashgar, A. (2021). Three dimensional MHD hybrid nanofluid Flow with rotating stretching/shrinking sheet and Joule heating. *CFD Letters*, 13(8), 1–19. doi: 10.37934/cfdl.13.8.119

[25] Lund, L. A., Asghar, A., Rasool, G., & Yashkun, U. (2023). Magnetized casson SA-hybrid nanofluid flow over a permeable moving surface with thermal radiation and Joule heating effect. *Case Studies in Thermal Engineering*, 50, 103510. doi: 10.1016/j.csite.2023.103510

[26] Asghar, A., Chandio, A.F., Shah, Z., Vrinceanu, N., Deebani, W., Shutaywi, M., & Lund, LA. (2023). Magnetized mixed convection hybrid nanofluid with effect of heat generation/absorption and velocity slip condition. *Heliyon*, 9(2), 13189. doi: 10.1016/j.heliyon.2023.e13189

[27] Asghar, A., Ying, T.Y., & Zaimi, K. (2022), Two-dimensional magnetized mixed convection hybrid nanofluid over a vertical exponentially shrinking sheet by thermal radiation, joule heating, velocity and thermal slip conditions. *Journal of Advanced Research in Fluid Mechanics and Thermal Sciences*, 95(2), 159–179. doi: 10.37934/arfmts.95.2.159179

[28] Saxena, A., & El-Sebaii, A.A. (2015). A thermodynamic review of solar air heaters. *Renewable and Sustainable Energy Reviews*, 43, 863–890. doi: 10.1016/j.rser.2014.11.059

[29] Kumar, S., & Verma, S.K. (2020). Three-dimensional simulation and experimental validation of solar air heater having sinusoidal rib. *Energy Sources, Part A: Recovery, Utilization, and Environmental Effects*, 1–19. doi: 10.1080/15567036.2020.1818007

[30] Chamoli, S., & Thakur, N.S. (2016) Correlations for solar air heater duct with V-shaped perforated baffles as roughness elements on absorber plate. *International Journal of Sustainable Energy*, 35(1), 1–20. doi: 10.1080/14786451.2013.857318

[31] Alam, T., & Kim, M.K. (2017). Heat transfer enhancement in solar air heater duct with conical protrusion roughness ribs. *Applied Thermal Engineering*, 126, 458–469. doi: 10.1016/j.applthermaleng.2017.07.181

[32] Bhandari, P., Rawat, K.S., Prajapati, Y.K., Padalia, D., Ranakoti, L., & Singh, T. (2024). A review on design alteration in microchannel heat sink for augmented thermohydraulic performance. *Ain Shams Engineering Journal*, 15(2), 102417). doi.: 10.1016/j.asej.2023.102417

[33] Bhandari, P., Padalia, D., Ranakoti, L., Khargotra, R., András, K., & Singh, T. (2023). Thermo-hydraulic investigation of open micro prism pin fin heat sink having varying prism sides. *Alexandria Engineering Journal*, 69, 457–468. doi: 10.1016/j.aej.2023.02.016

[34] Bhandari, P. (2022). Numerical investigations on the effect of multi-dimensional stepness in open micro pin fin heat sink using single phase liquid fluid flow. *International Communications in Heat and Mass Transfer*, 138, 106392. doi: 10.1016/j.icheatmasstransfer.2022.106392

[35] Bhandari, P., Prajapati, Y.K., & Uniyal, A. (2022). Influence of three dimensionality effects on thermal hydraulic performance for stepped micro pin fin heat sink. *Meccanica*, 58(11), 2113–2129. doi: 10.1007/s11012-022-01534-4

Co-published by
Institute of Fluid-Flow Machinery
Polish Academy of Sciences
Committee on Thermodynamics and Combustion
Polish Academy of Sciences

http://www.imp.gda.pl/archives-of-thermodynamics/

Experimental investigation and performance prediction of SAH using different arc rib roughness geometries – A comparative study

Jitendra Singh[a*], Atul Lanjewar[a]

[a] MANIT, Bhopal 462033, India
*Corresponding author email: jitendrasinghhbti285@gmail.com

Received: 24.02.2023; revised: 08.05.2023; accepted: 06.12.2023

Abstract

This study aims to investigate and compare the thermal performance of a solar air heater using a passive technique to enhance heat transfer between the absorber plate and the flowing fluid. The technique involves generating turbulence near the heat transferring surface through the use of artificial rib roughness. The study focuses on two different novel roughness geometries: full symmetrical arc rib roughness and half symmetrical arc rib roughness. By introducing additional gaps and varying the number of gaps in the roughness geometries, the study examines their effects on the solar air heaters thermal performance. The artificially roughened surface creates different turbulent zones, which are essential to the development of different types of turbulence in the vicinity of the heat transferring surface. The study finds that an optimal escalation in Nusselt number and friction factor by 2.36 and 3.45 times, respectively, occurs at certain gap numbers as 6 and ng as 5 for full symmetrical arc rib roughness. The maximum thermal-hydraulic performance parameter of 1.66 is attained at a Reynolds number of 6 000. The study also conducts correlation, mathematical modeling, and performance prediction under different operating circumstances.

Keywords: Full/Half symmetrical arc rib; Additional gap; Nusselt number; Thermohydraulic performance parameter

Vol. 45(2024), No. 1, 33–44; doi: 10.24425/ather.2024.150436

Cite this manuscript as: Singh, J., & Lanjewar, A. (2024). Experimental investigation and performance prediction of SAH using different arc rib roughness geometries - A comparative study. *Archives of Thermodynamics*, 45(1), 33–44.

1. Introduction

The most realistic and cost effective, immeasurable and straightforward reachable active non-conventional source of energy is solar energy.

Any country's access to energy resources has a significant impact on its commercial and scientific development. To solve the issue of total dependence on traditional energy sources, the industry must be modernized [1]. Fossil fuel deterioration is a significant problem that occurs everywhere in the world. By using energy intelligently and shifting toward unconventional energy sources, demand and supply are kept in balance. Room heating and ventilation, crop drying (for goods like tea, coffee, maize, fruits and vegetables) and aeration in the laundry sector are all uses of readily available solar energy [2].

Solar collectors, which convert solar radiation (including direct and indirect radiation) into heat energy and transmit it to a fluid, are an essential part of the solar air heater (SAH) system. Low SAH efficiency is brought on by the viscous sub-layer that covers the absorber plate. An effective method to disrupt the laminar sub-layer and raise the heat transfer coefficient h is to add rib components to the absorber surface [3]. The rib element in a roughened SAH generates turbulence at the absorber surface.

Nomenclature

A_p – absorber plate area, m^2
A_o – orifice area, m^2
C_d – orifice coefficient discharge
C_p – specific heat of flowing fluid (air), J·kg^{-1}K^{-1}
D_h – hydraulic diameter, m
d_1 – orifice pipe diameter, m
d_2 – orifice diameter, m
d/w – relative gap position
e – rib thickness, m
ee^+ – roughness Reynolds number
e/D_h – rib height relative to hydraulic diameter
fs – friction factor at smooth surface
fr – friction factor at rough surface
Fp – plate efficiency factor
Fo – heat removal factor
g – gap width, m
g' – gap width of additional gap
G – air mass velocity, kg·s^{-1}m^{-2}
G' – heat transfer function
g/e – gap width relative to rib height
g'/e – gap width of additional gap relative to rib height
H – duct height, m
h – convective heat transfer coefficient, W·m^{-2}K^{-1}
h_w – rate of heat loss due to wind, W·m^{-2}K^{-1}
I – solar radiation intensity, W·m^{-2}
k – thermal conductivity, W·m^{-1}K^{-1}
k_i – thermal conductivity (insulation), W·m^{-1}K^{-1}
L – test length, m
m – air mass flow rate, kg·s^{-1}
N – Number of glass cover
N_g – Number of symmetrical gaps over full arc
n_g – Number of additional gaps on symmetrical elements
Nu$_r$ – Nusselt number at rough surface
Nu$_s$ – Nusselt number at smooth surface
p – roughness pitch, m
p' – staggered rib pitch,
p_{atm} – atmospheric pressure, N·m^{-2}
p/e – roughness pitch relative to rib height
p'/p – staggered rib pitch relative to roughness pitch
Pr – Prandtl number
Q_u – useful heat gain through air, W
R – roughness function
Re – Reynolds number
r – staggered rib size, m
r/e – staggered rib length relative to rib height
St – Stanton number of roughened plate
t_e – edge thickness, m
t_i – edge insulation thickness, m
T_a – ambient temperature, K
T_f – average air temperature, K
T_i – initial temperature of air, K
T_o – average outlet temperature of air, K
T_p – average temperature of absorbing surface of the plate, K
U_b – bottom heat loss coefficient, W·m^{-2}K^{-1}
U_L – overall heat loss coefficient, W·m^{-2}K^{-1}
U_s – side heat loss coefficient, W·m^{-2}K^{-1}
U_t – top heat loss coefficient, W·m^{-2}K^{-1}
V – air velocity in SAH duct, m·s^{-1}
V_w – velocity wind, m·s^{-1}
W – duct width, m
W/H – aspect ratio

Greek symbols

α – angle of attack, degree
β – orifice diameter to pipe diameter
ρ_a – density at T_f, kg·m^{-3}
Δh_o – head difference at orifice plate, m
Δp_d – pressure difference along the test section, N·m^{-2}
Δp_o – pressure difference across orifice plate, N·m^{-2}
μ – dynamic viscosity, P·as
σ – Stefan Boltzmann constant
ε_g – emissivity glass cover
ε_p – emissivity absorber plate
$\tau\alpha$ – transmissivity–absorptivity product
η_{th} – thermal efficiency of solar air heater (SAH)
δ – bottom insulation thickness
η – thermohydraulic performance parameter (THPP)
ΔT – augmentation in temperature across the duct, ^{o}C

Abbreviations and Acronyms

SAH – Solar Air Heater
THPP – Thermohydraulic Performance Parameter

Although adding ribs to the absorber surface increases frictional losses, it also boosts the SAH system's effectiveness. The blower bills are increased by frictional losses as extra power is needed to create suction inside the duct so that fluid can flow as intended [4]. Many scientists have investigated the impacts of different rib designs on the heat transfer coefficient, the impact of friction factor on the pressure drop across the orifice meter (Δp_d) and thermal-hydraulic performance parameter (THPP) [5]. There is still a need to identify the best rib geometry - pattern, pitch and position for improved thermal and hydraulic performance.

The concept of rib roughness in a double pass SAH was applied to investigate the influence of discrete multi-V shaped and staggered rib on the performance of SAH [6]. Discrete multi-V shaped and staggered rib geometry performs better than discrete V-shaped with a staggered element [7]. A staggered V-shaped twisted rib was investigated using the LCT technique to visualize the fluid flow [5]. The thermal efficiency of SAH was improved with the use of double glazed finned steel absorber plate [8]. Augmentation in heat transfer rate is observed while using petal shaped and a quarter cylinder rib in compression with a square rib [9]. An experimental investigation has been conducted to investigate the performance of SAH duct roughened with expended metal-mesh roughness geometry [10]. A medical glass panel was installed in between the two layers of glass instead of the metal plate in a double pass solar air heater [11]. An experimental investigation was carried out by taking gaps in V-rib roughness with a staggered element [12]. Numerical analysis was conducted with novel V rib geometry [13]. Literature reveals the effect of different roughness geometries in several orientations such as transverse, inclined, V-up continuous, V-down

continuous, V-up discrete and V-down discrete rib arrangement, and the reported V-down discrete geometry is the best over other investigated geometries [14].

Continuous arc-shaped rib geometry is basic arc geometry. Experimental analysis has evolved by modifying arc roughness geometry in sequential order. The basic is continuous arc-shaped parallel wire rib roughness geometry [15]. Significant enrichment in Nusselt (Nu) number and friction factor (*f*) has been reported with the use of arc shaped roughness geometry [16]. Full width arc of continuous arc geometry with gap performs better over continuous arc geometry in terms of the Nu number and friction factor [17]. An experimental investigation was carried out with a broken arc rib combined with a staggered rib piece and concluded that due the presence of the staggered rib element in the broken arc rib more turbulence was generated, which leads to a high value of Nu number and friction factor [18]. Experimental investigation was conducted with arc rib with multiple gap roughness geometry [19] and came to conclude that the performance of arc rib with multiple gaps is better than continuous arc geometry [16] and broken arc shaped rib geometry [18]. Novel discrete symmetrical arc rib geometry was experimentally investigated with the aspect ratio *W*/*H* as 8 [20]. Symmetrical gap arc geometry and staggered element [21] shows better enrichment in Nu and f in comparison of an arc rib with multiple gap roughness geometry [19]. The comparison of single discrete arc roughness and double discrete arc roughness reveals that double discrete arc roughness has a higher THPP [22]. Multiple arc shaped roughness geometry shows the maximum enrichment in Nu and f with the ratio *W*/*w* as 5 and *W*/*w* as 7, respectively [23]. An experimental investigation was conducted with the use of novel discrete double arc reverse geometry [24] as well as a multiple arc with a gap [25] and a discrete multiple arc rib [26] revealing the behaviour of the flowing fluid.

1.1. Research gap

On the basis of a wide literature survey analysis, the following can be inferred:

1). Performance improvement of the continuous arc rib can be achieved by the provision of a gap in the continuous arc rib. Secondary flow refreshment by gap provision takes place. Also, flow acceleration through the gap interrupts boundary layer growth downstream near the reattachment zone.

2). Enhancement in heat transfer coefficient can be achieved by placing a staggered element in front of the gap as compared to the gap in arc rib geometry. Placing staggered elements leads to vortices mixing with the main flow.

3). Further improvement can be anticipated by gap provision in a considerably long continuous arc segment as it has unhindered boundary layer growth along this continuous arc segment. Gap provision is expected to break this unhindered boundary layer growth due to flow acceleration in the gap. This additional gap in the continuous arc segment is a novelty as it has not been explored by researchers to this date in the literature. It will lead to the discretization of a continuous arc segment that can lead to a higher *h* value from the absorber plate to the flowing fluid by shortening the symmetrical rib element length by giving an additional small gap that can reduce boundary layer formation as well as increase the flow acceleration. The purpose of this experimental study is to explore the discussed idea (providing an additional small gap) by using a discrete symmetrical arc rib with staggered rib roughness to see improvement in *h* and *f* values and also compare the performance of this improved SAH with that of smooth SAH.

4). As a result, experimental investigation of additional gaps in the present study (half symmetrical arc rib geometry and full symmetrical arc rib geometry) is necessary and its performance comparison to that of the existing best arc rib roughness geometry available in the literature [19] and [21]. If the performance is better, then providing an additional gap will indeed be a novelty.

5). Thus, the research gap manifests in improving the performance of existing best arc rib geometry by exploring the effect of an additional gap on a continuous arc segment of existing best arc rib roughness geometry available in the literature [19] and [21].

1.2. Objectives of the present study

The objectives of the present study are as follows:

1). To determine the effect of the main gap, additional symmetrical gap and staggered element of half symmetrical arc rib geometry and full symmetrical arc rib geometry on the heat transfer, pressure drop and THPP parameter of a roughened SAH duct.

2). To compare the THPP parameter of the proposed geometries with the existing best arc rib roughness geometry available in the literature [19] and [21].

3). To develop a correlation between the roughness function (*R*) and roughness Reynolds number (e^+) and heat transfer function (*G*') and roughness Reynolds number (e^+).

2. Experimental arrangement

The indoor test setup has been constructed as per ASHRAE, Standard [27] as illustrated in Fig. 1(a) for the experimental run of the roughened SAH duct. The test setup includes a control valve, blower, galvanised iron (GI) pipe, PVC hose pipe and a rectangular channel with an absorber plate on the top. Fig. 1(b) depicts a cross-sectional figure of the SAH duct channel. The indoor experimental duct which has the dimensions 2350 mm by 300 mm by 25 mm and a *W*/*H* ratio of 12 is shown in Fig. 1(c).

The experimental duct is 800 mm long at the inlet section, 1000 mm long at the test section and 550 mm long at the exit section. For adequate hot air mixing, baffles are implanted at the duct's exit section. As an absorber plate, a hot-rolled (1.2 mm thick) sheet with a span of 1000 mm is used. A test plate area of 1 000 mm by 300 mm is roughened using a copper wire with a 2 mm diameter and applied to improve absorptivity of black paint on the other side of the plate. An electric heater made of a nichrome wire emits a 1 000 W/m^2 constant heat flux over the absorber plate. A 50 mm thick thermocol is used to insulate the whole duct. A galvanized iron (GI) pipe is insulated from the

exit portion to the orifice plate. The customized insulating rope and plaster of paris are used to insulate the GI pipe.

To measure the mass flow rate (m) of the flowing fluid within the rectangular duct a digital manometer is mounted across the orifice plate. A control valve is put before the centrifugal blower to adjust m in the test channel. T-type thermocouples are located at the entrance section to measure the ambient air temperature, temperature at the top surface of the absorber plate and the temperature of heated air at the exit section under steady-state conditions. To measure the temperature of ambient air a single thermocouple is placed at the entrance of the SAH duct and the temperature of hot air leaving the duct is measured with 5 thermocouples that are placed span-wise at the transition section. The data logger uses thermocouples to capture temperature readings. The Δp_d along the test portion is measured using a digital micro-manometer.

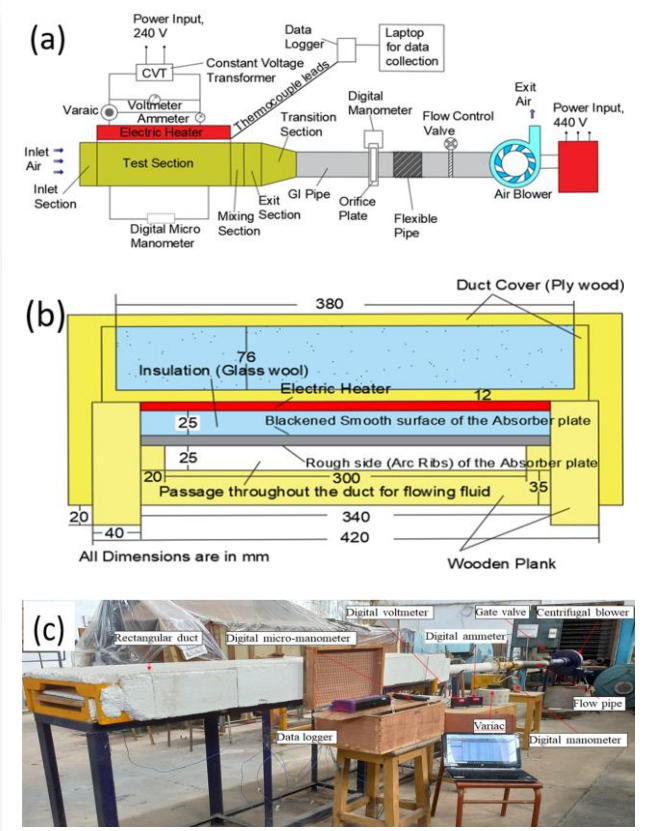

Fig. 1. (a) Outline of experimental set-up; (b) Cross-sectional view of rectangular duct; (c) Photograph of experimental set-up.

The optimal physiognomic behaviour of roughness geometries mentioned in [19], [21] and two different proposed roughness geometries, namely, half symmetrical arc rib geometry and full symmetrical arc rib geometry has been determined through experimental runs with a rectangular SAH duct (W/H ratio as 12).

The new geometry consists of a symmetrical arc segment with symmetrical gaps and additional gaps on symmetrical arc segments. The schematic and photographic representation of half symmetrical arc rib geometry and full symmetrical arc rib geometry is depicted in Fig. 2 and Fig. 3, respectively. Table 1 displays the roughness and performance metrics for the experimental inquiry.

3. Procedure of investigations

It is ensured that all the equipment is correctly connected and in operating condition before starting the experimental run. The

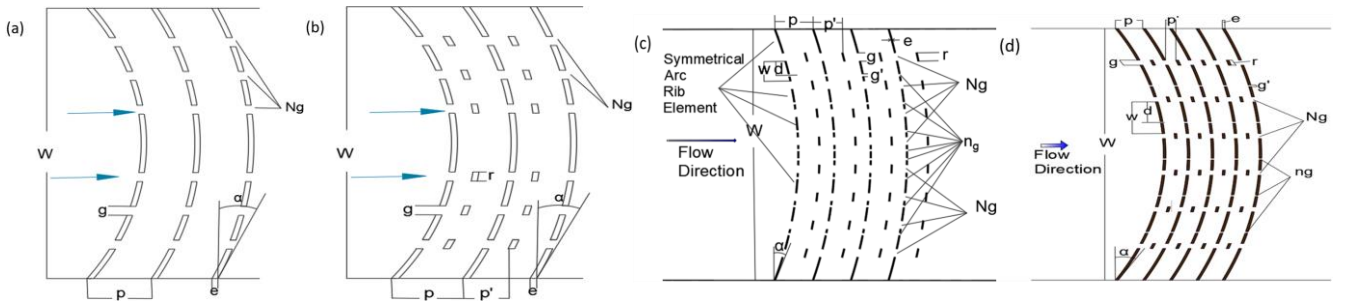

Fig. 2. Schematic view of different roughness geometries: (a) Arc rib with multiple gaps [19]; (b) Symmetrical gap arc geometry and staggered element [21]; (c) Half symmetrical arc rib geometry; (d) Full symmetrical arc rib geometry.

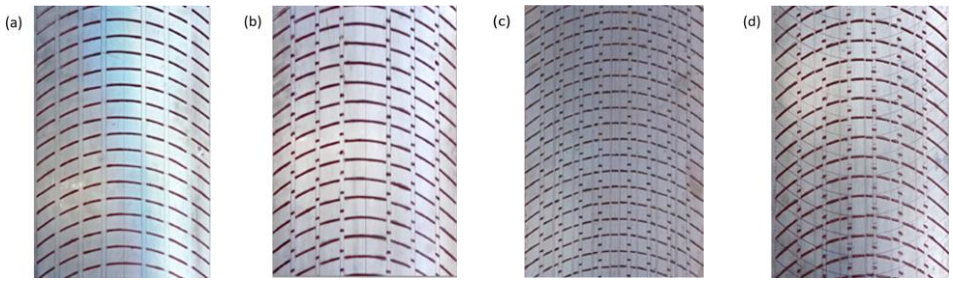

Fig. 3. Photographic view of different roughness geometries: (a) Arc rib with multiple gaps [19]; (b) Symmetrical gap arc geometry and staggered element [21]; (c) Half symmetrical arc rib geometry; (d) Full symmetrical arc rib geometry.

Table 1. Range of roughness parameters of the proposed roughness geometries.

Roughness Parameters	Arc rib with multiple gaps [19]	Symmetrical gap arc geometry and staggered element [21]	Half symmetrical arc rib geometry	Full symmetrical arc rib geometry
e	2.3	2.3	2.3	2.3
g/e	4	4	3	3
g'/e	-	-	1	1
r/e	-	4	3	3
p/e	10	10	10	10
p'/p	-	0.4	0.4	0.4
Ng	6	6	8	6
n_g	-	-	8	5
d/w	-	0.65	0.65	0.65

experimental setup takes 2–2.5 hours to reach the steady state. Experimental data are collected only after the steady state is achieved. For each roughened plate the atmospheric air inlet temperature (T_i), absorber plate surface temperature (T_p) at various locations, hot air temperature (T_o) at the exit section and pressure drop (ΔP_d) in the test section at various m through the duct are measured and recorded in order to evaluate Nu, *f* and THPP.

3.1. Data compilation

The observed parameters (T_i, T_o, T_p and ΔP_d are measured under steady-state conditions. For a certain Re these values are utilized to calculate Nu, *f* and THPP. The following relevant equations [21] are employed to compute air mass flow rate (m), useful heat gain through air (Q_{air}), convective heat transfer coefficient (h), Nusselt Number (Nu) and Friction factor (f):

$$m = C_d A_o \sqrt{\frac{2\rho_a (\Delta P)_o}{1 - \beta^4}}, \quad (1)$$

$$Q_{air} = mC_p(T_o - T_i), \quad (2)$$

$$h = \frac{mC_p(T_o - T_i)}{A(T_p - T_f)}, \quad (3)$$

$$\mathrm{Nu} = \frac{hD_h}{k}, \quad (4)$$

$$f = \frac{2(\Delta P)_d D_h}{4\rho_a L V^2}. \quad (5)$$

The accuracy and precision of experimental result of different parameters are measured during the test run [28]. The maximum uncertainty in evaluated parameters is 1.77–1.84 %, 4.03–7.49 %, 3.49–5.13 % for Re, Nu and *f* respectively. The least count and uncertainty values in the measurement of duct and rib dimensions are 0.1 mm (Vernier Caliper) and ±0.1 mm. A digital micro-manometer with the least count of 0.1 Pa and ±0.1 Pa of uncertainty is used in the measurement of pressure drop along the test section. Uncertainty in the measurement of temperature (T-Type, Copper-constantan thermocouple) is ±0.25°C (Holman 1971). The least count and uncertainty in the measurement of voltage and current for the heating effect are 1% and ±0.01, respectively.

3.2. Validation of setup arrangement for smooth plate

Experimental results for smooth plates are compared with theoretical results obtained from correlations given in the literature. Dittus-Boelter [29] and Bhatti and Shah [30] correlations given by Eq. (6) and Eq. (7), respectively, represent the theoretical Nusselt number (Nu_{th_s}) and friction factor (f_{th_s}):

$$\mathrm{Nu}_{th\_s} = 0.023\mathrm{Re}^{0.8}\mathrm{Pr}^{0.4}, \quad (6)$$

$$f_{th\_s} = f_s + 0.0175\left(\frac{D_h}{L}\right), \quad (7)$$

$$f_s = \left(1.0875 - 0.1125\frac{H}{W}\right) f_o, \quad (8)$$

$$f_o = 0.0054 + 2.3\times10^{-8}\,\mathrm{Re}^{1.5}, \quad (2100 \le \mathrm{Re} \le 3550), \quad (9)$$

$$f_o = 1.28\times10^{-3} + 0.1143\,\mathrm{Re}^{-0.311}, \quad (3500 \le \mathrm{Re} \le 10^7). \quad (10)$$

The experimental setup is validated using the Nu and *f* values for smooth plates obtained during the experimental run and the values of Nu and *f* obtained from correlations given in Eq. (6) and Eq. (7). Figure 4 indicates the variation of Nu and *f* with respect to Re for a smooth plate.

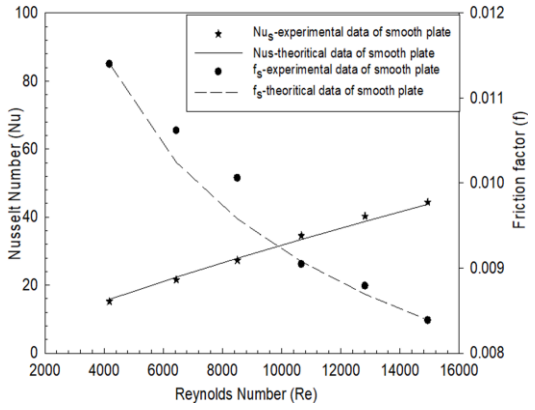

Fig. 4. Experimental and theoretical values of Nu and *f* for a smooth plate for the validation of experimental set-up.

The absolute average variation between the Nu and *f* values obtained through correlations and the Nu and *f* values obtained during the experimental study is 3.98% and 4.87%, respectively. The accuracy of the fabricated experimental setup is ensured by a small difference between experimental findings and theoretical Nu and *f* values.

4. Physiognomic appearance of flowing fluids

An increase in the Nusselt number for artificial roughened geometry is due to variation in the air flow field near the roughened plate. Numerous investigators have reported the influence of arc rib roughness on *h* because of the development of flow vortices along arc rib and also the enlargement of secondary flow as shown in Fig. 5(a) for roughness geometry [19] in which only three types of flow are present main/primary flow flows over the arc shaped rib, flow through the main gap and the secondary flow developed along the arc rib. The main flow flows over the arc rib is responsible for the reattachment point between the two consecutive ribs, the main flow through the main gap is responsible for turbulence generation and the secondary flow along the rib acts to disrupt the formation of boundary layer along the rib element. For roughness geometry [21], the flow pattern underside of the absorber surface is shown in Fig. 5(b).

The staggered element in front of each main gap is used for scattering the main flow along the side of the staggered element and to generate a turbulence zone between the free space of two consecutive main arc ribs. Applying the present roughness geometry, namely the full symmetrical arc rib results in a complex flow pattern near the roughened plate as shown in Fig. 5(c). The picture exhibits reattachment of the main flow behind the arc piece and segment element, secondary flow generation along the arc piece, secondary flow refreshment while passing through the gap, accelerating the main flow through an additional gap, secondary flow vortices generation, turbulence increase due to scattering of the main flow along the staggered rib and rapid mixing in turbulence wake region of the staggered rib. An additional gap in the symmetrical arc rib element accelerates the main flow and is scattered between the two consecutive staggered rib elements after passing through the gap and generates a turbulent region behind the main symmetrical arc rib element. Due to this, the area of wake region depresses.

An additional gap in the symmetrical arc rib element also hinders the formation of the secondary boundary sublayer along the arc rib. Acceleration in the main flow, scattering between the two consecutive staggered ribs and hindrance to the formation of the boundary sublayer along the arc rib element and its mixing with the main flow gives rise to the enhanced local Nu in the vicinity of a segment element downstream of the gap, leading to an increase in the average Nusselt number.

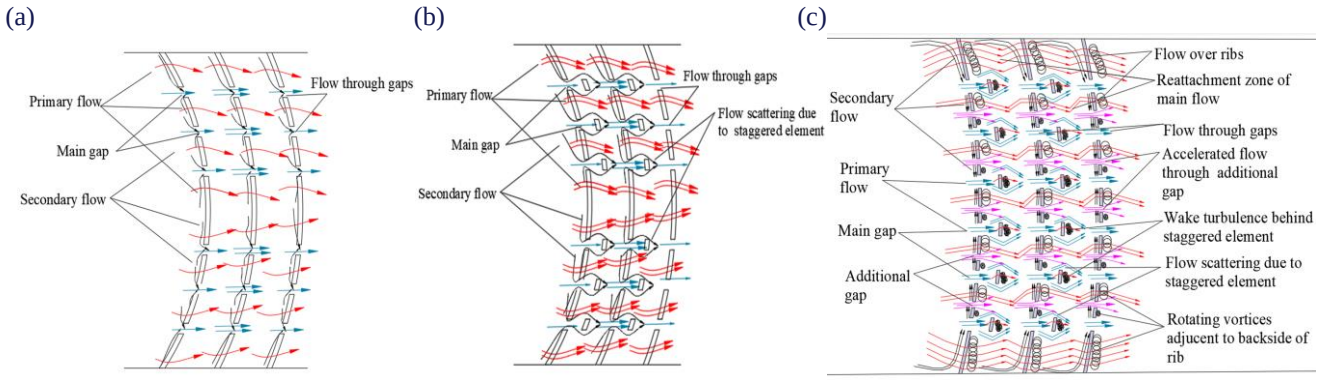

Fig. 5. Physiognomic appearance of flowing fluids over the test plate of different roughness geometries i.e.: (a) Arc rib with multiple gaps [19]; (b) Symmetrical gap arc geometry and staggered element [21]; (c) Full symmetrical arc rib geometry.

5. Experimental results and discussion

The current experimental analysis discloses the influence of the main gap, additional symmetrical gap and staggered element of half symmetrical arc rib geometry and full symmetrical arc rib geometry on *h*, *f* and THPP as shown in Figs. 6 to 8, respectively.

5.1. Variation of Nu and *f* with Re

Variation of Nu versus Re for the roughness geometries from [19, 21] and for two different proposed roughness geometries, namely half symmetrical arc rib geometry and full symmetrical arc rib geometry is shown in Fig. 6. A higher Re produces more turbulence that facilitates heat dissipation from the surface.

A high dissipation rate helps in achieving high Nu values. Nu increases with the increase in Re. The additional gap in the symmetrical arc rib accelerates the main flow, thus increasing turbulence. According to Fig. 6, an increase in Nu values is a result of diminution in viscous sublayer thickness with the increase in Re. The ratio of Nu for a roughened absorber surface to Nu for a smooth surface (Nu/Nu_s) for [19, 21] and two different proposed roughness geometries mentioned above is between 1.54–2.01, 1.72–2.22, 1.66–2.06 and 1.90–2.36, respectively. The highest range for the Nu/Nu_s ratio is 1.90 to 2.36 for full symmetrical arc rib geometry for the entire range of investigated Re.

The additional enrichment in *h* observed for the staggered rib with an additional gap in the symmetrical arc rib element in the full symmetrical arc rib over the staggered rib with the symmetrical arc rib can be accredited to the accelerated flow of air through the small additional gap in the symmetrical arc rib as shown in Fig. 5(c). The accelerated flow gets scattered between

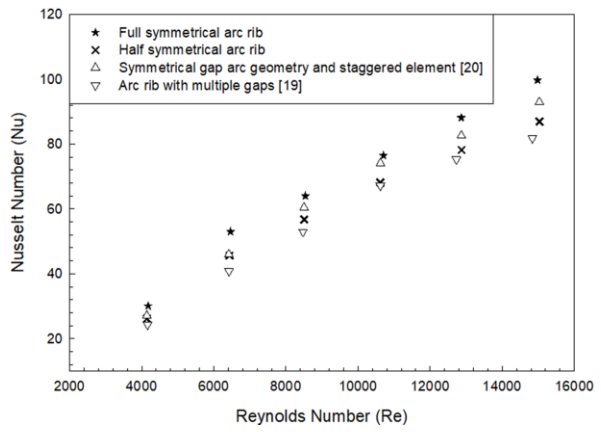

Fig. 6. Variation of Nu against Re at various roughness geometries.

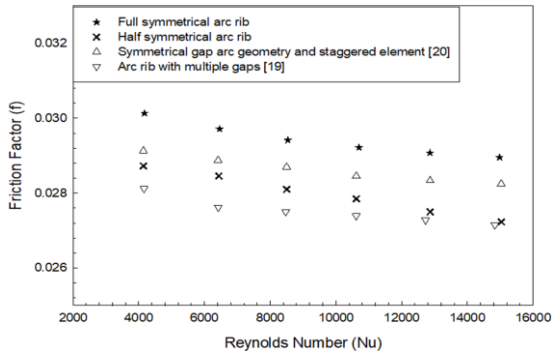

Fig. 7. Variation of *f* against Re at various roughness geometries.

the two consecutive staggered rib elements and generates a turbulent region behind the main symmetrical arc rib element. Due to this, the wake region depresses. The increment in the contact area between the flowing fluid and the heated plate between two consecutive ribs leads to a high h from the absorber surface.

The establishment of secondary flow along the arc rib element shows a considerable effect in disturbing the main flow. In the duct with arc rib roughness, the secondary flow is much stronger than compared to V-shaped rib roughness. The formation of boundary sub-layer along the arc rib shows an adverse effect on *h*. To suppress the effect of boundary sublayer, an additional gap is provided in the symmetrical arc rib, and due to this additional gap, a rise in the heat transfer rate is observed in comparison with the roughness geometry [19, 21].

The number of the main gaps N_g and the number of additional gaps n_g in half symmetrical arc rib roughness is 4, which means that the total number of main gaps N_g and additional gaps n_g of half symmetrical arc rib roughness is 8 over the span of the test plate as shown in Fig. 2(c) and Fig. 3(c), while the total number of main gaps N_g and additional gaps n_g in full symmetrical arc rib roughness is 6 and 5, respectively, over the span of the test plate as shown in Fig. 2(d) and Fig. 3(d). As the number of main gaps in the arc geometry increases, more free space between the consecutive rib elements are available for the main flow. The volume of flowing fluid passes through the free space without encountering the rib element increases. Turbulence in the vicinity of the absorber surface decreases resulting low *h* is perceived. Vortices generation near the rough surface contributes to heat removal from the heated surface. The half symmetrical arc rib roughness provides more open spaces in total, increase area between the rib elements for the fluid flow. The flow passes through the wider area with a low velocity and without encountering the rib elements, leading to a lower intensity of turbulence generation near the absorber surface.

Variation of *f* versus Re is shown in Fig. 7. Re has an adverse influence on *f*. There is a pressure difference between the sides of the rib. Equation 5 clearly indicates the impact of pressure difference and air flow velocity on the friction factor (*f*). The pressure difference on both sides of the rib element and the air flow velocity inside the duct participate cumulatively to determine *f*. For the entire range of Re as 4 000–16 000, the ratio of *f* for the roughened absorber surface to f for the smooth surface (f/f_s) for [19, 21] and two different proposed roughness geometries, namely half symmetrical arc rib geometry and full symmetrical arc rib geometry is 2.46–3.23, 2.54–3.37, 2.51–3.25 and 2.64–3.45, respectively. The maximum f/f_s ratio is 2.64–3.45 for full symmetrical arc rib geometry for the entire range of investigated Re.

By investigating the roughness geometry of [19] and [21], from the experimental results it is evident that the friction factor increases by employing the staggered rib in front of the main gap as ΔP_d increases in the duct along the test length as shown in Fig. 7. An additional gap in the symmetrical arc rib for half symmetrical arc rib roughness shows a positive effect on the friction factor as the additional gap provides free space for the secondary flow and as well as for the main flow as the friction factor of half symmetrical arc rib roughness is lower than in [21]. The friction factor increases as an additional gap in the symmetrical arc rib for full symmetrical arc rib roughness is introduced. This is due to a lower number of N_g and n_g in full symmetrical arc rib roughness than in half symmetrical arc rib roughness and due to a high value of ΔP_d in the duct.

5.2. Effect of THPP

The thermal enhancement of a roughened SAH escalates the frictional losses. Hence, it is essential to conclude the thermal performance of a roughened SAH by considering both thermal and frictional characteristics at the same time. Webb and Eckert [31] suggested the thermal-hydraulic performance parameter (THPP) that considered both thermal characteristics in terms of Nusselt number and frictional characteristic in terms of friction factor of a rough surface with reference to the smooth surface.

$$\mathrm{THPP} = \frac{\mathrm{Nu}/\mathrm{Nu}_s}{(f/f_s)^{1/3}}. \tag{11}$$

THPP higher than unity indicates the effectiveness of the SAH duct integrated with rib roughness. THPP is used to conclude the performance of various roughness geometry arrangements with respect to that of the smooth duct. Fig. 8 shows THPP versus Re.

The range of THPP variation is 1.14–1.40, 1.27–1.52, 1.23–1.46 and 1.38–1.66 for roughness geometries of [19, 21],

half symmetrical arc rib and full symmetrical arc rib. The maximum THPP is observed for the full symmetrical arc rib over the investigated range of Re. As Re increases, THPP increases and attains a maximum at Re equal to 6 000, then declines with the further increase in Re. The maximum variation of THPP is 1.38–1.66 for the full symmetrical arc rib.

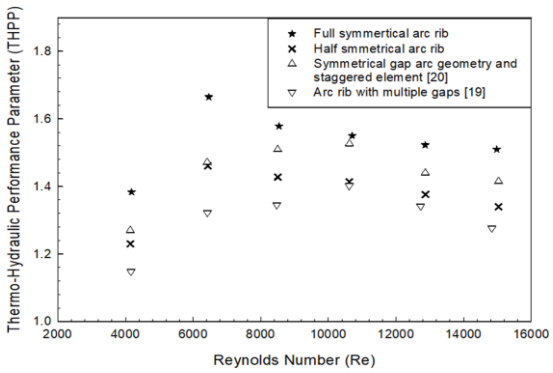

Fig. 8. Variation of THPP against Re for investigated geometries.

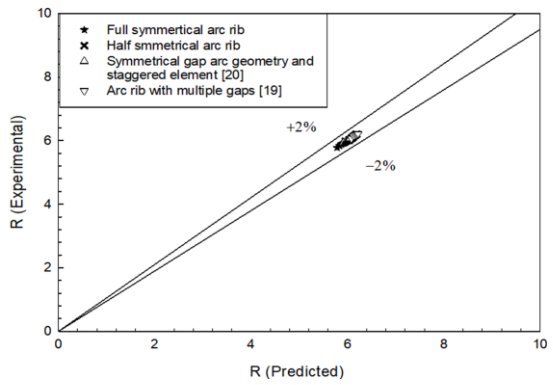

Fig. 9. Comparison of predicted and experimental values of *R* for different roughness geometries.

6. Correlation for *R* and *G'*

Empirical correlations have been developed by considering the combined effect of Re, e/D_h, e^+, f on the roughness function (R) [32] and heat transfer function (G') [33] as represented in Appendix A. It is seen that the maximum deviation among the predicted values and experimental values of R and G' was ± 2 % and ± 10 %, respectively, as shown in Fig. 9 and Fig. 10.

7. Thermal performance prediction

Thermal performance prediction of a single pass roughened rectangular duct of SAH was done with the correlation developed for R and G' as shown in Table 3 given in Appendix A. The mathematical model is established to analyze the heat discharge in the system. Different surface heat losses such as Q_t, Q_b, and Q_s, roughness parameters, properties of fluid and other relevant parameters are the performance parameters used for numerical analysis to investigate the thermal behaviour of the system. A flow diagram for the prediction of thermal performance of

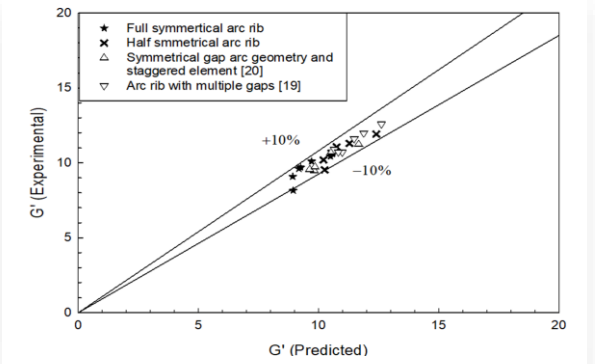

Fig. 10. Comparison of predicted and experimental values of *G'* for different roughness geometries.

SAH is shown in Fig. 11 followed by the step-by-step procedure (from Step 1 to Step 12) to calculate the thermal performance of a single pass roughened rectangular duct of SAH with the help of Eqs. (12) to (30).

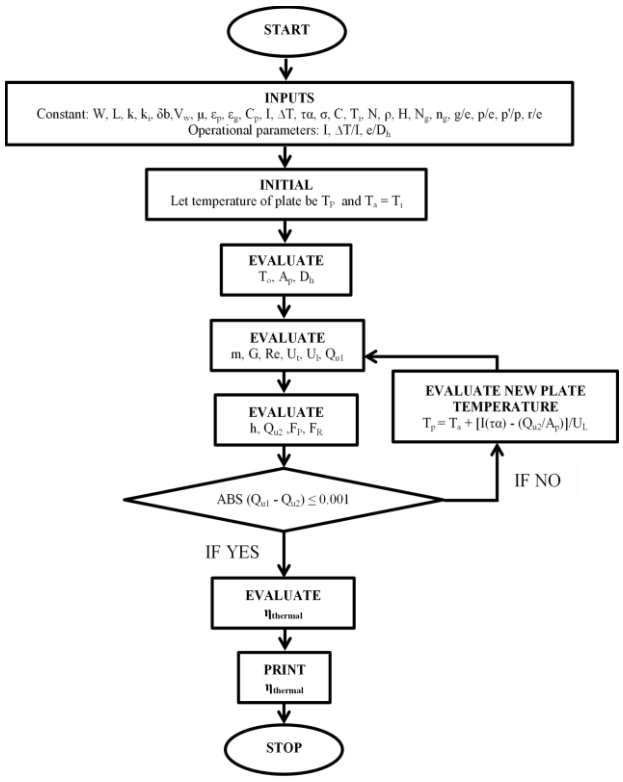

Fig. 11. Flow chart for prediction of thermal performance.

Step 1: The performance prediction is initiated with the selection of roughness and system parameters listed in Table 2.

Step 2: The inlet air temperature (T_i) is considered the ambient air temperature (T_a) as ambient air at the inlet section is sucked by a solar air heater duct. The outlet temperature (T_o) at the exit section is determined by using the inlet temperature (T_i) and temperature increment along the duct (ΔT).

$$T_o = \Delta T + T_i \,. \tag{12}$$

Table 2. Parameters used in the mathematical model for numerical analysis.

No.	System parameters	Values
1.	SAH duct channel parameters	L = 1 m, W = 0.3 m, H = 0.025 m, W/H = 12
2.	Properties of insulating material of SAH duct	k_i = 0.037 W/(mK), δ_b = 0.05 m, t_i = 0.05 m
3.	Parameters and properties of glass cover material of SAH duct	N = 1, ε_g = 0.88, $\tau\alpha$ = 0.80
4	Emissivity of test plate	ε_p = 0.90
5.	Solar intensity	I = 1000 W/m^2
6.	Wind velocity	V_w = 1 m/s
7.	Ambient temperature	T_a = 300 K
8.	Relative artificial roughness height	e/D_h = 0.0433
9.	Investigated range of Reynolds number	Re = 4 000–15 000

Step 3: To estimate the heat transfer rate from the test plate to the air, i.e. useful heat gain, the plate temperature (T_p) is initialized by giving it some value.

Step 4: The heat loss coefficient (U_L) is found by summation of different side heat loss coefficients such as U_t, U_b and U_s of the rectangular SAH duct:

$$U_L = U_t + U_b + U_s\,, \tag{13}$$

$$U_b = \frac{k_i}{\delta_b}\,, \tag{14}$$

$$U_s = \frac{(L+W)t_e k_i}{LWt_i}\,. \tag{15}$$

The top heat loss coefficient U_t is a function of T_p, T_a and many other parameters and is computed using Eq. (16) as suggested by Klein [34]:

$$U_t = \left[\frac{N}{\left(\frac{C}{T_p}\right)\left(\frac{T_p - T_a}{N+f}\right)^{et}} + \frac{1}{h_w}\right]^{-1} + \frac{\sigma(T_p^2 + T_a^2)(T_p + T_a)}{(\varepsilon_p + 0.00591Nh_w)^{-1} + \left[\frac{(2N+f-1)+0.133\varepsilon_p}{\varepsilon_g}\right] - N}\,, \tag{16}$$

where:

$$f = \left(1 + 0.089h_w - 0.1166h_w\varepsilon_p\right)(1 + 0.07866N), \tag{17}$$

$$et = 0.43\left(1 - \frac{100}{T_p}\right), \tag{18}$$

$$C = 520(1 - 0.000051s^2). \tag{19}$$

where s is the tilt of the collector (for a horizontal collector, s = 0). h_w is a function of wind velocity given by McAdams [35]:

$$h_w = 5.7 + 3.8\,V_w\,. \tag{20}$$

Step 5: The estimation of Qu_1 is done by Eq. (21):

$$Qu_1 = A_p\left[I(\tau\alpha) - U_L(T_p - T_a)\right]. \tag{21}$$

Step 6: The mass flow rate (m) as in Eq. (22), mass velocity (G) as in Eq. (23) and Re as in Eq. (24) are calculated as follows:

$$m = \frac{Qu_1}{C_p \Delta T}\,, \tag{22}$$

$$G = \frac{m}{WH}\,, \tag{23}$$

$$\mathrm{Re} = \frac{GD_h}{\mu}\,. \tag{24}$$

Step 7: Eq. (31), Eq. (32) and Eq. (33) and values from Table 3 given in Appendix A govern G' and R. G' and R further used to quantify the Stanton number and subsequent Nu number.

Step 8: Calculation of h and F_p from Eq. (25) and Eq. (26):

$$h = \frac{k\mathrm{Nu}}{D_h}\,, \tag{25}$$

$$F_p = \frac{h}{h + U_L}\,. \tag{26}$$

Step 9: Calculation of F_o as below:

$$F_o = \frac{mC_p}{U_L A_p}\left[\exp\left(\frac{F_p U_L A_p}{mC_p}\right) - 1\right]. \tag{27}$$

Step 10: Calculation of Qu_2 as below:

$$Qu_2 = F_o A_c[I(\tau\alpha) - U_L(T_o - T_a)]. \tag{28}$$

Step 11: Values of Qu_1 from Eq. (21) and Qu_2 are found from Eq. (28). If the deviation in values of Qu_1 and Qu_2 is higher than 0.1%, a new plate temperature $(T_p)_n$ is determined by an iteration method using the equation as follows:

$$T_p = T_a + \frac{\left[I(\tau\alpha) - \frac{Qu_2}{A_p}\right]}{U_L}\,. \tag{29}$$

Step 12: η_{th} of SAH is evaluated using Eq. (30) after the plate temperature is found:

$$\eta_{th} = F_o\left[(\tau\alpha) - \frac{U_L(T_o - T_i)}{I}\right]. \tag{30}$$

The theoretical efficiency found from Eq. (30) is equated with the experimental thermal efficiency of SAH to validate the mathematical model.

Figure 12 illustrates the thermal efficiency found from the mathematical model versus the experimental thermal efficiency for the arc rib with multiple gaps [19], symmetrical gap arc geometry and staggered element [21], half symmetrical arc rib and

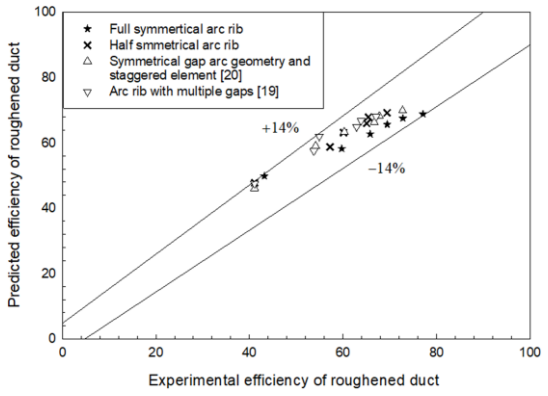

Fig. 12. Experimental and predicted thermal efficiencies for different roughness geometries.

full symmetrical arc rib. Figure 12 shows that for roughened surfaces, the deviations in thermal efficiencies found from the mathematical model and the experimental run lie within ±14%, indicating that the suggested mathematical model may be utilized to estimate SAH thermal performance.

8. Conclusions

The aim of the present investigation is to identify a way to enhance the heat transfer of the best arc rib geometry as per the literature, which is restricted by boundary layer rebuilding along its considerable long continuous arc segment. By adding another gap in the continuous arc segment, this unrestricted boundary layer redevelopment can be terminated. Investigating experimental results, novel arc rib roughness geometry outperforms in comparison to best arc rib geometry as per the literature. Novel arc rib geometry is the scientific contribution of the current study. To determine the impact of the proposed roughness geometry, namely, half symmetrical arc rib and full symmetrical arc rib geometry on *h*, *f*, and THPP, an experimental examination using a rectangular SAH duct with *W*/*H* of 12 has been carried out. The conclusions are as follows.

1). Half symmetrical arc rib and full symmetrical arc rib geometry show significant enhancement in heat transfer rate (*h*) with respect to the smooth duct.

2). The additional gap in the symmetrical arc rib elements influences the Nu and *f* values. The ranges of highest increment with respect to the smooth plate in Nu and *f* are 1.90–2.36 and 2.64–3.45 times, respectively, for full symmetrical arc rib geometry, while the increment in Nu and *f* values for half symmetrical arc rib geometry is 1.66–2.06 and 2.51–3.25, respectively.

3). The range of THPP for the full symmetrical arc rib and half symmetrical arc rib is 1.38–1.66 and 1.23–1.46, respectively.

4). THPP of existing roughness geometries of [19] and [21] has also been studied experimentally. It was found that the range of THPP for these geometries is 1.14–1.40 and 1.27–1.52, respectively, while the range of THPP for full symmetrical arc rib geometry (present study) is 1.38–1.66. Thus, the present study has the highest THPP for full symmetrical arc rib geometry. which is 1.66.

5). A correlation has been developed between *G'* and e^+ as well as between *R* and e^+. The maximum deviation in the experimental and theoretical values of *R* and *G'* is ±2% and ±10%, respectively.

6). The present mathematical model has been validated by comparing the thermal efficiency obtained from the mathematical model and from results obtained by experimental run.

Future research may be accompanied by investigating the effect of various geometrical constraints like p/e, p'/p, Ng, ng, d/w, r/e, e/D_h to better understand the overall behaviour of half symmetrical arc rib and full symmetrical arc rib geometries on the performance of SAH. Practically, it is tedious work to explore all parameters experimentally, so flow simulations can also be considered to investigate the flow patterns resulting from using half symmetrical arc rib and full symmetrical arc rib geometries.

Appendix A. Correlation development

Several investigators have established empirical correlations for the heat transfer coefficient and friction factor for a roughened SAH. The roughness function (*R*) given as in Eq. (31) and the roughness Reynolds number (e^+) given as in Eq. (32) is suggested by Nikurade [32]. The dimensionless flow velocity represented by *R*, in a control volume with enclosed edge roughness elements, shows the momentum loss caused by roughness. The single dimensionless indicator e^+ is used to represent optimum conditions for characterizing the performance of rough surface and flow parameters:

$$R = \sqrt{\frac{2}{f}} + 2.5 \ln\left(\frac{2e}{D_h}\right) + 3.75 , \tag{31}$$

$$e^+ = \mathrm{Re}\left(\frac{e}{D_h}\right)\sqrt{\frac{f}{2}} . \tag{32}$$

The dimensionless heat transfer function (*G'*) given by Eq. (33) indicates the competence of the rough surface in terms of heat transfer and temperature difference for the same controlled volume:

$$G' = \left[\left(\frac{f}{2\mathrm{St}}\right) - 1\right]\sqrt{\frac{2}{f}} + R . \tag{33}$$

Table 3. Constant coefficients for *R* and *G'* for investigated geometries.

Roughness Geometry	$R = C(e^+)^{C_0}$		$G' = C_1 + C_2(e^+) + C_3(e^+)^2$		
	C	C_0	C_1	C_2	C_3
Full symmetrical arc rib	5.3963	0.0224	10.6712	- 0.0883	0.0011
Half symmetrical arc rib	5.4398	0.0297	12.8759	- 0.1355	0.0017
Symmetrical gap arc geometry and staggered element [21]	5.6085	0.0174	13.0714	- 0.1575	0.0018
Arc rib with multiple gaps [19]	5.7535	0.0181	15.1026	- 0.1980	0.0022

Figure 13 represents *R* versus e^+ for an arc rib with multiple gaps [19], symmetrical gap arc geometry and staggered element [21], half symmetrical arc rib and full symmetrical arc rib. Eq. (31) and Fig. 13 indicate that *R* takes lower values for higher values of *f*. Figure 7 shows the highest *f* for the full symmetrical arc rib and Fig 13 shows a lower *R* for the full symmetrical arc rib.

Figure 14 represents *G'* versus e^+ for an arc rib with multiple gaps [19], symmetrical gap arc geometry and staggered element [21], half symmetrical arc rib and full symmetrical arc rib. Eq. (33) and Fig. 14 indicate lower *G'* at higher Nu, and Fig. 6 confirms that the highest Nu occurs for the full symmetrical arc rib and the lowest *G'* for the same full symmetrical arc rib.

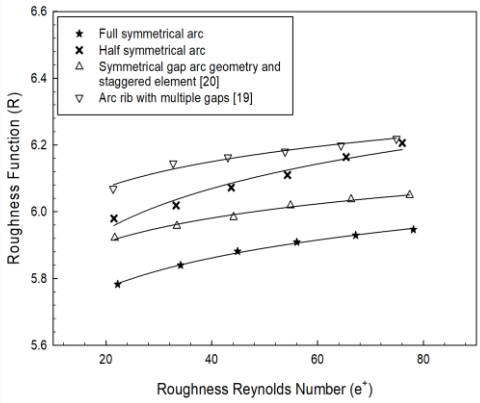

Fig. 13. Variation of R versus e^+ for investigated geometries.

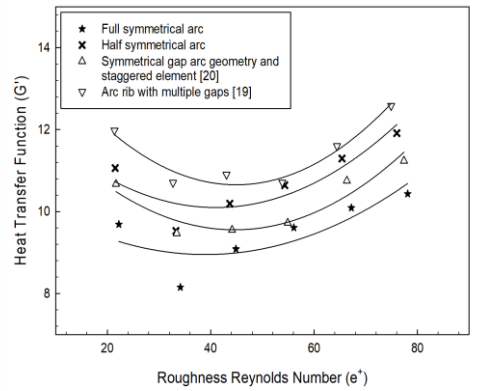

Fig. 14. Variation of G' versus e^+ for investigated geometries.

Correlations between R and e^+ and G' and e^+ are developed for an arc rib with multiple gaps [19], symmetrical gap arc geometry and staggered element [21], half symmetrical arc rib and full symmetrical arc rib. All roughness geometries have distinct coefficients and power indexes in the developed correlations between R and e^+ and between G' and e^+, as listed in Table 3.

Acknowledgements

The authors are extremely grateful to Maulana Azad National Institute of Technology Bhopal for providing experimentation amenities to accomplish this research work.

References

[1] Haldar, A., Varshney, L., & Verma, P. (2022). Effect of roughness parameters on performance of solar air heater having artificial wavy roughness using CFD. *Renewable Energy*, 184, 266–279. doi: 10.1016/j.renene.2021.11.088

[2] Bhuvad, S.S., Azad, R., & Lanjewar, A. (2022). Thermal performance analysis of apex-up discrete arc ribs solar air heater-an experimental study. *Renewable Energy*, 185, 403–415. doi: 10.1016/j.renene.2021.12.037

[3] Arunkumar, H.S., Kumar, S., & Vasudeva Karanth, K. (2022). Performance enhancement of a solar air heater using rectangular perforated duct inserts. *Thermal Science and Engineering Progress*, 34, 101404. doi: 10.1016/j.tsep.2022.101404

[4] Sureandhar, G., Srinivasan, G., Muthukumar, P., & Senthilmurugan, S. (2022). Investigation of thermal performance in a solar air heater having variable arc ribbed fin configuration. *Sustainable Energy Technologies and Assessments*, 52(PA), 102069. doi: 10.1016/j.seta.2022.102069

[5] Dheeraj Kumar, A.L. (2022). Nusselt number and friction characteristics of solar air heater roughened with novel twisted V-shaped staggered ribs using liquid crystal thermography. *Renewable Energy*, 110, 131932. doi: 10.1016/j.renene.2022.11.007

[6] Ravi, R.K., & Saini, R.P. (2016). Experimental investigation on performance of a double pass artificial roughened solar air heater duct having roughness elements of the combination of discrete multi V shaped and staggered ribs. *Energy*, 116, 507–516. doi: 10.1016/j.energy.2016.09.138

[7] Ravi, R.K., & Saini, R.P. (2018). Nusselt number and friction factor correlations for forced convective type counter flow solar air heater having discrete multi V shaped and staggered rib roughness on both sides of the absorber plate. *Applied Thermal Engineering*, 129, 735–746. doi: 10.1016/j.applthermaleng.2017.10.080

[8] Abbas, S., Yuan, Y., Hassan, A., Zhou, J., Ji, W., Yu, T., Rehman, U.U., & Yousuf, S. (2022). Design a low-cost, medium-scale, flat plate solar air heater: An experimental and simulation study. *Journal of Energy Storage*, 56, 105858. doi: 10.1016/j.est.2022.105858

[9] Zhang, Q., Wang, T., Hou, Q., Song, K., & Hu, W. (2022). Case Studies in Thermal Engineering Thermal hydraulic performance augmentation by petal-shaped ribs in a two-pass cooling channel. *Case Studies in Thermal Engineering*, 40, 102542. doi: 10.1016/j.csite.2022.102542

[10] Ayalew, Y.G. (2022). Experimental Investigation of Heat and Fluid Flow Characteristics on Expanded Metal Mesh Roughened Solar Collector. *Trends in Sciences*, 19(22).

[11] Salih, H.M. (2022). A comparative study for double pass solar air collector utilizing medial glass panel. *Archive of Mechanical Engineering*, 69(4), 729–747. doi: 10.24425/ame.2022.141524

[12] Jain, P.K., & Lanjewar, A. (2022). Experimental study of thermal augmentation in solar air heater roughened with aligned gaps in V-rib roughness with staggered element geometry. *Heat and Mass Transfer*, 58(4), 531–559. doi: 10.1007/s00231-021-03118-6

[13] Patel, L.A., & Singh, S. (2019). Experimental and numerical investigation of solar air heater with novel V rib. *Journal of Energy Storage*, 21.

[14] Karwa, R. (2003). Experimental studies of augmented heat transfer and friction in asymmetrically heated rectangular ducts with ribs on the heated wall in transverse, inclined, v-continuous and v-discrete pattern. *International Communications in Heat and Mass Transfer*, 30(2), 241–250. doi: 10.1016/S0735-1933(03)00035-6

[15] Saini, S.K., & Saini, R.P. (2008). Development of correlations for Nusselt number and friction factor for solar air heater with roughened duct having arc-shaped wire as artificial roughness. *Solar Energy*, 82(12), 1118–1130. doi: 10.1016/j.solener.2008.05.010

[16] Singh, A.P., Goel, V., Vashishtha, S., & Kumar, A. (2016). Heat Transfer Enhancement in a Solar Air Heater with Roughened Duct Having Arc-Shaped Elements as Roughness Element on the Absorber Plate. *Journal of the Institution of Engineers: Series C*, 97(3), 381–388. doi: 10.1007/s40032-016-0240-2

[17] Hans, V.S., Gill, R.S., & Singh, S. (2017). Heat transfer and friction factor correlations for a solar air heater duct roughened artificially with broken arc ribs. *Experimental Thermal and Fluid Science*, 80, 77–89. doi: 10.1016/j.expthermflusci.2016.07.022

[18] Gill, R.S., Hans, V.S., Saini, J.S., & Singh, S. (2017). Investigation on performance enhancement due to staggered piece in a broken arc rib roughened solar air heater duct. *Renewable Energy*, 104, 148–162. doi: 10.1016/j.renene.2016.12.002

[19] Jain, S.K., Agrawal, G.D., & Misra, R. (2020). Experimental investigation of thermohydraulic performance of the solar air heater having arc-shaped ribs with multiple gaps. *Journal of Thermal Science and Engineering Applications*, 12(1), 1–10. doi: 10.1115/1.4044427

[20] Azad, R., Bhuvad, S., & Lanjewar, A. (2021). Study of solar air heater with discrete arc ribs geometry: Experimental and numerical approach. *International Journal of Thermal Sciences*, 167, 107013. doi: 10.1016/j.ijthermalsci.2021.10701

[21] Ambade, J., & Lanjewar, A. (2019). Experimental investigation of solar air heater with new symmetrical GAP ARC GEOMETRY and staggered element. *International Journal of Thermal Sciences*, 146, 106093. doi: 10.1016/j.ijthermalsci.2019.106093

[22] Jain, P.K., Lanjewar, A., & Bhagoria, J.L. (2022). Heat transfer analysis of double discrete arc roughness with different relative rib altitudes and relate to a single discrete arc in the solar air heater. *International Journal of Ambient Energy*, 43(1), 6806–6828. doi: 10.1080/01430750.2022.2052959

[23] Singh, A.P., Varun, & Siddhartha. (2014). Effect of artificial roughness on heat transfer and friction characteristics having multiple arc shaped roughness element on the absorber plate. *Solar Energy*, 105, 479–493. doi: 10.1016/j.solener.2014.04.007

[24] Agrawal, Y., Bhagoria, J.L., Gautam, A., Kumar Chaurasiya, P., Arockia Dhanraj, J., Muthiya Solomon, J., & Salyan, S. (2022). Experimental evaluation of hydrothermal performance of solar air heater with discrete roughened plate. *Applied Thermal Engineering*, 211, 118379. doi: 10.1016/j.applthermaleng.2022.118379

[25] Pandey, N.K., Bajpai, V.K., & Varun. (2016). Experimental investigation of heat transfer augmentation using multiple arcs with gap on absorber plate of solar air heater. *Solar Energy*, 134, 314–326. doi: 10.1016/j.solener.2016.05.007

[26] Kumar, R., Goel, V., Singh, P., Saxena, A., Kashyap, A.S., & Rai, A. (2019). Performance evaluation and optimization of solar assisted air heater with discrete multiple arc shaped ribs. *Journal of Energy Storage*, 26, 100978. doi: 10.1016/j.est.2019.100978

[27] ASHRAE. (1977). Standard, Method of Testing to Determine the Thermal Performance of Solar Collector (93–97). ASHRAE.

[28] Kline, S.J., & McClintock, F. (1953). Describing uncertainties in single sample. *Mechanical Engineering*, 75, 3–8.

[29] Rosenhow, W.M., & Hartnett, J.P. (1973). *Handbook of Heat Transfer*. Mc Graw Hill. New York.

[30] Bhatti, M.S., & Shah, R.K. (1987). Turbulent and transition flow convective heat transfer. In *Handbook of Single-Phase Convective Heat Transfer* (pp. 4.1–4.166). Wiley. doi: 10.1016/0255-2701(88)87007-7

[31] Webb, R.L., & Eckert, E.R.G. (1972). Application of rough surfaces to heat exchanger design. *International Journal of Heat and Mass Transfer*, 15(9), 1647–1658. doi: 10.1016/0017-9310(72)90095-6

[32] Nikuradse, J. (1950). Laws of Flow in Rough Pipes. *NACA, Technical Memorandum* 1292. doi: 10.1016/s0882-6110(18)30184-6

[33] Dipprey, D.F., & Sabersky, R.H. (1963). Heat and momentum transfer in smooth and rough tubes at various Prandtl numbers. *International Journal of Heat and Mass Transfer*, 6(5), 329–353. doi: 10.1016/0017-9310(63)90097-8

[34] Klein, S.A. (2018). Calculation of flat-plate collector loss coefficients. In *Renewable Energy*, Chapter 29 (1st ed.). Routlegde. London. doi: 10.4324/9781315793245

[35] McAdams, W.H. (1954). Heat Transmission. McGraw Hill. New York.

Co-published by
Institute of Fluid-Flow Machinery
Polish Academy of Sciences
Committee on Thermodynamics and Combustion
Polish Academy of Sciences

http://www.imp.gda.pl/archives-of-thermodynamics/

Combustion characteristics of biochar from food processing waste

Jacek Kluska[a], Jakub Ramotowski[b]

[a]Insittute of Fluid Flow Machinery, Polish Academy of Sciences, Fiszera 14, 80-231 Gdańsk, Poland
[b]Gdańsk University of Technology, Faculty of Civil and Environmental Engineering and EkoTech Center, Narutowicza 11/12, 80-233 Gdańsk, Poland
*Corresponding author email: jkluska@imp.gda.pl

Received: 10.07.2023; revised: 12.02.2024; accepted: 24.03.2024

Abstract

This work examines biochar from carbonization of grape waste, and oat and buckwheat husks at 450ºC. The main aspects of the work concern the analysis of the fixed carbon and ash content in accordance with the European Standard. Obtained results showed that biochar from oat and buckwheat husk can be used for barbeque charcoal and barbeque charcoal briquettes production, whereas biochar derived from grape waste can be used for the charcoal briquettes production. Thermogravimetric analysis showed that biochar from grape stalk is characterized by the highest ignition and burnout performance, but in relation to the remaining samples, combustion process occurs in a narrow range of time and temperature. Obtained results showed that biochar from oat and buckwheat husks has properties, as well as combustion stability and reactivity, similar to commercial charcoal.

Keywords: Oat; Buckwheat; Grape; Biochar, Barbecue

Vol. 45(2024), No. 1, 45–51; doi: 10.24425/ather.2024.150437

Cite this manuscript as: Kluska, J., & Ramotowski, J. (2024). Combustion characteristics of biochar from food processing waste. *Archives of Thermodynamics*, 45(1), 45–51.

1. Introduction

The use of charcoal has increased significantly in the 21st century. This is related to the habits of society and the aspect of spending free time or organizing events, and to the fact that it is a source of heat in African countries [1]. According to the literature, the top charcoal-producing countries are Brazil, Nigeria, Ethiopia, Ghana, Tanzania, India and China, while the world production of charcoal already exceeds 50 million tons [2]. However, an important issue is the impact of charcoal production on the natural environment. Only in Kenya, from 1988, the reduction of land use and grasslands reached over 30%, whereas over 12% of Nigeria's forest has been lost since 1990 [3]. This situation, as well as legal regulations on environmental protection in individual countries, and an increase in the price of wood, led to finding alternative sources of charcoal production. This aspect has been presented by Kluska et al. [4], who indicated the possibility of producing charcoal from corn cobs. In these terms, Lu et al. [5] examined carbonization of palm

Nomenclature

D_f – burnout index, wt.%/min^4
Di – ignition index, wt.%/min^3
$(dw/dt)_{max}$ – maximum combustion rate, wt.%/min
$(dw/dt)_{mean}$ – mean combustion rate, wt.%/min
H_f – combustion index, °C
HHV – higher heating value, MJ/kg
S – combustion index, wt.%^{2}/min^2 °C^3
t – time, s
T – temperature, °C
T_f – burnout temperature, °C
t_f – burnout time, min
T_i – ignition temperature, °C
t_i – ignition time, min
T_p – maximum peak temperature, °C
t_p – maximum peak time, min
$\Delta t_{1/2}$ – time range of $(dw/dt)/(dw/dt)_{max}$ = 0.5, min
Y_i – mass fraction, kg/kg

fiber and eucalyptus. An interesting and promising material for biochar production is also sunflower waste [6], as well as rice straw and eggshells [7]. In addition, Hu et al. [7] indicated that biochar from rice straw is characterized by high NH_4^+ adsorption capacity.

This work presents the possibility of using food processing waste in the carbonization process, for the production of barbecue charcoal or briquettes. In recent years, due to increased consumption of wine and grape products, grape production reached over 79 million tons [8]. For this reason, grape processing waste is becoming an increasing problem in terms of waste management. In turn, buckwheat production reached almost 3 million tons [9], and due to the continuous increase in its consumption, the waste management problem becomes significant. In addition, world oat production reached over 20 million tons [10]. Characteristics of biochar from oat husk have been presented by Ferraz and Yuan [11] and Fan et al. [12] in terms of activated carbon preparation. In turn, buckwheat husk carbonization has been investigated by Yu et al. [13] in terms of the possibility of carbon materials production. Deiana et al. [14] showed the possibility of carbonization of grape stalks for activated carbon production, whereas del Pozo et al. [15] presented the characteristics of grape pomace pyrolysis and biochar.

The main aspects of the present work concern characteristics of combustion of obtained biochar samples, and comparatively, the commercial charcoal, using thermogravimetric analysis (TGA) and the determination of combustion, ignition and burnout indexes for comparing the quality of the analyzed samples as well as energy balance of the process. While the literature acknowledges the existence of biomass pyrolysis, there is a dearth of comprehensive findings pertaining to the carbonization process. Specifically, there is a lack of studies considering the energy balance and providing a detailed analysis of the energy derived from both liquid and gaseous products. Addressing this aspect is crucial, as per the European Biochar Certificate standards [4], where a significant portion (at least 70%) of the waste energy released during the combustion of pyrolysis gases is required to be utilized as a heating source or for drying biomass. The combustion characteristics of obtained biochars are interesting and show the potential for their use as an additive in the production of barbecue briquettes. This consideration is particularly significant in light of environmental protection laws and legislative measures in various countries aimed at preserving forest resources. This situation contributes to an escalation in the cost of wood waste and simultaneous deterioration in the quality of wood charcoal.

2. Materials and methods

2.1. Proximate analysis of raw materials

The proximate and ultimate analyses (Table 1) of the oat and buckwheat husks, grape pomace and stalk (waste from grain processing and the oil products industry), were conducted using an X-ray fluorescence spectrometer (S1 Titan, Bruker Scientific Instruments), a CHNS/O Flash 2000 Analyzer (Thermo Scientific) and EkotechLAB calorimeter. The technical analysis of the samples was determined in accordance with the EN 1860-2 Standard (*Appliances, solid fuels and firelighters for barbecuing – Part 2: Barbecue biochar and barbecue biochar briquettes – Requirements and test methods*).

Table 1. Proximate and ultimate analysis of oat and buckwheat husks, and grape waste.

	Grape stalks	Grape pomace	Oat husks	Buckwheat husks
HHV [MJ/kg]	18.12	17.11	17.7	18.54
Moisture [wt%, as delivered]	20.21	41.14	12.19	11.30
Proximate [wt.%$_{db}$][a]				
Volatiles	64.63	52.80	81.5	78.7
Fixed carbon	28.41	40.17	17	20
Ash	6.95	7.03	1.5	1.3
Ultimate [wt.%$_{db}$][a]				
C	46.21	53.61	48.73	51.25
H	5.77	5.21	7.33	7.01
O	47.65	40.89	40.08	38.05
N	0.37	0.29	3.86	3.69

[a]db – dry basis

2.2. Preparation of biochar

Experimental investigations were carried out in the laboratory scale reactor (Fig. 1) with a capacity of 3 l (400 mm in length and an internal diameter of 145 mm). During every experiment, the reactor chamber was firstly heated to 450ºC (and maintained with a PID controller) and then a crucible with a sample (1000 g for oat and buckwheat husk, 1000 g for grape stalk, and 1500 g for grape pomace) was loaded into the chamber. The final temperature was set at 450ºC and measured by two thermocouples placed 20 mm from the crucible wall and in the bed core, respectively. Once the desired temperature was reached, the process was stopped and the reactor was removed from the heating

chamber. The temperature of 450°C was set to maximize the yield of the solid fraction, with a fixed carbon content above 65%.

As for the liquid phase, the obtained products were collected using a steel cylinder (1 l) filled with isopropanol and kept at 0ºC, and three isopropanol-filled scrubbers were kept in cryostat at the temperature of −20ºC. Before, and after each experiment, the cylinder and all washers were weighed in order to perform mass balance.

The water content in the liquid products was analyzed by Karl-Fisher titrator, whereas the caloric value was determined using a calorimeter (EkotechLAB, Poland). The gaseous products were collected using tedlar bags and then analyzed by a gas chromatograph with a thermal conductivity detector (SRI Instruments 310).

The calorific value of a gaseous product was calculated according to the formula:

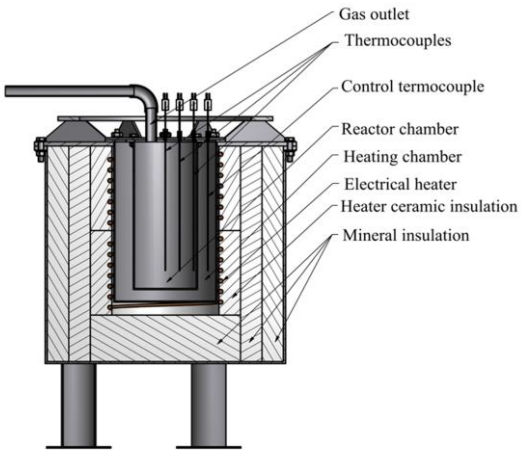

Fig. 1. Batch scale carbonization reactor.

$$\mathrm{HHV} = Y_{\mathrm{CO}} \cdot \mathrm{HHV}_{\mathrm{CO}} + Y_{\mathrm{CH_4}} \cdot \mathrm{HHV}_{\mathrm{CH_4}} + Y_{\mathrm{H_2}} \cdot \mathrm{HHV}_{\mathrm{H_2}} + Y_{\mathrm{N_2}} \cdot \mathrm{HHV}_{\mathrm{N_2}} + Y_{\mathrm{CO_2}} \cdot \mathrm{HHV}_{\mathrm{CO_2}}, \quad (1)$$

where HHV_i [MJ/kg] denotes the calorific value of the *i*-th gas component (i = CO, CH_4, H_2, N_2, CO_2), and Y_i represents its mass fraction [17].

2.3. Thermogravimetric analyses

In order to determine the combustion characteristics of biochar samples and commercial charcoal, TA Instruments SDT Q600 Thermogravimetric Analyzer was used. All samples were heated from 30 to 850ºC at the rate of 10 ºC/min. The mass of each sample was 6–8 mg, and the airflow rate was set, based on the research findings [17–19], at 100 ml/min.

Combustion characteristics of different fuels can be characterized using TGA analysis, by the intensity and rate of combustion, combustion reactivity or intensity of devolatilization [16,19]. A group of parameters, taking into account the ignition temperature (T_i), burnout temperature (T_b) and, respectively, the time of ignition (t_i) and burnout (t_b), maximum combustion rate $(dw/dt)_{max}$ and, respectively, temperature (T_{max}) and time (t_{max}), can be determined to compare the combustion reactivity of biochar samples [21,22]. Taking into account differential thermogravimetric (DTG) analysis, T_{max} and $(dw/dt)_{max}$ most often indicate reactivity, for which a high value of $(dw/dt)_{max}$ at low temperature T_{max} characterizes the high reactivity of the sample [20]. The *S* index determines the combustion reactivity of the sample according to the equation:

$$S = \frac{(dw/dt)_{max}(dw/dt)_{mean}}{T_i^2 T_b}, \quad (2)$$

where the ignition temperature (T_i) refers to the combustion reaction rate which reaches 1 wt.%/min, and the burnout temperature (T_b) pertains to the combustion rate decreasing to 1 wt.%/min [16,17]. The second index of combustion is H_f, which characterizes intensity and combustion rate [19]:

$$H_f = T_{max} \ln\left(\frac{\Delta T_{1/2}}{(dw/dt)_{max}}\right), \quad (3)$$

where T_{max} represents the temperature for which the mass loss rate reaches maximum value, $\Delta T_{1/2}$ is the range of temperature, in which $(dw/dt)/(dw/dt)_{max} = 0.5$ [19]. A low value of H_f indicates better combustion characteristics [23]. In order to determine the intensity of volatiles release, the ignition index D_i is defined as:

$$D_i = \frac{(dw/dt)_{max}}{t_i t_{max}}, \quad (4)$$

where t_{max} represents the time for which the mass loss rate reaches a maximum value. The ignition index indicates ignition performance and allows us to compare the ease of ignition of different samples. A higher D_i value indicates a faster start of a combustion process [24]. The burnout index D_f, which indicates whether the combustion process ends slowly or rapidly [20], is defined as:

$$D_f = \frac{(dw/dt)_{max}}{\Delta t_{1/2} t_p t_b}, \quad (5)$$

where $\Delta t_{1/2}$ is the time range in which $(dw/dt)/(dw/dt)_{max} = 0.5$. A high value of D_f means that the combustion process ends rapidly [25]. Furthermore, to characterize the stability of combustion, the process stability index (D_w) can be defined according to the equation:

$$D_w = \frac{(dw/dt)_{max}}{T_i T_{max}}. \quad (6)$$

The stability index D_w characterizes combustion stability between the ignition point and burnout point. A high value of this index indicates good stability of the combustion process [26].

3. Results and discussion

3.1. Characterization of heating rate during the carbonization process

Figure 2 presents the characteristics of oat and buckwheat husks, grape pomace and grape stalk samples. The experimental investigation showed that for the carbonization of corn stalk, the heating rate reached 10 °C/min at 20 mm from the wall and 9.2 °C/min in the core of the bed (Table 2). In the case of oat and buckwheat husks and grape pomace, the heating rate at the core of the reactor reached a similar value.

In the case of carbonization of oat and buckwheat husks a significant plateau can be observed. For the buckwheat husk sample, the slowdown in the heating rate attributed to the evaporation of moisture lasted approximately 100 minutes.

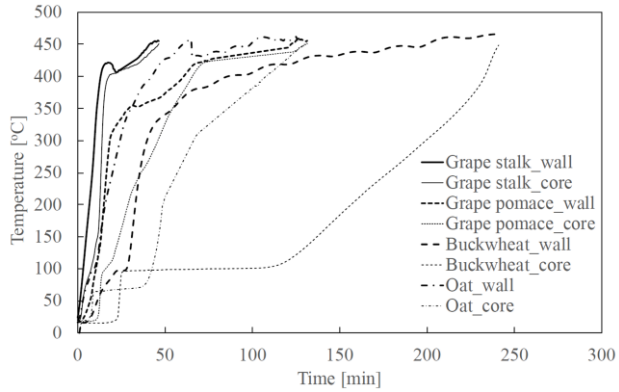

Fig. 2. Characteristics of the heating rate of the fixed bed.

Table 2. Characterization of fixed bed heating rate during carbonization process

		Grape stalk	Grape pomace	Oat husks	Buckwheat husks
Wall	[°C/min]	10.0	3.5	7.0	4.2
Core		9.2	3.4	3.3	5.2

The carbonization of grape pomace is characterized by two heating rate ranges. To reach 300°C near the wall, the average heating rate was 22 °C/min, and when it was reached the rate dropped to 1.5 °C/min. In the case of the core temperature, the heating rate reached 6.7 °C/min; however, after reaching 400°C, it dropped to 0.8 °C/min. A similar situation was observed for the buckwheat husk sample. Below the temperature of 300°C near the wall, the average heating rate was 22.1 °C/min, and above it, the rate dropped to 1.8 °C/min.

3.2. Proximate and ultimate analysis of biochar samples

Table 3 presents the proximate and ultimate analysis of obtained biochar from carbonization at 450ºC and from commercial charcoal. In accordance with the European Standard EN 1860-2:2005, biochar for barbeque charcoal production requires an ash content below 8% and fixed carbon above 75%. In the case of barbeque charcoal briquettes, ash content must be below 18% and fixed carbon content above 60% [16,27]. The obtained results showed that biochar from oat and buckwheat husk carbonization can be used to produce barbeque charcoal as well as barbeque charcoal briquettes. Biochar from the grape stalk and pomace can be used only to produce barbeque charcoal briquettes due to the low content of fixed carbon and high ash content in the case of the grape stalk, and fixed carbon content lower than 75% in the case of grape pomace. In addition, biochar from the grape stalk, due to high ash and low fixed carbon content, is characterized by the lowest higher heating value of 22.80 MJ/kg.

3.3. Energy balance of carbonization products

Table 4 presents the mass and energy balance of the liquid and gas products, which is significant in terms of energy management, including water content in the mixture of gases and tars. Due to International Biochar Initiative (IBI) and European Biochar Certificate (EBC) guidelines, which determine the parameters of biochars and their certification, at least 70% of excess heat from the carbonization process must be used (for drying biomass, generating electricity) to obtain certificates for biochar [27]. The present study results showed that carbonization at 450ºC of oat and buckwheat husks leads to the production of a significant amount of water (~35% and 29%, respectively) and

Table 3. Proximate and ultimate analysis of biochar samples from carbonization of oat and buckwheat husks, and grape waste, at 450ºC.

	Grape stalk	Grape pomace	Oat husks	Buckwheat husks	Commercial charcoal
HHV [MJ/kg]	22.80	29.95	28.92	28.76	29.71
Moisture	3.23	4.81	4.02	5.04	5.58
Proximate [wt.%$_{db}$][a]					
Volatiles	34.24	22.55	22.70	22.90	25.00
Fixed carbon	60.12	69.85	71.00	73.00	74.00
Ash	15.64	7.60	6.3	4.10	1.00
Ultimate [wt.%$_{db}$][a]					
C	62.75	64.38	55.13	63.57	71.34
H	2.99	2.99	3.34	3.34	3.36
O	33.76	32.34	41.19	32.70	24.82
N	0.50	0.29	0.34	0.39	0.48

[a]db – dry basis

Table 4. Characteristics of pyrolysis products – a mixture of liquid and gas fractions.

	Grape stalk	Grape pomace	Oat husks	Buckwheat husks
Biochar	43.51	34.32	32.16	36.25
Liquid+gas	56.49	65.68	67.84	63.75
Composition $_{liquid+gas}$				
Water content [%]	4.25	14.27	35.37	28.77
Bio-oil [%]	28.10	72.82	26.87	28.74
HHV [MJ/kg]				
Gases [%]	42.73	12.91	15.48	15.86
CO [%]	22.42	29.36	29.39	29.20
CO_2 [%]	65.66	58.39	54.65	57.83
H_2 [%]	1.31	1.26	1.27	1.16
CH_4 [%]	5.61	5.99	4.56	6.82
HHV [MJ/kg]	3.36	4.16	3.78	4.37
$HHV_{liquid+gas}$ [MJ/kg]	2.63	19.60	10.39	9.31
$HHV_{liquid+gas}$ [MJ/$kg_{feedstock}$]	1.43	12.14	6.82	5.58

gas mixture (~15%), whereas carbonization of grape stalk and pomace is characterized by lower water content (~4% and ~14%, respectively). In the case of grape stalk, the carbonization process led to high yields of gas (42%). Carbonization of grape pomace resulted in the production of high amount of bio-oils (~73%), which affected the calorific value of the derived liquid and gaseous products (19.6 MJ/kg), and the amount of energy in pyrolysis gases obtained from one kilogram of feedstock reached 12.14 MJ. Carbonization of oat and buckwheat husks was characterized by lower and similar calorific values of the derived liquid and gaseous products (10.39 and 9.31 MJ/kg, respectively), which translated to the energy amount of 6.82 and 5.58 MJ/kg $_{feedstock}$, respectively. Due to low bio-oils content, liquid and gaseous products of grape stalk carbonization were characterized by significantly lower calorific values (2.63 MJ/kg and 1.43 MJ/kg $_{feedstock}$).

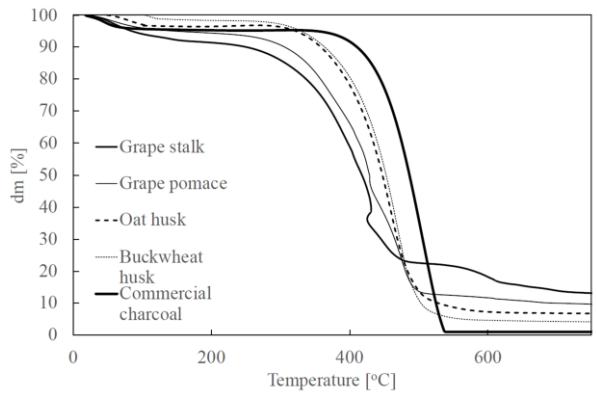

Fig. 3. TG curves for biochar from oat and buckwheat husks, grape waste and commercial charcoal.

3.4. Thermogravimetric investigation of oat and buckwheat husks

Figures 3 and 4 present characteristics of biochar combustion using thermogravimetric analysis. The TG analysis showed that the overall mass loss reached the maximum value for commercial charcoal, which is caused by the lowest ash content (1%), whereas the lowest overall mass loss has been observed for biochar from grape stalk with an ash content of 15%. Obtained results revealed that biochars from oat husks and buckwheat husks are characterized by a curve with a similar slope and overall mass loss.

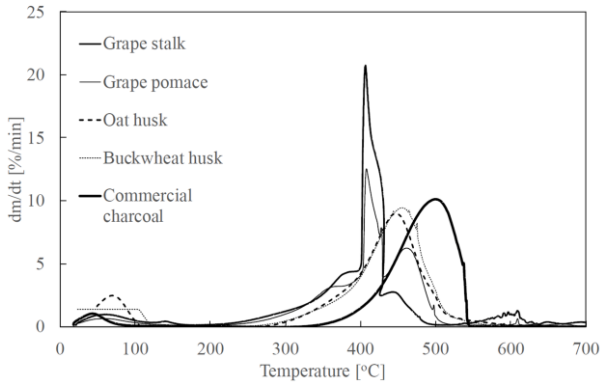

Fig. 4. DTG curves for biochar from oat and buckwheat husks, grape waste and commercial charcoal.

It was also found that ignition temperature (T_i), which refers to ignition performance, reached the highest value for the commercial charcoal (388ºC), while the lowest value was obtained for biochar from the grape stalk and pomace (286ºC and 299ºC, respectively), as given in Table 5. This aspect was also reflected in ignition time (t_i). The burnout process started the fastest for biochar from buckwheat husks and grape stalks (22 and 26 min, respectively), and the latest in the case of commercial charcoal (37 min). Proximate analysis of obtained samples (Table 3) indicates that biochar from grape stalks has the highest volatile content.

According to the literature, an increase in volatile matter leads to faster devolatilization and accelerates the ignition process at lower temperatures [18]. This is also reflected in the ignition index (D_i), which reached a higher value for biochar from the pomace stalk and indicates a faster start of the combustion process. In this case, $(dw/dt)_{max}$ and t_{max} were also significant (Table 5). Biochar from grape stalk reached the highest maximum mass loss rate (20.76 wt.%/min), but in relation to the remaining samples, in a narrow range of time and temperature ($\Delta t_{1/2}$ = 1.1 min). In this case, the biochar closest to commercial charcoal is biochar from oat husks, for which the ignition index D_i reached 8.23 wt.%/(min^3×10^{-3}), while for the commercial charcoal only 5.74 wt.%/(min^3×10^{-3}). Considering the burnout temperature (T_b), biochar from the grape stalk is characterized by the lowest value (473ºC), while the remaining samples have a burnout temperature above 500ºC. The maximum temperature was reached for the commercial charcoal (542ºC), for which this process was completed at the latest (52 min). High burnout temperature may be reflected in the difficulty of burning the sample,

Table 5. Characteristic combustion parameters.

		Grape stalk	Grape pomace	Oat husks	Buckwheat husks	Commercial charcoal
T_i	[°C]	286	299	327	327	388
T_b	[°C]	473	499	514	517	542
T_{max}	[°C]	407	408	447	455	500
$\Delta T_{1/2}$	[°C]	27	57	77	54	92
t_i	[min]	26	28	28	22	37
t_{max}	[min]	37	38	39	34	47
$\Delta t_{1/2}$	[min]	1.1	5.4	7.8	7.9	9.4
t_b	[min]	45	48	47	42	52
$(dw/dt)_{max}$	[%/min]	20.76	12.60	8.99	9.45	10.13
$(dw/dt)_{mean}$	[%/min]	3.32	3.80	4.34	4.53	6.29
S	[wt.%/(min^2 °C^3)]	17.84	10.70	7.08	7.73	7.81
D_i	[wt.%/(min^3×10^{-3})]	20.71	11.67	8.23	12.21	5.74
D_f	[wt.%/(min^4×10^{-5})]	1115.4	125.7	62.8	82.8	43.3
H_f	[°C×10^3]	106.96	616.12	959.19	795.67	1102.87

which leads to a longer time for completing the process of conversion. On the other hand, longer fuel combustion on the grill grate has its economic, positive aspects.

Burnout properties can also be correlated with the burnout index (D_f). The carried out study showed that biochar from grape waste is characterized by the highest values of D_f, which indicates that the combustion process ends faster than for other biochars [28]. However, the characteristics obtained indicate that despite the maximum value $(dw/dt)_{max}$ reached 20.76 %/min, the average value of mass loss reached only 3.32 %/min. This is caused by high ash content and extended time related to the heating of a sample and its afterburning after passing through the maximum combustion peak. In the case of commercial charcoal, $(dw/dt)_{max}$ reached 10.13 %/min, but the combustion process takes place less rapidly with an average value of mass loss of 6.29 %/min. Taking into account the combustion reactivity, biochar from grape stalks is characterized by the highest S index of 17.8 %^{2}/(min^2 °C^3), whereas biochars from oat and buckwheat husks reached similar values (7.08 and 7.73 %^{2}/(min^2·°C^3), respectively) to commercial charcoal (7.81 %^{2}/(min^2·°C^3)) which means similar combustion reactivity characteristics. In addition, the combustion index H_f reached the lowest value for biochar from the grape stalk, whereas for the commercial charcoal and biochar from oat husks, it reached the highest value. As regards the combustion stability index (D_f), biochars from oat and buckwheat husks showed values similar to commercial charcoal.

4. Conclusions

This work presents characteristics of biochar in terms of barbeque charcoal and briquette application. The experimental investigation was focused on the biochar from the carbonization of grape waste, and oat and buckwheat husks at 450ºC. The main aspects concern the analysis of the fixed carbon and ash contents in accordance with the European Standard. The study revealed that biochar from oat and buckwheat husks can be used for barbeque charcoal and barbeque charcoal briquettes production, whereas biochar from grape waste can be used for charcoal briquettes production. Combustion characteristics using thermogravimetric analysis showed that biochar from the grape stalk is characterized by the highest ignition and burnout performance, but compared to other samples, the combustion process occurs in a narrow range of time and temperature. It was found that biochar from oat and buckwheat husks has properties (the course of DTG curve), average and maximum value of mass loss, and combustion reactivity and stability, similar to commercial charcoal. Due to an increase in world production of oat and buckwheat as well as grape-derived food products, adding biochars from the carbonization of the food industry waste, may be an interesting alternative for wood resources and affect the economic and environmental aspects of the production of barbecue charcoal and briquette.

References

[1] Bekele, B., & Kemal, A.W. (2022). Determents of sustainable charcoal production in AWI zone; the case of Fagita Lekoma district, Ethiopia. *Heliyon*, 8, e11963. doi: 10.1016/j.heliyon.2022.e11963

[2] Rotowa, O.J., Egbwole, Z.T., Adeagbo, A.A., & Blessing, O.M. (2019). Effect of Indiscriminate Charcoal Production on Nigeria Forest Estate. *International Journal of Environmental Protection and Policy, 7, 134-139.* doi: 10.11648/j.ijepp.20190706.12

[3] Tabe-Ojong, M.P. Jr. (2023). Action against invasive species: Charcoal production, beekeeping, and Prosopis eradication in Kenya. *Ecological Economics*, 203, 107614. doi: 10.1016/j.ecolecon.2022.107614

[4] Kluska, J., Ochnio, M., & Kardaś, D. 2020. Carbonization of corncobs for the preparation of barbecue charcoal and combustion characteristics of corncob char. *Waste management*, 105, 560–565. doi: 10.1016/j.wasman.2020.02.036

[5] Lu, K.M., Lee, W.J., Chen, W.H., Liu, S.H., & Lin, T.C. (2012). Torrefaction and low temperature carbonization of oil palm fiber and eucalyptus in nitrogen and air atmospheres. *Bioresource Technology*, 123, 98–105. doi: 10.1016/j.biortech.2012.07.096.

[6] Angın, D. (2013). Effect of pyrolysis temperature and heating rate on biochar obtained from pyrolysis of safflower seed press cake. *Bioresource Technology*, 128, 593–597. doi: 10.1016/j.biortech.2012.10.150

[7] Xu, D., Cao, J., Li, Y., Howard, A., & Yu, K. (2019). Effect of pyrolysis temperature on characteristics of biochars derived from different feedstocks: A case study on ammonium adsorption capacity. *Waste management*, 87, 652-660. doi: 10.1016/j.wasman.2019.02.049

[8] Gubitosa, J., Rizzi, V., Laurenzana, A., Scavone, F., Frediani, E., Fibbi, G., et al. (2022). The "End Life" of the Grape Pomace Waste Become the New Beginning: The Development of a Virtuous Cycle for the Green Synthesis of Gold Nanoparticles

and Removal of Emerging Contaminants from Water. *Antioxidants*, 11, 994. https://doi.org/10.3390/antiox11050994

[9] Yuan, Y., Li, F., Han, N., Zeng, B., Imaizumi, Y., Na, R., et al. (2022). Exploring the Valorization of Buckwheat Waste: A Two-Stage Thermo-Chemical Process for the Production of Saccharides and Biochar. *Fermentation*. 8, 573. doi: 10.3390/fermentation8110573

[10] Jokinen, I., Pihlava, J.-M., Puganen, A., Sontag-Strohm, T., Linderborg, K.M., Holopainen-Mantila, U., et al. (2021). Predicting the Properties of Industrially Produced Oat Flours by the Characteristics of Native Oat Grains or Non-Heat-Treated Groats. *Foods*. 10(7), 1552. doi:10.3390/foods10071552

[11] Ferraz, F.M., & Yuan, Q. (2020). Performance of oat hulls activated carbon for COD and color removal from landfill leachate. *Journal of Water Process Engineering*, 33, 101040. doi: 10.1016/j.jwpe.2019.101040

[12] Fan, M., Marshall, W., Daugaard, D., & Brown, R.C. (2004). Steam activation of chars produced from oat hulls. *Bioresource Technology*, 93, 103–107. doi:10.1016/j.biortech.2003.08.016

[13] Yu, K., Zhang, Z, Jicai, L., & Liang C. (2021). Natural biomass-derived porous carbons from buckwheat hulls used as anode for lithium-ion batteries. *Diamond and Relatated Materials*. 119, 108553. doi: 10.1016/j.diamond.2021.108553

[14] Deiana, A.C., Sardella, M.F., Silva, H., Amaya, A., & Tancredi, N. (2009). Use of grape stalk, a waste of the viticulture industry, to obtain activated carbon. *Journal of Hazardous Materials*, 172, 13–19. doi: 10.1016/j.jhazmat.2009.06.095

[15] Pozo, C., Rego F, Puy N., Bartrolí, J., Fàbregas, E., Yang Y., et al. (2022). The effect of reactor scale on biochars and pyrolysis liquids from slow pyrolysis of coffee silverskin, grape pomace and olive mill waste, in auger reactors. *Waste Management*, 148, 106–116. doi: 10.1016/j.wasman.2022.05.023

[16] Xiong, S., Zhang, S., Wu, Q., Guo, X., Dong, A., & Chen, C. (2014). Investigation on cotton stalk and bamboo sawdust carbonization for barbecue charcoal preparation. *Bioresource Technology*, 152, 86–92. doi: 10.1016/j.biortech.2013.11.005

[17] Wang, C., Zhang, X., Liu, Y., & Che, D. (2012). Pyrolysis and combustion characteristics of coals in oxyfuel combustion. *Applied Energy*. 2012, 97, 264–273. doi: 10.1016/j.apenergy.2012.02.011

[18] Moon, C., Sung, Y., Ahn, S., Kim, T., Choi, G., & Kim, D. (2013). Effect of blending ratio on combustion performance in blends of biomass and coals of different ranks. *Experimental Thermal and Fluid Science*, 47, 232–240. doi: 10.1016/j.expthermflusci. 2013.01.019

[19] Mureddu, M., Dessì, F., Orsini, A., Ferrara F., & Pettinau, A. Air- and oxygen-blown characterization of coal and biomass by thermogravimetric analysis. *Fuel*, 2018, 212, 626–637. doi: 10.1016/j.fuel.2017.10.005

[20] Bilkic, B., Haykiri-Acma, H., & Yaman, S. (2020). Combustion reactivity estimation parameters of biomass compared with lignite based on thermogravimetric analysis. *Energy Sources, Part A: Recovery, Utilization, and Environmental Effects*, 45, 7068–7087. doi: 10.1080/15567036.2020.1851326

[21] Ronda, A., Della, Z.M. Gianfelice G., Ianez-Rodriguez, I., & Canu P. (2019). Smouldering of different dry sewage sludges and residual reactivity of their intermediates. *Fuel*, 247, 148–59. doi: 10.1016/j.fuel.2019.03.026

[22] Xie, W., Huang, J., Liu, J., Zhao, Y., Chang, K., Kuo, J., et al. (2018). Assessing thermal behaviors and kinetics of (co-) combustion of textile dyeing sludge and sugarcane bagasse. *Applied Thermal Engineering*, 131, 874–83. doi: 10.1016/j.applthermaleng.2017.11.025.

[23] Sieradzka, M., Gao, N., Quan, C., Mlonka-Medrala, A., & Magdziarz, A. (2020). Biomass thermochemical conversion via pyrolysis with integrated CO_2 capture. *Energies*, 13, 1050. doi: 10.3390/en13051050

[24] Kumar, R., & Singh, R.I. (2017). An investigation of co-combustion municipal sewage sludge with biomass in a 20kW BFB combustor under air-fired and oxygen-enriched condition. *Waste Management*, 70, 114–26. doi: 10.1016/j.wasman.2017.09.005

[25] Ma, Q., Han, L., & Huang, G. (2017). Evaluation of different water-washing treatments effects on wheat straw combustion properties. *Bioresource Technology*, 245, 1075–83. doi: 10.1016/j.biortech.2017.09.052

[26] Sarikaya, A.C., Acma, H.H., & Yaman S. (2019). Synergistic interactions during co-combustion of lignite, biomass, and their chars. *Journal of Energy Resources Technology*, 141, 122203. doi: 10.1115/1.4044057

[27] Godlewska, P., Ok, Y.S., & Oleszczuk, P. (2021). THE DARK SIDE OF BLACK GOLD: Ecotoxicological aspects of biochar and biochar-amended soils. *Journal of Hazardous Materials*, 403, 123833. doi: 10.1016/j.jhazmat.2020.123833

[28] Qian, W., Xie, Q, Huang, Y., Dang, J., Sun, K., Yang, Q., et al. (2012). Combustion characteristics of semicokes derived from pyrolysis of low rank bituminous coal. *Journal of Mining Science and Technology*. 22, 645-650. doi: 10.1016/ j.ijmst.2012.08.009

Co-published by
Institute of Fluid-Flow Machinery
Polish Academy of Sciences
Committee on Thermodynamics and Combustion
Polish Academy of Sciences

http://www.imp.gda.pl/archives-of-thermodynamics/

Experimental investigation of heat transfer and aerodynamic drag of novel heat sinks with lamellar fins

Aleksandr Terekh, Aleksandr Rudenko, Yevhenii Alekseik*

National Technical University of Ukraine "Igor Sikorsky Kyiv Polytechnic Institute", Educational and Scientific Institute of Atomic and Thermal Energy, 37, Beresteisky Av., Kyiv, 03056, Ukraine
*Corresponding author email: alexeik_kpi@ukr.net

Received: 14.05.2023; revised: 04.07.2023; accepted: 05.10.2023

Abstract

Heat transfer and aerodynamic drag of novel small-sized heat sinks with lamellar fins, designed for electronic cooling, were experimentally investigated under conditions of forced convection in the range of Reynolds numbers 1 250–10 500. It was found that a gradual reduction in the fin spacing from 6 mm to 3 mm with a 29° angle of taper between the outermost fins leads to an increase in the heat transfer intensity by 15–32% with a significant increase in aerodynamic drag compared to the surface with a constant fin spacing of 6 mm. Incomplete cross-section cutting of fins at the relative depth of 0.6 in addition to the gradual reduction in the fin spacing provides aerodynamic drag decrease by 5–20% and increase of heat transfer intensity by 18–20% in comparison with the similar heat sink without fins cutting. Proposed novel designs of heat sinks enabled us to decrease by 7°C–16°C the maximum overheating of the heat sink's base in the flow speed range from 2.5 m/s to 7.5 m/s at constant heat load. To ensure a constant value of maximum overheating of the heat sink base the inlet flow velocity for the surface with constant fin spacing should be 1.6–2 times higher than that for the heat sink with 29° taper angle between outermost fins and partially fins cutting. In this case, the aerodynamic drag for the latter will be higher only by 1.6–2.7 times, which is quite acceptable.

Keywords: Heat sink; Lamellar finning; Electronic cooling; Aerodynamic drag; Heat transfer

Vol. 45(2024), No. 1, 53–63; doi: 10.24425/ather.2024.150438

Cite this manuscript as: Tarekh, A., Rudenko, A., & Alekseik, Y. (2024). Experimental investigation of heat transfer and aerodynamic drag of novel heat sinks with lamellar fins. *Archives of Thermodynamics*, 45 (1), 53–63.

1. Introduction

Heat sinks are widely used for cooling various electronic, components (such as power semiconductors, LED, microprocessors, microchips and others) operating with a high specific heat load. To ensure their reliable operation over a long period of time of functioning these devices should be cooled because the failure rate of these components doubles with each increase in temperature by 10°C above the operating temperature (~ 80°C) of the electronic device [1].

Therefore, an important factor during the development of electronic devices is the choice of systems and methods of cooling, providing the most intensive heat removal from heat-loaded components while reducing their mass-size characteristics and minimizing manufacturing costs. In this regard, the development of new designs of heat sinks, allowing the removal of heat by air cooling, becomes relevant in terms of improving the efficiency and durability of electronic devices.

In the paper [2], heat transfer intensity and pressure losses of heat sinks with lamellar, cross-split and pinned fins were investi-

Nomenclature

b – width of the split fin, m
d – diameter, m
E – fin efficiency
Eu – Euler number
F – area, cross-section area, m^2
G – coolant flow rate, kg/s
h – height, fin height, m
k_u – conversion factor
L – length, m
Nu – Nusselt number
Q – heat flow, W
Re – Reynolds number
T – temperature, K
$\bar{T}$ – average temperature, K
t – fin spacing, m
u_c – cutting width, m
W – velocity, m/s
w – base width, m
Z – number of fins
ΔP – aerodynamic drag, Pa
ΔT – overheating, °C

Greek symbols

α – heat transfer coefficient, W/(m^2 K)
β – angle between fin and wall, °
δ – thickness, m
λ – heat conductivity coefficient, W/(m K)
ν – coefficient of kinematic viscosity, m^2/s
ρ – density, kg/m^3
φ – taper angle, °
Ψ – finning coefficient

Subscripts and Superscripts

1 – inlet of the heat sink
2 – outlet of the heat sink
all – total
b – base
c – cut
f – fin
h – hydraulic
los – losses
max – maximum
noz – nozzle
o, *on* – inlet of the working section
red – reduced

gated. The data presented in the paper show that in the range of Reynolds numbers 2 500–14 000, the heat sink with pin and split fins has the lowest thermal resistance. The smallest aerodynamic drag was observed for the lamellar heat sink.

The influence of geometrical characteristics of lamellar-finned heat sinks on heat exchange and pressure drop under conditions of forced convection (Re = 25 000–1 750 000) was studied experimentally in [3]. The authors found that the pressure drop along the heat sink increases with increasing fin height, Reynolds number and decreasing inter-fin gap. The average value of Nusselt numbers increases with the increasing Reynolds number, inter-fin gap, fin thickness and with the decreasing fin height.

In [4], on the basis of the lamellar-finned heat sinks, the original design of the combined lamellar-pinned heat sink, the pins of which are located in the gap between the adjacent lamellar fins, is developed. Both numerical and experimental studies of heat transfer and aerodynamic drag of such heat sinks under the conditions of forced convection in the range of flow velocities in the inter-fin gap from 6.5 m/s to 12.5 m/s have been conducted. The results indicate that the thermal resistance of the lamellar-pinned heat sink is about 30% lower than that of the plate-fin heat sink used as the basic one under the conditions of equal velocity of the incoming air flow. It is noted that the pins turbulate the flow in the inter-fin gap. As a result, the intensity of heat exchange increases, but at the same time its aerodynamic drag increases by 2.5–4 times.

Paper [5] presents the results of experimental studies of heat transfer and thermal resistance of plate-fin and lamellar-pinned heat sinks, which are made under conditions of natural convection. The data obtained indicate a higher intensity of heat transfer and lower thermal resistance by 20–40% in the lamellar-pinned heat sink compared with the traditional plate heat sink. The results of the paper are qualitatively consistent with the results of [4].

The purpose of the study published in [6] is to determine by computational fluid dynamics (CFD) modelling the optimal value of the ratio of the height of the Y-shaped pin fin to the height of the entire fin, which will, according to the authors, increase the cooling efficiency of the pin heat sinks of the new type. Obtained results show that for values of air velocity 0.5–2.5 m/s and the relative height of the pinned Y-fin (height of the straight part of the fin / overall fin height) H/A = 0.2–0.8, the optimum ratio of the relative height of fins is H/A = 0.6, corresponding to the lowest thermal resistance of a flat heat sink with pinned fins. In our opinion, it would be advisable to compare the received values of thermal resistances with values of resistances of the heat sink at H/A = 1.0 which would allow finding out a value of the received effect from the use of the Y-shaped fins.

In [7], the heat transfer and aerodynamic drag of the four designs of new flat lamellar-finned heat sinks with trapezoidal and stepped configurations of lamellar fins in the inlet flow rate variation range from 1 m/s to 5.5 m/s were experimentally studied. It was found that the stepped and trapezoidal fins provide higher thermal conductivity and lower aerodynamic drag compared to the basic plate-fin heat sink at the same flow velocity. The effective conductivity of the trapezoidal fin exceeds the conductivity of the rectangular fin by about 38% at the inlet flow velocity of 5 m/s in spite of the fin area reduction by 20%, and aerodynamic drag is reduced by 20% compared to the conventional plate-fin heat sink.

Studies of the thermo-aerodynamic characteristics and thermal resistance of heat sinks with stepped, trapezoidal plate and plate-fin stepped and trapezoidal fins were conducted in [8] using the CFD method. The results of research testify to the fact that stepped and cut fins allow for increasing the heat transfer

coefficient by 11–16% and decreasing the aerodynamic drag by 15–45% at the reduced area of fins, but at the same time the thermal resistance of heat sinks is increased by 15–25%. Installation of pins in three transverse planes of inter-fin gaps leads to an increase in the intensity of heat transfer by an average of 40% and an increase in aerodynamic drag by 3.5–7 times compared with the traditional lamellar fins, while reducing the thermal resistance by an average of 30–40%.

The paper [9] is aimed at the experimental and numerical study of convective heat transfer and flow characteristics of plate and cross-split finned heat sinks. The cutting width of the fins and the number of the cut fin parts were varied. Investigations were performed at the flow velocity from 1 m/s to 4 m/s and thermal power equal to 100 W. The results showed that the thermal resistance of the heat sink with a 1.5 mm fin width and six cut fin parts is 16.2% lower than that of the heat sink with plate solid fins at the same flow velocity.

In the publication [10], the heat transfer and aerodynamics of a flat tube with both continuous lamellar fins and cut lamellar fins, which were placed on the lateral flat surfaces of the flat tube in in-line and staggered order, were studied using numerical simulation. The authors have shown that full cross-section cutting of fins with a large number of cuts and small width of the cut leads to the intensification of heat exchange and its greatest effect is observed at the staggered arrangement of fins.

In [11], on the basis of collected data from more than 90 publications, the authors reviewed the issues that are aimed at improving the thermal performance of developed heat sinks with pin and lamellar fins by applying various heat exchange intensifiers: perforation in the pins of circular, triangular, rectangular, oval cross-section, turning the pins (not circular cross-section) around their axis by some angle, application of holes to the fins for natural and forced convection conditions.

A lot of publications are dedicated to the investigation of characteristics of small-sized heat dissipating flat surfaces with plate-split fins with the turning of incised parts of fins in relation to flow designed for cooling of electronic devices under forced convection (Re = 2 000–10 000). Results of the experimental study of heat transfer of such surfaces are presented in [12] and of aerodynamic drag – in [13]. In [14], eight types of surfaces with different cutting depths and angles of turning were experimentally investigated. The influence of fins cutting and turning of cut parts on thermal and aerodynamic characteristics of heat sinks is studied in [15] by means of CFD modelling. The authors [16] have experimentally established that the greatest intensifying effect is observed at a relative depth of fin cutting of 0.6. Partial cutting leads to a 15–20% increase in heat transfer intensity and resistance, and turning of incised parts of fins in relation to flow by angles φ equal to 30° and 45° allows for increasing the heat transfer intensity by 50–60% at a growth of aerodynamic drag by 1.7–2.5 times in comparison with traditional lamellar-finned surfaces. Similar results were obtained in [17] but with the use of CFD modelling. Generalization of experimental data on thermal and aerodynamic characteristics of heat sinks with different types of finning, including fins with partial cut, is presented in [18]. Partially cut fins have also proven themselves well in studies of thermo-aerodynamic characteristics of transversal finned tube packages. For example, the thermal efficiency of such packages with rolled petal finning was experimentally investigated in [19]. Results of the experimental study of heat transfer of tube packages with split spiral fins were presented in [20] and for aerodynamic drag – in [21]. Summarizing these works it can be said that cutting of fins leads to increasing the heat transfer intensity of tube packages by 30–35% with a moderate increase of aerodynamic drag by 40–45%.

Heat sinks with mesh-wire fins are of certain interest due to their original design. In work [22], materials on experimental research of convective heat transfer and aerodynamic drag of flat heat dissipating surfaces with mesh-wire fins in which geometrical characteristics of mesh fins and flow regime parameters were varied, are presented. Correlations for calculating the heat transfer coefficient for such surfaces based on experimental data are presented in [23]. Mesh-wire fins allow both transverse and longitudinal washing of mesh fins. The advantage of mesh fins is their high specific mass index, but the disadvantages are a rather low efficiency coefficient of mesh fins E, as well as the predisposition to contamination of mesh fins by indoor dust. Therefore, the use of such surfaces is recommended in clean rooms.

Thus, the plate and pin remain the most versatile and widely used fin shape with proven performance, cost and manufacturing techniques. On the other hand, searching for new geometry and shape of fins of the heat sink with the aim of extracting the maximum increase in heat dissipation of the heat sink while reducing (if possible) its aerodynamic drag and improving mass-size indicators is still going on. To meet such requirements, a novel design of heat dissipating surface with lamellar fins and a maximum angle of taper of edge fins 29° was developed [24], and results of its heat transfer characteristics and aerodynamic drag investigation are proposed.

2. Materials and methods

2.1. Research methodology

Studies of convective heat transfer and aerodynamic drag of surfaces with a flat base and lamellar fins under conditions of forced convection were carried out on the experimental setup, which is an open-type wind tunnel of a rectangular cross-section with dimensions (height × width) 40 × 85 mm (Fig. 1).

The flow part of the experimental setup consisted of a working section (1) 400 mm long and two calming sections (2) 700 mm long each. The detailed design of the working section is depicted in Fig. 1. The calming sections were intended for the alignment of flow velocity fields and static pressure. The flowing part was connected to the inlet nozzle (5) through the transition diffuser (3). The inlet nozzle was profiled along the lemniscate with an internal diameter of 42 mm. From the other side, the flowing part was connected to the suction centrifugal electric fan (6) through the transition confuser (4). The air flow rate through the fan was regulated smoothly by an autotransformer and by manual-operated dampers (8) to ensure flow rates less than 2 m/s (W_o < 2 m/s).

The investigated heat sink (10) was installed in the working section. Heating of the heat sink was carried out with a spiral

ohmic electric heater (12). It was placed inside an insulated casing with an outer diameter of 50 mm. The casing was poured with aluminium oxide powder (Al_2O_3) (13) to ensure uniform heat input and reliable contact between the heater and the base of the heat sink. The casing with the heater was tightly fixed to the centre of the back part of the base (11). An autotransformer was used to power the heater. The autotransformer was connected to the AC mains through a voltage stabilizer.

To study the aerodynamic drag of heat sinks, two nozzles with a diameter of 1 mm were placed in the walls of the working section at a distance of 50 and 120 mm from the flow inlet and

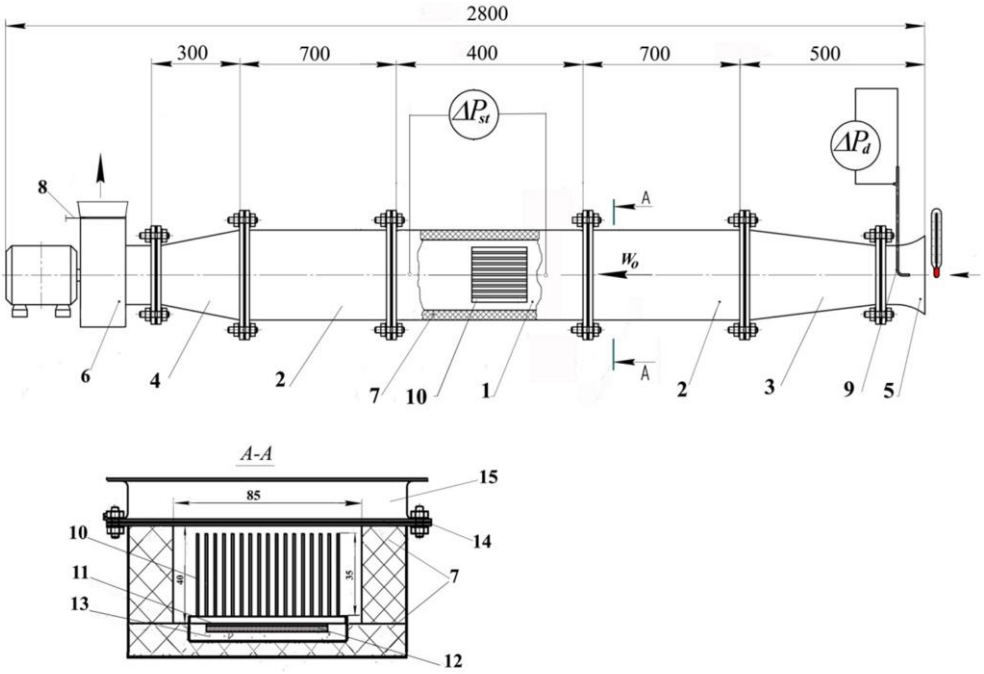

Fig. 1. Experimental setup: 1 – working section; 2 – calming sections; 3 – transition diffuser; 4 – transition confuser; 5 – inlet nozzle; 6 – electric fan; 7 – thermal insulation; 8 – damper; 9 – Prandtl-Pitot tube; 10 – investigated heat sink; 11 – base of the investigated heat sink; 12 – electric heater; 13 – aluminium oxide powder (Al_2O_3); 14 – cover of the working section; 15 – clamping frame.

outlet from the heat sink respectively for taking static pressures. According to the value of pressure difference between the inlet and outlet flow static pressure drops were determined with the help of a micromanometer MMN-240.

Figure 2 shows a photo of the experimental setup consisting of the following measuring instruments:

Fig. 2. Photo of the experimental setup.

- Prandtl-Pitot-Tube and micromanometer MMN-240 with accuracy class 1.0, which were used to determine the dynamic nozzle pressure;
- barometer-aneroid with accuracy class 1.0 to determine the ambient barometric pressure;
- mercury thermometer with a scale value of 0.1ºC for determining the air temperature at the nozzle inlet;
- a wattmeter with an accuracy class of 0.5 for measuring the electric power supplied to the heater of the surfaces under study;
- multichannel data acquisition module ICP CON I-7018.

Heat sinks of three designs were investigated (Figs. 3 and 4). It should be noted that the only difference between heat sinks of type 2 and type 3 was the fins cutting of the heat sink type 3. The main geometrical characteristics of the heat sinks under study are shown in Table 1.

The lamellar fins were soldered into longitudinal grooves 1 mm deep pre-milled in the base with a fin spacing of t_1 = 6 mm for the surface of type 1. For surfaces of types 2 and 3, the fin spacing at the flow inlet into the surface was 6 mm, and starting from the middle fin it decreased gradually on both sides and was 3 mm (t_2 = 3 mm) at the outlet of the finned surface. The taper angle between the fins varied from an angle $\varphi = 0°$ (the central fin) to an angle $\beta = 14.5°$ at the outermost fin. The greatest angle of taper between the two outermost fins was 29° ($\varphi = 29°$).

The full areas of the surfaces of types 1 and 2 had close values (the difference is less than 0.8%), in spite of the fact that the base area of the surface of type 2 decreased by ≈ 25%. Due to

the gradual increase in the fin length, the difference between the full areas of the surfaces turned out to be insignificant (Table 1). The total area of the surface of type 3 due to the cutting of fins was decreased relative to that of type 1 by 4.25%.

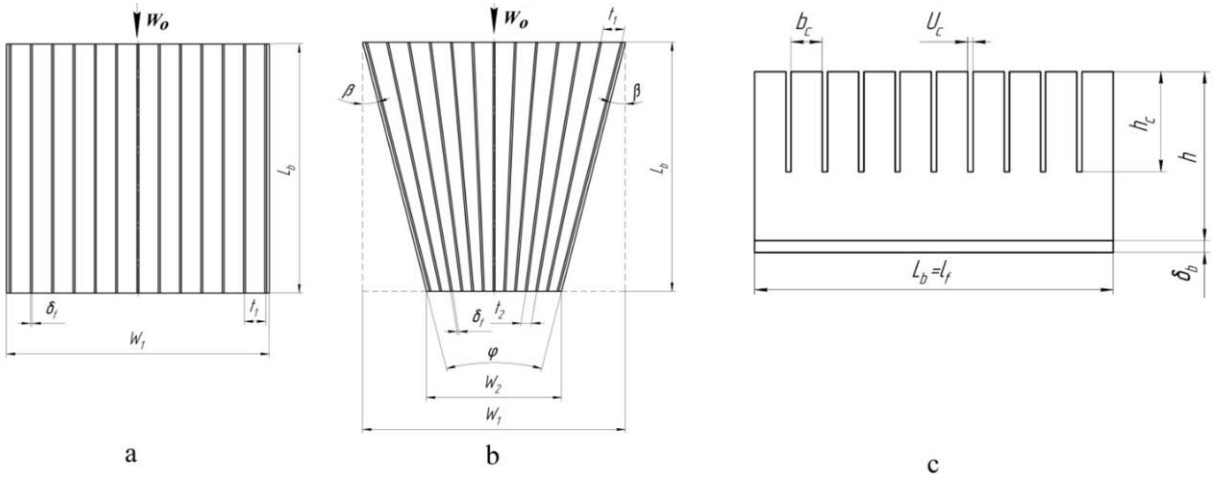

Fig. 3. Design of heat sinks: a – type 1; b – type 2; c – middle fin side view of the heat sink type 3.

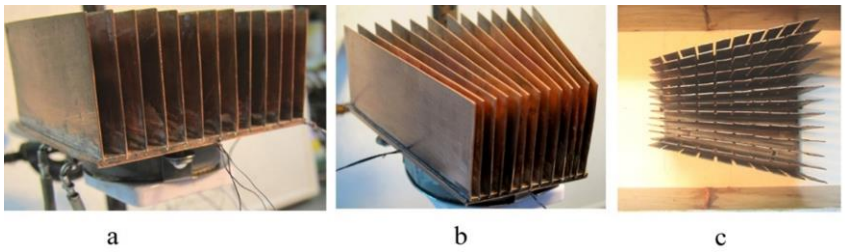

Fig. 4. External view of heat sinks: a – type 1; b – type 2; c – type 3.

Table 1. Geometric characteristics of heat sinks.

#	Parameter	Nomenclature	Units	Experimental heat sink type		
				1	2	3
1	Fin height	h	mm	35.5	35.5	35.5
2	Input/output fin pitch	t_1/t_2	mm	6/6	6/3	6/3
3	Fin thickness	δ_f	mm	0.5	0.5	0.5
4	Middle fin length	l_f	mm	70	70	70
5	Depth of cutting	h_c	mm	-	-	21
6	Cutting width	u_c	mm	-	-	1.0
7	Width of cut fin segments	b_c	mm	-	-	6.1
8	Input/output base width	w_1/w_2	mm	74/74	74/38	74/38
9	Base length	L_b	mm	70	70	70
10	Base thickness	δ_b	mm	2.5	2.5	2.5
11	Number of fins	Z		13	13	13
12	Hydraulic diameter	d_h	mm	11.0	11.0	11.0
13	Total surface area	F_{all}	cm^2	709.7	704.2	679.7
14	Area difference	Δ_F	%		0.8	4.25
15	Finning coefficient	Ψ	-	12.03	15.44	14.90
16	Maximal taper angle	φ	degree	0	29	29
17	Surface material	-	-	copper	copper	copper

The finning coefficient (a ratio between the overall area of the finned surface and the area of the surface without finning (base) $\Psi = F_{all}/F_b$) of the type 2 and 3 samples is significantly higher than that of the type 1 sample because of a smaller base area of the type 2 and 3 samples. This parameter is widely used for convective heat transfer calculation of finned tubes [25], data generalization [26] and investigation of convective heat transfer and aerodynamic drag of bundles of transversely finned tubes [27].

The temperature field of the base of the heat sink surfaces was determined using six (No. 1–6) T-type thermocouples (of wire diameter 0.1 mm), which were placed on the base of the

heat sink as shown in Fig. 5. Additional thermocouples No. 7–8 together with thermocouples No. 1–3 were intended for detecting the temperature changing along the symmetry line and the air flow direction connected with air velocity change. Signals from thermocouples through a multichannel data acquisition module ICP CON I-7018 were transferred to the computer, automatically recorded and displayed on the computer monitor.

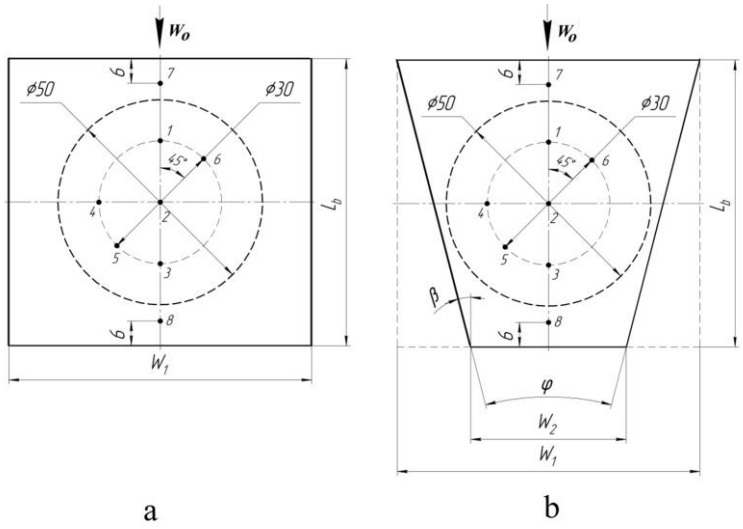

Fig. 5. Location of thermocouples on the heat sink base: a – heat sink type 1; b – heat sink type 2, 3; 1–8 – numbers of thermocouples.

The described above research methodology has such advantages: simplicity, reliability of methodology itself and obtained results. The impossibility of correct defining of contact thermal resistance on the border between the basic surface and fin can be named as a disadvantage of the methodology. This methodology can be applied for experimental investigation of heat and aerodynamic characteristics of flat heat sinks with different types of fins, including applying different heat transfer intensifiers, and heat sinks based on heat pipes.

2.2. Methods of measuring and processing experimental data

The study of patterns of convective heat transfer of heat dissipating surfaces was reduced to determining the dependences of Nusselt numbers, calculated from the reduced convective heat transfer coefficients (α_{red}), on Reynolds numbers.

The average temperature at the base of the heat dissipating surface was calculated as the average of thermocouples 1–6 (Fig. 5), using the ratio:

$$\overline{T}_b = \frac{\sum_{i=1}^{N} T_i}{N}, \quad (1)$$

where T_i – the base temperature at the mounting points of the thermocouples (1–6), $N = 6$ – the number of thermocouples.

The reduced heat transfer coefficient was determined directly from the results of measuring the temperature field of the heat sink base using the formula:

$$\alpha_{red} = \frac{Q - Q_{los}}{F_{all} \cdot (\overline{T}_b - T_{on})}, \quad (2)$$

where Q – power of the electric heater, W; Q_{los} – heat losses, W; F_{all} – total area of the heat transfer surface, m^2; T_{on} – air temperature at the inlet of the working section, K.

The amount of heat dissipated by the heat sink was determined by the values of electric power supplied to the heater, taking into account the heat loss through the base by heat conduction into the lower wall of the working section of the wind tunnel and the heat that is withdrawn by radiation. Preliminary experiments showed that the value of heat losses of heat sink amounts to 2–3% of the supplied electric power, and the heat dissipated from the surface by radiation did not exceed 2–2.5% of the total heat power dissipated by the heat sink.

The air flow rate in the inlet nozzle was determined by the ratio:

$$W_{noz} = \xi \sqrt{\frac{2g\Delta P_d}{\rho_{noz}}}, \quad (3)$$

where g – gravitational acceleration, m/s^2; ΔP_d – difference of full and static pressure, Pa, ρ_{noz} – air density in the nozzle, kg/m^3, $\xi = 0.99$ – correction factor, set on the basis of calibration of the Pitot-Prandtl tube.

According to the continuity equation, the flow velocity at the inlet to the working section before the heat sink was determined by the equation:

$$W_o = k_u \cdot W_{noz}, \quad (4)$$

where k_u – is the coefficient, which is defined as:

$$k_u = F_{noz}/F_{on}, \quad (5)$$

where F_{noz} – nozzle cross-section area, m^2; F_{on} – cross-section area at the inlet of the working section, m^2.

The air flow rate G in the cross-section of the working section was determined by the following dependence:

$$G = \rho_{noz} W_{noz} F_{noz}. \quad (6)$$

The hydraulic diameter of the heat sink cross-section d_h at the inlet (d_h = 11 mm) was taken as a defining size in Nusselt and Reynolds numbers, which proved to be good for defining size in similarity numbers [28]. The velocity in the working channel in front of the heat sink surface W_o was taken as a characteristic air velocity. The physical properties of air λ, ν, which are included in the expressions for the numbers Nu and Re, were related to the flow temperature at the inlet to the heat sink surface. The Nusselt and Reynolds numbers were determined as:

$$\mathrm{Nu}_{red} = \frac{\alpha_{red} \cdot d_h}{\lambda}, \quad (7)$$

$$\mathrm{Re}_e = \frac{W_o \cdot d_h}{\nu}, \quad (8)$$

where λ – air heat conductivity, W/(m·K); ν – air kinematic viscosity, m^2/s.

The aerodynamic drag of the investigated heat sinks was determined in the conditions of isothermal flow at air temperatures T_o = 290–300 K. Pressure losses caused by the heat sink were defined with taking into account friction pressure losses in the working section:

$$\Delta P = \Delta P_{stat} - \Delta P_{fric}, \quad (9)$$

where ΔP_{stat} – static pressure difference, Pa; ΔP_{fric} – friction pressure losses, Pa.

Based on ΔP values, the values of Euler's number Eu were determined:

$$\mathrm{Eu} = \frac{\Delta P}{\rho_{noz} \cdot W_o^2}. \quad (10)$$

2.3. Uncertainty analysis

In this work, uncertainty analysis of direct and indirect measurements was performed according to main recommendations of [29]. Direct measurements in this study include measurements of geometric parameters of the experimental setup and heat sinks, static and dynamic pressures, temperatures and heater electric power. Indirectly measured values are determined by calculations based on the results of direct measurements. These include: heat transfer coefficients α, flow velocity W, numbers: Reynolds Re, Nusselt Nu, Euler Eu.

The general uncertainty of a direct measurement consists of systematic and random errors [30]. Primary analysis of the experimental data has shown that the order of systematic and random errors is the same as for surface temperature measurement. Uncertainty of the other measurements was defined mainly by systematic errors connected with measurement apparatus errors and imperfection of the measurement method. The error of heat sinks geometrical parameters measurement was ±0.05 mm. Errors of direct measurements of regime parameters were defined by the accuracy class of measurement apparatus and chosen range of measurement.

The error of determining the surface temperature consists of the absolute error of thermocouples measurement and the error of thermocouples calibration. The absolute error of thermocouples measurement was equal to 0.25 K. The error of thermocouple calibration is not more than 0.2 K when an exemplary platinum-platinum-rhodium thermocouple is used for calibration. Then the absolute error of measurement of surface temperatures was:

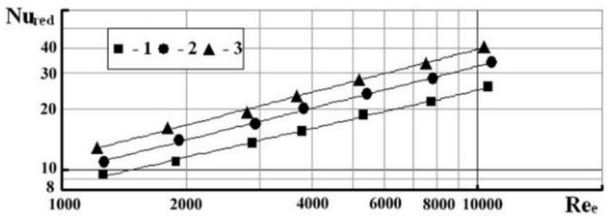

Fig. 6. Results of the study of heat sinks heat transfer: 1 – heat sink type 1; 2 – heat sink type 2; 3 – heat sink type 3.

$$e = [(0.25)^2 + (0.2)^2]^{0.5} \approx 0.3 \text{ K}. \quad (11)$$

The uncertainty of overall heat quantity which was transferred to the air was ±2.5%.

Experimental data of heat transfer investigation were used to calculate the uncertainty of the reduced heat transfer coefficient α_{red} and the corresponding Nusselt number.

The uncertainty of determining the Euler number is mainly related to the error in measuring the static pressure differences ΔP_{stat} before and after the lamellar-finned surface.

The stability and repeatability of obtained data was ensured by multiple measurements of parameters. Thus, the duration of temperature measurement at a steady state condition was 1.5–2 minutes which corresponded to 90–120 measurements, and fluctuations of inlet air temperature were insignificant (±0.3 K).

Performed calculations have shown that the relative uncertainty of the definition of heat transfer coefficient was not more than ±(5.4–6.7)%, of the Nusselt number ±(6.5–7.5)%, uncertainty of Reynolds number calculation was not more than ±5.5% and for Euler number ±(10–15)%.

3. Results and discussion

3.1. Heat transfer

The research of heat transfer was performed in the range of Reynolds numbers Re_e = 1 250–10 500. It was intended to obtain the dependencies between the Nusselt numbers and Reynolds numbers of such a type:

$$\mathrm{Nu}_{red} = C_q \cdot \mathrm{Re}_e^m, \quad (12)$$

where C_q – coefficient.

Experimental results for heat sinks of types 1–3 are shown in Fig. 6. Analysis of the data presented in Fig. 6 indicates that a gradual decrease in the fin spacing from 6 mm to 3 mm of heat sink type 2 leads to an increase in the intensity of heat transfer by 15–32% compared to the heat sink type 1 with constant fin

spacing (6 mm) due to a gradual increase in velocity in the inter-fin channels. The flow velocity increased 2 times from the inlet to the outlet (t_1 = 6 mm, t_2 = 3 mm).

Increasing the heat transfer intensity due to fin cutting (heat sink type 3) is explained as follows. The thickness of the boundary layer on the fins increases as flow moves along them when flowing on the type 1 heat sink (without fins cutting). This leads to the deterioration of heat transfer between fins and air flow. Partial cutting of fins into narrow sections, as it was done on the type 3 sample, leads to: destruction of the growing boundary layer, its disruption from the edges of the cut narrow parts, splitting it into thinner sections, increasing the flow disturbance in the area of fins cutting [15]. The combination of these factors and increasing the flow velocity in the inter-fin channels leads to an increase of the heat transfer intensity of the heat sink of type 3 by 35–55% in comparison with that of type 1.

Values of the exponent *m* in Eq. (12) for all investigated heat sinks exhibit small differences, but the tendency of their increasing is observed (Table 2).

3.2. Aerodynamic drag

Figure 7 presents the results of studies of aerodynamic drag of heat sinks of types 1–3 in the form of dependencies of Euler numbers (Eu) on Reynolds numbers (Re_e). These results can be generalized with such a function:

$$\mathrm{Eu} = C_S \cdot \mathrm{Re}_e^{-n}, \qquad (13)$$

where C_S – coefficient. Table 2 shows values of the exponent *n* and the C_S coefficient in Eq. (13).

Table 2. Values of the exponents *m*, *n* and coefficients *Cq*, C_S in Eqs. (12) and (13).

Heat sink type	t_1/t_2 m /mm	h_c/h	*m*	C_q	*n*	C_S
1	6/6	-	0.4715	0.3210	0.2409	1.7672
2	6/3	-	0.5188	0.2777	0.2268	12.259
3	6/3	0.6	0.5333	0.2894	0.1540	5.9526

The data in Fig. 7 demonstrate a high aerodynamic drag of heat sinks type 2 and 3, which is 7.5 times higher than that of type 1.

A high aerodynamic drag of the type 2 heat sink is connected with a gradually increasing velocity in the narrowing channels between the fins in which the outlet velocity is 2 times higher than the inlet velocity. Some decrease in the aerodynamic drag by 6–15% of the type 3 heat sink is connected, in our opinion, with the air flowing mainly from the inter-fin gaps of the outermost fins into the expanding channel formed by the straight side walls of the channel and the outermost fins, which resulted in a decreasing of the speed in the outermost inter-fin channels of the heat sink.

The proposed forms of correlations for heat transfer (12) and aerodynamic drag (13) are suitable for a wide range of heat sink geometrical sizes and fins quantity. But in some cases, additional experimental investigations are necessary for the specification of coefficients C_q, C_S and exponents *m* and *n*. Coefficients and exponents listed in Table 2 are applicable to heat sinks with the same ratio between the height, length, thickness and fin pitch, the same taper angle and relative depth of fin cutting as for the investigated heat sinks. Taking into account that the hydraulic diameter d_h was chosen as a defining size of Re and Nu numbers, significant changes in heat sink geometry need the correction of coefficients and exponents by means of additional study. It should be noted that the geometrical form of the heater does not influence the form of correlations for heat transfer and aerodynamic drag, but values of the base temperature and their distribution depend on the method of heating and additional investigations are necessary for their defining in any single case.

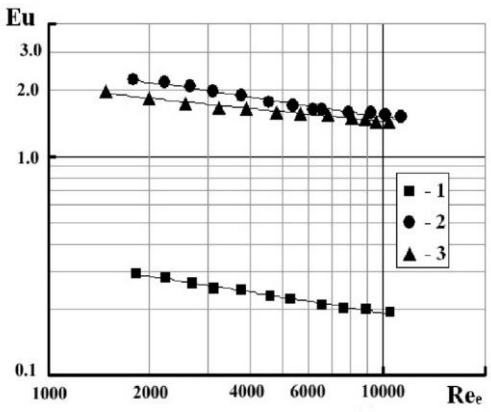

Fig. 7. Results of the study of aerodynamic drag of heat sinks: 1 – heat sink type 1; 2 – heat sink type 2; 3 – heat sink type 3.

3.3. Overheat temperature of heat sink base

One of the main parameters for the evaluation and selection of a finned sink for electronics cooling is the base overheating temperature ΔT at a given heat flow *Q*, which is removed from the heat loaded electronic components to the base of the heat sink. We distinguish between an average overheating temperature of the base and a maximum overheating temperature. The average overheating temperature is the difference between the average temperature of the base, which is averaged over the readings of thermocouples located on the base, and the value of the cooling medium temperature T_{on}: $\Delta\bar{T}_b = \bar{T}_b - T_{on}$. The maximum overheating temperature of the base is the difference between the maximum temperature of the base and the cooling medium temperature (air temperature at the inlet to the heat sink).

Figure 8 shows changes of the overheating temperature along the flow direction in the inter-fin channels of heat sinks type 1–3 according to the readings of thermocouples T1–T3, T7, T8 (Fig. 5). The dashed vertical lines indicate the boundaries of the heat sink, and lines I–I and II–II are the boundary within which the electric heater is installed on the base.

The curves ΔT = f(*L*) for the three types of heat sinks are qualitatively similar. At the inlet of the flow, the base overheating temperature is lower, because the flow has the air inlet temperature (T7), and as it moves deeper, it warms up, and the temperature of the base increases and has a maximum in the centre of the heater at point T2. Further, as the flow moves toward the outlet, the overheating temperature decreases slightly at point

T3, and at the outlet of the inter-fin channels has a temperature 3°C less than at point T2 for the type 1 heat sink. The overheating of the base of the type 1 heat sink remains high due to the fact that the average flow velocity in the inter-fin channels remains approximately constant. The overheating temperatures along the symmetry axis of the type 2 and 3 heat sinks differ significantly from the overheating temperatures of the type 1

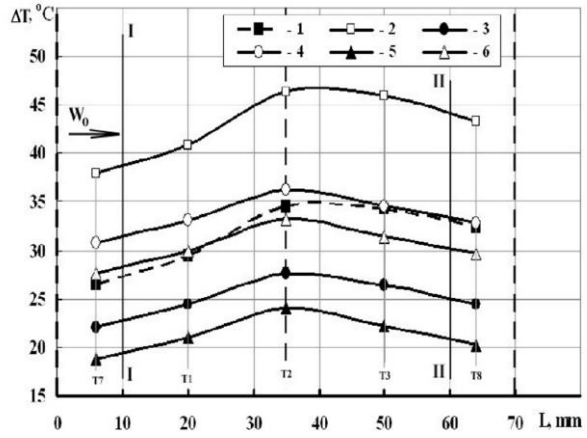

Fig. 8. Dependence of the overheating temperature ΔT of the heat sink base along the longitudinal axis of symmetry on the base length L at Q = 100 W: 1, 2 – heat sink of type 1 at W_o values 7.35 and 3.96 m/s; 3, 4 – heat sink of type 2 at W_o values 7.35 and 3.98 m/s; 5, 6 – heat sink of type 3 at W_o values 7.48 and 4.03 m/s; T1–T3, T7, T8 – numbers of thermocouples according to Fig. 5; I-I, II-II – boundaries of the electric heater body.

heat sink due to gradual narrowing of inter-fin channels from t_1 = 6 mm to t_2 = 3 mm and increase in velocity at the outlet by 2 times. For this reason, the level of overheating temperatures decreases at point T2 by 7°C and 10°C for heat sinks of type 2 and 3, respectively at inlet flow velocity $W_o \approx 7.4$ m/s.

For the air velocity $W_o \approx 4$ m/s, decreasing the overheating temperature in point T2 for heat sinks of type 2 and 3 in comparison with the heat sink of type 1 is 10°C and 13°C, accordingly. The type 3 heat sink with transverse incompletely cut fins has the lowest maximum overheating temperature at point T2 of the heat sinks compared. This can be explained by turbulizing of the flow due to its disruption from the edges of the incised parts of the fins, which leads to an increase in the intensity of heat transfer, while the temperature of the base decreases. In general, the level of temperature overheating along the length of the base for heat sinks of type 2 and 3 is significantly lower than that for the heat sink of type 1 at the same flow velocities and heat flow value of Q = 100 W.

Figure 9 shows experimental data for the dependence of the maximum overheating temperature of the base ΔT_{max} on the flow velocity at the inlet to the heat sink W_o.

Maximum overheating temperatures of the base for the three types of heat sinks decrease with the increasing speed, but the level of temperature overheating significantly differs. For heat sinks of type 2 and 3, the values of ΔT_{max} are 7.5–10°C lower and 10–13°C lower, respectively, than those of heat sink type 1. The explanation of this difference is the same as the described above difference between curves ΔT = f(L) depicted in Fig. 8.

The results presented in Fig. 9 also show that in order to achieve a constant maximum overheating temperature equal to ΔT_{max} = 40°C for the type 1 heat sink, the inlet air velocity must

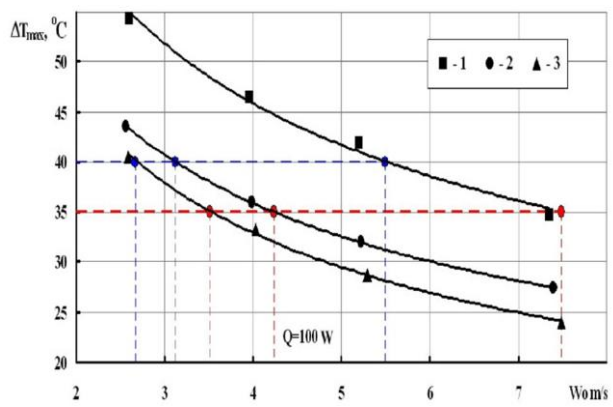

Fig. 9. Dependence of the maximum overheating temperature of the base ΔT_{max} on the flow velocity W_o at the inlet at Q = 100 W: 1 – heat sink of type 1; 2 – heat sink of type 2; 3 – heat sink of type 3.

Table 3. Comparison of the obtained data at the same Q and ΔT_{max}.

Heat sink type	Q, W	ΔT_{max}, °C	W_o, m/s	ΔP, Pa	$\Delta P_i / \Delta P_1$
1	100	40.0	5.49	9.1	1.0
2	100	40.0	3.12	25.4	2.79
3	100	40.0	2.67	14.0	1.54
1	100	35.0	7.48	15.5	1.0
2	100	35.0	4.24	42.4	2.74
3	100	35.0	3.51	24.0	1.55

be at least W_o = 5.5 m/s, for type 2 – W_o = 3.12 m/s, for type 3 – W_o = 2.67 m/s. For the maximum overheating temperature of the base ΔT_{max} = 35°C, the inlet flow velocities should be for the type 1 heat sink equal to W_o = 7.48 m/s, for type 2 – W_o = 4.24 m/s and for type 3 – W_o = 3.51 m/s (Table 3). Conclusively, we can say that the novel heat sinks of types 2 and 3 significantly reduce the maximum overheating temperature of the base.

The dependence of pressure loss ΔP on the inlet flow velocity W_o is depicted in Fig. 10. The dashed lines highlight the values of pressure losses at the maximum overheating temperature ΔT_{max} 35°C and 40°C. The relative growth of pressure losses at overheating of the base ΔT_{max} 40°C and 35°C is 2.74–2.79 times and 1.5 times for heat sinks of type 2 and 3, respectively (Table 3), which is quite acceptable.

4. Conclusions

Novel heat sinks with lamellar fins and variable fin spacing, designed for electronics cooling, have a high heat transfer intensity.

Gradually reducing the fin spacing leads to an increase in the heat transfer intensity by 15–30%.

The combination of factors of speed increasing in inter-fin gaps and partially cutting of fins allows us to increase the heat transfer intensity by 35–55% in comparison with the heat transfer intensity of traditional heat sinks with lamellar fins.

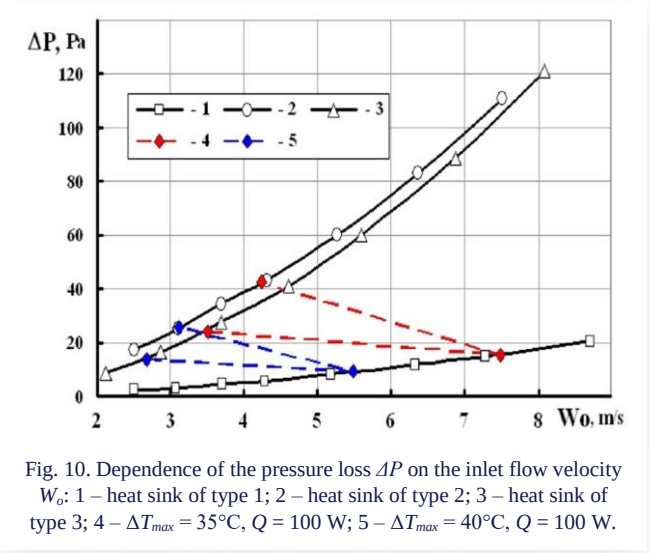

Fig. 10. Dependence of the pressure loss ΔP on the inlet flow velocity W_o: 1 – heat sink of type 1; 2 – heat sink of type 2; 3 – heat sink of type 3; 4 – ΔT_{max} = 35°C, Q = 100 W; 5 – ΔT_{max} = 40°C, Q = 100 W.

The aerodynamic drag of heat sinks with the gradually decreasing spacing between the fins increases by 7–7.5 times relative to the drag of traditional heat dissipating surfaces with lamellar fins.

The maximum overheating temperature of the base for the novel heat dissipating surfaces with gradually decreasing spacing between the fins is 7–13°C lower than that for traditional heat sinks with lamellar fins.

The pressure losses for the novel heat sinks at the same heat load and overheating temperature of the base are significantly reduced from 7–7.5 times to 1.54–2.74 times.

Novel designs of heat sinks allow for improving the mass-size indices by 20–25% at equal conditions.

References

[1] Gurrum, S.P., Suman, S.K., Joshi, Y.K., & Fedorov, A.G. (2004). Thermal Issues in Next-Generation Integrated Circuits. *IEEE Transactions on Device and Materials Reliability*, 4(4), 709–714. doi: 10.1109/tdmr.2004.840160

[2] Jonsson, H., & Moshfegh, B. (2001). Modeling of the thermal and hydraulic performance of plate fin, strip fin, and pin fin heat sinks-influence of flow bypass. *IEEE Transactions on Components and Packaging Technologies*, 24(2), 142–149. doi: 10.1109/6144.926376

[3] El-Sayed, S.A., Mohamed, S.M., Abdel-latif, A.M., & Abouda, A..E. (2002). Investigation of turbulent heat transfer and fluid flow in longitudinal rectangular-fin arrays of different geometries and shrouded fin array. *Experimental Thermal and Fluid Science*, 26(8), 879–900. doi: 10.1016/s0894-1777(02)00159-0

[4] Yu, X., Feng, J., Feng, Q., & Wang, Q. (2005). Development of a plate-pin fin heat sink and its performance comparisons with a plate fin heat sink. *Applied Thermal Engineering*, 25(2–3), 173–182. doi: 10.1016/j.applthermaleng.2004.06.016

[5] Haghighi, S.S., Goshayeshi, H.R., & Safaei, M.R. (2018). Natural convection heat transfer enhancement in new designs of plate-fin based heat sinks. *International Journal of Heat and Mass Transfer*, 125, 640–647. doi: 10.1016/j.ijheatmasstransfer.2018.04.122

[6] Lekaphol, T., Sompong, P., & Srisomporn, S. (2019). Optimal height ratio of Y-shape pin fin to plate fin of PPFHS. *IOP Conference Series: Materials Science and Engineering*, 501, 012062. doi: 10.1088/1757-899x/501/1/012062

[7] Chen, C.H., & Wang, C.C. (2015). A novel trapezoid fin pattern applicable for air-cooled heat sink. *Heat and Mass Transfer*, 51(11), 1631–1637. doi: 10.1007/s00231-015-1666-4

[8] Muneeshwaran, M., Sulaiman, M.W., Hsieh, C.H., Chai, M.L., & Wang, C.C. (2022). Heat transfer augmentation of heat sinks through increasing effective temperature difference. *Journal of Enhanced Heat Transfer*, 29(5), 37–55. doi: 10.1615/jenhheattransf.2022042106

[9] Chingulpitak, S., Chimres, N., Nilpueng, K., & Wongwises, S. (2016). Experimental and numerical investigations of heat transfer and flow characteristics of cross-cut heat sinks. *International Journal of Heat and Mass Transfer*, 102, 142–153. doi: 10.1016/j.ijheatmasstransfer.2016.05.098

[10] Feng, L., Du, X., Yang, Y., & Yang, L. (2011). Study on heat transfer enhancement of discontinuous short wave finned flat tube. *Science China Technological Sciences*, 54(12), 3281–3288. doi: 10.1007/s11431-011-4572-0

[11] Dhaiban, H.T., Hussein, M.A. (2019). The optimal design of heat sinks: A Review. *Journal of Applied and Computational Mechanics* 6(4), 1030–1043. doi: 10.22055/JACM.2019.14852

[12] Pismenniy, Ye.N., Burley, V.D., Terekh, A.M., Baranyuk, A.V., Tsvyashchenko, Ye.V. (2005). Heat transfer of flat-plating surfaces with cut fins at force convection. *Promyshlennaya teplotekhnika*, 27(4), 11–16 (in Russian).

[13] Baranyuk, A.V., Pismenniy, Ye.N., Terekh, A.M., Rohachev, V.A., Burley, V.D. (2006). Aerodynamic drag of flat-plating surfaces with cut fins at force convection. *Promyshlennaya teplotekhnika*, 28(4), 29–33 (in Russian).

[14] Pis'mennyi, E.N., Rogachev, V.A., Terekh, A.M., Polupan, G., Carvajal-Mariscal, I., & Nezym, V. (2006). An experimental study of enhancement of forced convection heat transfer from parallel plate fins with cuts. *Annals of the Assembly for International Heat Transfer Conference 13*. Begell House Inc. doi: 10.1615/ihtc13.p17.220

[15] Baranyuk, A.V., Nikolaenko, Y.E., Rohachov, V.A., Terekh, A. M., & Krukovskiy, P.G. (2019). Investigation of the flow structure and heat transfer intensity of surfaces with split plate finning. *Thermal Science and Engineering Progress*, 11, 28–39. doi: 10.1016/j.tsep.2019.03.018

[16] Baranyuk, A.V., Rogachev, V.A., Zhukova, Y.V., Terekh, A.M., & Rudenko, A.I. (2020). Experimental investigation of heat transfer of plane heat-removing surfaces with plate finning. *Journal of Engineering Physics and Thermophysics*, 93(4), 962–972. doi: 10.1007/s10891-020-02196-3

[17] Nikolaenko, Yu., Baranyuk, A., Rohachev, V., & Terekh, A. (2020). Numerical study of heat and aerodynamic drag of the radiator with lamellar split finning. *Archives of thermodynamics*, 41(1), 67–93. doi: 10.24425/ather.2020.132950

[18] Rohachev, V.A., Terekh, O.M., Baranyuk, A.V., Nikolaenko, Y.E., Zhukova, Y.V., & Rudenko, A.I. (2020). Heataerodynamic efficiency of small size heat transfer surfaces for cooling thermally loaded electronic components. *Thermal Science and Engineering Progress*, 20, 100726. doi: 10.1016/j.tsep.2020.100726

[19] Pis'mennyi, E.N., Terekh, A.M., & Rogachev, V. A. (1997). New Heat-Transfer Surfaces Made of Tubes with Rolled Petal Finning. *Heat Transfer Research*, 28(4-6), 398–401. doi: 10.1615/heattransres.v28.i4-6.270

[20] Terekh, A.M., Shapoval, O.E., & Pis'mennyy, E.N. (2001). The average-superficial heat exchange in banks of in-line tubes with split spiral fins in cross-flow. *Promyshlennaya teplotekhnika*, 23(1-2), 35–41 (in Russian).

[21] Shapoval, O.E., Pis'mennyy, E.N., & Terekh, A.M. (2001). Aerodynamic drag of transversely streamlined of in-lined tube bundles with split fins. *Promyshlennaya teplotekhnika*, 23(4-5), 63–68 (in Russian).

[22] Pismennyi, E.N., Rohachev, V.A., Terekh, A.M., Burley, V.D., & Razumovskyi, V.G. (2002). Heat transfer of flat surfaces with mesh-and-wire finning at forced convection. *Promyshlennaya teplotekhnika*, 24(4), 71–78 (in Russian).

[23] Pis'mennyi, E.N., Terekh, A.M., Rogachev, V.A., Burlei, V.D., & Rudenko, A.I. (2005). Calculation of Convective Heat Transfer of Plane Surfaces with Wire-Net Finning Immersed in a Cross-Flow. *Heat Transfer Research*, 36(1-2), 39–46. doi: 10.1615/heattransres.v36.i12.60

[24] Nishchik, A.P., Terekh, A.M., Rudenko, A.I., & Vozniuk, M.M.: *Lamellar-finned heat exchange surface*. Ukraine utility model patent. UA 140448 U, Feb. 25, 2020 (in Ukrainian).

[25] Yudin, V.F. (1982). *Heat Transfer in Cross-Finned Tubes*. Mashinostroenie, Leningrad (in Russian).

[26] Pis'mennyi, E.N., Terekh, A.M. (1993). Generalized method for convective heat transfer calculation in transversely streamed tube bundles with external ring and spiral-strip fins. *Teploenergetika*, 5, 52-56 (in Russian).

[27] Pis'mennyi, E. N. (2016). Study and application of heat-transfer surfaces assembled from partially finned flat-oval tubes. *Applied Thermal Engineering*, 106, 1075–1087. doi: 10.1016/j.applthermaleng.2016.06.081

[28] Pis'mennyi, E. N., Terekh, A. M., Polupan, G. P., Carvajal-Mariscal, I., & Sanchez-Silva, F. (2014). Universal relations for calculation of the drag of transversely finned tube bundles. *International Journal of Heat and Mass Transfer*, 73, 293–302. doi: 10.1016/j.ijheatmasstransfer.2014.02.013

[29] *ISO Guide to the Expression of Uncertainty in Measurement*. International Organization for Standardization (ISO), Geneva 1993 (Corrected and Reprinted 1995).

[30] Taylor, J.R. (1997). *Introduction to error analysis, the study of uncertainties in physical measurements*. University Science Book, Sausalito.

Co-published by
Institute of Fluid-Flow Machinery
Polish Academy of Sciences
Committee on Thermodynamics and Combustion
Polish Academy of Sciences

http://www.imp.gda.pl/archives-of-thermodynamics/

Evaluation of the effect of rotational speed and rheological nature on heat transfer of complex fluid between two cylinders

Abdeljalil Benmansour[a], Houssem Laidoudi[a*]

[a]Laboratory of Sciences and Marine Engineering, Faculty of Mechanical Engineering, USTO-MB, BP 1505, El-Menaouer, Oran, 31000, Algeria.
*Corresponding author email: houssem.laidoudi@univ-usto.dz

Received: 10.03.2023; revised: 27.05.2023; accepted: 06.12.2023

Abstract

This paper presents numerical results for flow behavior between a cold inner cylinder and a hot outer cylinder. Both cylinders are placed horizontally. The space separating the two compartments is completely filled with a fluid of a complex rheological nature. In addition, the outer container is subjected to a constant and uniform rotational speed. The results of this work were obtained after solving the differential equations for momentum and energy. The parameters studied in this research are: the intensity of thermal buoyancy, the speed of rotation of the outer container and the rheological nature of the fluid. These elements are expressed mathematically by the following values: Richardson number (Ri = 0 and 1), Reynolds number (Re = 1 to 40), power-law number (n = 0.8, 1 and 1.4) and Prandtl number (Pr = 50). The results showed that the speed of rotation of the cylinder and the rheological nature of the fluids have an effective role in the process of heat transfer. For example, increasing the rotational speed of the enclosure and/or changing the nature of fluid from shear-thickening into shear-thinning fluid improves the thermal transfer rate.

Keywords: Mixed convection; Rheological behavior; Steady simulation; CFD; Nusselt number

Vol. 45(2024), No. 1, 65–73; doi: 10.24425/ather.2024.150439

Cite this manuscript as: Benmansour, A. & Laidoudi, H. (2024). Evaluation of the effect of rotational speed and rheological nature on heat transfer of complex fluid between two cylinders. *Archives of Thermodynamics.* 45(1), 65–73.

1. Introduction

Numerical simulation has become one of the most important methods used in the study of complex fluids and heat transfer, due to its accuracy in calculation and saving time and money. This study is related to a huge range of engineering and industrial applications, among which we mainly mention: irrigation and water treatment techniques, thermal mechanics, chemical industries and others. Through numerical simulations, we can predict the thermodynamic behaviour of a fluid in any proposed geometry. This allows access to the calculation of some important coefficients in engineering applications such as the drag coefficient and average Nusselt number.

Recently, there have been many studies concerning the rate of heat transfer between two cylinders, by applying a set of conditions and elements. Chatterjee and Halder [1, 2] studied the free convection between two rotating cylinders and a square enclosure. The MHD effect was added to the system. The control of physical parameters was by the dimensionless number of Ra, Re and Ha. The results proved that these parameters have an influence on the heat transfer.

In general, if the case of the movement of fluid particles is only the force of gravity, then this type of heat transfer is called

Nomenclature

a – small dimension of inner cylinder, m
b – big dimension of inner cylinder, m
D – diameter of the outer enclosure, m
g – gravitational acceleration, m/s^2
n_s – normal vector
Nu – Nusselt number
p – pressure, N/m^2
p^* – dimensionless pressure
Pr – Prandtl number
Ri – Richardson number
T – temperature, K
u – dimensional velocity component in x-direction, m/s
u^* – dimensionless velocity component in x-direction
v – dimensional velocity component in y-direction, m/s
v^* – dimensionless velocity component in y-direction
x – dimensional coordinate in horizontal direction, m
x^* – dimensionless coordinate in horizontal direction
y – dimensional coordinate in vertical direction, m
y^* – dimensionless coordinate in vertical direction

Greek symbols

α – thermal diffusivity, Pa·s
β_T – coefficient of thermal expansion, K^{-1}
μ – dynamic viscosity, Pa·s
ν – kinematic viscosity, m^2/s
ρ – density, kg/m^3

Subscripts and Superscripts

c – cold
h – heat
l – local

natural as it has been studied by many researchers [3–5]. In this natural convection mode, some researchers have studied the effect of the geometric shape of the system [6–8], while others focused on the effect of fluid properties [9–11], another group of researchers was interested in studying the effect of gradual conditions [12–14]. Whereas if the cause is due to an external engine that pushes the fluid causing it to move, then in this case it is called thermal transfer by forced convective mode [15–17]. In this mode, some researchers studied the effect of flow velocity [18–20], others tested the effectiveness of the fluid in terms of heat transfer [21–23], and others touched on testing the effect of the geometrical configuration of the system [24, 25]. Finally, if they meet together, as is in our work, the type of heat transfer becomes a mixture, that is the natural type and the forced type at the same time [26–28]. This last mode of heat transfer is called also mixed convection [29–31]. In this type, the essential factors under examination are: the fluid velocity [32–34] and the intensity of thermal buoyancy force [35].

Laidoudi and Ameur [36] studied the mixed convection of power-law fluids between two rotating obstacles. The governing parameters here were: Re, Ri, n and the rotational direction of both cylinders. It was found that when the obstacles rotate in the same direction the heat transfer becomes negligible. Laidoudi and Ameur [37] also presented a numerical work about two fixed cylinders placed inside a big circular cylinder. This outer cylinder regularly rotated at uniform velocity. The arrangement of inner obstacles was taken into account. The results showed that the speed velocity of the outer obstacle, the power-law number and the arrangement of the inner obstacles influenced the rate of heat transfer inside the studied domain. There is also a set of ideas related to this type of research that can be included in this work [38–40]. There is also the effect of external factors on the mixed convection such as the magnetic field [41, 42].

After reviewing the complex fluids, it was found that they are defined by one mathematical model called the model of Ostwald. Indeed, this model combines the Newtonian fluid, shear-thinning fluid and shear-thickening fluid. In contrast, the mixed convection heat transfer is controlled by the non-dimensional number called Richardson number (Ri). This number gives the ratio of the effect of forced convection to the natural convection. So, when Ri = 0, there is only pure forced convection, but when Ri ≠ 0, there are both effects of forced and free convection.

By following the latest research of heat transfer between two obstacles with the rotation of the outer one, it is clear that there are not many works, especially with the presence of different shapes of the inner cylinder. Therefore, this work is considered a continuation of what was done by researchers Laidoudi and Ameur [36]. That is, the work involves numerical simulations of a complex fluid enclosed between two horizontal cylinders. The outer obstacle is hot and rotates at a constant speed while the inner obstacle is cold and stationary. A new thing in the present research is that the geometric shape of the inner obstacle is different from the rest of the previous shapes. Other elements studied in this work are: the intensity of thermal buoyancy, the rheological nature of the fluid and the speed of rotation of the outer container.

The relationship between this work and the previous work of Laidoudi and Ameur [36] is that in the previous work, the inner cylinder has a high temperature and the outer cylinder is cold, while here this proposition has been reversed, making this work new and supplementary to the previous one. The results of this work can be used in many applications, including: thermal insulation systems, high-performance heat exchangers, cooling systems in solar panels and others. This work can also be used in academic work related to thermal science and fluid mechanics.

2. Studied domain

A simplified model of the domain studied is presented in Fig. 1. The studied space includes two cylinders of different shapes placed horizontally. The inner cylinder has a geometric form shaped like a rhombus while the outer cylinder has a circular shape. In addition, the outer enclosure undergoes rotation at a constant speed ω. The outer cylinder is characterized by the diameter D while the interior is characterized by the dimensions a

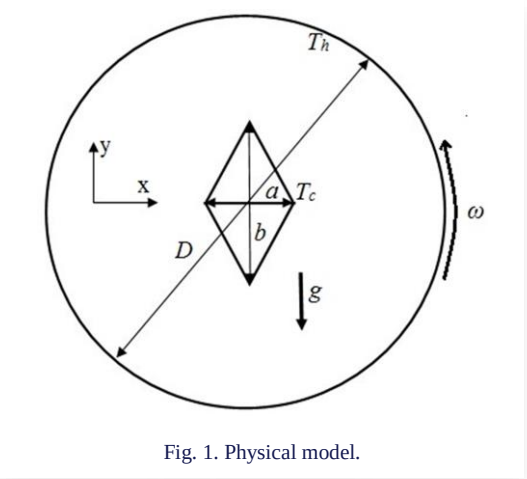

Fig. 1. Physical model.

and *b*. The values of these dimensions are given by the following ratios: $b/D = 0.4$ and $a/b = 0.5$. As for the heat distribution, it is as follows: the outer cylinder wall has a high temperature T_h, while the inner cylinder has a low wall temperature T_c. These temperatures are uniform and constant along the walls. As for the volume between the external and internal cylinders, it is filled with a complex fluid. The value of its thermal constants is given by the Prandtl number ($Pr = 50$) while the apparent dynamic viscosity is expressed by the Oswald model.

3. Mathematical formulation

The dynamic viscosity of this complex fluid is expressed as [36]:

$$\mu = m\left(\frac{I_2}{2}\right)^{\left(\frac{n-1}{2}\right)}, \tag{1}$$

where I_2 is given as [36]:

$$\left(\frac{I_2}{2}\right) = 2\left(\frac{\partial u}{\partial x}\right)^2 + 2\left(\frac{\partial v}{\partial y}\right)^2 + \left(\frac{\partial u}{\partial x} + \frac{\partial v}{\partial y}\right)^2. \tag{2}$$

The governing dimensionless numbers of Prandt, Reynolds and Richardson are expressed as [37]:

$$Pr = \frac{mc_p}{k\omega^{n-1}}, \tag{3}$$

$$Re = \frac{\rho(\omega.D)^{2-n}D^n}{m}, \tag{4}$$

$$Ri = \frac{g\beta_T \Delta T D}{(\omega.D)^2}, \tag{5}$$

where m, c_p, k, ρ, ω, β_T, n, and g denote the consistency index, specific heat capacity, thermal conductivity of fluid, fluid density, rotational speed, volume expansion coefficient, power-law index and gravitational acceleration.

The Prandtl number Pr describes the thermo-physical proprieties of the working fluid for example 6.01 is for the water, the Reynolds number Re shows the rotational speed of the outer cylinder and the Richardson number Ri describes the ratio between the natural and forced convection [1], [2] and [31].

When $n = 1$, the fluid is Newtonian. When $n = 1.4$, the fluid is shear-thinning. When $n = 0.8$, the fluid is shear-thickening. Furthermore, when Ri = 0, there is only a pure forced convection. For Ri = 1, the convection in this case is mixed. A Newtonian fluid ($n = 1$) means that the dynamic viscosity of the fluid is independent of the flow velocity. A shear-thinning fluid ($n < 1$) means that the higher the flow velocity, the lower the dynamic viscosity, whereas a shear-thickening fluid means that the higher the flow velocity, the higher the viscosity of the fluid.

The similarity numbers are placed in the basic equations of momentum and energy [1, 2] as follows:

$$\left(\frac{\partial u^*}{\partial x^*}\right) + \left(\frac{\partial v^*}{\partial y^*}\right) = 0, \tag{6}$$

$$u^*\frac{\partial u^*}{\partial x^*} + v^*\frac{\partial u^*}{\partial y^*} = -\frac{\partial p^*}{\partial x^*} + \frac{1}{\mathrm{Re}}\left(\frac{\partial \tau^*_{xx}}{\partial x^*} + \frac{\partial \tau^*_{yx}}{\partial y^*}\right), \tag{7}$$

$$u^*\frac{\partial v^*}{\partial x^*} + v^*\frac{\partial v^*}{\partial y^*} = -\frac{\partial p^*}{\partial y^*} + \frac{1}{\mathrm{Re}}\left(\frac{\partial \tau^*_{xy}}{\partial x^*} + \frac{\partial \tau^*_{yy}}{\partial y^*}\right) + \mathrm{Ri}T^*, \tag{8}$$

$$u^*\frac{\partial T^*}{\partial x^*} + v^*\frac{\partial T^*}{\partial y^*} = \frac{1}{\mathrm{PrRe}}\left(\frac{\partial^2 T^*}{\partial x^{*2}} + \frac{\partial^2 T^*}{\partial y^{*2}}\right), \tag{9}$$

where dimensionless parameters are defined by the following expressions:

$$(u^*, v^*) = \frac{(u,v)}{\omega.D}, p^* = \frac{p}{\rho(\omega.D)^2}, T^* = \frac{(T-T_C)}{(T_h-T_c)}, \tag{10}$$

$$(x^*, y^*) = \frac{(x,y)}{D}, \tau^* = \frac{\tau}{m(\omega^n)}. \tag{11}$$

In the equations above, the symbol (*) means the dimensionless quantities; x and y refer to the dimensions in the Cartesian coordinate system; u and v indicate the velocity components; p and T refer to the pressure and temperature, respectively, ω indicates the rotational speed.

The expressions for the local and average Nusselt numbers are given as:

$$Nu_L = \left[\frac{\partial T^*}{\partial n_s}\right], Nu = \frac{1}{A}\int Nu_L dA, \tag{12}$$

where n_s is the normal unit victor and A is the surface area. Nu is the average value of the local Nusselt number along the hot body.

The suitable boundary conditions for this domain are: for hydrodynamic conditions, no-slip condition with velocity components $u = 0$, $v = 0$ applied at the walls of inner and outer cylinders. Also, the outer enclosure has a rotating speed ω. For the thermal condition, around the inner obstacle $T = T_c$ and $T = T_h$ is considered at the outer cylinder.

At the beginning, Eqs. (6–9) were solved in the dimensional form, after which changes were applied to the results using Eqs. (10) and (11).

4. Numerical procedure

The computational grid was created by Gambit. The final form of this grid is shown in Fig. 2. The grid elements are irregular with the elements being centred around the inner obstacle, where the calculation is very accurate and important. The grid consists of 9 912 elements. This number was considered after a study was conducted showing the effect of number of elements on the obtained results. The results of this study are shown in Table 1.

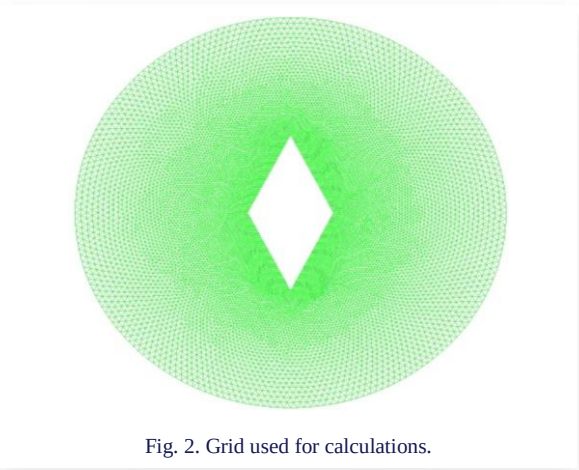

Fig. 2. Grid used for calculations.

As for the numerical solving, it was done by using the finite volumes method of the numerical simulator ANYS-CFX (14.5). The relative errors of computations were 10^{-8} for the continuity and momentum equations and 10^{-6} for the energy equation. The SIMPLEC algorithm was selected for pressure-velocity coupling. On the other hand, a high-resolution scheme was selected for solving the convective terms of the governing equations.

The accuracy of this method of calculation was verified by comparing our results with the previous results of Laidoudi and Ameur [36]. The results of this comparison are shown in Table 2. We note a strong match between the results.

Table 1. Grid independency test for Re = 20, Ri = 1 and n = 1.4.

Mesh	Element	Nu	Difference %
M1	4 956	1.21901	2.10
M2	9 912	1.19343	0.10
M3	19 824	1,19219	0.003
M4	39 648	1,19215	-

Table 2. Validation test for Re = 10 and Ri = 3.

n	Nu [36]	Nu (Present data)	Error %
0.6	3.15324	3.15114	0.066
1.0	2.61236	2.61134	0.040
1.6	1.41546	1.41411	0.095

5. Results and discussion

This work presents the results of the numerical simulation of a complex fluid trapped between two cylinders. The inner cylinder is cold while the outer one is hot and rotates at a constant and uniform speed. The aim of this study is to know how the heat transfer rate between the fluid and the inner cylinder alters under the influence of the rotational speed of the outer cylinder and the thermal buoyancy force. We mention here that the studied points are:

- The rheological nature of the fluid that changes with the value of the power–law number (n).
- The value of the rotational speed of the outer space. The speed of rotation increases with increasing value of Reynolds number.
- The intensity of thermal buoyancy effect. Indeed, the value of this intensity increases with the increasing value of the Richardson number.

Before starting to analyze the results, it is worth remembering that if the thermal buoyancy force is present, the cold spots of the fluid become denser, and this causes them to move to the lower side. Furthermore, the method of displaying the results of this research is similar to the previous methods such as [43–45].

Figure 3 shows the development of the streamlines in terms of Re and n at Ri = 0. In this case, there is no effect of buoyancy (pure forced convection). The movement of the fluid flow is only due to the rotation of the outer enclosure. Since the cylinder is circular, the movement of the flow within the space is also circular. With the inner cylinder acting as an obstacle, steady vortices appear behind the obstacle. It is clear that the size of these zones increases gradually with Re. Furthermore, there is no significant effect of streamlines with respect to power-law number (n). In general, it is noted that the fluid velocity is larger near the outer cylinder, while the velocity decreases gradually as we move towards the inner cylinder.

Figure 4 presents the same developments of the streamlines but with the effect of buoyancy force (Ri = 1). It is noticed that the effect of thermal buoyancy affects the three values of (n). It is also noted that with the presence of the thermal effect the vortex on the right develops positively, while the vortex on the left develops negatively. On the right-hand side, the movement of the cold fluid spots near the obstacle is opposite to the rotational motion, while on the left-hand side, it is in the same rotation direction of the outer cylinder. From here it is clear that there is an effect of the studied parameters on the heat transfer, which is analyzed later.

Figure 5 presents the contours of dimensionless temperature (isotherms) versus Re and n at Ri = 0. It is clear that there is a degradation of dimensionless temperature. The maximum value of the temperature is near the outer enclosure, and the lower value is around the inner cylinder. Through this distribution, we can know the distribution of temperature gradient in terms of the studied parameters. Through Fig. 5, it is clear that there is a change in the distribution of dimensionless temperature in terms of Re and n, especially around the inner cylinder.

Figure 6 shows the same developments of isotherms for the case of Ri = 1. In this case, the fluid is subjected to the movement as results from two main factors, namely, the rotational movement of the outer cylinder, as well as the cold spots becoming heavier, and this causes them to move downwards. Figure 6 also indicates the variation of temperature gradient in terms of Ri, Re and n. In addition to this, Fig. 6 shows the circulating motion of the fluid as a result of the circular tail of the isotherms at the bottom of the inner obstacle.

Figure 7 represents the change in the mean value of the Nusselt number in terms of the studied elements (Re, n and Ri). In general, the higher the rotational speed of the outer container (Re), the higher the value of Nu in both cases of Ri. Furthermore,

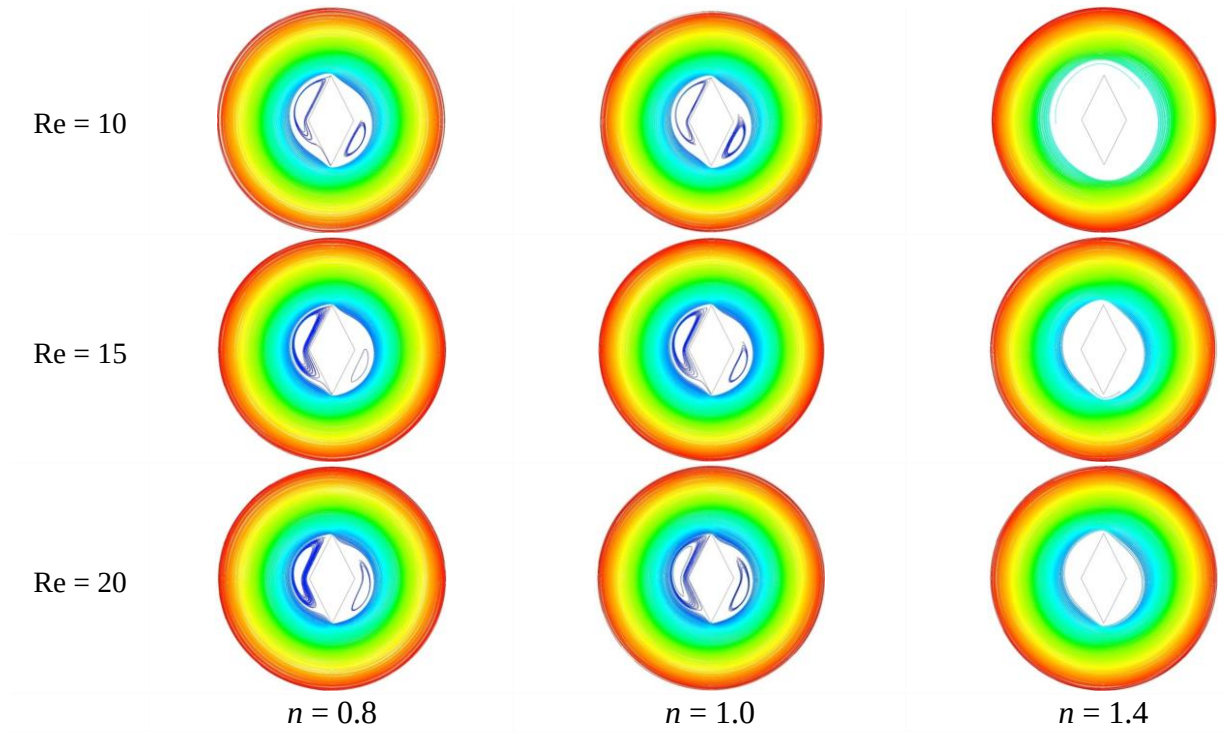

Fig. 3. Streamlines inside the studied domain in terms of Re and *n* at Ri = 0.

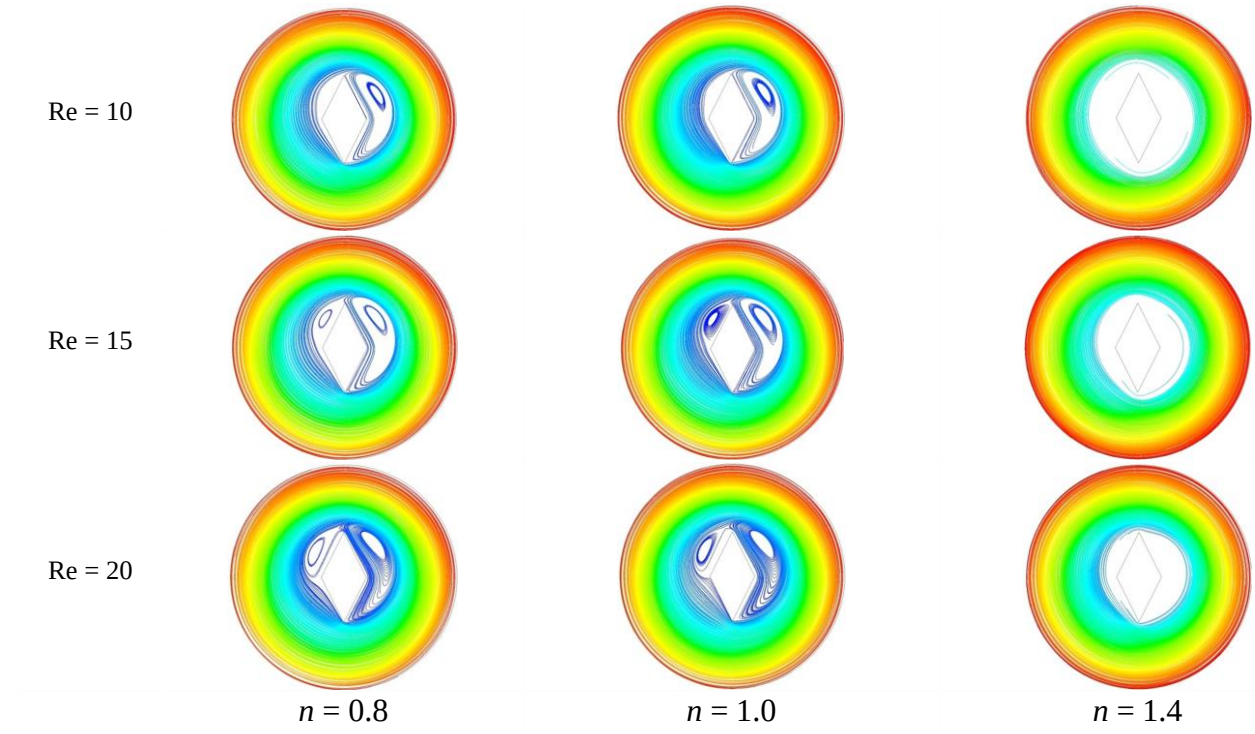

Fig. 4.Streamlines inside the studied domain in terms of Re and *n* at Ri = 1.

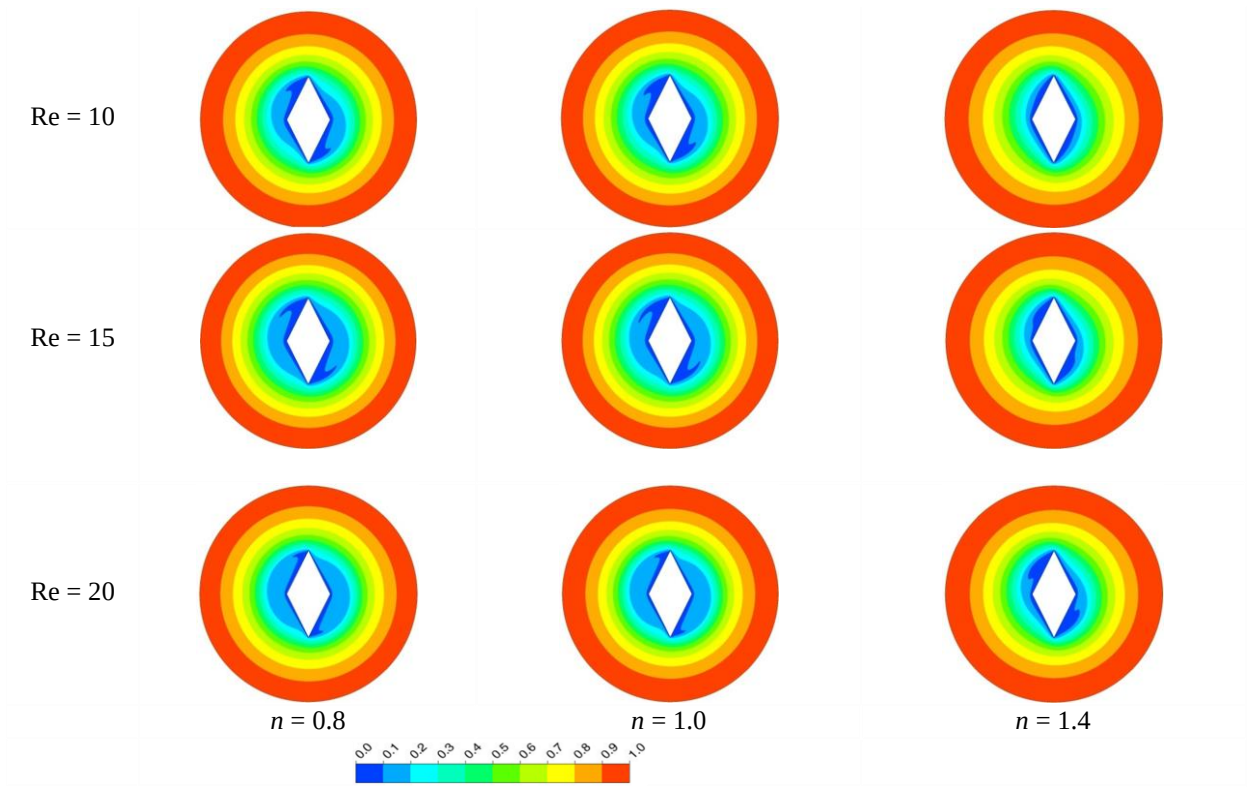

Fig. 5. Dimensionless temperature inside the studied domain in terms of Re and *n* at Ri = 0.

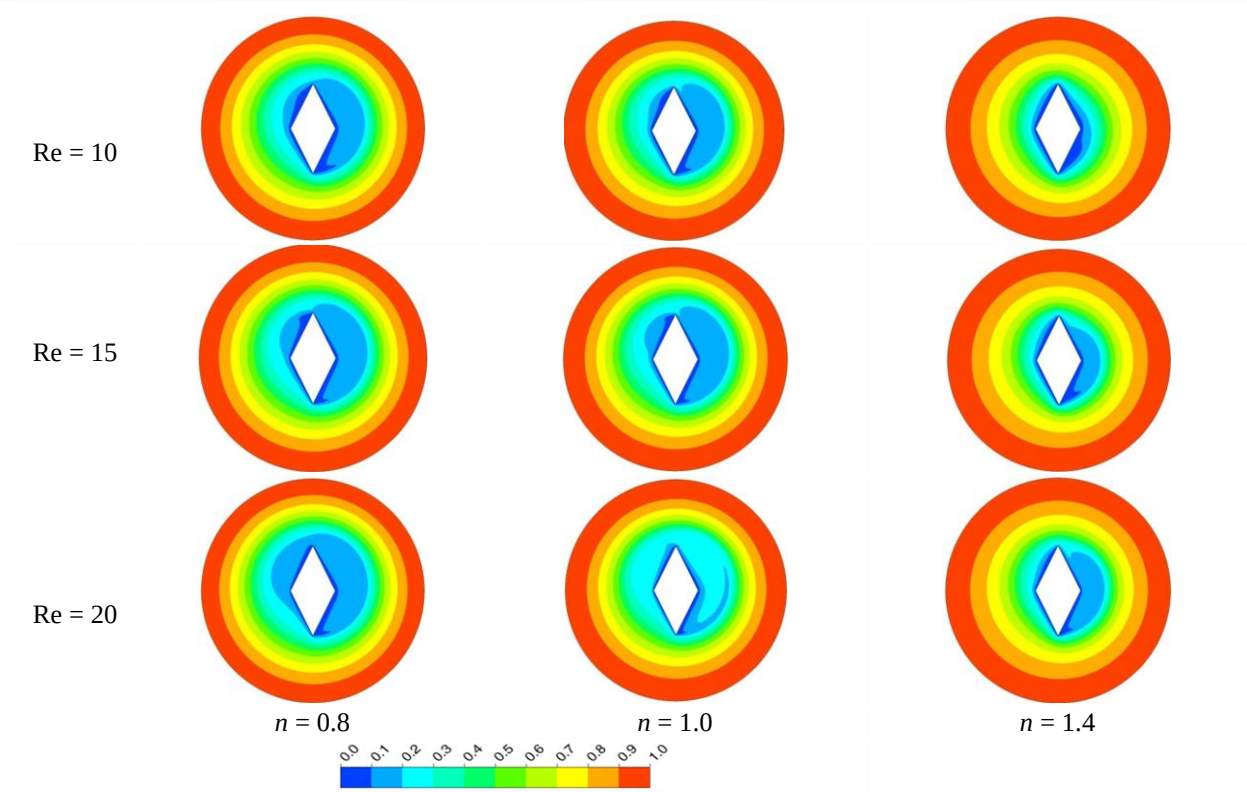

Fig. 6. Dimensionless temperature inside the studied domain in terms of Re and *n* at Ri = 1.

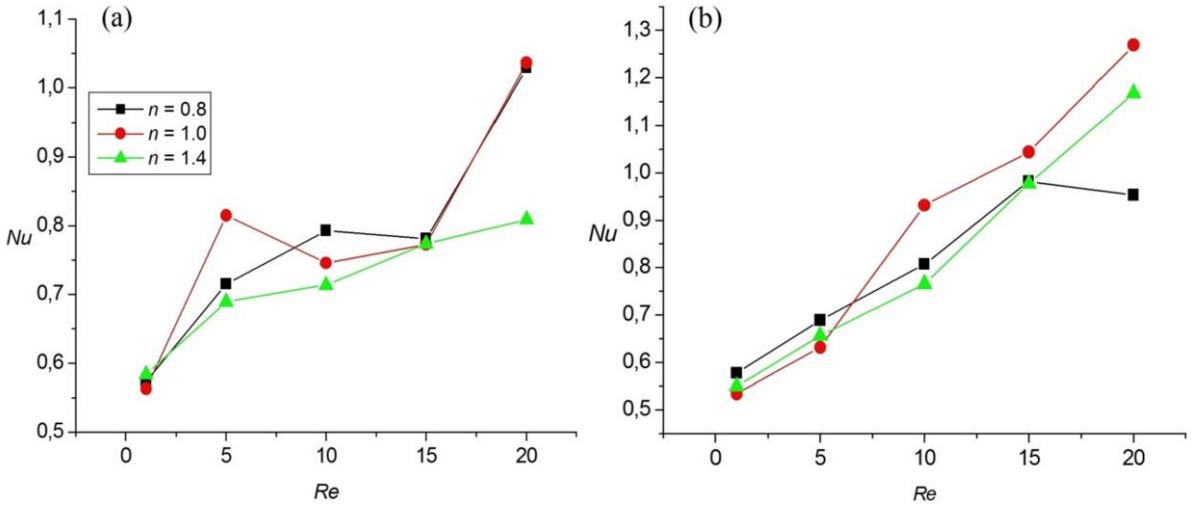

Fig. 7.Variation of Nu versus Re and n; (a) for Ri = 0. (b) for Ri = 1.

it is also noted that the increase of the value of *n* decreases the average value of Nu. This is explained as follows: for $n = 1.4$ this means that the nature of the fluid is complex (shear-thickening fluid). That is, the higher the flow velocity, the higher the dynamic viscosity value, and this dampens the movement of particles of the fluid, making the heat transfer slower. On the contrary, when $n = 0.8$ the fluid is shear-thinning. The viscosity of the fluid decreases with increasing the velocity of the flow, making the heat transfer faster. Finally, it can be concluded that the fluid being of shear- thickening type impedes heat transfer, making it more effective in thermal insulation applications.

5. Conclusions

A set of numerical simulations was achieved in order to study the thermal transfer between obstacles of different shape, temperature and stability pattern. Three types of fluids, whose effects on heat transfer were compared, are, in order: shear-thinning ($n = 0.8$); Newtonian ($n = 1$) and shear thickening ($n = 1.4$). The outer enclosure is also subjected to a circular motion. The effect of thermal buoyancy also was taken into account. Through our study of all these elements, we reached the following points:

- The heat transfer of the inner cylinder increases with the increase in the value of the rotational speed and thermal buoyancy.
- The study showed the presence of two vortices attached to the inner obstacle, the first on the right side and the other on the left side.
- The use of shear-thickening fluid is very effective in applications that include thermal insulation.

For future research related to this topic, we propose to include the influence of the magnetic field on this system with different angles of applications.

References

[1] Chatterjee, D., & Halder, P. (2014). MHD mixed convective transport in square enclosure with two rotating circular cylinders. *Numerical Heat Transfer, Part A*, 65(8), 802–824. doi: 10.1080/10407782.2013.846687

[2] Chatterjee, D., & Halder, P. (2016). Magnetoconvective transport in a lid-driven square enclosure with two rotating circular cylinders. *Heat Transfer Engineering*, 37(2), 198–209. doi: 10.1080/01457632.2015.1044416

[3] Yoon, H.S., Ha, M.Y., Kim, B.S., & Yu, D.H. (2009). Effect of the position of a circular cylinder in a square enclosure on natural convection at Rayleigh number of 10^7. *Physics of Fluids*, 21(4), 047101. doi: 10.1063/1.3112735

[4] Terekhov, V.I., & Ekaid, A.L. (2015). Turbulent natural convection inside a parallelepiped with heating of two opposite vertical walls. *High Temperature*, 53(3), 396–405. doi: 10.1134/S0018151X15020236

[5] Liao, C.C., & Lin, C.A. (2014). Transitions of natural convection flows in a square enclosure with a heated circular cylinder. *Applied Thermal Engineering*, 72(1), 41–47. doi: 10.1016/j.applthermaleng. 2014.02.071

[6] Laidoudi, H., Helmaoui, M., Bouzit, M., & Ghenaim, A. (2021). Natural convection of Newtonian fluids between two concentric cylinders of a special cross-sectional form. *Thermal Science*, 25(5B), 3701–3714. doi: 10.2298/TSCI200201190L

[7] Laidoudi, H. (2020). The role of concave walls of inner cylinder on natural convection in annular space. *Acta Mechanica Malaysia*, 3(2), 24–28. doi: 10.26480/amm.02.2020.24.28

[8] Laidoudi, H. (2020). Natural convection from four circular cylinders in across arrangement within horizontal annular space. *Acta Mechanica et Automatica*, 14(2), 98–102. doi: 10.2478/ ama-2020-0014

[9] Laidoudi, H. (2020). Enhancement of natural convection heat transfer in concentric annular space using inclined elliptical cylinder. *Journal of Naval Architecture and Marine Engineering*, 17(2), 89–99. doi: 10.3329/jname.v17i2.44991

[10] Masoumi, H., Aghighi, M.S., Ammar, A., & Nourbakhsh, A. (2019). Laminar natural convection of yield stress fluids in annular spaces between concentric cylinders. *International Journal*

of Heat and Mass Transfer, 138, 1188–1198. doi: 10.1016/j.ijheatmasstransfer.2019.04.092

[11] Tayebi, T., & Chamkha, A.J. (2021). Analysis of the effects of local thermal non-equilibrium (LTNE) on thermo-natural convection in an elliptical annular space separated by a nanofluid-saturated porous sleeve. *International Communications in Heat and Mass Transfer*, 129, 105725. doi:10.1016/j.icheatmasstransfer.2021.105725

[12] Yigit, S., & Chakraborty, N. (2017). Influences of aspect ratio on natural convection of power-law fluids in cylindrical annular space with differentially heated vertical walls. *Thermal Science and Engineering Progress*, 2, 151–164. doi: 10.1016/j.tsep.2017.05.008

[13] Chen, S., Liu, Z., Bao, S., & Zheng, C. (2010). Natural convection and entropy generation in a vertically concentric annular space. *International Journal of Thermal Sciences*, 49(12), 2439–2452. doi: 10.1016/j.ijthermalsci.2010.08.011

[14] Laidoudi, H. (2018). The effect of blockage ratio on fluid flow and heat transfer around a confined square cylinder under the effect thermal buoyancy. *Diffusion Foundations* 16, 1–11. doi: 10.4028/www.scientific.net/DF.16.1

[15] Cianfrini, M., Corcione, M., & Quintino, A. (2011). Natural convection heat transfer of nanofluids in annular spaces between horizontal concentric cylinders. *Applied Thermal Engineering*, 31(17–18), 4055–4063. doi: 10.1016/j.applthermaleng.2011.08.010

[16] Helmaoui, M., Laidoudi, H., Belbachir, A.,Ayad, A., & Ghaniam, A. (2020). Forced convection heat transfer from a pair of circular cylinders confined in ventilated enclosure. *Diffusion Foundations*, 26, 104–111. doi: 10.4028/www.scientific.net/DF.26.104

[17] Laidoudi, H., Helmaoui, M., Azeddine, B., Ayad, A. & Ghanaim, A. (2020). Effects of inlet and outlet ports of ventilated square cavity on flow and heat transfer, *Diffusion Foundations*, 26, 78–85. doi: 10.4028/www.scientific.net/DF.26.78

[18] Hussain, S., Jamal, M., & Ahmed, S.E. (2019). Hydrodynamic forces and heat transfer of nanofluid forced convection flow around a rotating cylinder using finite element method: The impact of nanoparticles. *International Communications in Heat and Mass Transfer*, 108, 104310. doi: 10.1016/j.icheatmasstransfer.2019.104310

[19] Chatterjee, D., & Mondal, B.(2012). Forced convection heat transfer from an equilateral triangular cylinder at low Reynolds numbers. *Heat and Mass Transfer*, 48(9), 1575–1587. doi: 10.1007/s00231-012-1006-x

[20] Habib, R.,Yadollahi, B., & Karimi, N. (2020). A Pore-Scale investigation of the transient response of forced convection in porous media to inlet ramp inputs. *Journal of Energy Resources Technologies*, 142(11), 112112. doi: 10.1115/1.4047968

[21] Alinejad, J., & Esfahani, J. A. (2014). Lattice Boltzmann simulation of forced convection over an electronic board with multiple obstacles, *Heat Transfer Research*, 45(3), 241–262. doi: 10.1615/HeatTransRes.2013005101

[22] Dey, P., & Das, A. K. (2016). A utilization of GEP (gene expression programming) met model and PSO (particle swarm optimization) tool to predict and optimize the forced convection around a cylinder. *Energy*, 95, 447–458. doi: 10.1016/j.energy.2015.12.021

[23] Rashidi, S., Dehghan, M., Ellahi, R., Riaze, M., & Jamal-Abad, M.T. (2015). Study of streamwise transverse magnetic fluid flow with heat transfer around an obstacle embedded in a porous medium. *Journal of Magnetism and Magnetic Materials*, 378, 128–137. doi: 10.1016/j.jmmm.2014.11.020

[24] Gupta, S.K., Ray, S., & Chatterjee, D. (2015).Forced convection heat transfer in power-law fluids around a semi circular cylinder at incidence. *Numerical Heat Transfer, Part A*, 67, 952–971. doi: 10.1080/10407782.2014.955335

[25] Selimefendigil, F., Öztop, H.F., & Abu-Hamdeh, N. (2020). Impacts of conductive inner L-shaped obstacle and elastic bottom wall on MHD forced convection of a nanofluid in vented cavity. *Journal of Thermal Analysis and Calorimetry*, 141, 465–482. doi: 10.1007/s10973-019-09114-7

[26] Laidoudi, H., & Makinde, O.D. (2021). Computational study of thermal buoyancy from two confined cylinders within a square enclosure with single inlet and outlet ports. *Heat Transfer*, 50(2), 1335–1350. doi: 10.1002/htj.21932

[27] Ramla, M., Laidoudi, H., & Bouzit, M. (2022). Behaviour of a non-Newtonian fluid in a helical tube under the influence of thermal buoyancy. *Acta Mechanica et Automatica*, 16, 111–118. doi: 10.2478/ama-2022-0014

[28] Laidoudi, H., & Bouzit, M. (2018). The Effect of Reynolds and Prandtl number on flow inside of plan channel of waved bottom wall under mixed convection. *Diffusion Foundations*, 16, 21–29. doi: 10.4028/www.scientific.net/DF.16.21

[29] Xiong, P.Y., Hamid, A., Iqbal, K., Irfan, M., & Khan, M. (2021). Numerical simulation of mixed convection flow and heat transfer in the lid-driven triangular cavity with different obstacle configurations. *International Communications in Heat and Mass Transfer*, 123, 105202. doi: 10.1016/j.icheatmasstransfer.2021.105202

[30] Singh, R.J., & Gohil, T.B. (2019). Numerical study of MHD mixed convection flow over a diamond-shaped obstacle using OpenFOAM. *International Journal of Thermal Sciences*, 146(7), 106096. doi: 10.1016/j.ijthermalsci.2019.106096

[31] Shulepova, E.V., Sheremet, M.A.H., Oztop, F., & Abu-Hamdeh, N. (2020). Mixed convection of Al2O3–H2O nanoliquid in a square chamber with complicated fin. *International Journal of Mechanical Sciences*, 165, 105192. doi: 10.1016/j.ijmecsci.2019.105192

[32] Ahmed, S.E., Mansour, M.A., Hussein, A.K., Mallikarjuna, B., Almeshaal, M.A., & Kolsi, L. (2019). MHD mixed convection in an inclined cavity containing adiabatic obstacle and filled with Cu–water nanofluid in the presence of the heat generation and partial slip. *Journal of Thermal Analysis and Calorimetry*, 138(2), 1443–1460. doi: 10.1007/s10973-019-08340-3

[33] Qureshi, M. A., Hussain, S., & Sadiq M.A. (2021). Numerical simulations of MHD mixed convection of hybrid nanofluid flow in a horizontal channel with cavity: Impact on heat transfer and hydrodynamic forces. *Case Studies in Thermal Engineering*, 27, 101321. doi: 10.1016/j.csite.2021.101321

[34] Fu, C., Rahmani, A., Suksatan, W., Alizadeh, S.M., Zarringhalam, M., Chupradit, S., & Toghraie, D.(2021). Comprehensive investigations of mixed convection of Fe–ethylene-glycol nanofluid inside an enclosure with different obstacles using lattice Boltzmann method. *Scientific Reports*, 11, 20710. doi: 10.1038/s41598-021-00038-7

[35] Yousefzadeh, S., Rajabi, H., Ghajari,N., Sarafraz, M., Akbari, O.A., & Goodarzi, M. (2020). Numerical investigation of mixed convection heat transfer behaviour of nanofluid in a cavity with different heat transfer areas. *Journal of Thermal Analysis and Calorimetry*, 140(3), 2779–2803. doi: 10.1007/s10973-019-09018-6

[36] Laidoudi, H., & Ameur H., (2020). Investigation of the mixed convection of power-law fluids between two horizontal concentric cylinders: Effect of various operating conditions. *Thermal Science and Engineering Progress*, 20, 100731. doi: 10.1016/j.tsep.2020.100731

[37] Laidoudi, H., & Ameur, H. (2022). Complex fluid flow in annular space under the effects of mixed convection and rotating wall of

the outer enclosure. *Heat Transfer*, 51(5), 3741–3767. doi: 10.1002/htj.22472.

[38] Al-Kouz, W., Aissa, A., Shamshuddin, M.D., Obai, Y., Sahnoun, M., Anwar Bég, O., & Toghraie, D. (2021). Heat transfer and entropy generation analysis of water-Fe3O4/CNT hybrid magnetic nanofluid flow in a trapezoidal wavy enclosure containing porous media with the Galerkin finite element method. *The European Physical Journal Plus*, 136(11), 1184. doi: 10.1140/epjp/s13360-021-02192-3

[39] Shamshuddin, M.D., Mabood, F., Rajput, G.R., Bég, O.A., & Badruddin, I.A. (2022) .Thermo-solutal dual stratified convective magnetized fluid flow from an exponentially stretching Riga plate sensor surface with thermophoresis. *International Communications in Heat and Mass Transfer*, 134(4), 105997. doi: 10.1016/j.icheatmasstransfer.2022.105997

[40] Shamshuddin, M.D., Ullah Khan, S., Bég, O.A., & Bég, T.A. (2020). Hall current, viscous and Joule heating effects on steady radiative 2-D magneto-power-law polymer dynamics from an exponentially stretching sheet with power-law slip velocity: A numerical study. *Thermal Science and Engineering Progress*, 20, 100732. doi: 10.1016/j.icheatmasstransfer.2022.105997

[41] Kadir, A., Bég, A.O., El Gendy, M., Bég, T.A., & Shamshuddin, M.D. (2019). Computational fluid dynamic and thermal stress analysis of coatings for high-temperature corrosion protection of aerospace gas turbine blades. *Heat Transfer*, 48(6), 2302–2328. doi: 10.1002/htj.21493

[42] Anwar Bég, O., Bég, T.A., Karim, I. , Khan, M.S., Alam, M.M., Ferdows, M., & Shamshuddin, MD. (2019). Numerical study of magneto-convective heat and mass transfer from inclined surface with Soret diffusion and heat generation effects: A model for ocean magnetic energy generator fluid dynamics. *Chinese Journal of Physics*, 60, 167–179. doi: 10.1016/j.cjph.2019.05.002

[43] Błasiak, P., & Pietrowicz, S. (2016). Towards a better understanding of 2D thermal-flow processes in a scraped surface heat exchanger. *International Journal of Heat and Mass Transfer*, 98, 240–256. doi: 10.1016/j.ijheatmasstransfer.2016.03.004

[44] Aliouane, I., Kaid, N., Ameur, H., & Laidoudi, H. (2021). Investigation of the flow and thermal fields in square enclosures: Rayleigh-Bénard's instabilities of nanofluids. *Thermal Science and Engineering Progress*, 25(2), 100959. doi: 10.1016/j.tsep.2021.100959

[45] Laidoudi, H., & Bouzit, M. (2017). The effect of asymmetrically confined circular cylinder and opposing buoyancy on fluid flow and heat transfer. *Defect and Diffusion Forum*, 374, 18–28. doi: 10.4028/www.scientific.net/DDF.374.18

Co-published by
Institute of Fluid-Flow Machinery
Polish Academy of Sciences
Committee on Thermodynamics and Combustion
Polish Academy of Sciences

http://www.imp.gda.pl/archives-of-thermodynamics/

Soret and Dufour effects on an unsteady MHD flow about a permeable rotating vertical cone with variable fluid properties

Temjennaro Jamir[a*], Hemanta Konwar[a]

[a]Kohima Science College, Jotsoma, Kohima 797001, India
*Corresponding author email: temjennarojamir.tj@gmail.com

Received: 05.08.2023; revised: 30.08.2023; accepted: 12.10.2023

Abstract

The objective of the present work is to examine the characteristics of unsteady incompressible magnetohydrodynamic fluid flow around a permeable rotating vertical cone. The effects of thermal radiation, viscous dissipation, and the Soret and Dufour effects are investigated in the analysis of heat and mass transfer. The viscosity of the fluid is considered inversely proportional to the temperature, and the thermal conductivity of the fluid is considered directly proportional to the temperature. The governing equations are converted into ordinary differential equations using suitable similarity transformations, which are then solved numerically using bvp4c from MATLAB. Results obtained in this study are in excellent correlation with previously conducted studies. The results demonstrate that the Dufour and Soret effects subsequently reduce the heat transit rate (by –3.3%) and mass transit rate (by –1.2%) of the system. It is also detected that fluids with higher viscosity tend to increase tangential skin friction (+8.9%) and azimuthal skin friction (+8.3%). The heat transit rate of the system is found to be more efficient for fluids with higher viscosity and lower thermal conductivity and Eckert numbers. Furthermore, the thickness of the momentum, thermal, and concentration boundary layers significantly reduces while the heat and mass transit rates (+17.8% and +18.3%, respectively) of the system become more efficient for greater values of the unsteadiness parameter.

Keywords: Rotating cone; Temperature-dependent viscosity; Temperature-dependent thermal conductivity; Viscous dissipation, Soret and Dufour effects

Vol. 45(2024), No. 1, 75–86; doi: 10.24425/ather.2024.150440

Cite this manuscript as: Jamir, T, & Konwar, H. (2024). Soret and Dufour effects on an unsteady MHD flow about a permeable rotating vertical cone with variable fluid properties. *Archives of Thermodynamics*, 45(1), 75–86.

1. Introduction

In a variety of applications and industrial processes, both heat and mass transfer are crucial. The equipment, such as gas turbines, various missile propulsion systems, space vehicles, satellites, nuclear reactors, and aircraft, extensively relies on double-diffusive mixed convection over rotating bodies [1].

Hering and Grosh [2] investigated laminar flow across a non-isothermal cone. Sparrow and Cess [3] investigated an axial magnetic field effect on flow and heat transfer over a revolving disc. A steady free convective flow along a vertical cone and a wedge under the influence of transverse magnetic field was presented by Chamkha [4]. Takhar et al. [5] discovered that when an axi-symmetric body spins in a forced flow field, the centrifugal force causes the fluid at the body surface to move outward in the radial direction.

Nomenclature

a^* – mean absorption coefficient
B_0 – magnetic field, T
C – species concentration, kg/m^3
C_{fy} – azimuthal skin friction
C_{fx} – tangential skin friction
C_0 – reference concentration
c_p – specific heat at constant pressure, J/(kgK)
C_w – sheet concentration
C_∞ – free stream concentration, kg/m^3
c_s – concentration susceptibility
Du – Dufour number, $= \frac{D_m K_T}{c_s c_p \nu_\infty}\left(\frac{C_w - C_\infty}{T_w - T_\infty}\right)$
D_m – mass diffusivity, m^2/s
Ec – Eckert number, $= \frac{xL\Omega^2 sin^2\alpha}{c_p(T_0 - T_\infty)}$
f_w – dimensionless suction/injection
$f(\eta)$– normal velocity component
$-f'(\eta)$ – tangential velocity component
g – acceleration due to gravity, m/s^2
$g(\eta)$ – azimuthal velocity component
Gr$_L$ – thermal Grashof number, $= g\beta_T cos\alpha(T_0 - T_\infty)\frac{L^3}{{\nu_\infty}^2}$
Hα^2 – square of Hartmann number, $= \frac{\sigma {B_0}^2 L^2(1-st^*)}{\mu_\infty}$
K_T – thermal diffusion ratio, kg/m^3
$k(T)$ thermal conductivity, W/(mK)
k_∞ – constant thermal conductivity
L – characteristic length, m
M – magnetic parameter, $= \frac{\mathrm{Ha}^2}{\mathrm{Re}_L}$
N – Buoyancy ratio, $= \frac{\beta_C(C_w - C_\infty)}{\beta_T(T_w - T_\infty)}$
Pr – Prandtl number, $= \frac{\mu_\infty c_p}{k_\infty}$
Rd – radiation, $= \frac{k_\infty a^*}{4\sigma^* T_\infty^3}$
Ri – Richardson number, $= \frac{\mathrm{Gr}_L}{{\mathrm{Re}_L}^2}$
Re$_L$ – Reynolds number, $= \frac{\Omega L^2 sin\alpha}{\nu_\infty}$
Re$_x$ – local Reynolds number, $= \frac{\Omega x^2 sin\alpha}{\nu_\infty(1-st^*)}$
Sc – Schmidt number, $= \frac{\nu_\infty}{D_m}$
Sr – Soret number, $= \frac{D_m K_T}{T_m \nu_\infty}\left(\frac{T_w - T_\infty}{C_w - C_\infty}\right)$
s – unsteadiness parameter
t^* – dimensionless time
t – time, s
T – fluid temperature, K
T_m – mean fluid temperature, K
T_w – sheet temperature, K
T_∞ – free stream temperature, K
T_0 – reference temperature, K
$\boldsymbol{V}$ – velocity vector
u, v, w – velocity along tangential, circumferential, normal direction respectively, m/s
w_0 – suction velocity, m/s
x, y, z – curvilinear coordinate, m

Greek Symbols

β_T, β_C – coefficients of thermal and mass expansion, K, kg
μ – dynamic viscosity, kg/(ms)
σ^* – Stefan Boltzmann constant, W/(m^{2}K^4)
μ_∞ – ambient fluid dynamic viscosity, kg/(ms)
ν – kinematic viscosity, m^2/s
$\phi(\eta)$ – dimensionless concentration
ν_∞ – kinematic viscosity of ambient fluid, m^2/s
$\theta(\eta)$ dimensionless temperature
ρ_∞ – constant fluid density, kg/m^3
Ω – angular velocity, 1/s
σ – electric conductivity, s/m
η – dimensionless variable, m
δ – temperature dependent viscosity, m^2/s
ε – temperature dependent thermal conductivity, W/(mK)
α – semi vertical angle, rad

The research mentioned above dealt with steady flows. For laminar flow across a vertical cone in a steady state for two-dimensional axi-symmetric issues, several authors identified comparable solutions. Because the spinning body's angular velocity varies over time or fluctuates abruptly in many real-life situations, the flow may be unstable. Ece [6] looked into the unsteady flow of a rotating symmetric body that is impulsively translating and spinning and established a solution. Chamkha and Al-Mudhaf [7] also analysed this unsteady fluid flow behaviour over a conical surface with heat generation/absorption, Anilkumar and Roy [8] took into account an unsteady rotating cone to analyse the flow of a rotating fluid. A study on mixed convection nanofluid flow past a vertical wedge was presented in the study conducted by Gorla et al. [9], the study concluded that upon enlarging the wedge angle the heat and mass transit rates could be improved. Another study on the flow across a cone/wedge for an Oldroyd-B fluid was considered in the study conducted by Reddy et al.[10]. Further, Reddy et al.[11] estimated non-linear thermal radiative nanofluid steady flow over a rotating cone and Saleem [12] accounted for third-grade fluid flow properties for a rotating cone. A study on water-based nanofluid through a conical surface with single and multi-wall carbon nanotubes was considered by Shah et al. [13]. Krishna et al. [14] presented an analysis of an unsteady magnetohydrodynamic (MHD) non-Newtonian flow over an exponentially accelerated surface under the influence of slip velocity in a rotating frame. The study showed that the presences of the rotation parameter significantly reduce the fluid primary velocity.

Furthermore, the Soret and Dufour effects were overlooked in all previous studies. When density variations occur in the flow regime, such impacts are considerable. In binary fluid mixtures, the Soret and Dufour effects are crucial, and are frequently found in the field of separation processes. When a species with a lower density than the ambient fluid is introduced in a fluid domain, Soret and Dufour impacts might become prominent. The Soret effect has been commonly used to separate isotopes in mixtures of extremely low molecular weight gases like hydrogen and helium, meanwhile, the Dufour effect has been shown to be beneficial for the separation of medium molecular weight gases like nitrogen and air. It has varied applications in the vapour deposition process for optical fibre fabrication, cooling applications, heat exchangers, steel industries, and to separate distinct polymers. These properties have been studied by Chamkha and Rashad [15] who considered unsteady fluid flow

for a rotating vertical cone with Soret and Dufour effect. Krishna et al. [16] accounted for rotating mixed convection flow past an infinite vertical plate to study the influence of the Soret effect, it was concluded that the Soret number promotes the concentration distribution. An analysis of the Soret and Dufour effects for fluid exhibiting relaxation/retardation time effect was performed by Yasir et al. [17] and Reddy [18] who considered Oldroyd-B liquid flow across a cone/wedge under the effects of Soret and Dufour. Saleem [19] accounted for Walter's B nanofluid flow about a rotating cone with the effect of Soret and Dufour. Taking into consideration the multi slip effect, Nadeem et al. [20] accounted for unsteady micropolar fluid flow over an exponential sheet under the influence of the thermophoretic effects. The study showed that for higher values of the thermophoresis parameter the temperature profile improved. Furthermore, this effect of Soret and Dufour was considered in studies conducted by Khan et al. [21] and Ghoneim [22].

Variations in viscosity and thermal conductivity affect the velocity and temperature profiles, resulting in various heat and mass transfer coefficients. However, these characteristics in each of the investigations listed above were deemed to be constant. Moreover, the temperature is known to affect fluid viscosity and thermal conductivity; for instance, Abd El-Aziz [23] considers water's absolute viscosity which reduces by 240% when temperatures increase from 10°C (μ = 0.0131 gcm^{-1}s^{-1}) to 50°C (μ = 0.00548 gcm^{-1}s^{-1}). In order to effectively anticipate flow behaviour, these variations in viscosity and thermal conductivity must be considered. Lai and Kulacki [24] took into account variable viscosity for a moving flat plate, while Prasad et al. [25] considered variable fluid properties for a stretching sheet. Mukhopadhyay [26] in his study considered variable viscosity and thermal conductivity for a porous stretching sheet. Khan et al. [27] accounted for micropolar fluid flow to study the temperature dependent fluid properties to analyse the heat transfer rate and flow properties. The study concluded that the variability in transport properties led to a rise in heat transfer and a decrease in skin friction. In another exploration Khan and Nadeem [28] presented a comparative study to understand the influence of the thermophoretic effects and the variable thermal conductivity on a linear/exponential stretching sheet using the bvp4c numerical technique. Further, Ahmad et al. [29] considered three dimensional bioconvective flow to analyse variable thermal conductivity over an exponentially stretching sheet.

The temperature distributions are altered by viscous dissipation, which acts as an energy source and has an impact on heat transfer rates. Whether the cone is being heated or cooled affects the significance of viscous dissipation. Malik et al. [30] accounted for fluid flow over a rotating cone to analyse the influence of viscous dissipation on the mixed convective fluid flow, the study revealed that the higher Eckert number promotes the heat transfer rate. Sambath et al. [31] conducted a numerical study of the effect of viscous dissipation on a chemically reacting MHD flow over a vertical cone. Also, dissipative MHD nanofluid flow past a vertical cone was taken into consideration in the study conducted by Ragulkumar et al. [32]. Further, Khan et al. [33] accounted for ternary nanomaterials to analyse the thermal conductivity performance with dissipation.

The preceding discussions have highlighted the significant influence of viscous dissipation, temperature-dependent viscosity and thermal conductivity, as well as the Soret and Dufour effects, on heat and mass transfer phenomena. However, additional investigation is necessary to examine the combined effect of these variables on the flow, heat and mass transfer in an unsteady mixed convection flow about a rotating vertical cone. To the best of the authors' knowledge, this issue is yet to be explored. The innovative aspect of the present model is the investigation of the unsteady MHD fluid flow across the rotating vertical cone while taking into consideration the temperature-dependent viscosity and thermal conductivity together with viscous dissipation and the Soret and Dufour effects. The purpose of this study is to provide a comprehensive understanding of the key parameters that influence the characteristics of momentum, thermal and concentration boundary layers, as well as the parameters that are of particular significance in engineering applications. The findings of this study have significant implications for the development and production of cone-shaped materials used in rotating condensers for seawater distillation, nuclear plants, thermal systems, rotating heat exchangers, space aircraft, and oil and gas industries, etc. The methodology employed in this work involves the application of appropriate similarity transformations to transform the governing system of equations into a solvable form. These transformed equations are subsequently solved using MATLAB's bvp4c solver to generate precise numerical solutions.

2. Mathematical formulation

Consider an unsteady, laminar, incompressible, axi-symmetric, electrically conducting and radiative fluid flow about a permeable vertical rotating cone in an ambient fluid with uniform angular velocity Ω. The cone surface has been estimated to have homogeneous fluid suction/injection with velocity w_0, and the viscosity and thermal conductivity of the fluid are deemed to be temperature dependent. The rectangular coordinate system (x, y, z) has been used, in which the *x*-axis is taken along the tangential direction, the *y*-axis is taken along a circular section, and the *z*-axis is normal to the cone, as shown in Fig. 1.

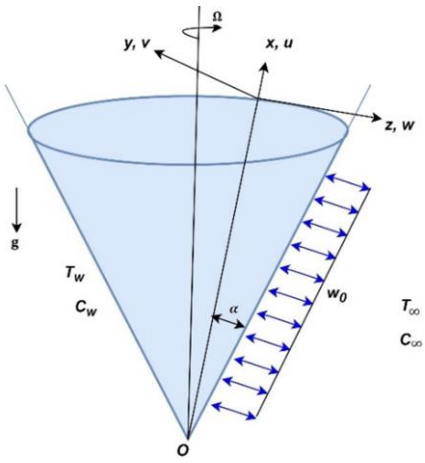

Fig. 1. Physical model and coordinate system.

The velocity components in the tangential, azimuthal and normal directions are taken as u, v and w respectively. In the normal direction, a homogeneous magnetic field of strength B_0 is applied. The ambient temperature T_∞ and concentration C_∞ are assumed to be constant, whereas the wall temperature T_w and wall concentration C_w are defined as $T_w = T_\infty + \frac{T_0 - T_\infty}{(1-st^*)^2}\left(\frac{x}{L}\right)$ and $C_w = C_\infty + \frac{C_0 - C_\infty}{(1-st^*)^2}\left(\frac{x}{L}\right)$. It is supposed that the surface of the cone is electrically insulated, and it is also expected that the magnetic Reynolds number is negligible. In this particular instance, it is feasible to disregard the induced magnetic field when comparing it to the applied magnetic field. In the absence of any applied or polarization voltage within the flow field, the electric field $\vec{E} = 0$. Therefore, the Navier-Stokes equations and Maxwell's equations are decoupled, and in the absence of the magnetic dissipation, the hall and ion slip effects, the only influence of the magnetic field is due to the Lorentz force [34]. The vector form of the governing equations is given below (Gnaneswara Reddy et al. [11]):

Conservation of mass:

$$\nabla . \boldsymbol{V} = 0 \, . \tag{1}$$

Conservation of momentum:

$$\rho_\infty \left(\frac{\partial u}{\partial t} + \boldsymbol{V}.\nabla u - \frac{v^2}{x}\right) = -\nabla p + \nabla(\mu(T)\nabla u) + g\rho_\infty[\beta_T(T - T_\infty) + \beta_C(C - C_\infty)]cos\alpha - \sigma {B_o}^2 u \, , \tag{2}$$

$$\rho_\infty \left(\frac{\partial v}{\partial t} + \boldsymbol{V}.\nabla v + \frac{uv}{x}\right) = -\nabla p + \nabla(\mu(T)\nabla v) - \sigma {B_o}^2 v \, . \tag{3}$$

Conservation of energy:

$$\rho_\infty c_p \left(\frac{\partial T}{\partial t} + \boldsymbol{V}.\nabla T\right) = \nabla(k(T)\nabla T) - \nabla q_r + \frac{D_m K_T \rho_\infty}{c_s}\nabla^2 C + \mu(T)(\nabla \boldsymbol{V}.\nabla \boldsymbol{V}). \tag{4}$$

Conservation of species:

$$\frac{\partial C}{\partial t} + \boldsymbol{V}.\nabla C = D_m \nabla^2 C + \frac{D_m K_T}{T_m}\nabla^2 T \tag{5}$$

Under the hypotheses stated above and using Boussinesq's approximation, Eqs. (1)–(5) reduce to (Tien and Tsuji [1], Chamkha and Al-Mudhaf [7], Saleem et al. [19]):

$$\frac{\partial u}{\partial x} + \frac{u}{x} + \frac{\partial w}{\partial z} = 0, \tag{6}$$

$$\frac{\partial u}{\partial t} + u\frac{\partial u}{\partial x} + w\frac{\partial u}{\partial z} - \frac{v^2}{x} = \frac{1}{\rho_\infty}\frac{\partial}{\partial z}\left(\mu(T)\frac{\partial u}{\partial z}\right) + g[\beta_T(T - T_\infty) + \beta_C(C - C_\infty)]cos\alpha - \frac{\sigma {B_o}^2}{\rho_\infty}u \, , \tag{7}$$

$$\frac{\partial v}{\partial t} + u\frac{\partial v}{\partial x} + w\frac{\partial v}{\partial z} + \frac{uv}{x} = \frac{1}{\rho_\infty}\frac{\partial}{\partial z}\left(\mu(T)\frac{\partial v}{\partial z}\right) - \frac{\sigma {B_o}^2}{\rho_\infty}v \, , \tag{8}$$

$$\frac{\partial T}{\partial t} + u\frac{\partial T}{\partial x} + w\frac{\partial T}{\partial z} = \frac{1}{\rho_\infty c_p}\frac{\partial}{\partial z}\left(k(T)\frac{\partial T}{\partial z}\right) - \frac{1}{\rho_\infty c_p}\frac{\partial q_r}{\partial z} + \frac{D_m K_T}{c_s c_p}\frac{\partial^2 C}{\partial z^2} + \frac{\mu(T)}{\rho_\infty c_p}\left\{\left(\frac{\partial u}{\partial z}\right)^2 + \left(\frac{\partial v}{\partial z}\right)^2\right\}, \tag{9}$$

$$\frac{\partial C}{\partial t} + u\frac{\partial C}{\partial x} + w\frac{\partial C}{\partial z} = D_m\frac{\partial^2 C}{\partial z^2} + \frac{D_m K_T}{T_m}\frac{\partial^2 T}{\partial z^2} \, . \tag{10}$$

The boundary conditions for the problem are (Chamkha and Al-Mudhaf [7], Saleem et al. [19]):

$$\begin{gathered} u(x,0,t) = 0, \quad v(x,0,t) = \frac{\Omega x sin\alpha}{(1-st^*)}, \quad w(x,0,t) = w_0 \, , \\ T(x,0,t) = T_w(x), \quad C(x,0,t) = C_w(x) \, , \\ u(x,\infty,t) = v(x,\infty,t) = 0, \quad T(x,\infty,t) = T_\infty, \\ C(x,\infty,t) = C_\infty \, . \end{gathered} \tag{11}$$

The radiative heat flux $\frac{\partial q_r}{\partial z}$ in Eq. (9) is simplified using the Rosseland approximation given by (Brewster [35]):

$$q_r = -\frac{4\sigma^*}{3a^*}\frac{\partial T^4}{\partial z} \, . \tag{12}$$

Because the temperature difference within the flow is very minimal, higher-order terms with a degree greater than one are ignored in $T - T_\infty$. By escalating T^4 into the Taylor series around T_∞, the linear structure of Eq. (12) can be obtained:

$$T^4 \approx 4T_\infty^3 T - 3T_\infty^4 \, . \tag{13}$$

Thus,

$$\frac{\partial q_r}{\partial z} = -\frac{16\sigma^* T_\infty^3}{3a^*}\frac{\partial^2 T}{\partial z^2} \, . \tag{14}$$

Additionally, the fluid viscosity is considered to vary as an inverse linear function of temperature ((Prasad et al. [25]):

$$\mu(T) = \frac{\mu_\infty}{1+\gamma(T-T_\infty)} = \frac{\mu_\infty}{1+\delta\theta} \, . \tag{15}$$

The variation of thermal conductivity is expressed as (Mukhopadhyay [26]):

$$k(T) = k_\infty\,(1 + b(T - T_\infty) = k_\infty(1 + \varepsilon\theta)\,, \qquad (16)$$

where $\delta = \gamma(T_w - T_\infty)$ is the viscosity parameter such that $\delta > 0$ for liquid, $\delta < 0$ for gas, and $\varepsilon = b(T_w - T_\infty)$ is the thermal conductivity parameter such that $b > 0$ for fluids like water and air while $b < 0$ for lubricating oil. The range of possibilities for ε is as follows: $0 \le \varepsilon \le 0.12$ for water, $0 \le \varepsilon \le 6$ for air, and $-0.1 \le \varepsilon \le 0$ for lubricating oils (Hermann, Schlichting and Gersten [36]). The viscosity parameter δ will be treated as negative and the thermal conductivity parameter ε as positive in the current problem for numerical computation. The following is the relation between the viscosity and temperature of water and air, which are the most commonly utilized fluids in industries (Lai and Kulacki [24]):

– based on T_∞ = 288 K (15°C); $1/\mu = 29{,}83(T - 258{,}6)$ for water,
– based on T_∞ = 293 K (20°C); $1/\mu = -123{,}2(T - 742{,}6)$ for air.

The following transformations can be used to convert Eqs. (6)–(10) into non-linear dimensionless ordinary differential equations (Anilkumar and Roy [8], Saleem [19], Chamkha and Rashad [15]):

$$\eta = \left(\frac{\Omega\sin\alpha}{\nu_\infty(1-st^*)}\right)^{\frac{1}{2}} z, \quad t^* = (\Omega\sin\alpha)t,$$
$$u = -\frac{\Omega x\sin\alpha}{2(1-st^*)} f'(\eta), \quad v = \frac{\Omega x\sin\alpha}{(1-st^*)} g(\eta), \qquad (17)$$
$$w = \left(\frac{\Omega\nu_\infty sin\alpha}{1-st^*}\right)^{\frac{1}{2}} f(\eta), \;\; T = T_\infty + (T_w - T_\infty)\theta(\eta),$$
$$C = C_\infty + (C_w - C_\infty)\phi(\eta)$$

With the above transformations Eq. (6) is satisfied identically and Eqs. (7)–(10) are obtained as follows (Eqs. (18)–(21)):

$$f''' - (1+\delta\theta)\left\{ s\left(f' + \frac{\eta}{2}f''\right) - \frac{f'^2}{2} + ff'' + 2g^2 + \frac{\delta}{(1+\delta\theta)^2}\theta' f'' + 2\mathrm{Ri}(\theta + N\phi) + Mf'\right\} = 0\,, \qquad (18)$$

$$g'' - (1+\delta\theta)\left\{ s\left(g + \frac{\eta}{2}\,g'\right) - f'g + fg' + \frac{\delta}{(1+\delta\theta)^2}\theta' g' + Mg\right\} = 0\,, \qquad (19)$$

$$\theta'' - \left\{\frac{1}{\mathrm{Pr}}\left(1 + \varepsilon\theta + \frac{4}{3Rd}\right)\right\}^{-1}\left\{ s\left(\frac{\eta}{2}\theta' + 2\theta\right) + f\theta' - \frac{1}{2}f'\theta - \frac{1}{\mathrm{Pr}}\varepsilon\theta'^2 - \frac{\mathrm{Ec}}{1+\delta\theta}\left(\frac{1}{4}f''^2 + g'^2\right) - \mathrm{Du}\,\phi''\right\} = 0\,, \qquad (20)$$

$$\phi'' + \mathrm{Sc}\left\{\frac{1}{2}f'\phi - f\phi' - s\left(\frac{\eta}{2}\phi' + 2\phi\right) + \mathrm{Sr}\,\theta''\right\} = 0\,, \qquad (21)$$

with the following boundary conditions:

– at η =0:

$$f(\eta) = f_w, \quad f'(\eta) = 0, \quad g(\eta) = 1, \quad \theta(\eta) = 1, \quad \phi(\eta) = 1, \qquad (22a)$$

– as $\eta \to \infty$:

$$f'(\eta) = g(\eta) = \theta(\eta) = \phi(\eta) = 0. \qquad (22b)$$

Here prime represents differentiation with respect to η and suction/injection velocity $f_w = w_0\sqrt{\frac{1-st^*}{\Omega\nu_\infty\sin\alpha}}$ is such that $f_w < 0$ indicates suction, $f_w = 0$ indicates impermeable rotating cone, and $f_w > 0$ indicates injection.

The parameters of engineering importance, i.e. skin friction coefficients, Nusselt number, and Sherwood numbers are defined as follows:

$$C_{fx} = \frac{2\mu(T)\left(\frac{\partial u}{\partial z}\right)_{z=0}}{\rho_\infty\left(\frac{\Omega x\sin\alpha}{1-st^*}\right)^2} = -\frac{\mathrm{Re}_x^{-1/2} f''(0)}{(1+\delta\theta)} \qquad (23)$$

$$C_{fy} = \frac{-2\mu(T)\left(\frac{\partial v}{\partial z}\right)_{z=0}}{\rho_\infty\left(\frac{\Omega x\sin\alpha}{1-st^*}\right)^2} = -\frac{2\mathrm{Re}_x^{-1/2} g'(0)}{(1+\delta\theta)} \qquad (24)$$

$$\mathrm{Nu}_x = \frac{-x\left\{k(T) + \frac{16\sigma^* T_\infty^3}{3a^*}\right\}\left(\frac{\partial T}{\partial z}\right)_{z=0}}{k_\infty(T_W - T_\infty)} = -\mathrm{Re}_x^{\frac{1}{2}}(1 + \varepsilon + \frac{4}{3Rd})\theta'(0) \qquad (25)$$

$$\mathrm{Sh}_x = \frac{-xD_m\left(\frac{\partial C}{\partial z}\right)_{z=0}}{D_m(C_w - C_\infty)} = -\mathrm{Re}_x^{1/2}\phi'(0) \qquad (26)$$

3. Numerical method for solution

The system of ordinary differential equations Eqs. (18)–(21) subject to the boundary conditions Eqs. (22a) and (22b) is turned into a system of first-order ordinary differential equations and then solved using MATLAB's built-in solver bvp4c (Shampine et al. [37]) with some initial guesses to yield numerical results. The process is shown below:

– Assume:

$$f = y_1\,, \quad f' = y_2\,, \quad f'' = y_3\,, \quad g = y_4\,, \quad ,g' = y_5\,, \qquad (27)$$
$$\theta = y_6\,, \quad \theta' = y_7\,, \quad \phi = y_8\,, \quad \phi' = y_9\,.$$

– Using Eq. (27) in the Eqs. (18)–(21), the following systems of first-order equations are obtained:

$$y_1' = y_2 \qquad (28)$$

$$y_2' = y_3 \qquad (29)$$

$$y_3' = (1+\delta y_6)\left[s\left(y_2 + \frac{\eta}{2}y_3\right) - \frac{1}{2}y_2^2 + y_1y_3 + 2y_4^2 + \frac{\delta}{(1+\delta y_6)^2}y_7y_3 + 2\mathrm{Ri}(y_6 + Ny_8) + My_2\right], \qquad (30)$$

$$y_3' = (1+\delta y_6)\left[s\left(y_2 + \frac{\eta}{2}y_3\right) - \frac{1}{2}y_2^2 + y_1y_3 + 2y_4^2 + \frac{\delta}{(1+\delta y_6)^2}y_7y_3 + 2\mathrm{Ri}(y_6 + Ny_8) + My_2\right], \qquad (30)$$

$$y_4' = y_5\,, \tag{31}$$

$$y_5' = (1+\delta y_6)\left[s\left(y_4+\frac{\eta}{2}y_5\right) - y_2y_4 + y_1y_5 + \frac{\delta}{(1+\delta y_6)^2}y_7y_5 + My_4\right], \tag{32}$$

$$y_6' = y_7\,, \tag{33}$$

$$y_7' = \frac{3Rd\mathrm{Pr}}{3Rd(1+\varepsilon y(6)-\mathrm{PrSrScDu})+4}\left[2s(y_6-\mathrm{DuScy}_8)+\frac{\eta s}{2}(y_7-\mathrm{DuScy}_9)+\frac{1}{2}y_2(\mathrm{DuScy}_8-y_6)+y_1(y_7-\mathrm{DuScy}_9)-\frac{1}{\mathrm{Pr}}\varepsilon {y_7}^2-\frac{\mathrm{Ec}}{1+\delta y_6}\left(\frac{1}{4}{y_3}^2+{y_5}^2\right)\right], \tag{34}$$

$$y_8' = y_9\,, \tag{35}$$

$$y_9' = \mathrm{Sc}\left[s\left(\frac{\eta}{2}y_9+2y_8\right)-\frac{1}{2}y_2y_8+y_1y_9\right]-\mathrm{ScSr}\left[\frac{3Rd\mathrm{Pr}}{3Rd(1+\varepsilon y(6)-\mathrm{PrSrScDu})+4}\left\{2s(y_6-\mathrm{DuScy}_8)+\frac{\eta s}{2}(y_7-\mathrm{DuScy}_9)+\frac{1}{2}y_2(\mathrm{DuScy}_8-y_6)+y_1(y_7-\mathrm{DuScy}_9)-\frac{1}{\mathrm{Pr}}\varepsilon {y_7}^2-\frac{\mathrm{Ec}}{1+\delta y_6}\left(\frac{1}{4}{y_3}^2+{y_5}^2\right)\right\}\right] \tag{36}$$

with boundary conditions:

– at η =0:

$$y_1 = f_w\,,\quad y_2 = 0,\quad y_4 = 1,\quad y_8 = 1, \tag{37a}$$

– as $\eta \to \infty$:

$$y_2 = 0,\quad y_4 = 0,\quad y_6 = 0,\quad y_8 = 0. \tag{37b}$$

4. Results and discussion

The outcomes are analysed using numerical computations for a variety of parameter values. In order to facilitate the investigation, the values assigned to Pr and Sc are taken into consideration for an electrically conducting fluid, namely metal ammonia suspensions (Pr = 0.78), contaminated by water vapour (Sc = 0.6). All the displayed figures are plotted for the fixed value of the parameter unless stated otherwise: Ri = 1; M = 1; N = 1; δ = –0.3; η = 0.1; Pr = 0.78; ε = 0.3; Rd = 0.2; Ec = 0.01; Du = 0.3; Sc = 0.6; Sr = 0.5; f_w = 0.1; s = 1.

Upon considering the steady state flow s = 0, and under the absence of Ri, Rd, Ec, Sr, Du and at constant wall temperature with constant δ and ε, the current results are compared to the previous results obtained by Sparrow and Cess [3], Chamkha and Rashad [15] as shown in Fig. 2, in order to determine the numerical method's reliability. Table 1 also shows a comparison of numerical values of heat transfer rate $-\theta'(0)$ by taking varying values of Pr, Ri with those obtained in the study conducted by Chamkha and Rashad [15] and Malik et al. [30]. Thus, the results plotted in Fig. 2 and the numerical data presented in Table 2 show that the results obtained using the current method are accurate and hence justify the reliability of the study conducted.

The outcomes of the ascending viscosity parameter δ are sketched in Figs. 3–6. As the fluid becomes more viscous the resistance to flow increments and thus the tangential and azimuthal velocities of the fluid are found to decrease; but an opposite trend on the tangential velocity of the fluid near the conical surface is also important to note in the current study. From Fig. 3 it is detected that the tangential velocity experiences a significant rise within the region $0 \le \eta < 1.7$ which then continues to deplete beyond $\eta > 1.7$. Hence it can be deduced that δ generates an escalation in the tangential velocity near the conical surface while producing a drop in velocity towards the edge of the boundary layer. The tangential and azimuthal skin friction improves by about 8.9% and 8.3%, respectively, when δ varies from –0.3 to –0.2 (see Table 2). Furthermore, as the viscosity of the fluid increases the interactions between particles decrease, and hence the temperature and solutal profiles gradually decay (see Fig. 5, Fig. 6), which weakens the thermal and solutal boundary layer thickness. The heat and mass transfer rates undergo growth by about 0.3% each when δ varies from –0.3 to –0.2 (see Table 2).

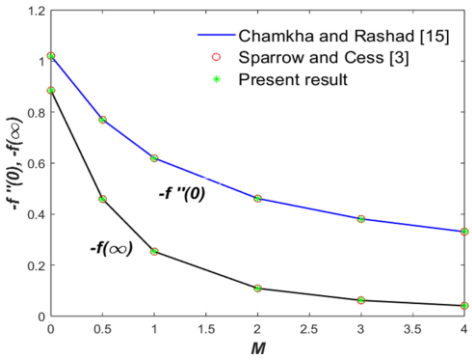

Fig. 2(a). Numerical results obtained for $-f''(0)$ and $-f(\infty)$ are compared for ascending values of M.

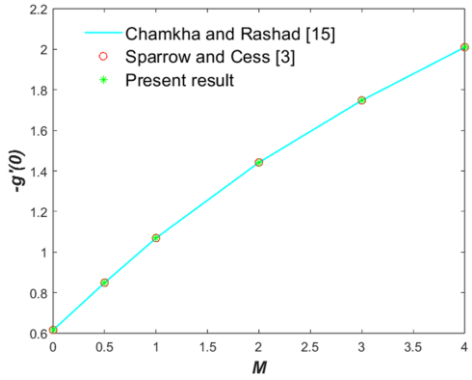

Fig. 2(b). Numerical results obtained for $-g'(0)$ are compared for ascending values of M.

Table 1. Numerical values of $-\theta'(0)$ compared for varying Pr, Ri.

Pr	Present Result			Malik et al. [30]			Chamkha and Rashad [15]		
	Ri			Ri			Ri		
	0	1	10	0	1	10	0	1	10
0.7	0.4291	0.6120	1.0173	0.4295	0.6121	1.0097	0.4299	0.6120	1.0097
10	1.4083	1.6076	2.3535	1.4110	1.5660	2.3581	1.4110	1.5662	2.3580

Table 2. Numerical values for the tangential $-f''(0)$ and azimuthal skin frictions $-g'(0)$, heat transfer rate $-\theta'(0)$ and the mass transfer rate $-\phi'(0)$.

δ	M	ε	Pr	Rd	Ec	Du	Sr	Sc	s	$-f''(0)$	$-g'(0)$	$-\theta'(0)$	$-\varphi'(0)$
–0.3	1	0.3	0.78	0.2	0.01	0.3	0.5	0.6	1	1.69556	1.22616	0.45051	1.10591
–0.2										1.84638	1.32767	0.45164	1.10969
	1.5									1.59682	1.33891	0.44650	1.09859
		0.5								1.69779	1.22684	0.44348	1.10728
			1							1.67406	1.21989	0.50553	1.09636
				0.4						1.64781	1.21217	0.57606	1.08379
					0.1					1.69701	1.22662	0.44200	1.10799
						0.5				1.69985	1.22747	0.43568	1.10894
							0.7			1.69949	1.22661	0.45107	1.09271
								1		1.64238	1.22090	0.44055	1.39664
									1.5	1.52572	1.31805	0.53074	1.30816

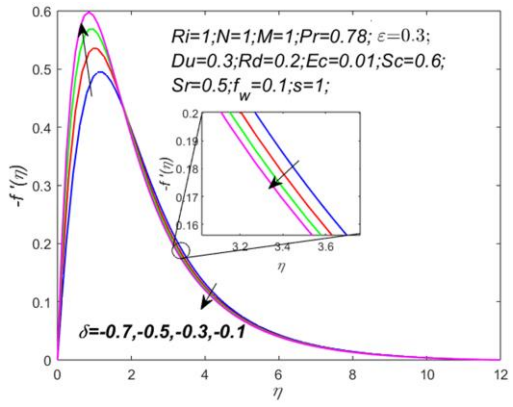

Fig. 3. $-f'(\eta)$ profiles for ascending δ.

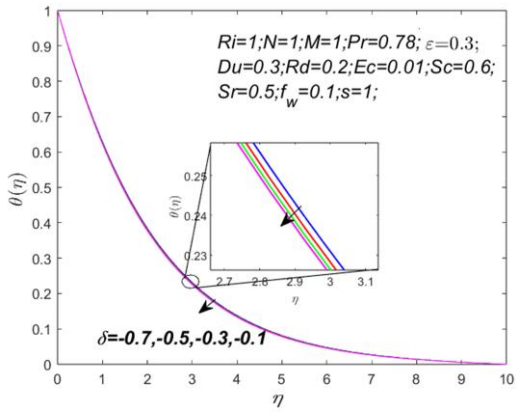

Fig. 5. $\theta(\eta)$ profiles for varying δ.

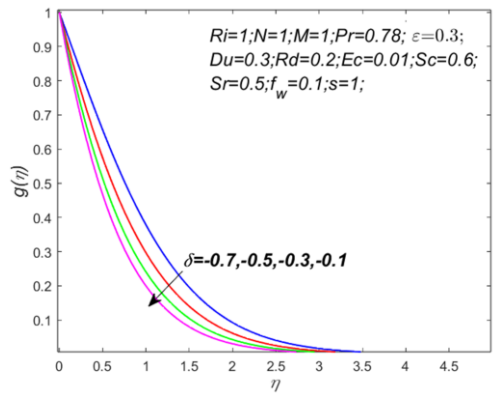

Fig. 4. $g(\eta)$ profiles for ascending δ.

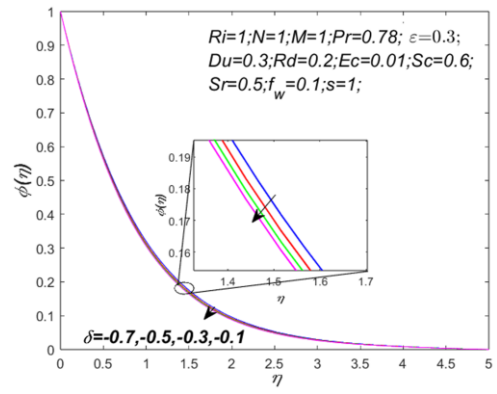

Fig. 6. $\phi(\eta)$ profiles for ascending δ.

Figures 7–8 exemplify that as the magnetic parameter M surges, the tangential and azimuthal velocities of the fluid decrease drastically. These results are due to the existence of Lorentz force which is a resistive force that occurs in the azimuthal direction when an electrically conducting fluid is exposed to a transverse magnetic field. Hence, the motion of the fluid is retarded by this force. Consequently, from Table 2 a draining effect on the tangential skin friction, heat, and mass transfer rates by about 5.8%, 0.9%, and 0.7%, respectively, is observed, while the azimuthal skin friction improves up to 9.2% when M is increased from 1.0 to 1.5.

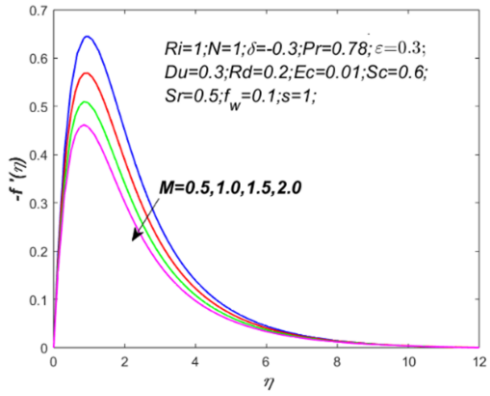

Fig. 7. $-f'(\eta)$ profiles for ascending M.

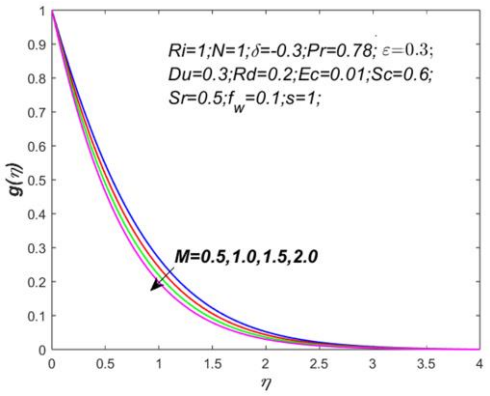

Fig. 8. $g(\eta)$ profiles for ascending M.

Figure 9 gives an estimation of the effect of ascending Prandtl number Pr accounted for air (0.72), electrolytic solution (1.00), water (7.00), and water at 4°C (11.40) on the temperature profile. In the figure, a decreasing trend in the temperature profile is observed. This result can be justified by the fact that higher Pr denotes lower thermal diffusivity, and thus the higher the fluid's Pr value the lower the temperature. From Table 2 it can be concluded that the tangential and azimuthal skin frictions along with the mass transfer rate diminish by about 1.3%, 0.5% and 0.9%, respectively, while the heat transit rate goes up to 12.2% when Pr varies from 0.78 and 1.00. Hence according to the results obtained, it can be said that fluids with lower Pr have higher thermal conductivities, allowing heat to flow more efficiently from the surface of the cone than fluids with higher. Thus, the cooling rate in the conducting fluid can be influenced by Pr.

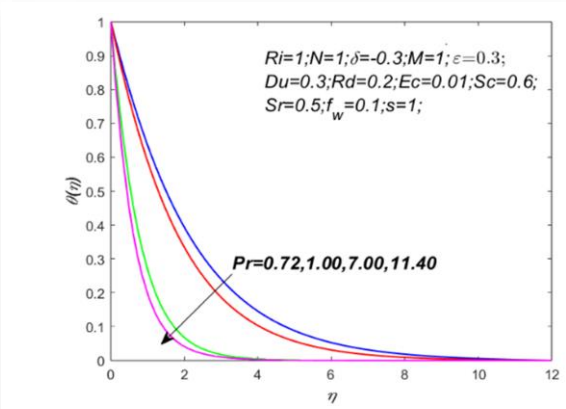

Fig. 9. $\theta(\eta)$ profiles for ascending Pr.

Figures 10–11 are plotted to depict the influence of temperature dependent thermal conductivity ε on the tangential velocity and temperature. Thermal conductivity improves the tangential velocity of the fluid and the ability to conduct heat increments which eventually improve the thermal boundary layer thickness.

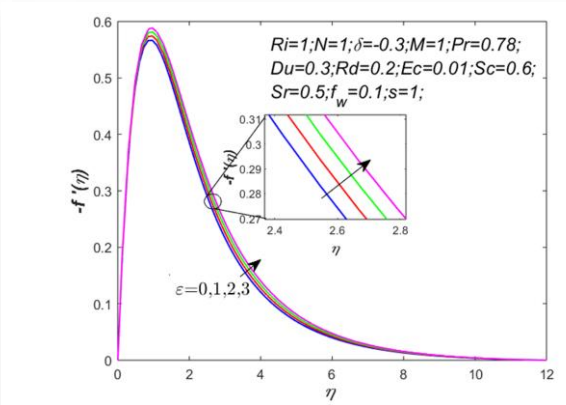

Fig. 10. $-f'(\eta)$ profiles for ascending ε.

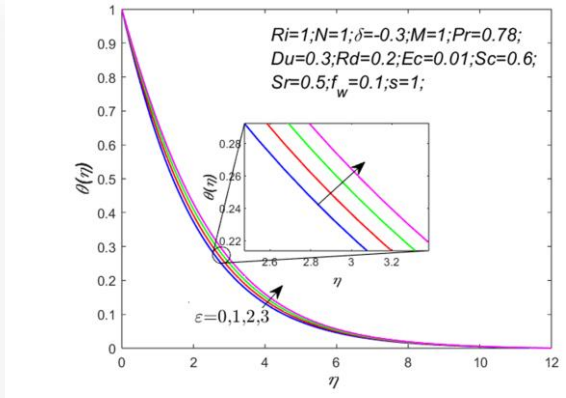

Fig. 11. $\theta(\eta)$ profiles for ascending ε.

From the result plotted in Fig. 10, it can also be deduced that the tangential velocity of the fluid near the conical surface re-

mains unaffected by ascending values of ε but gradually grows at a distance away from the conical surface. The tangential skin friction is found to undergo a growth up to 0.1% while the heat transfer rate degrades by about 1.6%; for ε varying from 0.3 to 0.5 (see Table 2).

The effect of Eckert (Ec) number on the tangential velocity and temperature profiles is presented in Figures 12–13. The Ec number is directly related to kinetic energy; increasing Ec directly leads to enhancement of the fluid's kinetic energy which consequently leads to the improvement of the fluid's tangential velocity and thickening of the thermal boundary layer. Moreover, from Fig. 12 it can be concluded that at the region near the conical surface, the effect of ascending Ec is equivalent to zero, however at a certain range of about $\eta > 0.5$ the change in pattern on the tangential velocity can be detected. According to findings reported in Table 2, varying Ec from 0.01 to 0.10 causes the heat transfer rate to be reduced by about 1.9%.

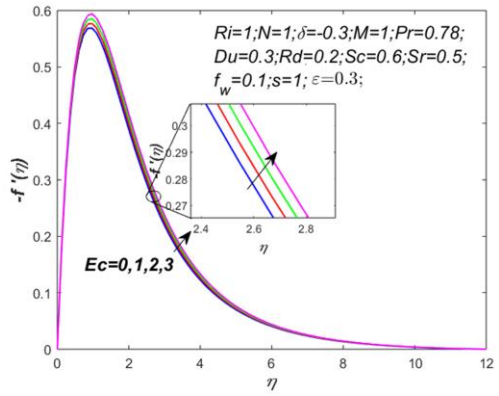

Fig. 12. $-f'(\eta)$ profiles for ascending Ec.

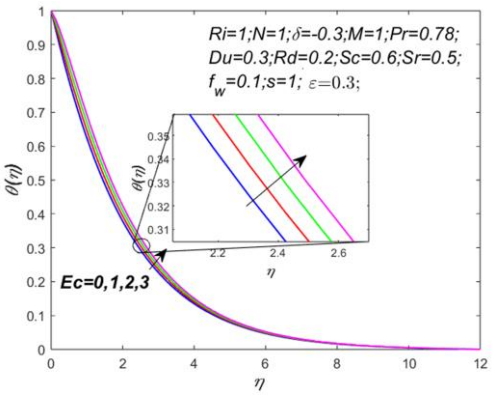

Fig. 13. $\theta(\eta)$ profiles for ascending Ec.

Figure 14 gives an illustration of the tangential velocity distribution of the fluid for ascending values of both the Soret (Sr) and Dufour (Du) numbers. As the temperature and mass flux in the fluid continuously increase, the tangential velocity profile is also found to be consequently increased. An illustration of the effect of Du on the temperature profile is found in Fig. 15; according to the illustration, the temperature profile undergoes a certain boost as Du increases. This is because at the boundary flow region, the kinematic viscosity starts to decrease as Du increases and thus the fluid's kinetic energy improves which consequently leads to the acceleration of the fluid and enhancement of the temperature profile. The influence of ascending Sr on the solutal profile is plotted in Fig. 16. The figure depicts that the solutal profile undergoes growth as Sr improves. This is because a higher Sr corresponds to a higher temperature gradient which consequently leads to higher convective flow and thus results in thickening of the concentration boundary layer.

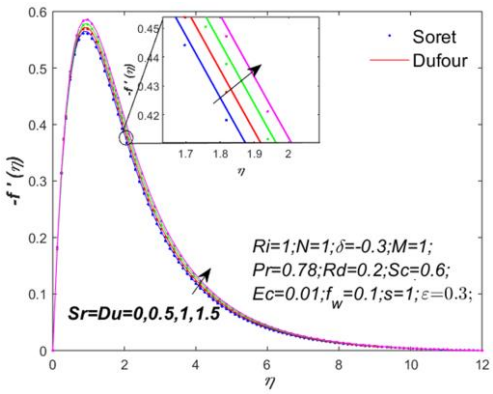

Fig. 14. $-f'(\eta)$ profiles for ascending Du, Sr.

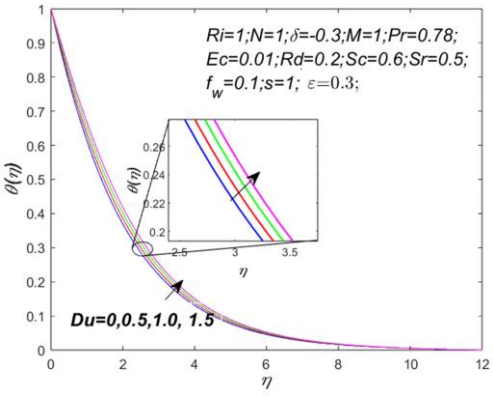

Fig. 15. $\theta(\eta)$ profiles for ascending Du.

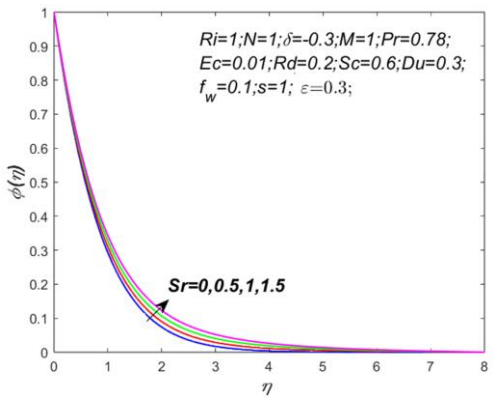

Fig. 16. $\phi(\eta)$ profiles for ascending Sr.

According to results shown in Table 2, it is certain that higher Du inflicts around a 3.3% drop in the heat transfer rate and higher Sr inflicts around a 1.2% drop in the mass transfer rate within the range of $0.3 \le Du \le 0.5$ and $0.5 \le Sr \le 0.7$.

Figure 17 gives an estimated graph showing the influence of ascending Schmidt (Sc) number plotted for hydrogen (0.22), water vapour (0.62), ammonia at 25°C (0.78), and CO_2 at 25°C (1.00). It is determined that the decline in concentration becomes more substantial for heavier species. This decrease in the solutal profile is further supported by the fact that Sc and species diffusivity are inversely related to each other. Thus, higher Sc implies lower species diffusivity, which consequently leads to depletion of the solutal profile. Results in Table 2 show that as Sc enhances from 0.6 to 1.0, the mass transfer rate improves up to 26.3% and deteriorates the tangential skin friction and the heat transfer rate around 3.2%, and 2.2%, respectively. Hence, the greater the mass transfer rate, the lower the fluid concentration boundary layer.

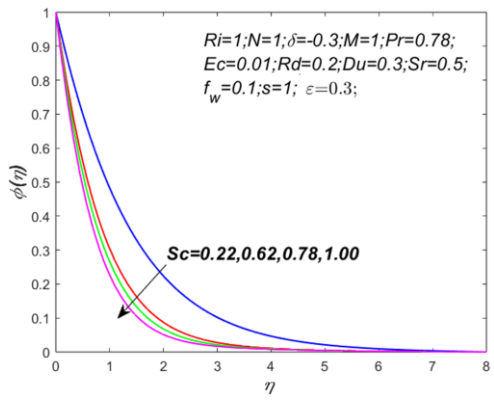

Fig. 17. $\phi(\eta)$ profiles for ascending Sc.

Results are presented for the tangential velocity, temperature, and solutal profiles in Figs. 18–20 for the ascending unsteady parameter s.

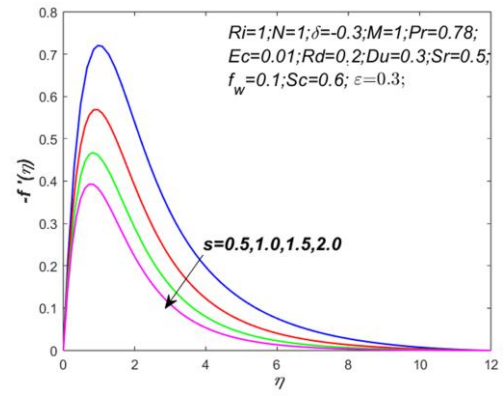

Fig. 18. $-f'(\eta)$ profiles for ascending s.

It is certain from the figures that ascending s leads to the decrement of the tangential velocity as well as the temperature and solutal profiles. Thus, it can be deduced that the rate of cooling becomes much faster in unsteady state flow as compared to those in steady flow. Also, mass transfer takes place at a slower pace in unsteady flows as compared to steady flows.

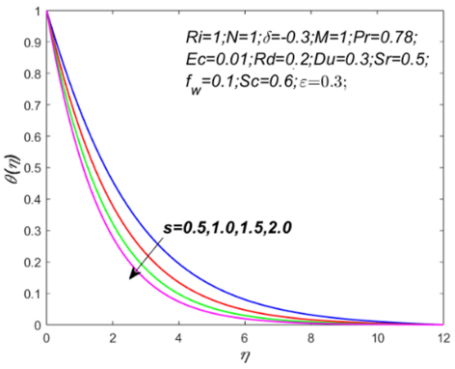

Fig. 19. $\theta(\eta)$ profiles for ascending s.

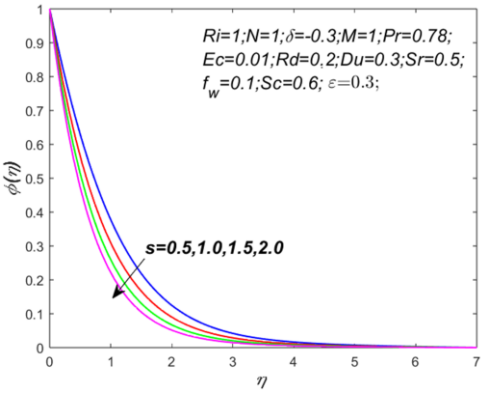

Fig. 20. $\phi(\eta)$ profiles for ascending s.

According to Table 2, it can be established that the tangential skin friction decreases significantly by about 10%, while leading to enhancement in the azimuthal skin friction, heat, and mass transfer rates by a significant percentage up to 7.5%, 17.8%, and 18.3%, respectively, as s varies from 1 to 1.5.

5. Conclusions

The study has been conducted to understand and numerically analyze the effects of the temperature dependent viscosity and thermal conductivity, viscous dissipation, and the Soret and Dufour effects on the boundary layers for the unsteady permeable rotating cone. The following are some of the conclusions that can be made regarding the problem under consideration:

The viscosity parameter δ has an opposite effect on the tangential velocity $-f'(\eta)$, i.e. near the surface of the cone the tangential velocity $-f'(\eta)$ increases, and away from the conical surface, the tangential velocity $-f'(\eta)$ decreases.

The growth of viscosity parameter δ reduces the azimuthal velocity $g(\eta)$, temperature $\theta(\eta)$ and concentration $\phi(\eta)$ profiles.

In the presence of a magnetic field, the Lorentz force acts to reduce the tangential velocity $-f'(\eta)$ and the azimuthal velocity $g(\eta)$ profiles.

With the growth in thermal conductivity ε and Eckert number Ec, the profiles of the tangential velocity $-f'(\eta)$ and the azimuthal velocity $\theta(\eta)$ grow. The increase in Dufour Du and Soret Sr numbers lead to growth of the temperature $\theta(\eta)$ and concentration $\phi(\eta)$ profiles, respectively.

If the viscosity parameter δ changes from −0.3 to −0.2 then the magnitude of the tangential skin friction $-f''(0)$ and the azimuthal skin friction $-g(0)$ increase up to 8.9% and 8.3% each. Similarly, if the unsteady parameter s increases to 1.5 from 1, then the azimuthal skin friction $-g'(0)$, the heat transfer rate $-\theta'(0)$ and the mass transfer rate $-\phi'(0)$ show 7.5%, 17.8% and 18.3% hikes, respectively.

The increment of thermal conductivity ε and Eckert number Ec from 0.3 to 0.5 and 0.01 to 0.1, respectively, causes a 1.6% and 1.9% drop in the heat transfer rate $-\theta'(0)$.

Varying Dufour Du and Soret Sr from 0.3 to 0.5 and 0.5 to 0.7, respectively, causes 3.3% and 1.2% drop-in the heat transfer rate $-\theta'(0)$ and the mass transfer rate $-\phi'(0)$. It is intended that the physics of flow across the permeable rotating cone may be used as the foundation for various engineering and scientific applications using our current model. Also, as a motivator for future experimental work, which appears to be missing now.

References

[1] Tien, C.L., & Tsuji, I.J. (1965). A theoretical analysis of laminar forced flow and heat transfer about a rotating cone. *Journal of Heat Transfer*, 87(2), 184–190. doi: 10.1115/1.3689069

[2] Hering, R.G., & Grosh, R.J. (1962). Laminar free convection from a non-isothermal cone. International Journal of Heat and Mass Transfer, 5(11), 1059–1068. doi: 10.1016/0017-9310(62)90059-5

[3] Sparrow, E.M., & Cess, R.D. (1962). Magnetohydrodynamic flow heat transfer about rotating disk. *Journal of Applied Mechanics*, 29, 181–187.

[4] Chamkha, A.J. (1996). Non-darcy hydromagnetic free convection from a cone and a wedge in porous media. *International Communications in Heat and Mass Transfer*, 23(6), 875–887. doi: 10.1016/0735-1933(96)00070-X

[5] Takhar, H.S., Chamkha, A.J., & Nath, G. (2003). Unsteady mixed convection flow from a rotating vertical cone with a magnetic field. *Heat and Mass Transfer*, 39, 297–304. doi: 10.1007/s00231-002-0400-1

[6] Ece, M. C. (1992). The initial boundary-layer flow past a translating and spinning rotational symmetric body. *Journal of Engineering Mathematics*, 26, 415–428. Doi: 10.1007/BF00042743

[7] Chamkha, A.J., & Al-mudhaf, A. (2005). Unsteady heat and mass transfer from a rotating vertical cone with a magnetic field and heat generation or absorption effects. *International Journal of Thermal Sciences*, 44, 267–276. doi: 10.1016/j.ijthermalsci.2004.06.005

[8] Anilkumar, D., & Roy, S. (2004). Unsteady mixed convection flow on a rotating cone in a rotating fluid. *Applied Mathematics and Computation*, 155(2), 545–561. doi: 10.1016/S0096-3003(03)00799-9

[9] Gorla, R.S.R., Chamkha, A.J., & Rashad, A.M. (2010). Mixed convective boundary layer flow over a vertical wedge embedded in a porous medium saturated with a nanofluid. *3rd International Conference on Thermal Issues in Emerging Technologies, Theory and Applications, Proceedings, ThETA3 2010*, 6(207), 445–451. doi: 10.1109/THETA.2010.5766429

[10] Reddy, M.G., Rani, M.V.V.N.L.S., Kumar, K.G., & Prasannakumara, B.C. (2018). Cattaneo–Christov heat flux and non-uniform heat-source/sink impacts on radiative Oldroyd-B two-phase flow across a cone/wedge. *Journal of the Brazilian Society of Mechanical Sciences and Engineering*, 40(2). doi: 10.1007/s40430-018-1033-8

[11] Gnaneswara Reddy, M., Padma, P., & Sudha Rani, M.V.V.N.L. (2019). Non-linear thermal radiative analysis on hydromagnetic nanofluid transport through a rotating cone. *International Journal of Applied and Computational Mathematics*, 5(3). doi: 10.1007/s40819-019-0654-7

[12] Saleem, S. (2021). Heat and Mass Transfer of Rotational Flow of Unsteady Third-Grade Fluid over a Rotating Cone with Buoyancy Effects. *Mathematical Problems in Engineering*, 2021. doi: 10.1155/2021/5544540

[13] Shah, Z., Alzahrani, E., Jawad, M., & Khan, U. (2020). Microstructure and Inertial Characteristics of MHD Suspended SWCNTs and MWCNTs Based Maxwell Nanofluid Flow with Bio-Convection and Entropy Generation Past a Permeable Vertical Cone. *Coatings*, 10(10), 998. doi: 10.3390/coatings10100998

[14] Krishna, M.V., Ahammad, N.A., & Chamkha, A.J. (2021). Radiative MHD flow of Casson hybrid nanofluid over an infinite exponentially accelerated vertical porous surface. *Case Studies in Thermal Engineering*, 27(7), 101229. doi: 10.1016/j.csite.2021.101229

[15] Chamkha, A.J., & Rashad, A.M. (2013). Unsteady Heat and Mass Transfer by MHD Mixed Convection Flow From a Rotating Vertical Cone With Chemical Reaction and Soret and Dufour Effects. *The Canadian Journal of Chemical Engineering*, 99, 991–10. doi: 10.1002/cjce.21894

[16] Krishna, M.V., Swarnalathamma, B.V., & Chamkha, A.J. (2019). Investigations of Soret, Joule and Hall effects on MHD rotating mixed convective flow past an infinite vertical porous plate. *Journal of Ocean Engineering and Science*, 4(3), 263–275. doi: 10.1016/j.joes.2019.05.002

[17] Yasir, M., Khan, M., & Malik, Z.U. (2023). Analysis of thermophoretic particle deposition with Soret-Dufour in a flow of fluid exhibit relaxation/retardation times effect. *International Communications in Heat and Mass Transfer*, 141, 106577. doi: 10.1016/j.icheatmasstransfer.2022.106577

[18] Gnaneswara Reddy, M. (2018). Cattaneo-Christov heat flux effect on hydromagnetic radiative Oldroyd-B liquid flow across a cone/wedge in the presence of cross-diffusion. *European Physical Journal Plus*, 133(24). doi: 10.1140/epjp/i2018-11844-0

[19] Saleem, S., Firdous, H., Nadeem, S., & Khan, A.U. (2019). Convective Heat and Mass Transfer in Magneto Walter's B Nanofluid Flow Induced by a Rotating Cone. *Arabian Journal for Science and Engineering*, 44(2), 1515–1523. doi: 10.1007/s13369-018-3598-z

[20] Nadeem, S., Khan, M.N., & Abbas, N. (2020). Transportation of slip effects on nanomaterial micropolar fluid flow over exponentially stretching. *Alexandria Engineering Journal*, 59(5), 3443−3450. doi: 10.1016/j.aej.2020.05.024

[21] Khan, S.A., Hayat, T., Khan, M.I., & Alsaedi, A. (2020). Salient features of Dufour and Soret effect in radiative MHD flow of viscous fluid by a rotating cone with entropy generation. *International Journal of Hydrogen Energy*, 45(28), 14552–14564. doi: 10.1016/j.ijhydene.2020.03.123

[22] Ghoneim, N.I., Reddy, M.G., & Megahed, A.M. (2021). Numerical solution for natural convection fluid flow along a vertical cone with variable diffusivity and wall heat and mass fluxes embedded in a porous medium. *International Journal of Modern Physics C*, 32(06), 2150074. doi: 10.1142/S0129183121500741

[23] Abd El-Aziz, M. (2007). Temperature dependent viscosity and thermal conductivity effects on combined heat and mass transfer in MHD three-dimensional flow over a stretching surface with Ohmic heating. *Meccanica*, 42(4), 375–386. doi: 10.1007/s11012-006-9051-5

[24] Lai, F.C., & Kulacki, F.A. (1990). The effect of variable viscosity on convective heat transfer along a vertical surface in a saturated porous medium. *International Journal of Heat and Mass Transfer*, 33(5), 1028–1031. doi: 10.1016/0017-9310(90)90084-8

[25] Prasad, K.V., Vajravelu, K., & Datti, P.S. (2010). The effects of variable fluid properties on the hydro-magnetic flow and heat transfer over a non-linearly stretching sheet. *International Journal of Thermal Sciences*, 49(3), 603–610. doi: 10.1016/j.ijthermalsci.2009.08.005

[26] Mukhopadhyay, S. (2009). Unsteady boundary layer flow and heat transfer past a porous stretching sheet in presence of variable viscosity and thermal diffusivity. *International Journal of Heat and Mass Transfer*, 52(21–22), 5213–5217. doi: 10.1016/j.ijheatmasstransfer.2009.04.013

[27] Khan, M.N., Nadeem, S., & Muhammad, N. (2020). Micropolar fluid flow with temperature-dependent transport properties. *Heat Transfer*, 49(4), 2375–2389. doi: 10.1002/htj.21726

[28] Khan, M.N., & Nadeem, S. (2021). A comparative study between linear and exponential stretching sheet with double stratification of a rotating Maxwell nanofluid flow. *Surfaces and Interfaces*, 22, 100886. doi: 10.1016/j.surfin.2020.100886

[29] Ahmad, S., Khan, M.N., & Nadeem, S. (2022). Unsteady three dimensional bioconvective flow of Maxwell nanofluid over an exponentially stretching sheet with variable thermal conductivity and chemical reaction. *International Journal of Ambient Energy*, 43(1), 6542–6552. doi: 10.1080/01430750.2022.2029765

[30] Malik, M.Y., Jamil, H., Salahuddin, T., Bilal, S., Rehman, K.U., & Mustafa, Z. (2016). Mixed convection dissipative viscous fluid flow over a rotating cone by way of variable viscosity and thermal conductivity. *Results in Physics*, 6, 1126–1135. doi: 10.1016/j.rinp.2016.11.027

[31] Sambath, P., Sankar, D.S., & Vishwanathan, K.K. (2020). A numerical study of dissipative chemically reactive radiative MHD flow past a vertical cone with non-uniform mass flux. *International Journal of Applied Mechanics and Engineering*, 25(1), 159–176. doi: 10.2478/ijame-2020-0011

[32] Ragulkumar, E., Palani, G., Sambath, P., & Chamkha, A.J. (2023). Dissipative MHD free convective nanofluid flow past a vertical cone under radiative chemical reaction with mass flux. *Scientific Reports*, 13(1), 1–13. doi: 10.1038/s41598-023-28702-0

[33] Khan, S.A., Hayat, T., & Alsaedi, A. (2022). Thermal conductivity performance for ternary hybrid nanomaterial subject to entropy generation. *Energy Reports*, 8, 9997–10005. doi: 10.1016/j.egyr.2022.07.149

[34] Beg, O.A., Ghosh, S., & Bég, T. (2011). *Applied Magnetofluid Dynamics: Modelling and Computation* (1st ed.). LAP Lambert Academic Publishing.

[35] Brewster, M.Q. (1992). *Thermal Radiative Transfer and Properties*. John Wiley & Sons Ltd. New York.

[36] Schlichting, H., & Gersten, K. (2017). *Boundary-Layer Theory*. (9th ed.). Springer Berlin Heidelberg. doi: 10.1007/978-3-662-52919-5

[37] Shampine, L., Kierzenka, J., & Reichelt, M. (2000). Solving boundary value problems for ordinary differential equations in MATLAB with bvp4c. *Tutorial Notes*, 75, 2751–27. https://classes.engineering.wustl.edu/che512/bvp_paper.pdf [accessed 14 Nov. 2023].

Co-published by
Institute of Fluid-Flow Machinery
Polish Academy of Sciences
Committee on Thermodynamics and Combustion
Polish Academy of Sciences

http://www.imp.gda.pl/archives-of-thermodynamics/

Waste plastic oil as an alternative fuel: A review

Amardeep[a, b*], Rakesh Kumar[b], Naveen Kumar[c]

[a]Indian Institute of Technology (ISM), Dhanbad, 826004, India
[b]G L Bajaj Institute of Technology and Management, Greater Noida,201306, India
[c]Delhi Technological University, Delhi, 110042, India
*Corresponding author email: amardce2012@gmail.com

Received: 19.07.2023; revised: 20.12.2023; accepted: 19.01.2024

Abstract

Today, with the high population density of the world, the energy demand is increasing continuously. Global dependency on fossil fuels is very strong and there is a compelling need to reduce our energy consumption in order to offset greenhouse gas emissions. Due to regularly increasing prices of fossil fuels alternative fuels are needed to fulfill the requirements of developing countries like India. Plastics in today's world have become crucial. They are excessively used in industry, as well as in households and other fields due to their lightweight, durability, and design flexibility. Plastic demand is growing day by day, which now poses a huge environmental threat. The current study summarizes the use of WPO (waste plastic oil) in the diesel engine and also concludes the combustion, performance, and emission parameters. After an exhaustive literature search, some interesting results have been found. The study reveals that when using WPO as an alternative source in a diesel engine, the combustion, performance, and emissions are similar to those using conventional diesel fuel. An enhanced BTE (brake thermal efficiency) and reduced emissions of unburned hydrocarbons (UBHC) and carbon monoxide (CO) are reported.

Keywords: Waste plastic oil; Diesel engine; Performance; Emissions and combustion

Vol. 45(2024), No. 1, 87–97; doi: 10.24425/ather.2024.150441

Cite this manuscript as: Amardeep, Kumar, R., & Kumar N. (2024). Waste plastic oil as an alternative fuel: A review. *Archives of Thermodynamics*, 45(1), 87–97.

1. Introduction

Plastic manufacturing has expanded from 15 million tonnes in 1964 to 311 million tonnes in 2014 and is expected to quadruple again in the next 20 years, with plastics increasingly servicing various applications [1]. Plastic packaging has always been and will remain the major use, and packaging actually accounts for 26% of the overall amount of plastics used. Not only does plastic packaging have direct economic benefits, but it can also lead to improved resource production levels [2].

In India, 1.2 kg/year, per capita plastic waste was generated during 2016–2017 while in 2019–2020 it was 2.5 kg/year, per capita plastic waste generated. It is observed that over the last five years (2016–2020) per capita plastic waste has almost doubled. In 2019–2020, Delhi, Goa and Kerala produced the highest

Nomenclature

Abbreviations and Acronyms

BMEP – brake mean effective pressure
BP – brake power
BSFC – brake specific fuel consumption
BTE – brake thermal efficiency
EGT – exhaust gas temperature
HDPE – high-density polyethylene
HC – hydrocarbons
HRR – heat removal rate
IDP – ignition delay period
LDPE – low-density polyethylene
PP – polypropylene
PPO – plastic pyrolysis oil
PS – polystyrene
PET – polyethylene terephthalate
SFC – specific fuel consumption
UBHC – unburned hydrocarbons
WPO – waste plastic oil

amount of plastic waste per capita while Sikkim, Nagaland and Tripura produced the lowest per capita plastic waste [3]. But in the financial year 2020–2021, Maharashtra generated 443,724 metric tons of waste plastic which is the highest among all the states in India. [4]. As per the CPCB (Central Pollution Control Board) report (2019–20), only 50% of plastic waste is recycled [5]. In India, the plastics market is estimated to be over 8 million tonnes per year. Over 10 000 metric tonnes of plastic each day are manufactured in India, and India imports almost the same amount from most other countries. In India, individuals consume approximately 3 kg of plastic per capita, which is significantly lower compared to developed countries where the per capita plastic intake ranges from 30 kg to 40 kg. Most of them come from the food and packaging industry. Most plastics are recycled. However, this is often not possible because due to a lack of adequate demand control about 43% of non-recycled plastic waste is polyethylene, coming mostly from containers and packaging [6]. Considerable attention was paid to the development of biodiesel as an option to petro-diesel due to concerns about the supply of recoverable fossil fuel supplies and the environmental issues created by the use of these fossil fuels [7]. In order to turn it into liquid fuel to solve the problem of liquid fossil energy depletion, pyrolysis of plastic waste has now been attracting considerable interest from researchers. Studies began with the investigations of the properties of liquid fuel derived from various types of plastics. Plastics are among the most frequently used materials in our everyday lives and contribute greatly to society. They are commonly used in the wrapping and processing of items such as electronics, vehicles, etc. The deterioration of organic waste paper takes 1–3 weeks, and 8–10 weeks for cotton fabric, but it would take a million years for plastic to degrade. Plastics are lightweight and can be shaped simply. They expose non-corrosive behavior. The scenario of plastic waste thermal conversion into liquid fuel has indeed been applied to the combining of different forms of plastics. Two types of plastics are primarily available. The results from either the plastic pyrolysis mixture showed that the liquid produced was less than the individual plastic pyrolysis in contrast.

2. Waste plastic to oil conversion

The process of converting waste plastic into oil involves utilizing techniques like pyrolysis, catalytic cracking, and hydrothermal liquefaction. These methods utilize controlled heat and pressure to break down the complex polymer structures of plastic into smaller hydrocarbon molecules. By addressing the issue of plastic waste accumulation, this conversion process holds the potential to yield both environmental and energy benefits. On the other hand, challenges related to consistent feedstock quality, process optimization, and effective management of byproducts need to be overcome through ongoing research and technological advancements to ensure the efficiency, environmental sustainability, and economic feasibility of this promising alternative solution.

From Fig. 1 it is shown that the oil extraction journey from waste plastics begins with the collection of waste plastics from

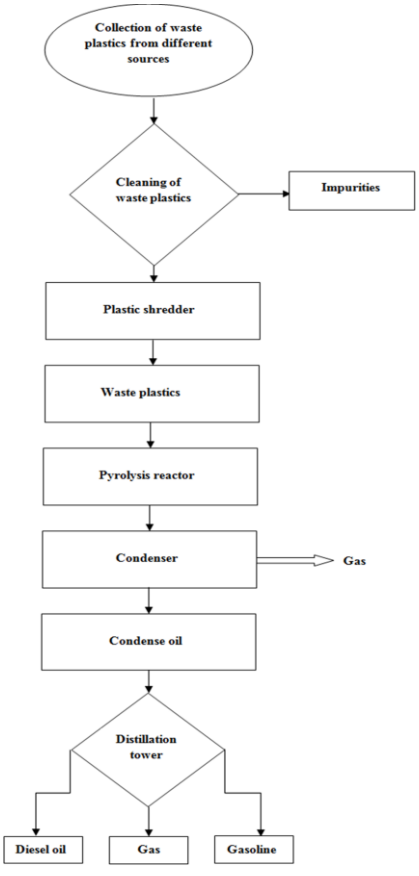

Fig. 1. Flow processes of waste plastic into oil.

diverse sources, such as rivers households, industries, and commercial establishments [8]. The World Bank reports that plastics constitute approximately 5% to 12% of the total global waste generation, which is around 20% to 30% of the waste's total weight [9]. After gathering waste plastics from various origins, it is essential to separate the waste plastics from any additional impurities and materials [10]. Once cleaned, the waste plastics are directed to a plastic shredder. This mechanical apparatus breaks down the plastics into smaller, consistent pieces. Pyrolysis has achieved significant acceptance as a technique that predominantly produces liquid products known as bio-oil. This process also produces char, a solid by-product, as well as a gas. The nature and composition of these liquid and solid products are influenced by the pyrolysis operational circumstances [11]. Dehydration, decarboxylation, and dehydrogenation occur during the initial stage. But in the latter phases, a high-molecular-weight thermal cracking compound occurs, resulting in char and gaseous products such as CO_2 (carbon dioxide), CO (carbon monoxide) and CH_4 (methane) [12].

Plastic waste pyrolysis has emerged as a promising and sustainable solution to address the growing global issue of plastic waste management. Anthony and his colleagues, in their study [13] highlighted the escalating demand for plastic products and the challenges associated with plastic waste disposal. In response, they proposed plastic pyrolysis as an innovative approach to not only manage plastic waste effectively but also harness its potential by converting it into valuable plastic pyrolysis oil. The research compared the technical and economic aspects of substituting diesel oil in diesel engines with WPO and found that it holds substantial promise as a viable alternative. The financial benefits of such a project are substantial, with the potential to significantly boost the economy. Cross et al. [14] highlighted the significance of interdisciplinary collaboration, underlining the need for a strong, cohesive team with a solid engineering foundation. Their project provided valuable practical experience and insights into managing complex tasks.

Mathur et al. [15] emphasized the influence of plastic grades on the pyrolysis process. They conducted pyrolysis using Grade 5 plastic materials (polypropylene) and obtained 1.65 liters of oil from 1.5 kg of plastic waste. This observation underscores the importance of carefully selecting plastic types and grades to optimize oil production, shedding light on the significance of choosing appropriate materials for efficient pyrolysis. Bouaphengphanh et al. [16] delved into the pyrolysis process, exploring the impact of temperature and extraction duration. They found that the process's starting temperature and duration significantly affect oil yields. Among various plastic types, HDPE (High-density polyethylene) emerged as the most productive, achieving approximately 88% conversion, and producing oil that closely resembled diesel. In contrast, PET (Polyethylene terephthalate) failed to yield oil, highlighting variations in plastic behavior during pyrolysis. Desai et al. [17] focused on the environmental and energy benefits of converting plastic waste into synthesis gas emphasizing the potential to mitigate environmental hazards associated with plastic waste and generate components for creating new products.

Chavan et al. [18] investigation into thermal pyrolysis highlighted its efficiency, cleanliness, and effectiveness in dealing with plastic waste. Polypropylene and polystyrene were identified as top oil producers, while PET offered high gasoline yields. This process effectively addressed the dual challenges of managing plastic waste and mitigating fuel shortages by converting plastics into a valuable fuel source. Santaweesuk et. al [19] underscored the importance of precise temperature, time, and energy control in pyrolysis. This ensured controlled and less reactive processes while employing waste plastics to derive WPO using both conventional pyrolysis and distillation methods. Patni et al. [20] conducted an experiment to address key challenges in plastic waste pyrolysis. Their endeavors emphasized the need to scale up the process, minimize waste handling costs, and reduce production costs. With the right infrastructure and financial support, large quantities of plastic waste could be efficiently converted into viable alternatives to fossil fuels. Jha et al. [21] demonstrated the effectiveness of catalytic pyrolysis in converting various plastic waste types into clean fuel, significantly reducing carbon emissions and environmental burdens. Srinivas et al. [22] confirmed that pyrolysis effectively converts waste plastic into valuable fuel, addressing the problem of plastic waste and its environmental impact. Fivga et al. [23] assessed the technical and economic viability of plastic waste pyrolysis, highlighting its fuel energy efficiency and self-sufficiency in thermal energy. Sensitivity analyses were conducted to determine the impact of waste disposal charges on fuel production costs, emphasizing the cost-effectiveness and environmental benefits of utilizing plastic waste for sustainable fuel production. Medrano et al. [24] explored the potential of mechanical material separation processes before pyrolysis to enhance the efficiency and quality of pyrolysis oil production from diverse plastic waste streams. Sharuddin et al. [25] highlighted the flexibility and adaptability of the pyrolysis process in converting substantial energy from plastic waste into valuable products, making it a practical solution for plastic waste management. Chiwara et al. [26] successfully designed a laboratory-scale pyrolysis unit for converting plastic solid waste into pyrolysis oil, achieving optimal process throughput. Tahir et al. [27] conducted experiments aimed at optimizing the production of liquid fuel through pyrolysis. Their study emphasized the crucial correlation between temperature variations and the resulting quality of liquid fuel products. Walendziewski et al. [28] explored the impact of temperature on the pyrolysis process and the efficiency of thermal and catalytic cracking. Higher temperatures were found to increase conversion rates and gasoline fraction production, and the use of cracking catalysts improved the process's overall efficiency.

In conclusion, plastic waste pyrolysis has gained considerable attention as a sustainable solution for plastic waste management and the production of valuable resources. These studies collectively emphasize the potential of this technology to not only address environmental challenges but also provide economic and energy benefits. Through precise control of process parameters, careful material selection, and innovative approaches, plastic waste pyrolysis holds the promise of mitigating

the negative environmental impacts of plastic waste while offering solutions to energy and economic challenges.

3. Physical properties of extracted oil from waste plastics

The physical characteristics of liquid oil generated from different plastic waste types can vary significantly, impacting their suitability for various applications and necessitating tailored processing and treatment approaches.

3.1. Density

Density is a crucial parameter that quantifies the relationship between an object's mass and its known volume. Calculating density holds significant importance in various applications, especially in the context of fuel and engine performance. A higher fuel density can significantly impact engine performance, while a lower density can contribute to the rapid evaporation of oil. In either scenario, there exists the potential for severe damage to the engine [29]. Figure 2 presents data illustrating the density values of various waste plastic oil samples in comparison to diesel fuel. Specifically, the density of LDPE (Low-density polyethylene) is measured at 0.778 g/cm³, whereas PE (Polyethylene) bags and diesel fuel exhibit densities of 0.854 g/cm³ and 0.838 g/cm³, respectively [30].

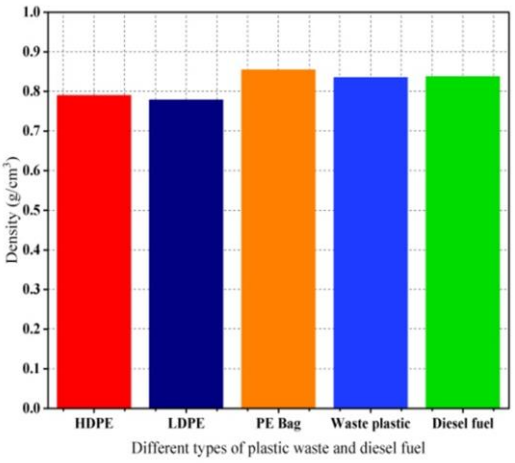

Fig. 2. Density of liquid oil produced from different types of plastic waste.

3.2. Kinematic viscosity

The kinematic viscosity of bio-oil is conventionally assessed at a temperature of 40°C as a means of gauging its fluidity characteristics. This viscosity measurement plays a crucial role in assessing the stability of liquid fuel while it is in storage [31].

Figure 3 provides a visual representation of the kinematic viscosity values for converted waste plastic oils and diesel fuel. Specifically, diesel fuel exhibits a kinematic viscosity of 3.37×10^{-6} m^2/s, whereas PP (Polypropylene), HDPE (High-density polyethylene), and PS (Polystyrene) show kinematic viscosities of 2.27×10^{-6} m^2/s, 1.63×10^{-6} m^2/s and 1.1×10^{-6} m^2/s, respectively [32].

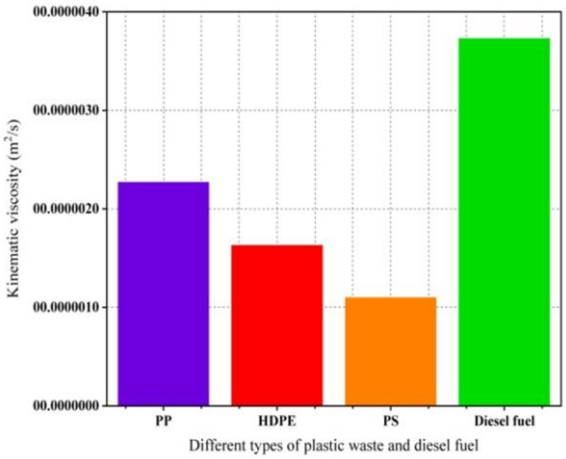

Fig. 3. Kinematic viscosity of liquid oil produced from different types of plastic waste.

3.3. Higher heating value (HHV)

The heating value of a fuel can be expressed in two ways: the higher heating value (HHV), also known as the gross calorific value, and the lower heating value (LHV), or net calorific value. The HHV signifies the heat liberated during fuel combustion when both the original water and the water produced during combustion are in a condensed state [33].

Figure 4 illustrates a comparative analysis of the higher heating values between diesel fuel and various waste plastic oils. Specifically, the HHV for diesel fuel is measured at 46.67 MJ/kg, whereas waste plastic oils such as LDPE, PE bags, tires, and mixed plastic exhibit HHV values of 38.45 MJ/kg, 41.45 MJ/kg, 43.22 MJ/kg, and 44.4 MJ/kg, respectively [34].

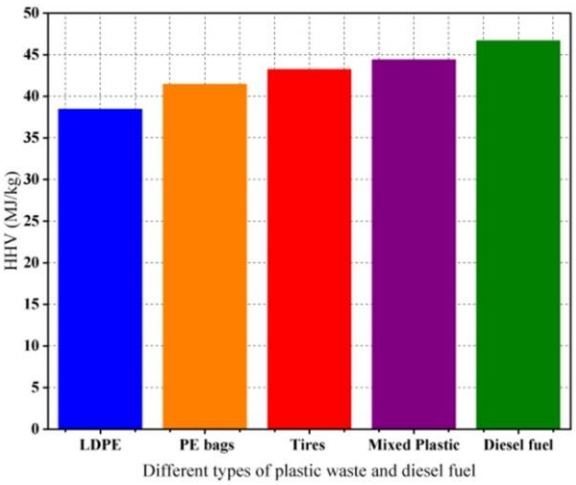

Fig. 4. Higher heating values of liquid oil produced from different types of plastic waste.

3.4. Viscosity

Viscosity is a property that undergoes fluctuations based on factors like feedstock, pyrolysis conditions, temperature, and various other variables.

It is worth noting that as viscosity increases, fuel consumption, engine temperature, and the overall engine workload tend to rise as well. Conversely, if the oil's viscosity becomes excessively high, it can lead to undesirable consequences such as heightened friction within the system [35]. The viscosity measurement for LDPE has been determined to be 1.73 mm²/s, which is notably lower than the viscosities of all the other fuels depicted in Fig. 5.

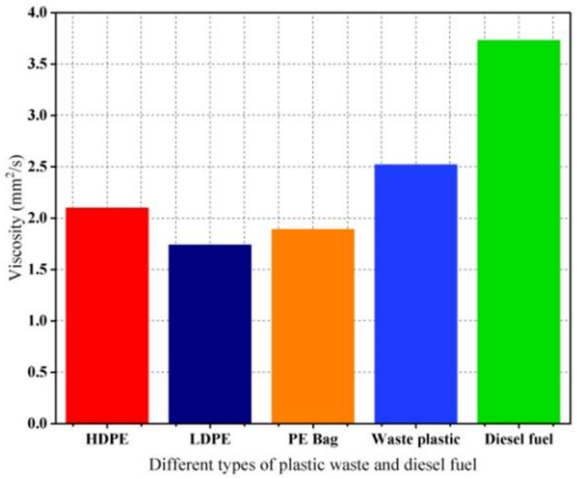

Fig. 5. Viscosity of liquid oil produced from different types of plastic waste.

3.5. Flash point

The flash point is defined as the minimum temperature at which a fuel can ignite. To assess the flash point of petroleum and related products, the Indian standard IS1448, P20 is commonly employed. Typically, any flash point measurement below 60°C is indicative of the substance's combustibility [29].

Figure 6 provides a clear depiction of the flash points for various waste plastic oils and diesel fuel. Specifically, the flash points for PVC (Polyvinyl chloride), HDPE, and diesel fuel are recorded at 40°C, 48°C, and 52°C, respectively [36].

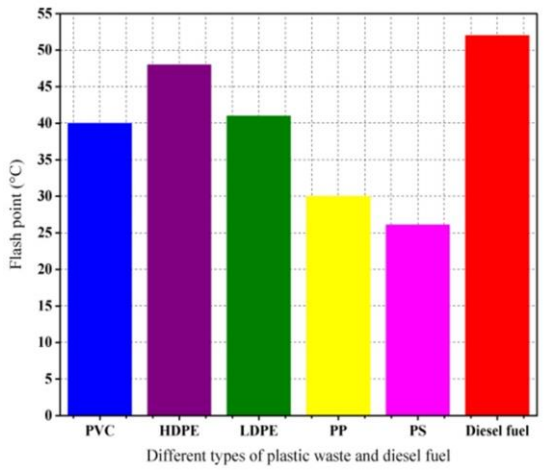

Fig. 6. Flash point of liquid oil produced from different types of plastic waste.

3.6. Pour point

The pour point is defined as the temperature at which oil no longer flows when cooled at a standardized rate within a prescribed apparatus. This parameter is critical in assessing the suitability of oil for use in low-temperature environments and applications [35].

The pour points of PP, HDPE and PS are < –45°C, –15°C and –67°C, respectively, as shown in Fig. 7. Lower value of the pour point shows that the fuel is not suitable in cold weather areas [36].

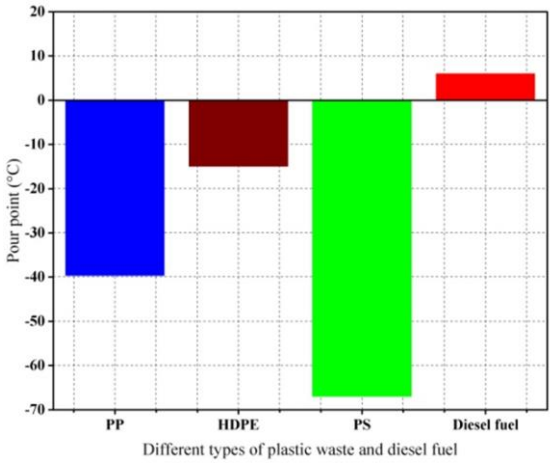

Fig. 7. Pour point of liquid oil produced from different types of plastic waste.

3.7. Ash content

The ash content in oil refers to the noncombustible residue it contains. From Fig. 8 it is clear that the ash content of LDPE is much higher than for other extracted waste plastic oil and diesel.

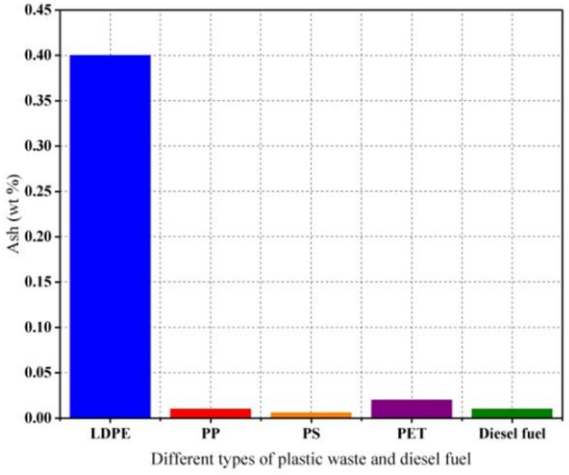

Fig. 8. Ash content of liquid oil produced from different types of plastic waste.

3.8. Water content

Water content in waste plastic oil hampers its fuel efficiency by disrupting combustion, lowering energy output, and raising emissions. It corrodes equipment, forms clogging sludge, reduces energy density, causes ignition issues, and affects stability. Proper handling and treatment are essential to enhance the utility of waste plastic oil as a fuel.

Figure 9 clearly shows that the PS and PET have the highest water content as compared to other extracted plastic waste oil and diesel fuel. The water content of PS, PET and diesel fuel is 0.67 ppm, 0.57 ppm and 0.05 ppm, respectively [32, 34, 36].

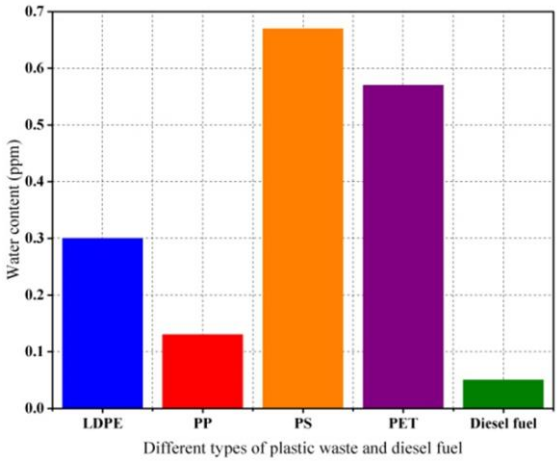

Fig. 9. Water content of liquid oil produced from different types of plastic waste.

4. Diesel engine fuelled with waste plastic oil

The utilization of waste plastic oil (WPO) as an alternative fuel source for diesel engines represents a groundbreaking innovation with substantial environmental benefits. This approach not only mitigates plastic waste but also maximizes the use of existing diesel engine infrastructure. The process of converting waste plastics into usable fuel not only aligns with sustainability efforts but also holds the potential to reduce fuel costs significantly. Table 1 compiles a selection of research studies that delve into the application of waste plastic oil in diesel engines. These investigations scrutinize various facets of engine performance, emissions, and fuel properties when integrating WPO as a fuel source. The collective findings underscore the promise of WPO as a greener fuel alternative, emphasizing its role in plastic waste reduction and the enhancement of engine efficiency.

The studies included in Table 1 collectively demonstrate a growing interest in the utilization of waste plastic oil as a sustainable alternative fuel for diesel engines. These research endeavors reveal that WPO derived from various plastic sources through different conversion methods can be effectively incorporated into diesel engines, offering notable benefits such as improved brake thermal efficiency, reduced emissions of carbon

Table 1. Studies on the utilization of waste plastic oil (WPO) in diesel engines.

Authors	Findings	Ref.
Janarthanan et al.	Diesel engine running on plastic pyrolysis-derived fuel, 6% improvement in brake thermal efficiency (BTE), reduced emissions of unburned hydrocarbons (UBHC) and CO emission.	[37]
Churkunti et al.	In-cylinder temperatures increase during high loads, while nitrogen oxides decrease with diesel content. Variations occur due to the pyrolysis method and the plastic type.	[38]
Singh et al.	Plastic pyrolysis oil (PPO) combustion with delayed ignition and high in-cylinder pressure. Oxygen in PPO reduces emissions. Up to 50% PPO blend effective with slight CO increase.	[39]
Maithomklang et al.	WPO is not favourable for direct use in diesel engines, suggested as a blend component. WPO has a lower soot oxidation temperature, promoting sustainability.	[40]
Peng et al.	Catalysts offer benefits over thermal cracking in fuel production, but more upgrading is needed. Techno-economic evaluation conducted for commercial viability.	[41]
Chowdhury et al.	The review highlights challenges in biomass conversion using pyrolysis and emphasizes the need for complete energy and material balances.	[42]
Naima et al.	The engine runs efficiently on 100% WPO with a slightly longer ignition delay. Oil derived from waste engine oil is suitable as fuel for diesel engines.	[43]
Mani et al.	WPO results in higher cylinder peak pressure and efficient combustion, but increased NOx emissions. Higher hydrocarbon levels with more fuel.	[44]
Harshal et al.	Waste plastic pyrolysis oil is a viable substitute for diesel engines, with significantly higher thermal efficiency. Promising and efficient fuel option.	[45]
Ghorpade et al.	Blends with up to 50% WPO effective, but higher percentages lead to engine issues and increased emissions.	[46]
Anup et al.	WPO demonstrates higher thermal efficiency and lower UHBC emissions but a 5% increase in CO emissions compared to diesel.	[47]
Saleem et al.	Investigation into using microwave technology to extract oil from plastic waste for efficient energy and material resource production.	[48]
Sasikumar et al.	Focus on the pyrolysis process for mixed plastic waste, offering a holistic and sustainable approach to waste management and recycling.	[49]
Bockhorn et al.	Exposure of polypropylene to fractional pyrolysis at varying temperatures alters product composition, influencing reaction mechanisms.	[50]
Nakhate et al.	Successful experiments using plastic waste to produce plastic oil, with a potential for distillation to enhance properties.	[51]
Miandad et al.	Catalytic pyrolysis with modified natural zeolite catalysts enhances liquid oil production from plastic waste.	[52]

Table 2. Studies on pyrolysis of waste plastics and its environmental impact.

Authors	Findings	Ref.
Shah et al.	Gasification and pyrolysis compared to incineration, with environmental and efficiency benefits. Challenges with product gas removal and CO emissions.	[53]
Wongkhorsub et al.	Plastic pyrolysis oil effectively replaces diesel but results in slightly lower engine performance. Oil quality is linked to desulfurization cost.	[54]
Khan et al.	Thermal pyrolysis of mixed plastic offers a cost-effective method for resource recovery with minimal char production.	[35]
Miandad et al.	Pyrolysis produces valuable liquid oil and char, influenced by factors like temperature, retention time, feedstock, and catalysts.	[55]
Ibrahim et al.	Pyrolysis has applications in carbon dating, thermal cleaning, refining, and petrochemical industries for gasoline and aromatic compound production.	[56]
Fahmy et al.	Combining solar pyrolysis with hydrogen production as an environmentally friendly approach for the future.	[57]
Verma et al.	Pyrolysis process, its products, and efforts to upgrade bio-oil for various practical uses.	[58]
Xun Hu et al.	Summary of bio-oil production through slow, fast, and catalytic pyrolysis techniques, with a focus on the reaction pathway.	[59]
Yansaneh et al.	Extensive interest and research efforts in thermal and catalytic pyrolysis of plastic waste, highlighting its potential for waste management.	[60]
Bridgwater et al.	Fast pyrolysis as a technology for liquid fuel production and the challenges of upgrading the produced liquids for various applications.	[61]
Li et al.	Bio-pyrolysis liquefaction technology and its adaptability, rapid reaction rates, and conversion efficiency.	[62]
Pandey et al.	Pyrolysis as an efficient method for recovering monomers or pyrolysis liquid from plastic waste, influenced by factors such as catalysts and temperature.	[63]
Uzochukwu et al.	Pyrolysis as an environmentally friendly method for plastic waste disposal and resource recovery.	[64]
Miandad et al.	Factors influencing the efficiency of catalytic pyrolysis; highlighting the potential of catalysts to improve product quality.	[65]
Oasmaa et al.	The need for REACH (Registration, Evaluation, Authorisation and Restriction of Chemicals) registration of pyrolysis liquid and the importance of ensuring positive sustainability impacts.	[66]
Papuga et al.	Growing academic and industrial interest in pyrolysis, particularly catalytic pyrolysis, and its potential for plastic waste management.	[67]
Xayachak et al.	Experiment evaluating the cetane number of oil produced through pyrolysis of plastic waste, showing potential as an alternative fuel.	[68]
Sasikumar et al.	An investigation into technologies and operational conditions for the recovery of plastic waste, emphasizing the role of operating temperature.	[69]

monoxide (CO) and unburned hydrocarbons (UHBC), and the potential for lower fuel costs. Notably, the use of catalysts in the pyrolysis process and the blending of WPO with diesel have been identified as methods to enhance combustion efficiency and address some of the challenges associated with direct WPO utilization.

Table 2 compiles a selection of research studies focusing on the pyrolysis of waste plastics and its environmental consequences. Pyrolysis, a thermal degradation process, has gained prominence as a promising approach to address the burgeoning challenge of plastic waste management. The studies presented here investigate various aspects of pyrolysis, including the use of different catalysts, feedstocks, and reaction conditions, and delve into the subsequent environmental implications. As the world grapples with mounting concerns related to plastic pollution, understanding the effects of plastic pyrolysis on emissions, energy recovery, and the fate of by-products is essential. The studies assembled in Table 2 collectively underscore the significance of pyrolysis as a viable technology for transforming plastic waste into valuable resources while also addressing environmental concerns. From investigating the influence of catalysts to assessing the composition of pyrolysis products, these studies offer valuable insights into the optimization of pyrolysis processes. Furthermore, an improved understanding of emissions, energy recovery, and the potential uses of by-products plays a pivotal role in enhancing the sustainability of this waste management approach. As the world seeks sustainable solutions to the plastic waste crisis, these studies provide a foundation for informed decision-making and further research endeavors in the field of pyrolysis technology.

In Table 3, we present an overview of studies focused on the operation of diesel engines using waste plastic oil and various blends with conventional diesel fuels. These studies investigate a range of parameters, including engine performance, emissions, and combustion characteristics. The use of WPO and its blends in diesel engines is a compelling area of research, offering potential environmental and economic advantages. This table summarizes key findings and trends from the selected studies, providing valuable insights into the utilization of WPO and its impact on engine operation.

The amalgamation of findings across various research papers (Table 3) reveals consistent patterns and certain notable inconsistencies. The bulk of the research suggests a notable enhancement in brake thermal efficiency (BTE) when WPO is blended with conventional diesel fuel. However, when it comes to the trends in carbon monoxide emissions, the literature paints a less clear picture. Some studies demonstrate a decrease in CO emissions, but, conversely, the majority reports an increase.

Similarly, the in-cylinder pressure results exhibit variability and lack a fixed pattern across these studies. Regarding emissions parameters, there is a consistent trend of increased levels

Table 3. Brief of diesel engine operated with waste plastic oil and blends; BSFC – brake specified fuel consumption, BTE – brake thermal efficiency, CD – combustion duration, SFC – specific fuel consumption , HRR – heat removal rate, EGT – exhaust gas temperature, IDP – ignition delay period.

Used engine specification	Combustion and performance parameters	Emission parameters	Ref.
Single cylinder, 4-stroke, water-cooled, variable speed 1500-180 rpm, with a fuel injection pressure of 220 bar.	BTE (↓), SFC (↑), HRR (↑), EGT (↓), IDP (↑)	NO (↑), smoke (↓), CO_2 (↑)	[70]
Single cylinder, 4-stroke, Common Rail, Bosch CP4.1, direct injection, with a fuel injection pressure of 180 MPa.	In-cylinder pressure (↓), HRR (↑)	CO (↑), HC (↑)	[71]
Single cylinder, 4 strokes DI, air-cooled diesel engine @constant speed, with an injection time of 23°CA bTDC and injection pressure of 21 MPa	BTE (↑), BSFC (↓), In-cylinder pressure (↑), HRR (↑)	smoke (↑), CO (↑), NOx (↑), HC (↑)	[72]
Kirloskar TV1, water-cooled, 1500rpm constant speed, 5.2 kW, single cylinder, 661.45 CC with a compression ratio of 17.5:1	In-cylinder pressure (↓), IDP (↓), CD (↑), HRR (↑), BTE (↑)	NOx (↑), CO (↑), HC (↑),	[73]
Kirloskar, 240 PE, VCR, Single Cylinder and 4-stroke Engine, Water-cooled, 3.5 kW at 1500 rpm, with Displacement Volume 661 CC.	BP (↑), BTE (↑), BMEP (↑)	CO (↓), CO_2 (↑), NOx (↑)	[74]
Single cylinder, 4 S, Diesel Engine, Kirloskar, model: TV1, 1500 rpm constant speed, with 5.2 kW rated power	IDP (↑), BTE (↑), SFC (↓), HRR (↓) BTE (↑)	NOx (↑), CO (↑), CO2 (↑)	[75]
4 cylinder in-lines T/C, DI, rated power 70 kW, CR 17.5:1, with injection timing 12°CA bTDC and Nozzle opening pressure 23 MPa.	In-cylinder pressure (↑), BSFC (↓), BTE (↑) HRR (↑)	CO(↑), NOx (↑)	[76]
4-stroke, CI, air-cooled, single-cylinder, constant-speed diesel engine.	BTE (↓)	CO_2 (↑), NOx (↓), CO (↓)	[77]
AKSA, 4 cylinder, Diesel engine, constant RPM@ 1500, Rated power 68 kW.	IDP (↑), HRR (↑), BTE (↓)	CO_2 (↑), NOx (↑), CO (↑)	[78]

of nitrogen oxides, hydrocarbons, and various other emissions constituents when waste plastic oil is introduced into diesel engines. These findings collectively provide valuable insights into the complex interplay between WPO and diesel engines, shedding light on performance enhancements, emissions variations, and the need for further research to optimize this eco-friendly fuel source.

6. Conclusions

Overall, after the exhaustive literature, it is found that fuel from plastic pyrolysis has the potential to be a viable alternative to conventional diesel fuel, with improvements in engine performance and reduced emissions. However, further studies are needed to explore the long-term effects of using pyrolysis fuel, as well as to optimize the pyrolysis process for commercial application. Some findings are listed below.

- The utilization of waste plastic oil (WPO) in diesel engines shows promising results, with improvements in BTE (brake thermal efficiency) and reductions in UBHC (unburned hydrocarbons) and CO emissions.
- The characteristics of plastic pyrolysis oil (PPO) have been analyzed, and the compound analysis confirms the presence of alkanes and aromatic components.
- Different types of plastics yield varying amounts and qualities of pyrolysis oil, with HDPE (high-density polyethylene) and PS (polystyrene) showing higher oil yields compared to other types.
- The use of catalysts in pyrolysis processes, such as zeolites and base catalysts, offers advantages over thermal cracking, but further upgrading is needed for commercial application.
- Pyrolysis presents a viable remedy for the management of waste plastic as it converts plastic waste into valuable liquid oil and gas fuels, reducing environmental pollution.
- The direct use of waste plastic oil in diesel engines may require blending with diesel fuel to reduce engine performance issues but blends up to 50% have shown promise.
- The pyrolysis process can produce oil, gas, and char, which can be used in various applications, such as energy production and environmental remediation.
- The pyrolysis process is influenced by factors such as temperature, feedstock composition, catalysts, and reaction time, which affect the quality and quantity of the products.
- Pyrolysis technology requires optimization in terms of energy efficiency, waste handling costs, and production costs to make it economically viable and sustainable.
- Further research is needed to address challenges in scale-up, waste handling, and product quality as a waste management and fuel production technology.

References

[1] Ellen MacArthur Foundation. (2016). The New Plastics Economy. https://www3.weforum.org/docs/WEF_The_New_Plastics_Economy.pdf [accessed 8 Jan. 2023].

[2] Damodharan, D., Sathiyagnanam, A.P., Rana, D., Saravanan, S., Rajesh Kumar, B., & Sethuramasamyraja, B. (2018). Effective utilization of waste plastic oil in a direct injection diesel engine using high carbon alcohols as oxygenated additives for cleaner emissions. *Energy Conversion and Management*, 166, 81–97. doi: 10.1016/j.enconman.2018.04.006

[3] Central Pollution Control Board. (2019). Annual Report 2019-20. https://cpcb.nic.in/uploads/plasticwaste/Annual_Report_2019-20_PWM.pdf [accessed 8 Jan. 2023].

[4] Statista. (2022). (Statistical Report). https://www.statista.com/statistics/report-content/statistic/1168513 [accessed 8 Jan. 2023].

[5] India Today. (2022, October 27). Why plastic pollution continues unchecked in India. https://www.indiatoday.in/environment/story/why-plastic-pollution-continues-unchecked-in-india-2289887-2022-10-27 [accessed 8 Jan. 2023].

[6] Ahamed, A., Veksha, A., Yin, K., Weerachanchai, P., Giannis, A., & Lisak, G. (2020). Environmental impact assessment of converting flexible packaging plastic waste to pyrolysis oil and multi-walled carbon nanotubes. *Journal of Hazardous Materials*, 390, 121449. doi: 10.1016/j.jhazmat.2019.121449

[7] Baena-González, J., Santamaria-Echart, A., Aguirre, J.L., & González, S. (2020). Chemical recycling of plastic waste: Bitumen, solvents, and polystyrene from pyrolysis oil. *Waste Management*, 118, 139–149. doi: 10.1016/j.wasman.2020.08.035

[8] Schwarz, A.E., Ligthart, T.N., Boukris, E., & van Harmelen, T. (2019). Sources, transport, and accumulation of different types of plastic litter in aquatic environments: A review study. *Marine Pollution Bulletin*, 143, 92–100. doi: 10.1016/j.marpolbul.2019.04.029

[9] Kibria, M.G., Masuk, N.I., Safayet, R., Nguyen, H.C., & Mourshed, M. (2023). Plastic waste: Challenges and opportunities to mitigate pollution and effective management. *International Journal of Environmental Research*, 17, 20. doi: 10.1007/s41742-023-00507-z

[10] NetPLASMAK. Recycling Machinery (2023). Washing and separation systems. https://www.netplasmak.com/washing-and-separation-systems [accessed 12 Jan. 2023].

[11] Mohan, D., Pittman, C.U., & Steele, P.H. (2006). Pyrolysis of wood/biomass for bio-oil: A critical review. *Energy and Fuels*, 20, 848–889. doi: 10.1021/ef0502397

[12] Tripathi, M., Sahu, J.N., & Ganesan, P. (2016). Effect of process parameters on production of bio-char from biomass waste through pyrolysis: A review. *Renewable and Sustainable Energy Reviews*, 55, 467–481. doi: 10.1016/j.rser.2015.10.122

[13] Anthony, J., Nikhil Gopal, D., Gowda, M., & Sharma, A. (2019). A review paper on extraction of fuel from waste plastic by pyrolysis. *International Journal of Research and Analytical Reviews*, 6(1), 473–475. doi: 10.1016/j.rser.2023.113799

[14] Cross, J.P.M., Kumar, R.P., Rajan, R.P., Ali, M.J., & Joshua, R.C. (2018). Design and fabrication of extraction of fuel from waste plastic using pyrolysis. *International Journal of Advance Research and Innovative Ideas in Education*, 4(2), 1795–1799.

[15] Mathur, K., & Shubham, C. (2016). Extraction of pyrolysis oil from waste plastics. *International Research Journal of Engineering and Technology*, 3(4), 1649–1652.

[16] Bouaphengphanh, N., Savengsuksa, V., & Phonepaseuth, P. (2017). Oil extraction from plastic waste using pyrolysis process. International Conference on "The Conservation and Development", 23 November 2017 at Souphanouvong University, Luang Prabang, Lao PDR. doi: 10.13140/RG.2.2.12455.57764

[17] Desai, K.S., Shirodkar, R.R., Yerunkar, A.U. & Sinha, K. (2016). Crude oil extraction from waste plastic. *International Journal of Scientific Research*, 5(4), 625–627.

[18] Chavan, K.M. (2021). Extraction of fuel from plastic waste by pyrolysis treatment. *International Journal of Research in Engineering and Science*, 9(7), 4–10.

[19] Santaweesuk, C., & Janyalertadun, A. (2017). The production of fuel oil by conventional slow pyrolysis using plastic waste from a municipal landfill. *International Journal of Environmental Science and Development*, 8(3), 168–173. doi: 10.18178/ijesd.2017.8.3.941

[20] Patni, N., Shah, P., Agarwal, S., & Singhal, P. (2013). Alternate strategies for conversion of waste plastic to fuels. *International Scholarly Research Notices*, 902053. doi: 10.1155/2013/902053.

[21] Jha, K.K., & Kannan, M.T.K. (2020). Alternate fuel preparation in low cost from waste plastic. *Materials Today: Proceedings*, 37 Part 2, 3656–3657. doi: 10.1016/j.matpr.2020.09.802

[22] Srinivas, K.R., Kumawat, N.R., Gogoi, P.J., & Yadav, R.P.S. (2022). Extraction of bio-diesel from waste plastic through pyrolysis process. *International Journal of Engineering Research & Technology*, 10(10), 66–70.

[23] Fivga, A., & Dimitriou, I. (2018). Pyrolysis of plastic waste for production of heavy fuel substitute: A techno-economic assessment. *Energy*, 149, 865–874. doi: 10.1016/j.energy.2018.02.094

[24] Fulgencio-Medrano, L., García-Fernández, S., Asueta, A., Lopez-Urionabarrenechea, A., Perez-Martinez, B.B., & Arandes, J.M. (2022). Oil production by pyrolysis of real plastic waste. *Polymers*, 14(3), 553. doi: 10.3390/polym14030553

[25] Sharuddin, S.D.A., Abnisa, F., Daud, W.M.A.W., & Aruoa, M.K. (2018). Pyrolysis of plastic waste for liquid fuel production as prospective energy resource. *IOP Conference Series: Materials Science and Engineering*, 334, 01200. doi: 10.1088/1757-899X/334/1/012001

[26] Chiwara, B., Makhura, E., & Danha, G. (2017). Pyrolysis of plastic waste into fuel and other products. *Sixteenth International Waste Management and Landfill Symposium*, 2 – 6 October 2017, S. Margherita di Pula, Cagliari, Italy.

[27] Tahir, R., & Altway, A. (2019). Production of liquid fuel from plastic waste using integrated pyrolysis method with refinery distillation bubble cap plate column. *Energy Reports*, 5, 70–77. doi: 10.1016/j.egyr.2018.11.004

[28] Walendziewski, J. (2002). Engine fuel derived from waste plastics by thermal treatment. *Fuel*, 473–481. doi: 10.1016/S0016-2361(01)00118-1

[29] Kumar, S.L., Radjarejesri, S., & Raj Jawahar, R. (2020). Characterization of waste plastic oil as biodiesel in IC engines. *Materials Today: Proceedings*, 33(1), 833–838. doi: 10.1016/j.matpr.2020.06.272

[30] Sharma, B.K., Moser, B.R., Vermillion, K.E., Doll, K.M., & Rajagopalan, N. (2014). Production, characterization and fuel properties of alternative diesel fuel from pyrolysis of waste plastic grocery bags. *Fuel Processing Technology*, 122, 79–90. https://doi.org/10.1016/j.fuproc.2014.01.019.

[31] Adhikari, S., Nam, H., & Chakraborty, J.P. (2018). Chapt. 8 - Conversion of Solid Wastes to Fuels and Chemicals Through Pyrolysis, In: *Waste Biorefinery* (pp. 239–263). Elsevier. doi: 10.1016/B978-0-444-63992-9.00008-2

[32] Panda, A.K., Singh, R.K., & Mishra, D.K. (2010). Thermolysis of waste plastics to liquid fuel: A suitable method for plastic waste management and manufacture of value-added products - A world prospective. *Renewable and Sustainable Energy Reviews*, 14(1), 233–248. doi: 10.1016/j.rser.2009.07.005

[33] Sheng, C., & Azevedo, J.L.T. (2005). Estimating the higher heating value of biomass fuels from basic analysis data. *Biomass and Bioenergy*, 28(5), 499–507. doi: 10.1016/j.biombioe.2004.11.008

[34] Syamsiro, M., Saptoadi, H., Norsujianto, T., Noviasri, P., Cheng, S., Alimuddin, Z., et al. (2014). Fuel oil production from municipal plastic wastes in sequential pyrolysis and catalytic reforming reactors. *Energy Procedia*, 47, 180–188. doi: 10.1016/j.egypro.2014.01.212

[35] Khan, M.Z.H., Sultana, M., & Al-Mamun, M.R. (2016). Pyrolytic waste plastic oil and its diesel blend: fuel characterization. *Journal of Environmental and Public Health*, 7869080. doi: 10.1155/2016/7869080

[36] Mani, M., Nagarajan, G., & Sampath, S. (2011). Characterisation and effect of using waste plastic oil and diesel fuel blends in compression ignition engine. *Energy*, 36(1), 212–219. doi: 10.1016/j.energy.2010.10.049

[37] Janarthanan, K., & Sivanandi, P. (2022). Extraction and characterization of waste plastic pyrolysis oil for diesel engines. *Journal of Cleaner Production*, 366, 132924. doi: 10.1016/j.jclepro.2022.132924

[38] Churkunti, P.R., Mattson, J., Depcik, C., & Devlin, G. (2016). Combustion analysis of pyrolysis end of life plastic fuel blended with ultra-low sulfur diesel. *Fuel Processing Technology*, 142, 212–218. doi: 10.1016/j.fuproc.2015.10.021

[39] Singh, R.K., Ruj, B., Sadhukhan, A.K., Gupta, P., & Tigga, V.P. (2020). Waste plastic to pyrolytic oil and its utilization in CI engine: Performance analysis and combustion characteristics. *Fuel*, 262, 116539. doi: 10.1016/j.fuel.2019.116539

[40] Maithomklang, S., Wathakit, K., Sukjit, E., Sawatmongkhon, B., & Srisertpol, J. (2022). Utilizing waste plastic bottle-based pyrolysis oil as an alternative fuel. *ACS Omega*, 7(24), 20542–20555. doi: 10.1021/acsomega.1c07345.

[41] Peng, Y., Wang, Y., Ke, L., Dai, L., Wu, Q., Cobb, K., et al. (2022). A review on catalytic pyrolysis of plastic wastes to high-value products. *Energy Conversion and Management*, 254, 115243. doi: 10.1016/j.enconman.2022.115243

[42] Zaman, C.Z., Pal, K., Yehye, W.A., Sagadevan, S., Shah, S.T., Adebisi, G.A., et al. (2017). Pyrolysis: A sustainable way to generate energy from waste. In *Pyrolysis*, InTech Open. doi: 10.5772/intechopen.69036

[43] Naima, K., & Liazid, A. (2013). Waste oils as an alternative fuel for diesel engine. *Journal of Petroleum Technology and Alternative Fuels*, 4(3), 30–43. doi: 10.5897/JPTAF12.026

[44] Wongkhorsub, C., & Chindaprasert, N. (2013). A comparison of the use of pyrolysis oils in diesel engine. *Energy and Power Engineering*, 5(4B), 350–355. doi: 10.4236/epe.2013.54B068.

[45] Harshal, R.P., & Shailendra, M.L. (2013). Waste plastic pyrolysis oil as an alternative fuel for CI engine - A review. *Research Journal of Engineering Sciences*, 2(2), 26–30.

[46] Ghorpade, S.S., Patil, R.R., Kumar, V.S., & Harish, V.R. (2017). Extraction of plastic oil and experimental evaluation of diesel engine with blends of diesel and plastic pyrolysis oil. *TroIndia*, 4(6). 34–37.

[47] Anup, T.J., & Watwe, V. (2014). Waste plastic pyrolysis oil as alternative for SI and CI engines. *International Journal of Innovative Research in Science, Engineering and Technology*, 3(7). 14680–14687.

[48] Towijaya, K., Anam, K., & Lestari, W.D. (2022). Identification of cetane number in solar fuel from pyrolysis of plastic waste. *Biomedical and Mechanical Engineering Journal*, 2(1), 6–10. doi: 10.33005/biomej.v2i1.47

[49] Saleem, R., Naz, M.Y., Shukrullah, S., & Shoukat, B. (2022). Microwave pyrolysis of plastic waste materials into hydrogen and carbon. In *Energy and Environment* (pp. 157–167). doi: 10.1007/978-981-19-6688-0_10

[50] Bockhorn, H., Hornung, A., Hornung, A, & Schawaller, D. (1999). Kinetic study on thermal degradation of polypropylene and polyethylene. *Journal of Analytical and Applied Pyrolysis*, 48(2), 93–109. doi: 10.1016/S0165-2370(98)00131-4

[51] Nakhate, A.S., & Saharabuddhe, O. (2017). Grade analysis of pyrolysis oil by step distillation. *International Journal of Mechanical and Production Engineering*, 5(6), 120–124.

[52] Miandad, R., Rehan, M., Barakat, M.A., Aburiazaiza, A.S., Khan, H., Ismail, I.M., et al. (2019). Catalytic pyrolysis of plastic waste: Moving toward pyrolysis based biorefineries. *Frontiers in Energy Research*, 7, 27. doi: 10.3389/fenrg.2019.00027

[53] Shah, H.H., Amin, M., Iqbal, A., Nadeem, I., Kalin, M., Soomar, A.M., et al. (2022). A review on gasification and pyrolysis of waste plastics. *Frontiers in Chemistry*, 10, 960894. doi: 10.3389/fchem.2022.960894

[54] Wongkhorsub, C., & Chindaprasert, N. (2013). A comparison of the use of pyrolysis oils in diesel engine. *Energy and Power Engineering*, 5 (4B), 350–355. doi: 10.4236/epe.2013.54B068

[55] Miandad, R., Barakat, M.A, Aburiazaiza, A.S., Rehan, M., & Nizami, A.S. (2016). Catalytic pyrolysis of plastic waste: A review. *Process Safety and Environmental Protection*, 102, 822–838, doi: 10.1016/j.psep.2016.06.022

[56] Al-Haj Ibrahim, H. (2020). Introductory chapter: pyrolysis. In *Recent Advances in Pyrolysis*, InTech Open. doi: 10.5772/intechopen.90366

[57] Fahmy, T.Y.A., Fahmy, Y., Mobarak, F., El-Sakhawy, M., & Abou-Zeid, R.E. (2020). Biomass pyrolysis: Past, present, and the future. *Environment, Development and Sustainability*, 22, 17–32. doi: 10.1007/s10668-018-0200-5

[58] Varma, A.K., Shankar, R., & Mondal, P. (2018). A review on pyrolysis of biomass and the impacts of operating conditions on product yield, quality, and upgradation. In *Recent Advancements in Biofuels and Bioenergy Utilization* (pp. 227–259). doi: 10.1007/978-981-13-1307-3_10

[59] Hu, X., & Gholizadeh, M. (2019). Biomass pyrolysis: A review of the process development and challenges from initial researches up to the commercialisation stage. *Journal of Energy Chemistry*, 39, 109–143. doi: 10.1016/j.jechem.2019.01.024

[60] Yansaneh, O.Y., & Zein, S.H. (2022). Recent advances on waste plastic thermal Pyrolysis: A critical overview. *Processes*, 10(2), 332. doi: 10.3390/pr10020332

[61] Bridgwater, T., Meier, D., & Radlein, D. (1999). An overview of fast pyrolysis of biomass. *Organic Geochemistry*, 30(12), 1479–1493. doi: 10.1016/S0146-6380(99)00120-5

[62] Li, J., Li, N., & Qiao, Y. (2020). Biomass pyrolysis liquefaction technique: state of research and development trends. *IOP Conference Series Earth and Environmental Science*, 558, 022016. doi: 10.1088/1755-1315/558/2/022016

[63] Pandey, U., Stormyr, J.A., Hassani, A., Jaiswal, R., Haugen, H.H., & Moldestad, B.M. E. (2020). Pyrolysis of plastic waste to environmentally friendly products. In *Energy Production and Management in the 21st Century IV* (pp. 61–74), WIT Press. doi: 10.2495/EPM200071

[64] Uzochukwu Eze, W., Umunakwe, R., Obasi, H.C., Ugbaja, M.I., Uche, C.C., & Madufor, I.C. (2021). Plastics waste management: A review of pyrolysis technology. *Clean Technologies and Recycling*, 1(1), 50–69. doi: 10.3934/ctr.2021003

[65] Miandad, R., Barakat, M.A., Aburizaiza, A., Rehan, M. & Nizami, A.S. (2016). Catalytic pyrolysis of plastic waste: A review. *Process Safety and Environmental Protection*, 102, 822–838. doi: 10.1016/j.psep.2016.06.022

[66] Qureshi, M. S., Oasmaa, A., Pihkola, H., Deviatkin, I., Tenhunen, A., Mannila, J., et al. (2020). Pyrolysis of plastic waste: Opportunities and challenges. *Journal of Analytical and Applied Pyrolysis*, 152, 104804. doi: 10.1016/j.jaap.2020.104804

[67] Papuga, S., & Djurdjevic, M. (2022). Catalytic pyrolysis of plastic waste and molecular symmetry effects: A review. *Symmetry*, 15(1), 38. doi: 10.3390/sym15010038

[68] Xayachak, T., Haque, N., Parthasarathy, R., King, S., Emami, N., Lau, D., et al. (2022). Pyrolysis for plastic waste management: An engineering perspective. *Journal of Environmental Chemical Engineering*, 10(6), 108865. doi: 10.1016/j.jece.2022.108865

[69] Sasikumar, C., Senthilkumar, C., Sarweswaran, R., & Kannan, R. (2022). Pyrolysis of plastic waste for a better environmental system. *Materials Today: Proceedings*, 64(1). doi: 10.1016/ j.matpr.2022.05.388

[70] Mohan, R.K., Sarojini, J., Rajak, U., Verma, T. N., & Ağbulut, Ü. (2023). Alternative fuel production from waste plastics and their usability in light-duty diesel engine: Combustion, energy, and environmental analysis. *Energy*, 265, 126140. doi: 10.1016/j.energy.2022.126140

[71] Januszewicz, K., Hunicz, J., Kazimierski, P., Rybak, A., Suchocki, T., Duda, K., et al. (2023). An experimental assessment on a diesel engine powered by blends of waste-plastic-derived pyrolysis oil with diesel. *Energy*, 281, 128330. doi: 10.1016/j.energy.2023.128330

[72] Sekar, M., Praveenkumar, T. R., Dhinakaran, V., Gunasekar, P., & Pugazhendhi, A. (2021). Combustion and emission characteristics of diesel engine fueled with nanocatalyst and pyrolysis oil produced from the solid plastic waste using screw reactor. *Journal of Cleaner Production*, 318, 128551. doi: 10.1016/j.jclepro.2021.128551

[73] Muthukumar, K., & Kasiraman, G. (2023). Downcycling of one-time used plastic waste to DICI engine combustion energy through pyrolysis with less NOx emission. *Process Safety and Environmental Protection*, 175, 744–752. doi: 10.1016/ j.psep. 2023.05.097

[74] Jena, P., Raj, R., Tirkey, J.V., & Kumar, A. (2023). Experimental analysis and optimization of CI engine performance using waste plastic oil and diesel fuel blends. *Journal of the Energy Institute*, 109, 101286. doi: 10.1016/j.joei.2023.101286

[75] Singh, R.K., Ruj, B., Sadhukhan, A.K., Gupta, P., & Tigga, V.P. (2020). Waste plastic to pyrolytic oil and its utilization in CI engine: Performance analysis and combustion characteristics. *Fuel*, 262, 116539. doi: 10.1016/j.fuel.2019.116539

[76] Mangesh, V.L., Padmanabhan, S., Tamizhdurai, P., & Ramesh, A. (2020). Experimental investigation to identify the type of waste plastic pyrolysis oil suitable for conversion to diesel engine fuel. *Journal of Cleaner Production*, 246, 119066. doi: 10.1016/j.jclepro.2019.119066

[77] Mani, M., & Nagarajan, G. (2009). Influence of injection timing on performance, emission and combustion characteristics of a DI diesel engine running on waste plastic oil. *Energy*, 34(10), 1617–1623. https://doi.org/10.1016/j.energy.2009.07.010

[78] Kalargaris, I., Tian, G., & Gu, S. (2017). Combustion, performance and emission analysis of a DI diesel engine using plastic pyrolysis oil. *Fuel Processing Technology*, 157, 108–115. doi: 10.1016/j.fuproc.2016.11.016

Co-published by
Institute of Fluid-Flow Machinery
Polish Academy of Sciences
Committee on Thermodynamics and Combustion
Polish Academy of Sciences

http://www.imp.gda.pl/archives-of-thermodynamics/

Allometry of nanoparticles in diesel-biodiesel blends for CI engine performance, combustion and emissions

Mohd Mujtaba Ahmed[a*], Harveer Singh Pali[a], Mohammad Mohsin Khan[a]

[a] Department of Mechanical Engineering, National Institute of Technology Srinagar, J&K 190006 India
* Corresponding author email: mohdmujtabaahmed5@gmail.com

Received: 08.07.2023; revised: 02.11.2023; accepted: 04.01.2024

Abstract

Most countries in the world are facing two major challenges, one is the increase in the demand for energy consumption difficult to fulfill because of limited fossil fuel, and the second is the emission norms specified by many countries. Various methods are adopted to reduce emissions from engines but that leads to sacrificing the performance of CI engines. To eradicate this problem in the present study, the nanoparticles like (TiO_2) are used with different particle sizes 10–30 nm, 30–50 nm and 50–70 nm induced in B20 (20% biodiesel and 80% diesel) with the constant volume fraction of 100 ppm, and utilized in the diesel engine without any modifications. The results showed that the incorporation of TiO_2 nanoparticles improves the combustion of hydrocarbons and reduces the emissions of CO, unburned hydrocarbon concentration, NO_x and soot. Moreover, among three sizes of the nanoparticles, those with size 30–50 nm showed interesting results with the reduction in brake-specific energy consumption, NO_x, smoke and HC by 2.9%, 16.2%, 35% and 10%, respectively, compared to other blends used in the study, and hence the blend with the nanoparticle of size 30–50 nm is expected to be a more promising fuel for commercial application in CI engines.

Keywords: Biodiesel; Nanoparticle; CI engine; Engine performance; Engine combustion; Exhaust emission.

Vol. 45(2024), No. 1, 99–108; doi: 10.24425/ather.2024.150442

Cite this manuscript as: Ahmed, M.M., Pali, H.S., & Khan, M.M. (2024). Allometry of nanoparticles in diesel-biodiesel blends for CI engine performance, combustion and emissions. *Archives of Thermodynamics*, 45(1), 99–108.

1. Introduction

Due in part to their great thermal efficiency and high reliability, diesel-fuelled engines are frequently used as prime movers in the transportation and industrial sectors. Diesel engine reliance has grown, resulting in higher fossil fuel usage [1]. On the other hand, heavy-duty vehicles that run on traditional fuels like diesel are the biggest producers of greenhouse gas emissions [2]. Using sustainable alternatives like biofuels in place of fossil fuels can help cut down on carbon emissions [3].

For the production of biodiesel, raw resources such as vegetable oil and animal fat are used. The materials used to produce biodiesel undergo transesterification as this is a commonly used method for biodiesel production [4, 5], which restructures their molecules and makes them acceptable as a replacement for diesel engines [6–8]. There are also drawbacks to neat biodiesel, including higher emissions of NO_x, limited energy yield, and high specific fuel consumption [9]. By fulfilling particular fuel criteria, the use of additives has demonstrated its ability to get beyond these restrictions [3, 10, 11]. Microscale-sized additions show a slight reduction in emissions; however, studies show that

Nomenclature

Abbreviations and Acronyms

ASTM – American Society of Testing Materials
bTDC – before top dead center
B20N30 – 20% biodiesel + 80% diesel + 100 ppm TiO_2 (10–30 nm)
B20N50 – 20% biodiesel + 80% diesel + 100 ppm TiO_2 (30–50 nm)
B20N70 – 20% biodiesel + 80% diesel + 100 ppm TiO_2 (50–70 nm)
BP – brake power
BSEC – brake specific energy consumption
BSFC – brake specific fuel consumption
BTE – brake thermal efficiency
CA – crank angle
CHRR – cumulative heat release rate
CI – compression ignition
CPP – cylinder peak pressure
HRR – heat release rate
NO_x – oxides of nitrogen
UHC – unburned hydrocarbons
VCR – variable compression ratio
WCO – waste cooking oil
XHC – amount of unburned hydrocarbons
XCO – amount of carbon monoxide
XNO_x – amount of oxides of nitrogen

the use of big additive particles may negatively impact combustion performance, increasing emissions and decreasing efficiency [12–14]. The higher density of the droplets holding additives, which makes it challenging to have a homogeneous combination of fuels and additives, could be the cause of this phenomenon. Additionally, this can cause the droplets holding the addition to settle, resulting in sedimentation. Another drawback is that larger particles require longer times to complete physical and chemical processes when combined with base fuel, increasing ignition delay. Increased exhaust emissions and incomplete combustion are caused by a longer delay period. Thus, the use of large-sized additives in biodiesel blends is embarrassed by these criteria.

However, by adding nanosized metal oxide particles (100 nm) to biodiesel blends, these restrictions can be bypassed. They have distinct advantages to micro-sized additives, including a larger surface-to-volume ratio, stronger thermal conductivity, and superior lubricating qualities [15]. A nanofluid is created when nano-particles are combined with a base, like water, fuel, biofuels, etc. The nanofluid has various advantages over the base fluid, including better lubricity and increased thermal conductivity. The effective transport of heat, which is crucial during engine combustion, is made possible by these qualities. Additionally, nanoparticles with relatively tiny diameters prevent sedimentation by improving their dispersion and causing more chaotic movements. Owing to the nanofluid advanced thermal conductivity, which was described earlier, when it is injected into the combustion chamber through the fuel injector, there may be a greater heat exchange between the biodiesel and air. Compared to the combustion of plain fuel, this immediately primes the air-fuel mixture for spontaneous combustion, shortening the ignition delay. So, with lesser emissions, improved combustion and engine performance can be attained.

Experimental research has been done on biodiesel compositions using nanoparticle additions to power diesel engines. Jiaqiang et al. [16] investigated how nanoparticle size affected the diffusion stability of alumina (13 and 28 nm) added to biodiesel made from jatropha. The 13 nm nano-particles with a 0.1 volume percentage were said to have unchanged stability for more than a year. Kumar et al. [17] studied how ferric nanoparticles affected the characteristics of a biodiesel-powered diesel engine. The research noticed an increased brake thermal efficiency (BTE), reduced fuel consumption, and decrement in the amount of carbon monoxide (XCO) and hydrocarbon (XHC) after adding 1 percent in volume of ferrofluid nano-additive to B20. Prabu et al.[18] used alumina (Al_2O_3) and cerium (CeO_2) nanoparticles to experimentally study the performance parameters of a traditional diesel-fuelled engine. They noted that the addition of nanoparticles often reduced the delay and expedited early combustion start and that Al_2O_3 as a nano additive produced a greater BTE than nanoceria.

Ramesh et al. [19] studied the impact of diffusing alumina nanoparticles to biodiesel made from chicken litter on an engine performance, emissions, and combustion style. They claimed that alumina nanoparticle-added biodiesel had a higher BTE than plain biodiesel fuel. Silva et al. [20] examined the impact of Pongamia biodiesel (B20) containing TiO_2 nano-particles on diesel engine combustion. With the exception of nitrogen oxides, the fuels that were combined with nanoparticles burned more efficiently and produced significantly fewer pollutants (NO_x). The fuel mixture with 75 ppm of nanoparticles, according to the authors, showed the most encouraging results. Kao et al. [21] made combustion tests employing fuels containing an aqueous aluminium nanofluid in a diesel engine. They saw an increase in the burning rate when the aqueous aluminium nanofluid was present. Similarly, Xin et al. [22] hypothesized that adding nanoceria as a nano additive increased combustion efficiency, probably as a result of the increased pressure and lengthened burning time.

The extreme possible cylinder-pressure of nano-particles mixed fuel was also observed to be greater than that for neat conventional diesel, and nanoparticle-blended fuels were linked to shorter igniting delays than traditional diesel fuel [22]. Kumar et al. [23] examined the effects of injection pressure and nano CeO_2 (80 ppm) on a biodiesel-powered diesel engine thermal behaviour (B20). At the greatest injection pressure of 240 bar, the cerium oxide nanoparticle-doped fuel showed improved performance with decreased emissions [15, 23].

Sajith et al. [24] studied experimentally the effects of nanoceria as a fuel-additive in Jatropha biodiesel. According to their findings, utilizing plain biodiesel had a lower BTE at full load than using nanoparticle-dispersed biofuel. Additionally, the fuel formulation treated with CeO_2 nanoparticles showed decreased NO_x concentrations (XNO_x). Additionally, Mirzajanzadeh et al. [25] claimed that burning fuel that contained cerium oxide nanoparticles (40–50 nm in size) and waste cooking oil (WCO) significantly reduced NO_x emissions. The biggest reduction in XNO_x was 18.9% for the highest concentration of CeO_2

nanoparticles utilized by the authors, which was 90 ppm. This research used many variable concentrations of the nano additives, including 30, 60, and 90 ppm. Selvan et al. [26] reported that running the tested diesel engine on fuel formulations including CeO_2 nanoparticles resulted in a 54% reduction in XNO_x.

The type of biodiesel and the various characteristics of the nanoparticles used as an additive could have a significant impact on how well an engine performs when using diesel and biodiesel fuel mixes with nano additives (kind, magnitude, morphology, oxide layer width and volume fraction). Numerous studies have been conducted to determine the impacts of several biodiesel kinds and various volume concentrations of nanoparticles. The effect of nanoparticle size on engine performance and emission characteristics, however, is little understood. This study, which examines the performance, combustion and emission characteristics of a diesel engine running on a blend of biodiesel (WCO) and diesel fuel (B20), which contains TiO_2 nanoparticles of various sizes (10–30 nm, 30–50 nm and 50–70 nm), intends to fill this knowledge gap as a result. Measurements and analyses were made for performance factors, such as brake thermal efficiency (BTE), brake-specific energy consumption (BSEC), cylinder peak pressure (CPP), and heat release rate (HRR), as well as engine tailpipe emissions, such as XCO, XHC, XNO_x, and smoke opacity.

1.1. Background of TiO_2 nanoparticle as a combustion catalyst in diesel engines

TiO_2 is an indispensable component of biodiesel thanks to the high proportion of oxidation it contains. TiO_2 nanoparticles are extensively utilized in the production of a variety of products, such as paints, plastics, textiles, cosmetics, and coatings. Around the world, millions of metric tonnes of TiO_2 are produced in manufacturing facilities each year. One of the benefits of using TiO_2 is that it has a high dispersion quality. The addition of the nanoparticle to the biodiesel does not result in a change in the viscosity of the fuel, in contrast to the addition of pentanol and other additives. There aren't many pieces of research that back up the claim that vegetable oil and organic solvents can achieve a 99% dispersion rate. In addition to this, their thermal qualities are significantly enhanced, and they have the ability to resist corrosion. These TiO_2 nanoparticles are produced by a process known as sol-gel fabrication. Figure 1 shows the physical appearance and specifications of TiO_2 nanoparticles incorporated into the B20 fuel blend. When the temperature in the combustion chamber rises, the TiO_2 nanoparticle discharges its oxygen molecule, which increases the rate of combustion, resulting in proper combustion and hence reducing emissions at the exhaust. The following equations illustrate the reactions occurring during the combustion process:

$$2TiO_2 \rightarrow Ti_2O_3 + 0.5O_2\,, \quad (1)$$

$$(2x+y)\,TiO_2 + C_xH_y \rightarrow [(2x+y)_2]\,Ti_2O_3 + x2CO_2 + y2H_2O, \quad (2)$$

$$4TiO_2 + C_{soot} \rightarrow 2Ti_2O_3 + CO_2\,, \quad (3)$$

$$Ti_2O_3 + NO \rightarrow 2Ti_2O_2 + 1/2\,N_2\,. \quad (4)$$

Specifications	Volumes
Purity (%)	99.9
Colour	White solid
Titanium content (%)	58.36
Oxygen content (%)	41.05
Solubility nature	Insoluble in water
Molecular weight (gm/mol)	79.87
Density (gm/cm³)	4.29
Boiling point (⁰C)	2972
Melting point (⁰C)	1843

Fig. 1. Physical appearance and specifications of TiO_2 nanoparticle.

2. Materials and methods

2.1. Fuel Blend Preparation

Biodiesel from waste cooking oil (WCO) collected from the local mess and restaurants has been produced from the process of transesterification in the laboratory with similar conditions adopted by the previous experiment [27], and its physicochemical properties have been evaluated with ASTM standards with B20 (80% diesel and 20% biodiesel) which is itemized in Table 1. Various dimensions of Titanium oxide nanoparticles (i.e., 10–30 nm, 30–50 nm, and 50–70 nm) have been used in the preparation of test fuels. Table 2 shows the nomenclature of the samples used in the study. The produced fuels were designated as B20N30, B20N50 and B20N70. The two-step process in which magnetic stirring followed by ultrasonication was used to blend the nanoparticles and B20 fuel to form a homogenous mixture with a good distribution of TiO_2 nanoparticles in the test fuel. Figure 2 depicts the physical appearance of produced test fuels. All the test samples, after two-step physical stabilization, were used immediately in the engine.

Table 1. Tested values obtained for physicochemical properties of B20 blend.

Physicochemical Properties	B100	B20	Diesel	ASTM Standards
Higher heating value (MJ/kg)	37.9	40.23	43.2	D240
Flash point (⁰C)	370	67	321	D93
Density kg/m³	877	852	820	D4052
Kinematic viscosity (cSt)	4.5	3.8	3.4	D445

Table 2. Nomenclature of test sample used in the study.

Nomenclature	Understanding
B20	20% biodiesel +80% diesel
B20N30	20% biodiesel + 80% diesel + 100 ppm TiO_2 (10–30 nm)
B20N50	20% biodiesel + 80% diesel + 100 ppm TiO_2 (30–50 nm)
B20N70	20% biodiesel + 80% diesel + 100 ppm TiO_2 (50–70 nm)

Fig. 2. Physical appearance of test fuel blends.

2.2. Test setup and experimentation

The testing of various test fuels was conducted on a single-cylinder variable VCR diesel engine with a hydraulic dynamometer and compression ratio of 16:1. The setup was also integrated with the sensors which measure the fuel flow rate, load, cylinder pressure, the position of crank angle and air flow rate. The engine performance metrics are measured with the help of engine software provided with the setup. The concentration of exhaust gases like CO, HC, NO_x, O_2 and CO_2 were measured with the help of a multi-gas analyzer. The AVL smoke meter was attached with the setup for recording the emissions data. Table 3 and Table 4 provide the range and resolution of the instruments that are used in the experiment for test execution. Figure 3 shows a schematic illustration of the experimental setup

Table 3: Specifications of setup.

Description	Value/Description
Basic engine	Kirloskar
Make	TECH - ED
Diameter bore (mm)	80
Length of stroke (mm)	110
Compression ratio (CR)	12:1 to 20:1
Speed (constant)	1500 rpm
Rated brake power (kW)	Up to 4
Normal injection pressure (bar)	180
Dynamometer	Hydraulic dynamometer

Table 4. Specifications of gas analyzer and smoke meter.

Item	Range	Resolution
Pressure (bar)	0.344–75	0.0069
HC emissions (ppm)	0–15 000	1
Smoke opacity	0–100	0.01
NO_x emissions (ppm)	0–5 000	1
CO_2 emissions (vol %)	0–20	0.01
O_2 emissions (vol %)	0–25	0.1
CO emissions (vol %)	0–9.99	0.001

2.3. Uncertainty analysis

Uncertainty analysis in laboratory experiments examines how uncertain any measurements are. It enables the estimation of a physical variable's numerical value and the impact of instrumentation faults on that value. Equation 5 was used in this study to compute the uncertainty of a depending variable utilizing measurement errors for parameters which are independent like

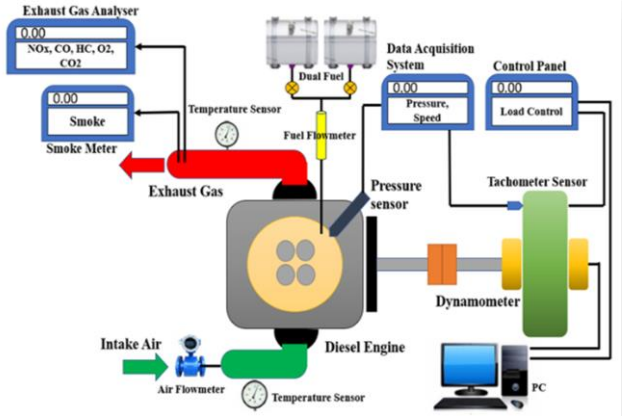

Fig. 3. Schematic illustration of experimental setup.

load, speed and fuel flow rate. Table 5 lists the determined uncertainty values for several constraints.

$$W_R = ([(\partial_R/\partial x_1)\, w_1]^2 + [(\partial_R/\partial x_2)\, w_2]^2 + \ldots + [(\partial_R/\partial x_n)\, w_n]^2)^{1/2}. \quad (5)$$

Table 5. Percentage uncertainty values of some parameters in the study.

Quantity	Uncertainty (%)
Load	0.64
Speed	0.55
Flow rate of fuel	0.9
BSEC	1.8
Concentration of NO_x	2.1
Concentration of HC	2.3
Concentration of CO	1.8
Smoke	0.98

3. Results and discussion

3.1. Brake thermal efficiency

BTE describes the effective transformation of energy present in the injected fuel into valuable work. Figure 4 illustrates the effects of various test fuels on BTE of the setup for different loads, and it is detected that BTE increases with the increment in engine load [28]. The engine is equipped with the software which calculates the BTE on the basis of Eq. (6). When the engine is fuelled with biodiesel and its blends, a slight decrement in the BTE has been observed. The credit for this reduction falls on the biodiesel's lower calorific value, which lowers the cumulative

energy of the test fuel blend [29, 30]. The examination also revealed that the incorporation of TiO_2 nanoparticles of various sizes enhances the brake thermal efficiency of the engine [31]. Moreover, among the three sizes of TiO_2 nanoparticles, the optimum values of BTE are noted for the blend containing the nanoparticles of size 30–50 nm size as compared to those of 10–30 nm and 50–70 nm. The causes for this enhancement are fuel oxidation leading to proper combustion, high surface-to-volume ratio and improved catalytic activity because of smaller size nanoparticles (30–50 nm). Further, smaller size (10–30 nm) particles also diminish the fuel properties, as they may not improve the density and viscosity of the test fuel blends. The BTE increments for the blend B20N50, as compared to B20N30 and B20N70, are 3.42% and 6.45% at full load.

$$BTE = \frac{\text{Brake power}}{\text{Heat realeased}} = \frac{\text{Brake power}}{\text{mass of fuel consumed x calorific value}}. \quad (6)$$

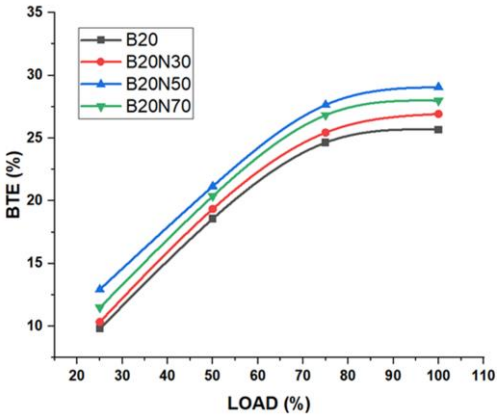

Fig. 4. Variations of brake thermal efficiency for various fuel blends with respect to load.

3.2. Brake specific energy consumption

Generally, brake specific energy consumption (BSEC) shows the consumption of energy per unit, which is the specific output of the engine (BP). This is higher when the load is low and becomes reduced when the load is increased up to 80% of the full load of the engine [32]. The illustrated data in Fig. 5 reflects that among all the test blends of nano additives doped fuel blends, that with the nanoparticle size of 30–50 nm shows the lowest BSEC. The B20 blend had superior fuel preparation when TiO_2 nano additives were added, which improved the heat flow between the air and fuel droplets. This must have aided in improving combustion and reducing ignition delay. Due to the efficient use of the injected fuel, these factors probably helped lower BSEC. According to the findings of the current investigation, energy consumption appears to be significantly influenced by particle sizes. B20 + (30–50) nm (B20N50) and B20 + (50–70) nm (B20N70) were at the extremities of the tested fuel formulation, with the former revealing the smallest BSEC and the latter the lowest BSEC. One might draw the generalization that energy combustion declined as nanoparticle size increased. As was previously said, smaller particle sizes result in an increase in the surface-to-volume ratio, helping to achieve

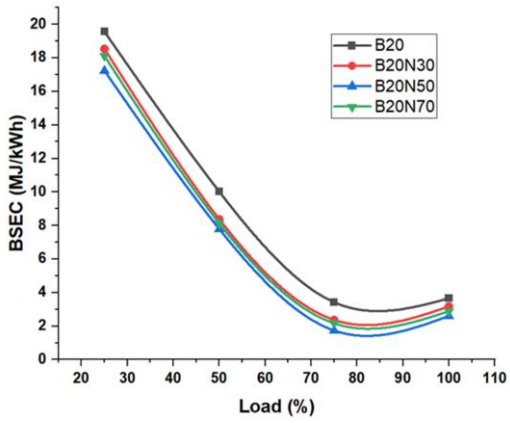

Fig. 5. Variations of brake specific energy consumption for various fuel blends with respect to load.

consistent air-fuel mixing. This accelerates heat transport, shortening the ignition delay. A shorter ignition delay enhances combustion and lowers BSEC.

In the current investigation, a nanoparticle size of 30–50 nm (B20N50) was shown to have the lowest BSEC. Due to the lesser density, a nanoparticle that was too small could not have been able to travel to different areas of the combustion chamber effectively, leading to uneven fusing. This probably lengthened the ignition delay, resulting in inefficient combustion and a small increase in BSEC as a result.

3.3. Cylinder peak pressure

The efficiency of combustion is indicated by the cylinder peak pressure (CPP). A higher cylinder pressure can typically be reached if the fuel mixture completely burns during the premixed phase. Additionally, this leads to higher power production and lower emissions [33]. As per the data in Fig. 6, CPP obtained using fuels fused with TiO_2 nanoparticles was higher than that of B20 without additives.

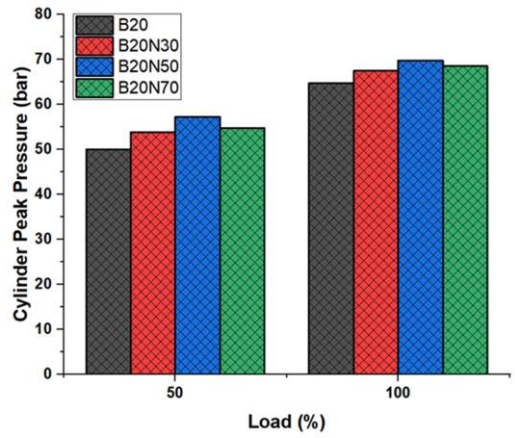

Fig. 6. Variations of cylinder peak pressure for various fuel blends with respect to partial and full load.

TiO_2 nanoparticles must have served as a heat carrier medium when they were added to the B20 fuel mixture, encourag-

ing heat transmission between the fuel drops and air. This phenomenon must have accelerated the fuel droplet evaporation, shortening the delay. As a result, compared to B20 without additives, the autoignition temperature was reached more quickly. These elements helped to provide a higher cylinder peak pressure around the top dead center (TDC) and smooth combustion. The fuel formulation with 30–50 nm nanoparticles had the highest peak of 56.7 bar and 72.3 bar at partial load and full load, respectively, compared to the other two, also this is by 9.35% higher than for B20. As observed in the case of B20 + (50–70) nm (B20N70), less heat transfer occurs when the surface-to-volume ratio drops as the particle size grows. Out of the three fuel variations, B20 fuel had the lowest peak cylinder pressure measurement (see Fig. 6).

3.4. Heat release rate

This is the major factor for analysing the combustion process of the engine which shows the heat released per degree crank angle in the cylinder [34]. The heat release rate (HRR) while operating under full load at 26°CA bTDC is shown in Fig. 7. The phases of combustion are called "premixed combustion", "controlled combustion" and "late combustion", respectively. During the ignition delay period, a negative slope is produced as a result of the cooling effect induced by fuel evaporation. When loaded to its maximum capacity, the B20N30 blend has an HRR of 58.54 J/°CA. Because of their higher viscosity, lower rate of vaporization, larger molecular weight and slower burning velocity, other biodiesel blends have a lower heat release rate.

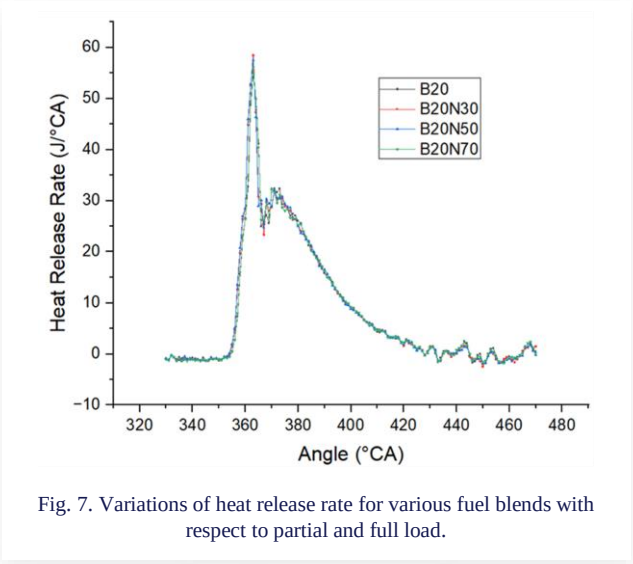

Fig. 7. Variations of heat release rate for various fuel blends with respect to partial and full load.

The blend B20N50 possessed a higher heat release rate comparable to the B20 heat release rate of 54.91 J/°CA. This is because a longer delay between the ignition and combustion led to a higher fuel deposit. When compared to B20, blends with TiO_2 nanoparticles of size 30–50 nm (B20N50) have a superior fuel-air combination, which results in a higher quantity of heat release [35].

3.5. Cumulative heat release rate

Figure 8 displays the total heat released for each of the tested fuel blends. The total amount of heat released during the premixed and diffused combustion phases of fuel combustion is shown by these measurements [32, 36]. The beginning and end

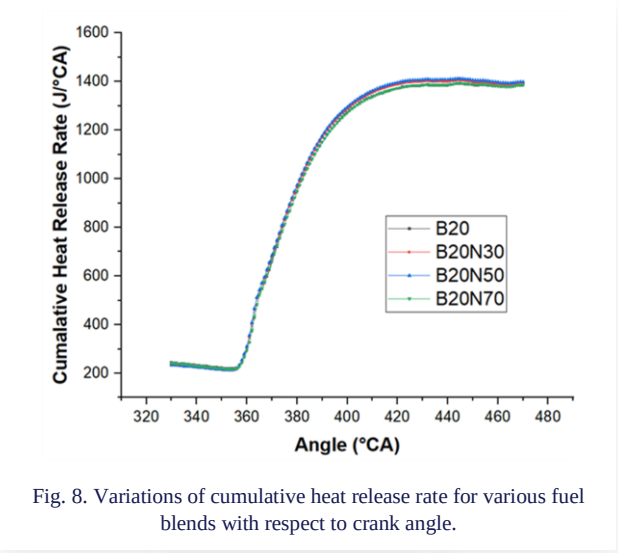

Fig. 8. Variations of cumulative heat release rate for various fuel blends with respect to crank angle.

of combustion, the kind and quality of the fuel, and the rate of pressure rise inside the cylinder are only a few of the variables that affect the total amount of heat released. The addition of TiO_2 nanoparticles worked as a catalyst for the catalytic oxidation of CO and UHC to CO_2, promoting combustion. Additional energy was released as a result, which would have otherwise remained as unburned fuel in the exhaust.

The power output rose in line with the cumulative heat release during combustion caused by the added energy. B20 + (30–50) nm (B20N50) exhibited the greatest cumulative heat release of 1412.3 J, which is 3.5%, 1.4% and 1.2% higher than the other three test samples B20, B20N30 and B20N70 used in the experiment, respectively.

3.6. TiO_2's catalytic properties and emission regulation

For a catalyst to be effective in the combustion of diesel engines, it must possess the following three qualities: complete hydrocarbon oxidation, avoiding the creation of nitrogen oxides, and having good thermal stability [37]. TiO_2 can contribute oxygen to the oxidation of soot and hydrocarbons. The fact that a TiO_2 catalyst may donate O_2 for the oxidation reaction and activates at low temperatures (typically 300–500°C) makes it special. High temperatures are required for combustion in diesel engines; the diesel flame typically reaches a temperature of around 1 700°C. The chemical interactions between nitrogen and oxygen are likely to produce nitrogen oxides at this high temperature. TiO_2 nanoparticles served as a catalyst and encouraged more thorough combustion of the fuel that was injected. Because nitrogen has a high activation energy, the average cylinder temperature drops during the conversion of NO to N_2. This also contributes to the reduction of nitrogen oxide production. Additionally, TiO_2 nanoparticles great heat stability promotes their catalytic

activity. TiO_2 goes through early oxidation after the initial combustion is accomplished. This is due to the thermal stability of nano titanium, which also makes it active after re-oxidation for additional catalytic action. Thus, as demonstrated in Eqs. (2)–(4), the concentrations of CO, HC, and NO_x and soot are reduced by oxidation and reduction reactions that occur in TiO_2 nanoparticles.

TiO_2 catalytic activity is strongly correlated with its surface area. The carbon combustion activation temperature was seen to drop from 700°C to 300°C when the surface area of TiO_2 nanoparticles increased 20 times [38]. The size of the nanoparticle is decreased to produce a larger surface area. When soot and UHC that have adhered to the combustion chamber walls come into touch with the nanoparticles, they oxidize to CO_2, reducing tailpipe emissions and enhancing fuel efficiency. Small TiO_2 nanoparticles are thus preferred since they have a stronger catalytic effect.

3.6.1. Unburned hydrocarbon concentration

The fluctuations of unburned hydrocarbon concentration (UBHC) for the various fuel preparations under various engine load levels are shown in Fig. 9. Higher values were seen at full load when HC grew along with the load. The level of HC emissions was lowest when the engine was running at part load, and quickly went up when it was running at full load. It was found that B20 fuel without additives had the highest HC of any fuel mix. This is explained by the poor combustion caused by the increased viscosity, less penetration and dispersion. When nanoparticles were added, a relatively low energy reaction allowed nano titanium to donate oxygen atoms. This occurred as a result of the catalytic action of TiO_2 as stated in Eqs. (1)–(3). This indicates that titanium oxide contributed oxygen to the reduction of UHC, resulting in the production of titanium trioxide, CO_2 and water [39].

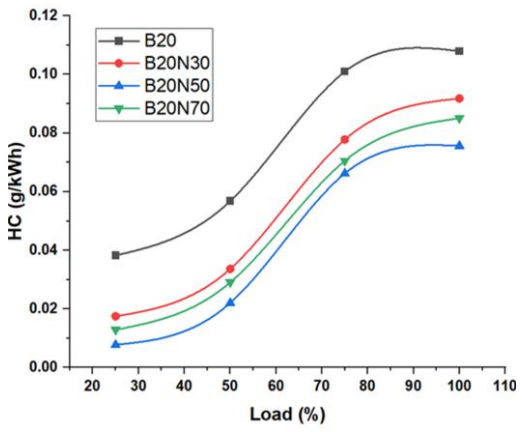

Fig. 9. Variations in HC emission for various fuel blends with respect to load.

Similar to the outcome previously reported by [40], diesel fuel HC was reduced by 7% when combined with TiO_2 nanoparticles compared to pure diesel. The lowest HC was found in the particle size range of B20 + (10–30) nm (B20N30). Although 10 nm-sized nanoparticles offered a larger surface area, poor dispersion must have resulted from the nanoparticles agglomeration and poor transport properties. Due to the nanoparticles inability to reach the areas where CO and HC creation were occurring, there was poor combustion and a modest rise in HC. According to the findings of this study, the B20N50 fuel composition was linked to the most substantial HC decrement of 35% when compared to B20 without any additives.

3.6.2. Carbon monoxide concentration

The lack of oxygen for the oxidation reaction is the primary cause of CO production. The full conversion of CO to CO_2 is complicated when the temperature at which carbon is activated is high, as it usually is in diesel engine combustion [36]. However, because the activation temperature is higher, the conversion process takes longer. TiO_2 serves as a catalyst and lowers the temperature when added to fuel. Consequently, the conversion of CO to CO_2 can take place at low temperatures. This phenomenon might allow for a more thorough conversion of CO to CO_2, which would result in less CO. As shown in Fig. 10, B20 + (30–50) nm (B20N50) demonstrates the lowest CO value of the three nanoparticle doped fuel formulations, while B20 + (50–70) nm (B20N70) displays the highest. Nevertheless, these values were by 129.4% and 78.2% lower than the corresponding values for B20 without additives.

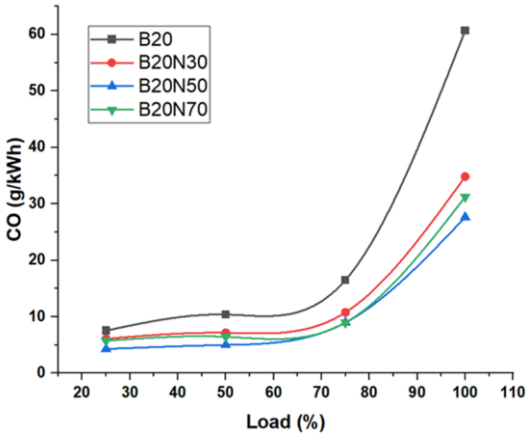

Fig. 10. Variations in CO emissions for various fuel blends with respect to load.

3.6.3. Smoke opacity findings

Unburned carbon molecules produced at the initial stage of combustion make up smoke. The main causes of smoke production are a lack of oxygen as well as the quenching action that takes place close to the cylinder wall. Carbon particles that function as a barrier to heat transfer are deposited at the wall surface as a result of quenching. As a result, the power output is reduced, frictional losses rise, and fuel consumption follows. The TiO_2 nanoparticle addition has a significant catalytic impact on reducing the soot production. The addition of TiO_2 lowers the carbon activation temperature to between 200°C and 500°C. Equation (3) demonstrates that this temperature mainly enhances the oxidation of soot particles to CO_2. As a result, TiO_2 lessens the smoke production and emission. In conjunction with Pongamia

biodiesel [41], also it showed the decreased smoke opacity at 50 ppm and 100 ppm TiO_2 nanoparticle concentrations. When the TiO_2 nanoparticle amount was raised from 50 ppm to 100 ppm [42], an 8% decrease in smoke opacity was noticed. The fuel formulation with 30–50 nm-sized nanoparticles, or B20 + (30–50) nm (B20N50), exhibited the lowest soot emission of the three nanoparticle sizes taken into account in the current investigations (Fig. 11). The measured value for the operation of the B20 gasoline without additives was 53% greater than the observed value.

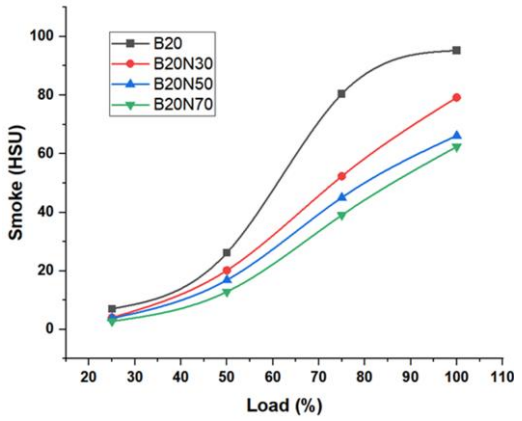

Fig. 11. Variations in smoke opacity emission for various fuel blends with respect to load.

3.6.4. The concentration of oxides of nitrogen

When utilized in diesel engines, biodiesel has a significant disadvantage in the emission of nitrogen oxides. Due to an abundance of oxygen, a hot combustion temperature, and a lengthy residence period, NO_x is formed. Fuel-borne oxygen encourages the oxidation of N_2 during biodiesel combustion. The increased combustion temperature that is present in the combustion chamber further benefits this. There are several methods used to minimize NO_x in the emissions from tailpipes [43]. These methods, while lowering NO_x, also raise HC and CO levels or lower engine performance.

According to the findings shown in Fig. 12, combustion of the B20 without additives produced the largest NO_x emissions under all situations of load. B20 + (30–50) nm (B20N50) had the lowest NO_x value among the fuel formulations containing nanoparticles, which was 7.5% less than the comparable values observed for B20 + (10–30) nm (B20N30) and B20 + (50–70) nm (B20N70).

A unique method for decreasing NO_x and other emissions without sacrificing or even modestly boosting engine performance is to utilize TiO_2 as a catalyst in engines. Equation (4), which describes how TiO_2 first undergoes a reaction to generate Ti_2O_3, can be used to explain how TiO_2 has a catalytic activity on NO_x reduction. By interacting with nitrogen oxides, this is further reduced to TiO_2, freeing nitrogen. Due to the greater activation energy of N_2, TiO_2 nanoparticles aid in lowering the temperature of the fuel-air mixture during this phase. The performance of diesel engines was also examined by Gracia and

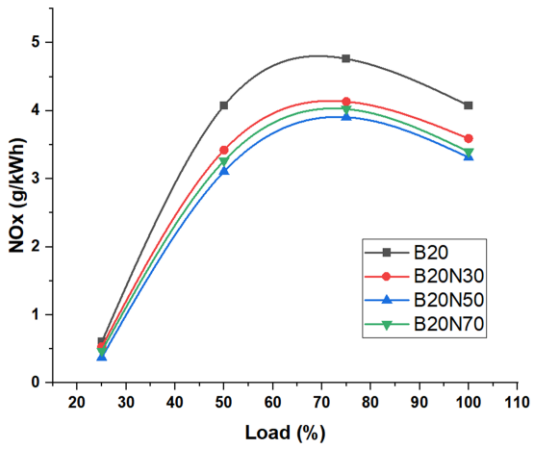

Fig. 12. Variations in NO_x emissions for various fuel blends with respect to load.

Rodreguaz [44] utilizing Pongamia biodiesel with TiO_2 nanoparticles. TiO_2-doped esters showed lower NO_x values for all loads, according to the authors.

4. Conclusions

The engine characteristics of several B20-based fuel forms that contained TiO_2 nanoparticles of different sizes were investigated through experiments. The research also used B20 which had no additives, for comparison. On the basis of the results, the following deductions and conclusions can be made:

- TiO_2 worked as a catalyst and significantly contributed to better engine combustion by raising BTE and lowering BSFC. The differences observed were significantly influenced by the nanoparticle size. The most notable reduction in BSEC by 6.4 %, when compared to the additive-free B20, was caused by nanoparticles smaller than 30 nm.
- The results showed that the B20+(30–50) nm (B20N50) fuel formulation was also linked to the highest rates of heat release and the highest pressures in the cylinders, the B20N30 blend has a heat release rate of 58.54 J/°CA and 72.3 bar, respectively, which is higher than that of the other blends and additive-free B20.
- By acting as a catalyst, TiO_2 lowered the temperature at which carbon begins to oxidize, which aided in converting the HC, CO and soot to CO_2 in the quenching regions of the combustion chamber and lowered engine exhaust emissions. Additionally, compared to other fuel formulations containing nanoparticles of different sizes or shapes, the B20 + (30–50) nm (B20N50) fuel formulation produced the least emissions. This result underlined the significance of the fuel nano additive size.

TiO_2 helped to decrease the NO_x at a relatively low level by assisting nitrogen oxides in oxidation-reduction processes and subsequently in their conversion to nitrogen. Once more, it was discovered that 30–50 nm–sized nano titanium were superior to their 10–30 nm and 50–70 nm–sized counterparts in terms of reducing NO_x.

Acknowledgements

The research acknowledges the Renewable Energy and Alternatives Fuels Lab, Mechanical Engineering Department, National Institute of Technology Srinagar, India. The research was not supported by any other funding societies.

References

[1] Muradin, M. (2020). Environmental impact assessment of organic waste conversion technology for additives to liquid fuels. *Polityka Energetyczna - Energy Policy Journal*, 23(1), 135–150. doi: 10.33223/epj/118731

[2] Agarwal, A.K. (2007). Biofuels (alcohols and biodiesel) applications as fuels for internal combustion engines. *Progress in energy and combustion science*, 33(3), 233–271. doi: 10.1016/j.pecs.2006.08.003

[3] Dinesha, P., Kumar, S., & Rosen., M.A. (2019). Combined effects of water emulsion and diethyl ether additive on combustion performance and emissions of a compression ignition engine using biodiesel blends. *Energy*, 179, 928–937. doi: 10.1016/j.energy.2019.05.071

[4] Wen, Z., & Petera, J. (2017). Numerical analysis of the effect of Hydrodynamics and operating conditions on biodiesel synthesis in a rotor-stator spinning disk reactor. *Chemical and Process Engineering*, 38(2), 265–281. doi: 10.1515/cpe-2017-0020

[5] Wen, Z., & Petera, J. (2015). CFD numerical simulation of biodiesel synthesis in a spinning disc reactor. *Chemical and Process Engineering*, 36(1), 21–37. doi: 10.1515/cpe-2015-0002

[6] Rakopoulos, C.D., Antonopoulos, K.A., Rakopoulos, D.C., Hountalas, D.T., & Giakoumis, E.G. (2006). Comparative performance and emissions study of a direct injection Diesel engine using blends of Diesel fuel with vegetable oils or biodiesels of various origins. *Energy Conversion and Management*, 47(18–19), 3272–3287. doi: 10.1016/j.enconman.2006.01.006

[7] Sureshkumar, K., Velraj, R., & Ganesan R. (2008). Performance and exhaust emission characteristics of a CI engine fueled with Pongamia pinnata methyl ester (PPME) and its blends with diesel. *Renewable Energy*, 33(10), 2294–2302. doi: 10.1016/j.renene.2008.01.011

[8] Muralidharan, K., Vasudevan, D., & Sheeba, K.N. (2011). Performance, emission and combustion characteristics of biodiesel fuelled variable compression ratio engine. *Energy*, 36(8), 5385–5393. doi: 10.1016/j.energy.2011.06.050

[9] An, H., Yang, W.M., Maghbouli, A., Li, J., Chou, S.K., & Chua, K.J. (2013). Performance, combustion and emission characteristics of biodiesel derived from waste cooking oils. *Applied Energy*, 112, 493–499, doi: 10.1016/j.apenergy.2012.12.044

[10] Agarwal, D., Kumar, L., & Agarwal, A.K. (2008). Performance evaluation of a vegetable oil fuelled compression ignition engine. *Renewable Energy*, 33(6), 1147–1156. doi: 10.1016/j.renene.2007.06.017

[11] Alptekin, E. (2017). Emission, injection and combustion characteristics of biodiesel and oxygenated fuel blends in a common rail diesel engine. *Energy*, 119, 44–52. doi: 10.1016/j.energy.2016.12.069

[12] Bertola, A., Li, R., & Boulouchos, K. (2003). Influence of Water-Diesel Fuel Emulsions and EGR on Combustion and Exhaust Emissions of Heavy Duty DI-Diesel Engines equipped with Common-Rail Injection System. *SAE Technical Paper*. doi: 10.4271/2003-01-3146

[13] Qi, D.H., Geng, L.M., Chen, H., Bian, Y.Z., Liu, J., & Ren, X.C. (2009). Combustion and performance evaluation of a diesel engine fueled with biodiesel produced from soybean crude oil. *Renewable Energy*, 34(12), 2706–2713. doi: 10.1016/j.renene.2009.05.004

[14] Izquierdo, J.F., Montiel, M., Palés, I., Outón, P.R., Galán, M., Jutglar, R., Villarrubia, M., Izquierdo, M., Hermo, M.P., & Ariz, X. (2012). Fuel additives from glycerol etherification with light olefins: State of the art. *Renewable and Sustainable Energy Reviews.* 16(9), 6717–6724. doi: 10.1016/j.rser.2012.08.005

[15] Kumar, S., Dinesha, P., & Bran, I. (2019). Experimental investigation of the effects of nanoparticles as an additive in diesel and biodiesel fuelled engines: a review. *Biofuels*, 10(5), 615–622. doi: 10.1080/17597269.2017.1332294

[16] E, J., Guanlin, L., Zhang Z., Han, D., Chen, J., Wei K., Gong J., & Yin, Z. (2019). Effect analysis on cold starting performance enhancement of a diesel engine fueled with biodiesel fuel based on an improved thermodynamic model. *Applied Energy*, 243, 321–335. doi: 10.1016/j.apenergy.2019.03.204

[17] Kumar, S., Dinesha, P., & Bran, I. (2017). Influence of nanoparticles on the performance and emission characteristics of a biodiesel fuelled engine: An experimental analysis. *Energy*, 140, 98–105. doi: 10.1016/j.energy.2017.08.079

[18] Prabu, A. (2018). Nanoparticles as additive in biodiesel on the working characteristics of a DI diesel engine.*Ain Shams Engineering Journal*, 9(4), 2343–2349. doi: 10.1016/j.asej.2017.04.004

[19] Ramesh, D.K., Dhananjaya Kumar, J.L., Hemanth Kumar, S.G., Namith, V., Basappa Jambagi, P., & Sharath, S. (2018). Study on effects of Alumina nanoparticles as additive with Poultry litter biodiesel on Performance, Combustion and Emission characteristic of Diesel engine. *Materials Today Proceedings*, 5(1), 1114–1120. doi: 10.1016/j.matpr.2017.11.190

[20] D'Silva, R., Fernandes, N., Menezes, M., D'Souza P., Pinto, V., Kaliveer, V., Gopalakrishna, B.K., & Bhat, T. (2019). Effect of TiO_2 nanoparticle concentration in Pongamia Pinnata methyl ester on performance and emission characteristics of CI engine. *AIP Conference Proceedoings*, 2080(1). doi: 10.1063/1.5092909

[21] Mitchell, M.R., Link, R.E., Kao, M.J., Ting, C.C., Lin, B.F., & Tsung, T. T. (2008). Aqueous aluminum nanofluid combustion in diesel fuel. *Journal of Testing and Evaluation*, 36(2), 186–190. doi: 10.1520/JTE100579

[22] Xin, Z., Tang, Y., Man, C., Zhao, Y., & Ren, J. (2013). Research on the impact of CeO_2-based solid solution metal oxide on combustion performance of diesel engine and emissions. *Journal of Marine Science and Application*, 12, 374–379. doi: 10.1007/s11804-013-1197-7

[23] Kumar, S., Dinesha, P., & A. Rosen, M. (2019). Effect of injection pressure on the combustion, performance and emission characteristics of a biodiesel engine with cerium oxide nanoparticle additive. *Energy*, 185, 1163–1173. doi: 10.1016/j.energy.2019.07.124

[24] Sajith, V., Sobhan, C.B., & Peterson, G.P. (2010). Experimental investigations on the effects of cerium oxide nanoparticle fuel additives on biodiesel. *Advances in Mechanical Engineering*, 2. doi: 10.1155/2010/581407

[25] Mirzajanzadeh, M., Tabatabaei, M., Ardjmand, M., Rashidi, A., Ghobadian, B., Barkhi, M., & Pazouki, M. (2015). A novel soluble nano-catalysts in diesel-biodiesel fuel blends to improve diesel engines performance and reduce exhaust emissions. *Fuel*, 139, 374–382. doi: 10.1016/j.fuel.2014.09.008

[26] Selvan, V.A.M., Anand, R.B., & Udayakumar, M. (2009) Effects of cerium oxide nanoparticle addition in diesel and diesel-biodiesel-ethanol blends on the performance and emission characteristics of a CI engine. *ARPN Journal of Engineering and Applied Sciences*, 4(7), 1–6.

[27] Ahmed, M.M., Pali, H.S., & Khan, M.M. (2022). Experimental analysis of diesel/biodiesel blends with a nano additive for the performance and emission characteristics of CI Engine. *International Journal of Engine Research*, 24(11), 4500–4508. doi: 10.1177/14680874221132958

[28] Pali, H.S., Kumar, N., & Alhassan, Y. (2015). Performance and emission characteristics of an agricultural diesel engine fueled with blends of Sal methyl esters and diesel. *Energy Conversion and Management*, 90, 146–153. doi: 10.1016/j.enconman.

2014.10.064

[29] Hosseini, S.H., Taghizadeh-Alisaraei, A., Ghobadian, B., & Abbaszadeh-Mayvan, A. (2017). Effect of added alumina as nano-catalyst to diesel-biodiesel blends on performance and emission characteristics of CI engine. *Energy*, 124, 543–552. doi: 10.1016/j.energy.2017.02.109

[30] Karthikeyan, S., Elango, A., & Prathima, A. (2016). The effect of cerium oxide additive on the performance and emission characteristics of a CI engine operated with rice bran biodiesel and its blends. *International Journal of Green Energy*, 13(3), 267–273. doi: 10.1080/15435075.2014.952419

[31] Reddy, S.N K., & Wani, M.M. (2020). A comprehensive review on effects of nanoparticles-antioxidant additives-biodiesel blends on performance and emissions of diesel engine. *Applied Science and Engineering Progress*, 13(4), 285–298. doi: 10.14416/J.ASEP.2020.06.002

[32] Sharma, A., Pali, H.S., Kumar, M., Singh, N.K., Singh, Y., & Singh, D. (2022). Study the effect of optimized input parameters on a CRDI diesel engine running with waste frying oil methyl ester-diesel blend fuel with ZnO nanoparticles: a response surface methodology approach. *Biomass Conversion and Biorefinery*, 13, 13127−13152. doi: 10.1007/S13399-021-02158-6

[33] Gürü, M., Koca, A., Can, Ö., Çinar, C., & Şahin, F. (2010). Biodiesel production from waste chicken fat based sources and evaluation with Mg based additive in a diesel engine. *Renewable Energy*, 35(3), 637–643. doi: 10.1016/j.renene.2009.08.011

[34] Bednarski, M., Orliński, P., Wojs, M., & Gis, M. (2020). Evaluation of the heat release rate during the combustion process in the diesel engine chamber powered with fuel from renewable energy sources. *Bulletin of the Polish Academy of Sciences, Technical. Sciences*, 68(6), 1333–1339. doi: 10.24425/bpasts.2020.135394

[35] Pan, W., Yao, C., Han, G., Wei, H., & Wang, Q. (2015). The impact of intake air temperature on performance and exhaust emissions of a diesel methanol dual fuel engine. *Fuel*, 162, 101–110. doi: 10.1016/j.fuel.2015.08.073

[36] Hussain Vali, R., Hoang, A.T., Wani, M.M., Pali H.S., Balasubramanian, D., Arici, M., Said, Z., & Nguyen, X.P. (2022). Optimization of variable compression ratio diesel engine fueled with Zinc oxide nanoparticles and biodiesel emulsion using response surface methodology. *Fuel*, 323, 124290. doi: 10.1016/j.fuel.2022.124290

[37] Pali, H.S., Sharma, A., Kumar, M., Annakodi, V.A., Nguyen, V.N., Singh, N.K., Singh, Y., Balasubramanian, D., Deepan-raj, B., Truong T.H., & Nguyen, P.Q.P. (2023) Enhancement of combustion characteristics of waste cooking oil biodiesel using TiO2 nanofluid blends through RSM. *Fuel*, 331(part 1). doi: 10.1016/j.fuel.2022.125681

[38] Logothetidis, S., Patsalas, P., & Charitidis, C. (2003). Enhanced catalytic activity of nanostructured cerium oxide films. *Materials Science and Engineering: C*, 23(6–8), 803–806. doi: 10.1016/j.msec.2003.09.081

[39] Mei, D., Li, X., Wu, Q., & Sun, P. (2016). Role of Cerium Oxide Nanoparticles as Diesel Additives in Combustion Efficiency Improvements and Emission Reduction. *Journal of Energy Engineering*, 142(4), 1–6. doi: 10.1061/(asce)ey.1943-7897.0000329

[40] Shaisundaram, V.S., Chandrasekaran, M., Mohan Raj, S., & Muraliraja, R. (2020). Investigation on the effect of thermal barrier coating at different dosing levels of cerium oxide nanoparticle fuel on diesel in a CI engine. *Intenational Journal of Ambient Energy*, 41(1), 98–104. doi: 10.1080/01430750. 2018.1451385

[41] Appavu, P., & Ramanan, M.V. (2020). "Study of emission characteristics of a diesel engine using cerium oxide nanoparticle blended pongamia methyl ester. *International Journal of Ambient Energy*, 41(5), 524–527. doi: 10.1080/01430750.2018.1477063

[42] Seela, C.R., Sankar, B.R., Kishore, D., & Babu, M.V.S. (2019). Experimental analysis on a DI diesel engine with cerium-oxide-added Mahua methyl ester blends. *International Journal of Ambient Energy*, 40(1), 49–53. doi: 10.1080/01430750.2017.1360203

[43] Singh, Y., Pali, H.S., Singh, N.K., Sharma, A., & Singla, A. (2022). Effect of nanoparticles as additives to the biofuels and their feasibility assessment on the engine performance and emission analysis - A review. *Proceeding of the Institution of Mechanical Engineers, Part E: Journal of Process Mechanical Engineering*, 237(2). doi: 10.1177/09544089221109723

[44] Fernández-García, M., & Rodriguez, J.A. (2011). Metal Oxide Nanoparticles. In: *Encyclopedia of Inorganic and Bioinorganic Chemistry*. Chichester, UK, John Wiley & Sons, Ltd; eibc0331. doi: 10.1002/9781119951438.eibc0331

Co-published by
Institute of Fluid-Flow Machinery
Polish Academy of Sciences
Committee on Thermodynamics and Combustion
Polish Academy of Sciences

http://www.imp.gda.pl/archives-of-thermodynamics/

Experimental investigations of CI engine performance using ternary blends of n-butanol/biodiesel/diesel and n-octanol/biodiesel/diesel

Ashish Kumar Singh[a], Harveer Singh Pali[a*], Mohammad Mohsin Khan[a]

[a]Mechanical Engineering Department, National Institute of Technology Srinagar, J&K 190006, India
*Corresponding author email: hspali@nitsri.ac.in

Received: 03.07.2023; revised: 16.09.2023; accepted: 05.11.2023

Abstract

This study explored the ternary blends of biodiesel-diesel-n-butanol and biodiesel-diesel-n-octanol on common rail direct injection (CRDI) diesel engines. The compositions of fuels, which varied from 0% to 100%, were altered by up to 5%. On the basis of their properties, these blends were chosen, with various concentrations of alcohol at 5% and 10%, 5% diesel, and the remainder being biodiesel. Two ternary fuel blends of waste cooking oil biodiesel (90–85%), diesel (5%), and butanol (5–10%), namely BD90D5B5 and BD85D5B10, and subsequently, another two ternary similar blends of waste cooking oil biodiesel (90–85%), diesel (5%), and octanol (5–10%), namely BD90D5O5 and BD85D5O10, were used to conduct the experiments. The experiments were done with varying injection pressure from 17° to 29° crank angle (CA) before top dead centre (bTDC). The optimum condition for the blends is achieved at 26°CA bTDC for 80% loading. So, the engine trials were conducted on 26°CA bTDC to attain the results. The BD90D5O10 blend achieved the lowest brake specific fuel consumption (BSFC) reading of 0.308 kg/kWh while operating at full load. The maximum brake thermal efficiency (BTE) was 31.46% for BD90D5B5. The maximum heat release rate (HRR) achieved with BD85D5O5 fuel blend was 58.54 J/°CA. The quantity of carbon monoxide that BD85D5B10 created was the lowest (25.86 g/kWh). BD85D5B10 had a minimal unburned hydrocarbon emission of 0.157 g/kWh while operating at full load. Oxides of nitrogen (NO_x) were emitted in the maximum quantity by BD85D5O10, which was equal to 6.01 g/kWh. This study establishes the viability of blends of biodiesel and alcohol as an alternative for petro-diesel in the future to meet the growing global energy demand.

Keywords: Biodiesel; Ternary blends; Performance; Combustion; Emission

Vol. 45(2024), No. 1, 109–118; doi: 10.24425/ather.2024.150443

Cite this manuscript as: Singh, A.K., Pali, H.S., & Khan, M.M. (2024). Experimental Investigations of CI Engine Performance using Ternary Blends of n-Butanol/Biodiesel/Diesel and n-Octanol/Biodiesel/Diesel. *Archives of Thermodynamics*, 45(1), 109–118.

1. Introduction

The increasing need for energy is closely related to the expansion of the human population. The need for energy has been satiated by petrochemicals and other products derived from petroleum. However, the world economy's utter reliance on fossil fuels is hastening the exhaustion of these resources and wreaking havoc on the environment [1]. The goal is to switch to renewable energy sources and abandon fossil fuels to slow down global warming [2]. Biodiesel, solar, wind, and tidal energy are popular alternatives. The most financially sound and ecologically responsible option currently available is biodiesel. It is made up of lipids derived from both plants and animals [3].

Nomenclature

Abbreviations and Acronyms

aTDC – after top dead centre
ASTM – American Society for Testing and Materials
bTDC – before top dead centre
BD85D5B10 – biodiesel (85%) + diesel (5%) + butanol (10%)
BD85D5O10 – biodiesel (85%) + diesel (5%) + octanol (10%)
BD90D5B5 – biodiesel (90%) + diesel (5%) + butanol (5%)
BD90D5O5 – biodiesel (90%) + diesel (5%) + octanol (5%)
BMEP – brake mean effective pressure
BSFC – brake specific fuel consumption
BTE – brake thermal efficiency
CI – compression ignition
CN – cetane number
CO – carbon monoxide
CO_2 – carbon dioxide
CRDI – common rail direct injection
UHC – unburnt hydrocarbon
HRR – heat release rate
ISO – International Organization for Standardization
NO_x – oxides of nitrogen
ppm – parts per million
WCO – waste cooking oil

.

Biodiesel's high manufacturing cost prevents commercialization. 70%–85% of biodiesel production costs are raw ingredients. Atabani et al. [4] observed that biodiesel production from waste cooking oil (WCO) can mitigate human activities' negative environmental effects. WCO must first be processed before being released into the environment for disposal. However, the cost of such pre-treatment is significant, leading to waste dumping directly into landfills. Correspondingly, Guarieiro et al. [5] reported that the US generated 10 million tonnes of soybean-derived waste cooking oil and China 4.5 million tonnes.

However, Suhaimi et al. [6] showed that biodiesel has some mechanical issues while operating on diesel engines, due to its low calorific value, high viscosity, and pour point. Alcohols and cold flow improvers have been tested to improve biodiesel quality [7]. Ramalingam et al. [8] showed that ethanol may increase chemical qualities. However, ethanol also changes other basic physico-chemical properties. Consequently, it develops a challenge to formulate an appropriate mixture that may effectively replace traditional diesel in diesel engines.

The disadvantage of lower alcohols, as Rosa [9] demonstrated, is that they are less solubilized and less miscible with diesel, and they are also more prone to separate at low temperatures. In a similar vein, Li et al. [10] found that carbon-rich alcohols would be used as a resource owing to the attributes that they possess in terms of both their thermal and physico-chemical properties. Cardoso et al. [11] reported significant cetane numbers for higher alcohols, easily miscible to diesel. Due to the positive stimulus of exhaust emissions, butanol has been recently accepted as a fuel additive in CI engines, according to Kumar et al. [12].

The diesel-1-pentanol combination was studied by Yesilyurt et al. [13] in a CI engine utilizing a range of blending ratios ranging from 10 to 25%. The blending ratios were presented in a diesel engine. It has been found that diesel engines can run on a mixture of diesel and pentanol, that is 75% pentanol and 25% diesel. This mixture may be used as a fuel. Kumar et al. [14] studied diesel engine performance and emissions using diesel-n-butanol binary mixes. The experimental study suggests diesel-butanol mixes might power the next generation engines in the near future. According to research conducted by Izzudin et al. [15], the ternary mixes of diesel, n-butanol and biodiesel were enhanced to reach higher performance levels while simultaneously reducing emissions. Diesel at a volumetric percentage of 65.5%, n-butanol at a volumetric concentration of 23.1%, and cotton seed oil at a volumetric concentration of 11.4% were determined to be the optimal concentrations. This occurs although the brakes use more fuel overall. When the matching mixes are employed, there is a significant reduction in the emissions of nitric oxide, carbon monoxide, and unburned hydrocarbons; the percentages of each are 11.33%, 45.17%, and 81.45%, respectively.

Charoensaeng et al. [16] investigated the use of mixtures of diesel, palm oil and n-butanol as an alternative fuel for diesel engines. In ternary blends, increasing the amount of butanol decreased NO_x, CO, CO_2 and smoke emissions while increasing unburned hydrocarbon (UHC) emissions and brake thermal efficiency.

The prominence of fine-tuning injection timing has increased due to recent advancements in alternative fuels, including biodiesel derived from renewable sources such as vegetable oils and animal fats, as well as higher alcohols like butanol and pentanol. Recent studies have demonstrated that the advancement of injection timing using biodiesel, due to its elevated cetane number, has the potential to improve thermal efficiency and mitigate the release of nitrogen oxides (NO_x) emissions. On the contrary, the adjustment of injection timing in a retarded manner may be deemed important in order to mitigate the occurrence of knock and effectively tackle premature combustion challenges. Furthermore, it has been observed in several studies, such as those conducted by Yan et al. [17] and Zhang et al. [18], that advancing the injection timing can enhance combustion efficiency and reduce particle emissions for higher alcohols.

The analysis of relevant material discussed earlier illustrates the relevance of biodiesel concerning the fulfilment of current fuel requirements. In addition to this, it discusses the advantages and disadvantages of using used cooking oil as a feedstock to create biodiesel. Research on diesel, biodiesel and higher alcohol blends in CI engines promotes alcohol use. Higher alcohols have a higher calorific value, cetane number, and diesel and biodiesel miscibility. The efficient use of biodiesel will reduce the amount of diesel needed. This study investigates the feasibility of using ternary blends of biodiesel, diesel and n-butanol or biodiesel, diesel and octanol in common rail direct-injection diesel engines with varying injection parameters that must be updated.

2. Materials and methods

Used cooking oil was the source material for the synthesis of biodiesel in this particular investigation. It was offered at vari-

ous restaurants in and around Srinagar in Jammu & Kashmir, India. The transesterification process synthesized methyl ester at the Renewable Energy and Alternative Fuel Lab of the National Institute of Technology in Srinagar, in Jammu & Kashmir. For a chemical reaction, potassium hydroxide and methanol were used, first as a catalyst and then, as a solvent. The following reaction parameters were used to achieve a biodiesel yield of 95.4%: a temperature of 60℃, a reaction period of 120 minutes, a molar ratio of 6:1, a catalyst concentration of 1.5%, and a stirrer speed of 1050 revolutions per minute. The biodiesel met all of the requirements outlined in the ASTM D6751 standard, including its colour, physical features and chemical properties. The properties of diesel, WCO and biodiesel are compared and contrasted in Table 1.

Biodiesel has a high viscosity, but its calorific value is relatively low. On the other hand, its cetane number is relatively high. The quantity of energy required to pump gasoline is increased as the viscosity of the fuel is increased since this results in less fuel being atomized during the spraying process. Alcohols and biodiesel were mixed to provide a solution to these problems. The incorporation of n-butanol and n-octanol into biodiesel helped to enhance its kinematic viscosity, as well as its cloud and pour points, and its density. In order to establish a composition that was consistent throughout, many different amounts of biodiesel-diesel-n-butanol and biodiesel-diesel-n-octanol were combined in a flask with a circular bottom using a magnetic stirrer. Between 0 and 100% of the total fuel, the proportion of each fuel was adjusted in 5% increments. A stability test lasting for four weeks was carried out on each combination while the circumstances remained the same. Because the other blends exhibited constraints such as a lower flash and fire point, miscibility, and calorific value, tests were conducted further for property characterization on blends that contained more than 85% biodiesel, 5% diesel, and 10% n-butanol. These blends met the criteria for selection.

The same behaviour was seen throughout various concentrations of biodiesel, diesel and n-octanol mixtures. Because the other blends exhibited limitations, including a lower flash and fire point, miscibility and calorific value, blends that contained 85% biodiesel, 5% diesel and 10% n-octanol were chosen for further property characterization. Blends with n-octanol content of more than 20% have flash and ignition temperatures lower than 32℃. As a consequence of this, the use of n-octanol combinations that have a higher concentration is very hazardous. Nomenclature for the test fuel blends is given in Table 2.

The fuel properties of biodiesel-diesel-n-butanol and biodiesel-diesel-n-octanol blends were used to choose the blends BD90D5B5, BD85D5B10, BD90D5O5 and BD85D5O10. These blends may be found in Table 3.

Table 1. Physico-chemical properties of diesel, waste cooking oil, and biodiesel.

Property	Diesel	WCO	Biodiesel	Limits	ASTM Standards
Density [kg/m³] at 15℃	828	916.7	876	860–890	D1298
Kinematic viscosity [cSt] at 40℃	2.39	42.53	4.76	1.9–6.0	D445
Flash point [℃]	60	327	120	60–190	D93
Fire point [℃]	54	332	160	-	D93
Cloud point [℃]	0	14	5	-	D2500
Calorific value [MJ/kg]	42	38.9	39.6	-	D1826

Table 2. Nomenclature of test fuel blends used.

Fuel	% of Biodiesel	% of Diesel	% of n-Butanol	% of n-Octanol
Biodiesel	100	-	-	-
Diesel	-	100	-	-
BD90D5B5	90	5	5	-
BD85D5B10	85	5	10	-
BD90D5O5	90	5	-	5
BD85D5O10	85	5	-	10

Table 3. Biodiesel, diesel, n-butanol, n-octanol, and biodiesel blends fuel characteristics.

Fuel	Biodiesel	Diesel	n-Butanol	n-Octanol	BD90D5B5	BD85D5B10	BD90D5O5	BD85D5O10
Density [kg/m³]	876	828	815	821	862.15	859.55	862.45	860.15
Kinematic viscosity [cSt]	4.76	2.39	2.89	5.32	3.6	2.55	3.8	4.07
Flash point [℃]	120	60	49	63	65	54	75	67
Cloud point [℃]	5	0	–32	–27	–2	–4	–2	–3
Pour point [℃]	–7	–15	–38	–32	–6	–9	–5	–6
Calorific value [MJ/kg]	39.6	42	34.65	37.1	40.21	40.05	40.44	40.15

3. Experimental setup and measurements

A 5.2 kW air cooled and common rail direct injection (CRDI) engine was operated at 1500 rpm, the injection pressure was set to 220 bar, and the injection time was varied from 17° to 29°CA bTDC. The engine's specifications are provided in Table 4. The engine's configuration is shown pictorially in Fig. 1. A differential air flow sensor is used to get the readings for the air velocity. Pressure is meticulously captured using piezoelectric sensors, synchronized with a crankshaft encoder. The sensors provide data at every 0.5°CA increment of crankshaft rotation, and this process is repeated for 100 cycles. To measure the flow of fuel, a regular burette was used. An eddy current dynamometer was coupled to the test engine to load the engine. The establishment of emissions present in the air was by using the AVL Digas analyzer. AVL smoke meter was used to determine the smoke opacity.

Table 4. Specification of Engine test rig.

Make & Model	KIRLOSKAR AV1
No. of strokes	Four stroke
Bore x stroke	80 mm x 110 mm
Injection pressure	220 bar
Volume	661 cc
Compression ratio	16.5:1
Rated power	5.2 kW
Rated speed	1500 rpm
Dynamometer	
Description	Specifications
Working principle	Eddy current
Arm length	185 mm
Speed	1200–2200
Power capacity	10 kW

During the tests, a string of one hundred cycles was continuously recorded. Then those data were fed into software to calculate the combustion parameter. The experiment used the ISO 8178 test cycles and mode number D2 as its guidelines. In order to guarantee the accuracy of the results, the measurements were carried out three times, and the analysis was carried out using an average of the results from all three attempts.

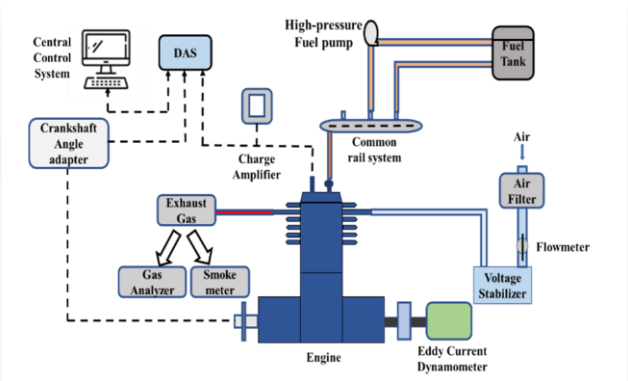

Fig. 1. Engine setup schematic diagram.

4. Results and discussion

Experiments were performed at the varying injection parameters from 17° to 29°CA bTDC for obtained test fuel blends and optimized parameters were found at 26°CA bTDC. Results are shown for the varying injection parameters with test fuel blends at 80% load, i.e. 5.2 bar and with varying load at 26°CA bTDC in the following sub-sections concerned with the engine performance, combustion and emissions.

4.1. Performance characteristics

4.1.1. Brake specific fuel consumption (BSFC)

Figure 2 illustrates the correlation between BSFC with injection timing and brake mean effective pressure (BMEP). BSFC indicates how efficiently engines convert fuel energy into useful work. As illustrated in Fig. 2(a), for biodiesel alcohol blends, the best BSFC is attained at retarded injection timing (26°CA bTDC) at 80% load whereas diesel gives the best results at 23°CA bTDC. Figure 2(b) illustrates the variation of BSFC for 26°CA bTDC. BSFC drops as the load on the engine increases from 0 to 100. The BSFC is higher at light loads but drops as the strain on the engine rises. The lowest specific fuel consumption for ternary blends is 0.292 kg/kWh for

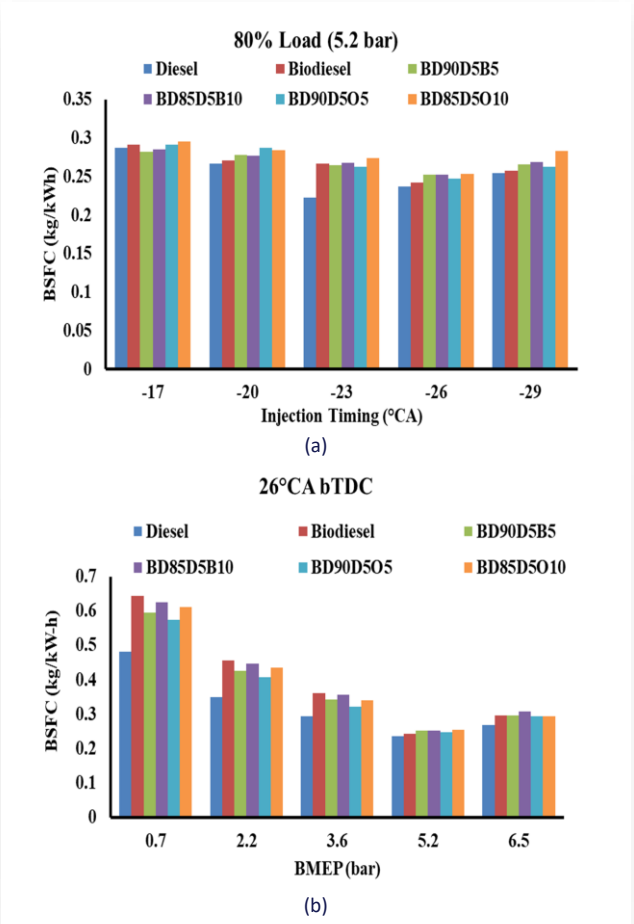

Fig. 2. Variation of BSFC with injection timing and BMEP.

BD90D5O10, which is 8.5% higher than diesel consumption but 5.1% lower than that of the BD85D5B10 mix. The BD85D5B10 blend uses the largest amount of fuel among all the ternary blends, at 0.308 kg/kWh. This is primarily because of the lower calorific value and higher viscosity of the blends. Because it has a lower calorific value than other fuels, biodiesel has the highest BSFC at 0.36 kg/kWh [19].

4.1.2. Brake thermal efficiency (BTE)

The relation between BTE with injection timing and brake mean effective pressure (BMEP) for a variety of combinations is seen in Fig. 3. In a diesel engine that uses compression ignition, BTE is established by the ratio of fuel to air, the compression ratio, the fuel's characteristics, and the fuel's combustion [20,21]. Figure 3(a) gives the variation of BTE with injection timing. It is found that diesel has the highest value of 32.2% at 23°CA bTDC for 80% load, while biodiesel blends have a peak BTE of 31.46% for BD90D5B5 at 26°CA bTDC. This is because blends of biodiesel, diesel and alcohol have a higher calorific value and low cetane number which allows for delayed combustion as compared to that of biodiesel alone [22]. Figure 3(b) depicts the variation of BTE at 26°CA bTDC for all fuel blends at varying load. BD90D5B5 had the highest BTE at 31.46%, which is 1.08% greater than that of biodiesel and 0.9% lower than that of diesel. Because of its higher viscosity and lowered calorific value, BTE for biodiesel is shown to have a lower value. At full load, the biodiesel-diesel-alcohol mix BD85D5B10 had the lowest thermal efficiency at the brakes at 28.15%. This is because biodiesel, diesel and n-octanol blends have a lower heating value but a more significant latent heat content than pure diesel or biodiesel alone [23].

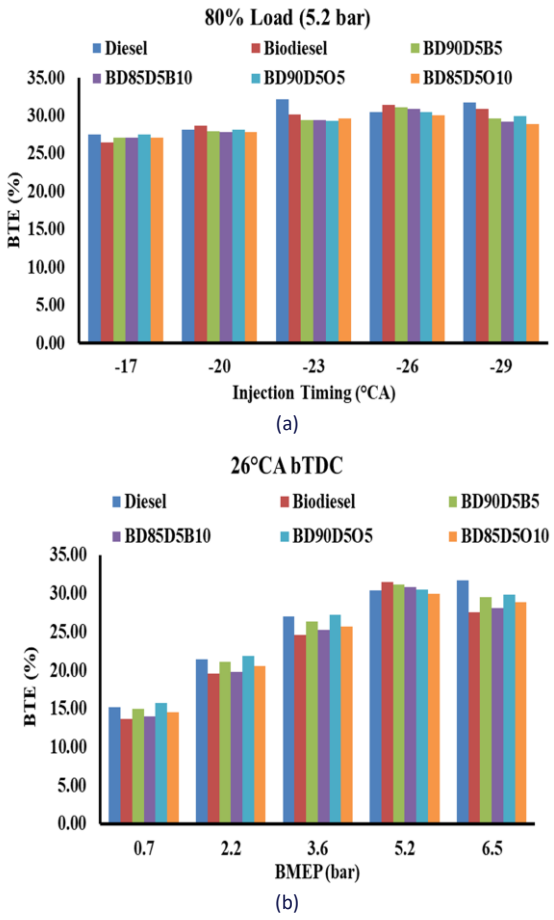

Fig. 3. Brake thermal efficiency variation with injection timing and BMEP.

4.2. Combustion characteristics

4.2.1. In-cylinder pressure

Figure 4 depicts the variation in peak pressure of the cylinder gas as a function of BMEP at 26°CA bTDC for mixtures of biodiesel, diesel and alcohol. The rise of in-cylinder gas pressure is directly proportional to the fuel used during the premixed combustion process. Because it has a higher cetane number than diesel, biodiesel has a shorter ignition delay than diesel. Because of the increased fuel evaporation rate, a high cetane number results in a shorter ignition delay time. Combustion using premixed air and fuel uses less fuel than combustion using diesel. When there is a decrease in cetane number (CN) for increased concentration of alcohols, the peak pressure of biodiesel goes down, while the peak pressure of the alcohol blend goes up [24]. In comparison to the other biodiesel-diesel-alcohol combinations, the fuel BD85D5O10 has the highest cylinder gas pressure at 2°CA aTDC when it is loaded to its maximum capacity. This pressure is the one that is most analogous to the diesel cylinder pressure. Subsequently, similar test fuels may be created; the longer the ignition delay the higher the gas pressure would be produced. Similar conclusion has been report by Gainey et al. [25].

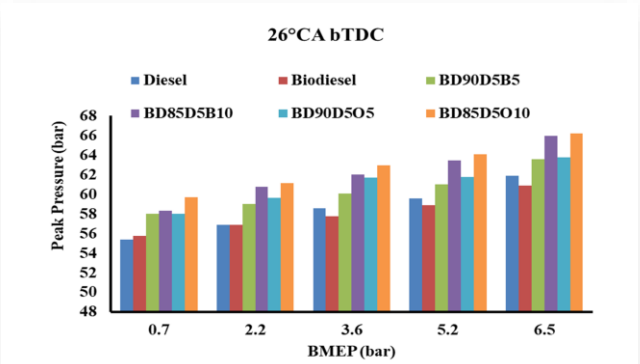

Fig. 4. Variation of in-cylinder peak pressure.

4.2.2. Heat release rate (HRR)

The heat release rate while operating under full load at 26°CA bTDC is shown in Fig. 5. The phases of combustion are called "premixed combustion", "controlled combustion" and "late combustion", respectively. During the ignition delay period, a negative slope is produced as a result of the cooling effect induced by fuel evaporation. When loaded to its maximum capacity, the BD90D5O5 blend has a heat release rate of 58.54 J/°CA. Because of its higher viscosity, lower rate of vaporization, larger molecular weight and slower burning velocity, biodiesel has a lower heat release rate than diesel. The biodiesel,

diesel and alcohol blends possess higher heat release rates comparable to diesel's heat release rate of 54.91 J/°CA. This is because a longer delay between ignition and combustion leads to a higher fuel deposit. When compared to biodiesel, blends of biodiesel and diesel with alcohol have a superior fuel-air combination, which results in a higher quantity of heat release [26].

4.2.3. Ignition delay

The ignition delay plays a role in the behaviour of the combustion process. The viscosity and density of the fuel govern the length of the physical delay. In contrast, the duration of the chemical delay is determined by the temperature and pressure of the combustion chamber, in addition to the swirl ratio and fuel properties [27]. The ignition delay of the test fuels at 26°CA bTDC is shown in Fig. 6. When increasing the load from 0% to 100%, the duration of the ignition delay drops to a lower value. All of the tested fuels had a shorter ignition delay observed when the load on the engine was low. This was because the temperature of the cylinder wall and the temperature of the residual gas were both lower, which caused the delay to last longer. The most considerable delay period for BD85D5B10 and BD85D5O10 blends was 13.7°CA and 13.95°CA, respectively, when the load was at its maximum capacity of 100%. This is comparable to the ignition delay in diesel engines. The ignition delay of biodiesel-diesel-n-butanol and biodiesel-diesel-n-octanol blends is longer than that of biodiesel alone. This is because both of these blends have a lower cetane number and a higher latent heat of vaporization [24].

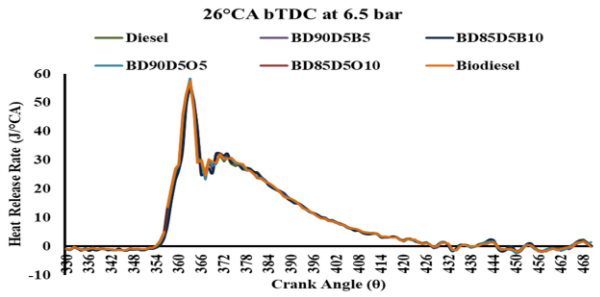

Fig. 5. Variation of heat release rate with crank angle at IT 26°CA bTDC.

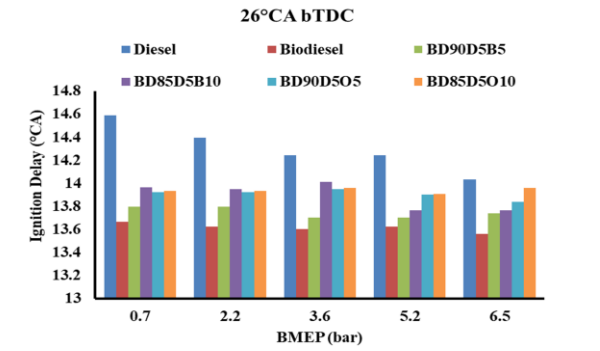

Fig. 6. Variation in ignition delay with BMEP.

4.3. Emission characteristics

4.3.1. Carbon monoxide (CO)

The variation in carbon monoxide (CO) emissions caused by combinations of biodiesel, diesel and alcohol is seen in Fig. 7. A rich fuel-air ratio and low oxygen content of blends increases the amount of carbon monoxide emissions. To reduce CO emissions, air must be heated [28]. Figure 7(a) shows that CO emissions of test fuel blends have been found lesser at 26°CA bTDC while diesel has lesser emissions at 23°CA bTDC. Biodiesel has more time to mix with air, leading to a more complete and controlled combustion process, which can further reduce CO emissions. Diesel has more CO emissions than biodiesel and ternary blends of biodiesel-diesel-alcohol at retarded injection timing. Figure 7(b) shows that the BD85D5B10 blend has the lowest CO emission rate of 25.86 g/kWh at full load condition at retarded injection timing of 26°CA bTDC, this rate is 36% lower than that of diesel. Because both biodiesel and alcohol fuels include oxygen as part of their chemical structure, they need less oxygen to complete the burning process. When more alcohol is added to mixtures of biodiesel, diesel and alcohol, CO emissions are reduced [29]. Because n-butanol fuel has a more considerable oxygen content than n-octanol fuel, biodiesel-diesel-n-butanol blends release less CO than biodiesel-diesel-n-octanol blends.

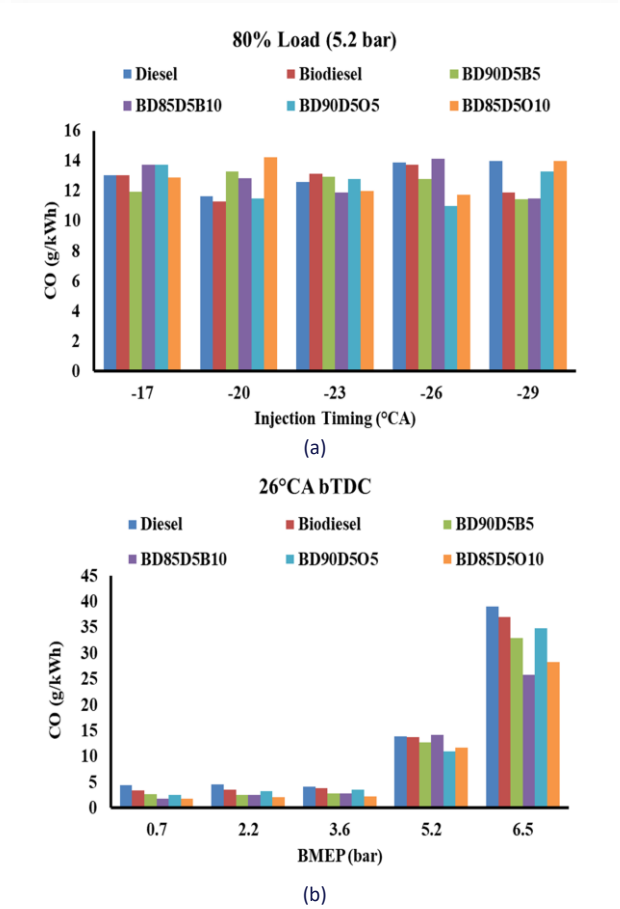

Fig. 7. Variation of carbon monoxide with injection timing and BMEP.

4.3.2. Unburnt hydrocarbons (HC)

When determining the overall quality of the combustion, hydrocarbon emissions are a crucial factor. The variation in the amount of unburned hydrocarbon emissions is seen in Fig. 8. When compared to diesel and biodiesel, biodiesel-diesel-alcohol combinations release less HC. Figure 8(a) has given best results for HC emissions at 26°CA bTDC, while diesel is characterized by lower HC emission at 23°CA bTDC. By delaying injection, biodiesel blends have more time to mix with air, leading to a more controlled and complete combustion process, which can further reduce HC emissions. Retarding injection further results in higher release of HC emissions. When operating at full capacity at 26°CA bTDC, Figure 8(b) shows that the BD85D5B10 engine has the lowest emissions. The unburned hydrocarbon content of BD85D5B10 is 0.157 g/kWh, which is 23.4% lower than that of diesel and 20.3% lower than that of biodiesel. The proportion of oxygen in biodiesel, diesel and alcohol blends directly correlates to the amount of emitted unburned hydrocarbons [30].

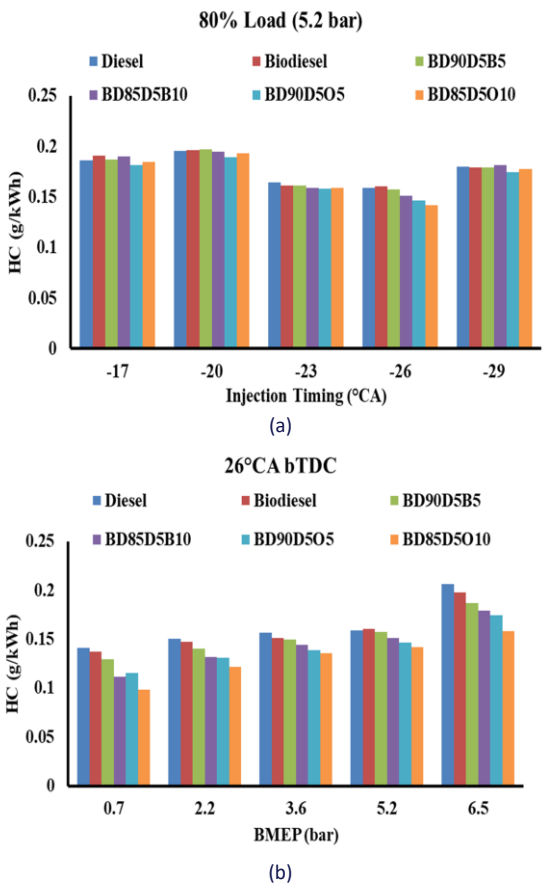

Fig. 8. Unburnt hydrocarbon variation with injection timing and BMEP.

4.3.3. Oxides of nitrogen (NO_x)

The oxygen content, in-cylinder temperature and residence duration are the three factors contributing to NO_x generation [31]. The impact that combinations of biodiesel, diesel and alcohol have on the emissions of NO_x is seen in Fig. 9. Figure 9(a) depicts variation of NO_x with varying injection timing. NO_x emissions increase for retarded injection timing due to the fact that retarded injection period can result in better combustion for biodiesel alcohol blends, leading to the formation of higher temperature combustion resulting in higher NO_x emissions at 29°CA bTDC. Figure 9(b) shows that NO_x emissions are lower for biodiesel-diesel-alcohol blends and for biodiesel than for diesel fuel at lower loads while higher at full load. The BD85D5O10 blend has a maximum NO_x emission of 6.01 g/kWh while operating under full load, which is 6.8% higher when compared to diesel at 26°CA bTDC. Because of their higher latent heat of vaporization and lower calorific value, n-butanol and n-octanol blends have a higher combustion temperature and generate more nitrogen oxide [24]. At full load, biodiesel's NO_x output is 5.45 g/kWh.

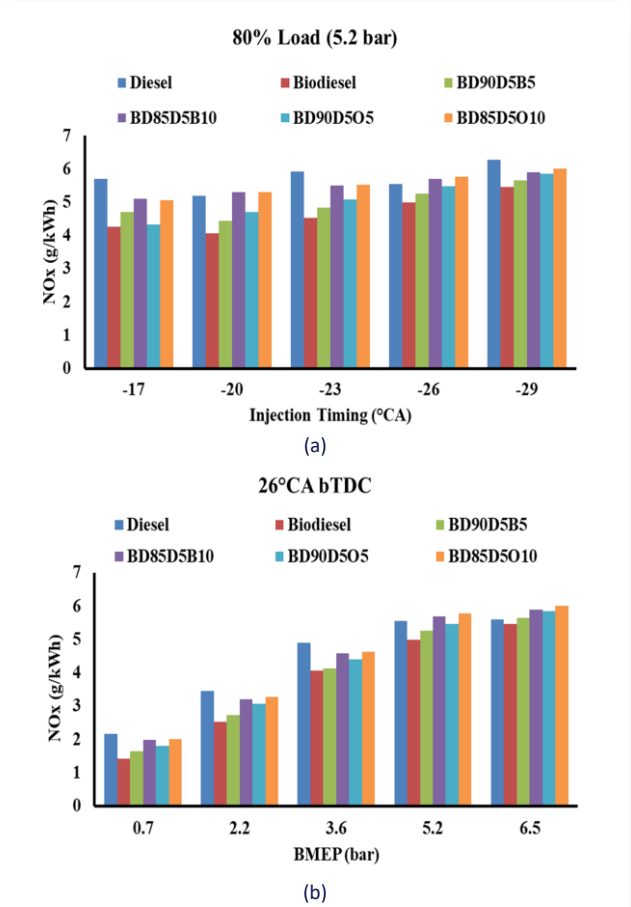

Fig. 9. Variation of oxides of nitrogen with injection timing and BMEP.

4.3.4. Smoke opacity

The range of smoke opacities produced by fuel blends is seen in Fig. 10. Figure 10(a) exhibits variation of smoke opacity percentage with various injection timing at 80% load. It shows that biodiesel-diesel-alcohol combinations yield lower smoke opacity than diesel at 26°CA bTDC. Because ester groups are present, biodiesel has oxygen molecules as part of its chemical makeup. This oxygen speeds up and promotes more thorough

combustion of biodiesel, which would lessen the production of smoke at retarded injection timing. Figure 10(b) shows the fluctuation of smoke opacity with load at 26°CA bTDC. The BD90D5B10 combination generates 34.55% less smoke than diesel at full load, yielding 21.71% less smoke than pure biodiesel. A higher amount of fuel injected into the engine's cylinders increases the amount of smoke generated at maximum load [32]. A longer ignition delay time and higher volatility can potentially improve the performance of fuel-air mixtures. To put it another way, the presence of oxygen in the fuel prevents the formation of soot [18].

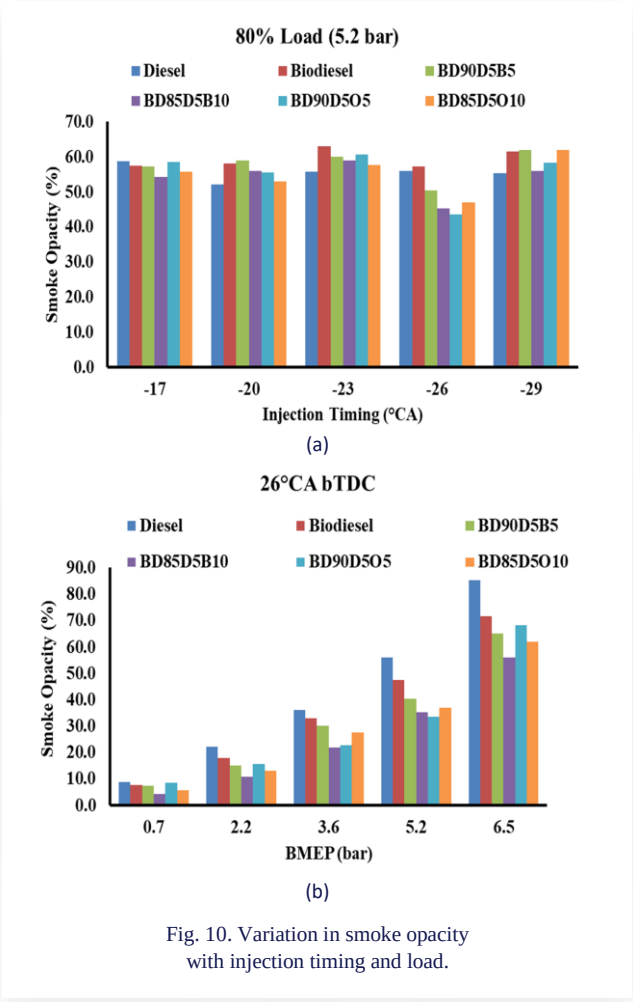

Fig. 10. Variation in smoke opacity with injection timing and load.

5. Conclusions

The fuel properties of biodiesel were enhanced by adding diesel, n-butanol and n-octanol as blending stocks. The 5% mix of diesel initiates the combustion of fuel due to a lower ignition temperature of diesel. Optimal outcomes for various fuel mixtures can be achieved by adjusting the injection time to 26°CA bTDC, which effectively balances performance, combustion efficiency and emissions. The chosen timing facilitates comprehensive mixing, resulting in a decrease in NO_x emissions, alongside producing cleaner combustion with a reduced amount of particle emissions. Consequently, this timing option is seen as advantageous for the purpose of sustainable and efficient engine running. The following outcomes are achieved from the research:

- The BD90D5O10 blend has the lowest BSFC when compared to the other blends at full load conditions when injected at 26°CA bTDC. Its performance was by 1.01% lower as compared to pure biodiesel and 8.5% superior to diesel. At injection timing of 23°CA bTDC, diesel has the lowest BSFC of 0.223 g/kWh for 80% loading.
- The BD90D5B5 blend has the highest BTE content (31.46%) of all the test fuel blends at full load with 26°CA bTDC. It was found by 1.08% higher than for biodiesel and comparable to that of diesel.
- At full load and 26°CA bTDC, the BD85D5O10 blend achieved the most significant in-cylinder pressure. Compared to diesel, it was 6.55% higher, while for biodiesel was 8.04% lower. The rate at which BD85D5O5 releases heat is the greatest. It had a lower energy content than diesel by 6.65% and higher than biodiesel by 5.65% for injection timing of 26°CA bTDC.
- The test fuel BD85D5B10 and BD85D5O10 blends at full load had a delay period of 13.7°CA and 13.95°CA, respectively, which was the most significant delay period.
- The CO emissions of test fuel blends were found to be lower at the injection timing of 26°CA bTDC, whereas diesel emissions were found to be lower at the injection timing of 23°CA bTDC. The BD85D5B10 blend had the lowest CO emission rate, which was 25.86 g/kWh at full load condition when the injection time is retarded to 26°CA bTDC. This amount is by 36% lower than diesel's value.
- The best results for HC emissions were achieved at 26°CA bTDC, although diesel had lower levels of HC emission at 23°CA bTDC. The unburned hydrocarbon content of BD85D5B10 was 0.157 g/kWh, which was lower by 20.3% than the unburned hydrocarbon content of biodiesel and lower by 23.4% than the unburned hydrocarbon content of diesel.
- There was an increase in NO_x formation at 29°CA bTDC when the injection time was retarded because of the fact that a retarded injection periods contribute to improved combustion for biodiesel alcohol blends. When operating at full load, the BD85D5O10 blend produced maximum NO_x emissions of 6.01 g/kWh, which were by 6.8% greater than the NO_x emission produced by diesel at 26°CA bTDC.
- At 26°CA bTDC, biodiesel-diesel-alcohol blends exhibited lower smoke opacity than diesel. At full load, the BD90D5B10 combination emitted 34.55% less smoke than diesel and 21.71% less smoke than pure biodiesel.

Performance and combustion were improved when diesel was blended with biodiesel, and the amounts of pollutants produced were reduced significantly. Consequently, biodiesel-diesel-n-butanol and biodiesel-diesel-n-octanol blends proved as feasible fuels for internal combustion engines.

References

[1] Singh, A.K., Sharma, A., & Kumar, N. (2014). *Performance and Emission Analysis of a CI Engine in Dual Mode with CNG and Karanja Oil Methyl Ester*. SAE Tech. Pap. doi: 10.4271/2014-01-2327

[2] Deep, A., Kumar, N., Kumar, M., Singh, A., Gupta, D., & Patel, J.S. (2015). *Performance and emission studies of diesel engine fuelled with orange peel oil and n-butanol alcohol blends*. SAE Tech. Pap. doi: 10.4271/2015-26-0049

[3] Kumar, N., & Pali, H.S. (2016). Effects of n-Butanol Blending with Jatropha Methyl Esters on Compression Ignition Engine. *Arabian Journal for Science and Engineering*. 41, 4327–36. doi: 10.1007/s13369-016-2127-1

[4] Atabani, A.E., & Al Kulthoom, S. (2020). Spectral, thermoanalytical characterizations, properties, engine and emission performance of complementary biodiesel-diesel-pentanol/octanol blends. *Fuel*, 282, 118849. doi: 10.1016/j.fuel.2020.118849

[5] Guarieiro, L.L.N., de Souza, A.F., Torres. E.A., & de Andrade, J.B. (2009). Emission profile of 18 carbonyl compounds, CO, CO2, and NOx emitted by a diesel engine fuelled with diesel and ternary blends containing diesel, ethanol and biodiesel or vegetable oils. *Atmospheric Environment*, 43, 2754–61. doi: 10.1016/J.ATMOSENV.2009.02.036

[6] Suhaimi, H., Adam, A., Mrwan, A.G., Abdullah, Z., Othman, M.F., Kamaruzzaman, M.K., et al. (2018). Analysis of combustion characteristics, engine performances and emissions of long-chain alcohol-diesel fuel blends. *Fuel*, 220, 682–91. doi: 10.1016/j.fuel.2018.02.019

[7] Pali, H.S., Sharma, A., Kumar, M., Annakodi, V.A., Nguyen, V.N., Singh, N.K., et al. (2022). Enhancement of combustion characteristics of waste cooking oil biodiesel using TiO2 nanofluid blends through RSM. *Fuel*, 331, 125681. doi: 10.1016/j.fuel. 2022.125681

[8] Ramalingam, S., & Mahalakshmi, N.V. (2020). Influence of Moringa oleifera biodiesel-diesel-hexanol and biodiesel-diesel-ethanol blends on compression ignition engine performance, combustion and emission characteristics. *RSC Advances*, 10, 4274–85. doi: 10.1039/c9ra09582a

[9] Rosa, J.S., Altafini, C.R., Wander, P.R., Telli, G.D., & Rocha L.A.O. (2019). Wet ethanol fumigation on a compression ignition engine: effects of air intake throttled. *Journal of the Brazilian Society of Mechanical Sciences*, 41, 1–16. doi: 10.1007/s40430-019-2023-1

[10] Li, Y., Tang, W., Abubakar, S., & Wu, G. (2020). Construction of a compact skeletal mechanism for acetone–n–butanol–ethanol (ABE)/diesel blends combustion in engines using a decoupling methodology. *Fuel Processing Technology*, 209, 106526. doi: 10.1016/j.fuproc.2020.106526

[11] Cardoso, C.C., Celante, V.G., De Castro, E.V.R., & Pasa, V.M.D. (2014). Comparison of the properties of special biofuels from palm oil and its fractions synthesized with various alcohols. *Fuel*, 135, 406–412. doi: 10.1016/j.fuel.2014.07.019

[12] Kumar, N., & Sidharth. (2018). Some Studies on use of ternary blends of diesel, biodiesel and n-octanol. *Energy Sources, Part A: Recovery, Utilization, and Environmental Effects*, 40, 1721–1728. doi: 10.1080/15567036.2018.1486902

[13] Yesilyurt, M.K., Yilbasi, Z., & Aydin, M. (2020). The performance, emissions, and combustion characteristics of an unmodified diesel engine running on the ternary blends of pentanol/safflower oil biodiesel/diesel fuel. *Journal of Thermal Analysis and Calorimetry*, 140, 2903–294. doi: 10.1007/s10973-020-09376-6

[14] Kumar, N., Bansal, S., Vibhanshu, V., & Singh, A. (20123). *Utilization of blends of Jatropha Oil and N-butanol in a naturally aspirated compression ignition engine*. SAE Tech. Pap., doi: 10.4271/2013-01-2684

[15] Izzudin, I., Yusop, A.F., Sapee, S., Hamidi, M.A., Yusri, I.M., Mamat, R., et al. (2020). Experimental studies of single cylinder engine run on diesel-biodiesel-butanol blends. *IOP Conference Series: Materials Science and Engineering*, 863. doi: 10.1088/1757-899X/863/1/012060

[16] Charoensaeng, A., Khaodhiar, S., Sabatini, D.A., & Arpornpong, N. (2018). Exhaust emissions of a diesel engine using ethanol-in-palm oil/diesel microemulsion-based biofuels. *Environmental Engineering Research*, 23, 242–249. doi: 10.4491/eer.2017.204

[17] Yan, J., Gao, S., Zhao, W., & Lee, T.H. (2021). Study of combustion and emission characteristics of a diesel engine fueled with diesel, butanol-diesel and hexanol-diesel mixtures under low intake pressure conditions. *Energy Conversion and Management*, 243, 114273. doi: 10.1016/j.enconman.2021.114273

[18] Zhang, T., Munch, K., & Denbratt, I. (2015). An Experimental Study on the Use of Butanol or Octanol Blends in a Heavy Duty Diesel Engine. *SAE International Journal of Fuels and Lubricants*, 8, 610–621. doi: 10.4271/2015-24-2491

[19] Kumar, K., & Sharma, M.P. (2016). Performance and emission characteristics of a diesel engine fuelled with biodiesel blends. *International Journal of Renewable Energy Research*, 6, 658–62. doi: 0.5383/ijtee.13.02.007

[20] Sharbuddin Ali, S., & Swaminathan, M.R. (2020). Effective utilization of waste cooking oil in a diesel engine equipped with CRDi system using C8 oxygenates as additives for cleaner emission. *Fuel*, 275, 118003. doi: 10.1016/j.fuel.2020.118003

[21] Pradeepraj, R., & Rajan, K. (2020). Performance Analysis of Diesel Engine using Moringa Oil Methyl Ester with Fumigation Technique. *International Journal of Innovative Technology and Exploring Engineering*, 9, 1783–1786. doi: 10.35940/ijitee.b7242.019320

[22] Patil, K.R., & Thipse, S.S. (2015). Experimental investigation of CI engine combustion, performance and emissions in DEE–kerosene–diesel blends of high DEE concentration. *Energy Conversion and Management*, 89, 396–408. doi: 10.1016/j.enconman.2014.10.022

[23] Atelge, M.R. (2022). Investigation of a ternary blend of diesel/ethanol/n-butanol with binary nano additives on combustion and emission: A modeling and optimization approach with artificial neural networks. *Fuel Processing Technology*, 229, 107155. doi: 10.1016/j.fuproc.2021.107155

[24] Santhosh, K., & Kumar, G.N. (2020). Impact of 1-Hexanol/diesel blends on combustion, performance and emission characteristics of CRDI CI mini truck engine under the influence of EGR. *Energy Conversion and Management*, 217, 113003. doi: 10.1016/j.enconman.2020.113003

[25] Gainey, B., & Lawler, B. (2021). The role of alcohol biofuels in advanced combustion: An analysis. *Fuel*, 283, 118915. doi: 10.1016/j.fuel.2020.118915

[26] Pan, W., Yao, C., Han, G., Wei, H., & Wang, Q. (2015). The impact of intake air temperature on performance and exhaust emissions of a diesel methanol dual fuel engine. *Fuel*, 162, 101–110. doi: 10.1016/j.fuel.2015.08.073

[27] Thomas, J.J., Manojkumar, C.V., Sabu, V.R., & Nagarajan, G. (2020). Development and validation of a reduced chemical kinetic model for used vegetable oil biodiesel/1-Hexanol blend for engine application. *Fuel*, 273, 117780. doi: 10.1016/j.fuel.2020.117780

[28] Singh, D., Sharma, D., Soni, S.L., Inda, C.S., Sharma, S., Sharma, P.K., et al. (2021). A comprehensive review of biodiesel production from waste cooking oil and its use as fuel in compression ignition engines: 3rd generation cleaner feedstock. *Journal of Cleaner Production*, 307, 127299. doi: 10.1016/j.jclepro.2021.127299

[29] Jamrozik, A., Tutak, W., Pyrc, M., Gruca, M., & Kočiško, M. (2018). Study on co-combustion of diesel fuel with oxygenated

alcohols in a compression ignition dual-fuel engine. *Fuel*, 221, 329–345. doi: 10.1016/j.fuel.2018.02.098

[30] No, S.Y. (2020). Utilization of Pentanol as Biofuels in Compression Ignition Engines. *Frontiers in Mechanical Engineering*, 6, 1–19. doi: 10.3389/fmech.2020.00015

[31] Aldhaidhawi, M., Chiriac, R., & Badescu, V. (2017). Ignition delay, combustion and emission characteristics of Diesel engine fueled with rapeseed biodiesel – A literature review. *Renewable* and *Sustainable Energy Reviews*, 73, 178–86. doi: 10.1016/j.rser.2017.01.129

[32] Teoh, Y.H., Yu, K.H., How, H.G., & Nguyen, H.T. (2019). Experimental investigation of performance, emission and combustion characteristics of a common-rail diesel engine fuelled with bioethanol as a fuel additive in coconut oil biodiesel blends. *Energies*, 12, 1–17. doi: 10.3390/en12101954

Co-published by
Institute of Fluid-Flow Machinery
Polish Academy of Sciences
Committee on Thermodynamics and Combustion
Polish Academy of Sciences

http://www.imp.gda.pl/archives-of-thermodynamics/

Experimental validation of a dynamic lumped parameter model of an automotive cabin

Ramon de Paoli Mendes[a], Juan José Garcia Pabon[b], Willian Moreira Duarte[a], Luiz Machado[a]

[a]Federal University of Minas Gerais, Av. Pres. Antônio Carlos, Belo Horizonte/MG 31270-901, Brazil
[a]Federal University of Itajubá, Av.. BPS, Itajubá/MG 37500 903, Brazil
*Corresponding author email: ramondepaoli@yahoo.com.br

Received: 12.06.2023; revised: 09.10.2023; accepted: 06.12.2023

Abstract

The objective of this work is to propose a thermal model for predicting the average air temperature inside the passenger cabin of a small-sized car that uses an HVAC system. The adopted model is a lumped parameter model that accounts for nine heat sources acting on the cabin. Additionally, the model presents a methodology for calculating the temperature at the evaporator outlet considering a linear temperature drop between its inlet and outlet as a function of sensitive heat, latent heat, evaporator input temperature, absolute humidity, enthalpy and specific heat. Sixteen experimental tests were conducted on a commercial vehicle under various operating conditions to validate the presented model. The maximum average relative deviation between the experimental and theoretical results was 17.73%.

Keywords: Thermal model; Automotive cabin; HVAC

Vol. 45(2024), No. 1, 119–128; doi: 10.24425/ather.2024.150444

Cite this manuscript as: de Paoli Mendes, R., Garcia Pabon, J.J., Moreira Duarte, W., & Machado, L. (2024). Experimental validation of a dynamic lumped parameter model of an automotive cabin. *Archives of Thermodynamics* 45(1), 119–128.

1. Introduction

The temperature control in the automotive cabin constitutes the main objective of the vehicle's HVAC system. The search for thermal comfort increases the consumption of the air conditioning system and consequently the fuel consumption. The use of air conditioning leads to an increase in total fuel consumption of 23 to 41% [1]. Additionally, in the United States alone, before 2004 around 26 billion liters of fuel were used annually, to ensure passenger thermal comfort [2].

Some of the most commonly used criteria for evaluating thermal comfort, such as the predicted mean vote (PMV) and the percentage of dissatisfied people (PPD), use the thermal energy stored in the human body and individual metabolic rate as a reference for evaluation [3,4]. The PMV and PPD equations can be found in ISO 7730 standard [5]. Both PMV and PPD depend on the cabin temperature, which is why it is necessary to understand how the cabin temperature varies.

In this sense, Shimizu et al. [6] investigated the transient thermal loads acting on the automotive cabin. In their article, they showed that in the air conditioning recirculation mode, the main thermal load is radiation, accounting for about 50% of the total. However, when air renewal is enabled, the main thermal

Nomenclature

A – area, m^2
B – extinction coefficient
C – specific heat at constant pressure, J/ (kg K)
C – solar radiation factor
h – enthalpy, J/kg
H – heat exchange coefficient, W/(m² K)
$\dot{I}$ – solar irradiance, W/m²
k – thermal conductivity, W/ (m K)
m – mass, kg
$\dot{m}$ – mass flow rate, kg/s
n – rotation speed, rpm
N – number
P – pressure, Pa
$\dot{Q}$ – thermal load, W
T – temperature, ºC
U – overall heat transfer coefficient, W/(m² K)
Y – radiation ratio
V – speed, km/h

Greek symbols

α – angle with the horizontal, rad
β – solar angle, rad
ϕ – relative humidity [%]
λ – plate thickness, m
θ – angle of solar incidence, rad
ρ – reflectivity coefficient
τ – transmissivity
ω – absolute humidity

Subscripts and Superscripts

amb – environmental
ap – apparent
air – air
atm – atmospheric
c – clarity
cab – cabin
dif – diffuse solar radiation
dir – direct solar radiation
e – external
eev – evaporator inlet
exa – exhaustion
$hvac$ – air conditioning system
i – internal
ind – indirect solar radiation
lat – latent
lv – steaming
met – metabolic
mot – engine
p – people
ref – reflected solar radiation
ren – renovation
rec – recirculation
s – saturation
sev – evaporator output
sen – sensitive
$vent$ –ventilation
w – water
z – Zenith

Abbreviations and Acronyms

MARD– Mean Absolute Relative Deviation
PMV – predicted mean vote
PPD – percentage of dissatisfied people

load to be countered is the ventilation thermal load, corresponding to about 50% of the total. Michalek et al. [7] considered the energy balance in the automotive cabin as the sum of metabolic loads, loads that pass through the windows, and loads inside the vehicle, such as infiltration and engine loads. In their work, the energy balance was written considering the average temperature of the automotive cabin, and the comparison of the dynamic model with experimental results obtained good proximity. Khayyam et al. [8] described in their work the modeling of the automotive cabin as a function of the thermal loads acting on it. In their work, they considered the metabolic thermal loads, direct solar radiation, diffuse solar radiation, reflected solar radiation, environmental radiation, exhaust system load, motor load, ventilation load, and HVAC load. Jha et al. [9] proposed in their model that the main thermal loads are solar radiation, infiltration thermal load, fan motor thermal load, internal combustion engine thermal load, floor load, and metabolic thermal load. The method used by Jha et al. [9], as well as by Khayyam et al. [8] to calculate solar radiation is presented in the ASHRAE handbook [10]. In the study of Khayyam et al. [8], the model is used in conjunction with an energy management system achieving a 47% reduction in energy consumption. In the research presented by Jha et al. [9], the model is validated in a wind tunnel and steady-state conditions, with the largest difference between predictions and experimental results being 15%.

Marcos et al. [11] calculated the metabolic thermal load using the ISO 7730 standard. The window thermal load was determined by adding the thermal loads that entered through convection due to the temperature difference between the glass and the cabin air. The authors found the temperature of the glass by performing thermodynamic balance on it, considering a steady state. In their model, the authors considered that the energy fraction that enters through the opaque lateral and rear parts of the vehicle is negligible compared to the thermal load that enters through the windows. They validated the presented model using experimental data measured in a BMW series 1 with different types of occupancy and speed, and the largest difference between experimental results and simulations was 4.6°C. Torregrosa-Jaime et al. [12] presented a similar work, where they developed and validated a thermal model for an ALTRA Daily electric van.

Fayazbakhsh and Bahrami [13] described a transient thermal model of the automotive cabin, similar to the one presented by Khayyam et al. [8]. They calculated the direct, diffuse, and reflected incident radiation using the method proposed by ASHRAE [10] and determined the enthalpies of humid air using the equations presented by Wilhelm [14]. Their work showed that the thermal loads from reflected radiation, the engine, and the exhaust were negligible, while the thermal loads from direct radiation and ventilation had the most significant impact on the total thermal load of the cabin.

Lee et al. [15] proposed a transient model to predict the internal temperature of a car cabin. The model assumed that the air properties inside the cabin are spatially uniform, the thermal load of passengers is 158 W per person, heat exchange by radiation between internal components of the cabin is negligible, the heat transfer coefficient between the cabin and the environment is calculated as a function of vehicle speed, and thermal loads from the floor and trunk are negligible. The authors also considered that the transmissivity and absorptivity properties are dependent on the angle of incidence of the radiation and modeled these properties according to the ASHRAE [16]. They validated the model in a climate chamber with a roller dynamometer, and the deviation between the model results was 5%. Finally, the authors used the model to simulate modifications in the vapor compression cycle and compared the performance of the air conditioning system operating with the refrigerants R134a, R152a, R444A, R445A, and R1234yf, with the latter being the best-performing fluid. Selow et al. [17] presented a similar work, including a model of the car cabin in the air conditioning system, but they used an empirical model for the car cabin.

Due to new vehicle technologies such as electric or hybrid cars, it becomes necessary to understand how the various systems that compose them affect the consumption of electrical energy by the vehicle and how this impacts the used battery. In this sense, the works of Ramsey et al. [18], and Liu and Zhang [19] address the thermal modeling of the automotive cabin, focusing on how the HVAC system impacts the vehicle's energy consumption. For larger vehicles, the same thermal loads act upon them. However, considering the properties of air as homogeneous throughout the entire vehicle is not possible. In this regard, Delgado et al. [20] studied the thermal modeling of a bus and obtained results for separate regions between passengers and the driver.

As regards the finite volume technique, it has a relatively high computational cost compared to the concentrated parameter model used in the aforementioned works. There are many studies using the finite volume simulation approach [21–23]. The use of finite volume techniques for thermal modeling of environments in many situations is due to the lack of knowledge of the equations that model a given process. For example, a thermal model of the automotive cabin that considers the inflow temperature through the HVAC system analytically was found only in Ramsey´s work [18] and it utilizes the entropy information at the inlet and outlet of the evaporator to calculate the evaporator's outlet temperature.

Therefore, this study not only thermally models the cabin but also adds a methodology for calculating the inflow air temperature in the cabin, as a function of sensitive heat, latent heat, evaporator input temperature, absolute humidity, enthalpy, and specific heat. This approach allows the modeling of the temperature at the evaporator outlet considering a linear drop with its inlet. It serves as a temperature estimate for the calculation of the refrigerating thermal load. In the following chapter, the thermal model is presented, followed by a description of the apparatus and experimental conditions used for comparative analysis with experimental data. Next, the results are evaluated and discussed, and finally, the conclusions are drawn.

2. Thermal model

Geometrically, the automotive cabin was modeled in 10 parts: front panel and glass, right and left side panels, right and left side glass, roof, floor, rear panel, and rear glass. Figure 1 presents the modeling of the car separated into opaque and translucent parts. The car parts were used in the thermal load calculations and the individual areas are represented in Table 1.

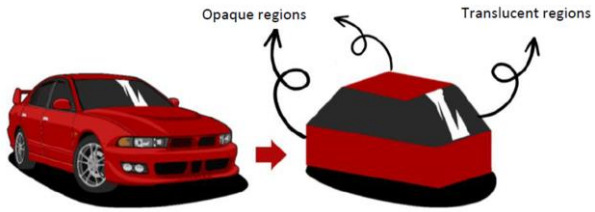

Fig. 1. Automotive cabin regions.

To quantify the thermal loads inside the cabin, knowledge of the dimensions of each region and, also, of the properties of the materials is necessary. Table 1 shows the area, surface inclination relative to the horizontal, and transmissivity of the glass, which were obtained based on the SpaceFox vehicle used in the model validation.

Table 1. Geometric model information.

Surface	Area [m²]	Inclination [deg]	Transmissivity
Front glass	0.936	30	0.78
Left side glass	0.7339	80	0.36
Right side glass	0.7339	80	0.36
Rear window	0.576	30	0.78
Roof	3.6	–	–
Right panel	3.26	–	–
Left panel	3.26	–	–
Front panel	0.66	–	–
Floor	3.6	–	–
Rear panel	0.66	–	–

This model considers 9 types of thermal loads acting on the cabin. These include the metabolic thermal load ($\dot{Q}_{met}$), direct solar radiation thermal load ($\dot{Q}_{dir}$), diffuse solar radiation thermal load ($\dot{Q}_{dif}$), reflected solar radiation thermal load ($\dot{Q}_{ref}$), internal combustion engine thermal load ($\dot{Q}_{mot}$), exhaust system thermal load ($\dot{Q}_{exa}$), environmental thermal load ($\dot{Q}_{amb}$), ventilation thermal load ($\dot{Q}_{vent}$), and HVAC system thermal load ($\dot{Q}_{hvac}$). The variation of the cabin's average temperature (T_{cab}) over time can be calculated as a function of the sum of the thermal loads entering the cabin:

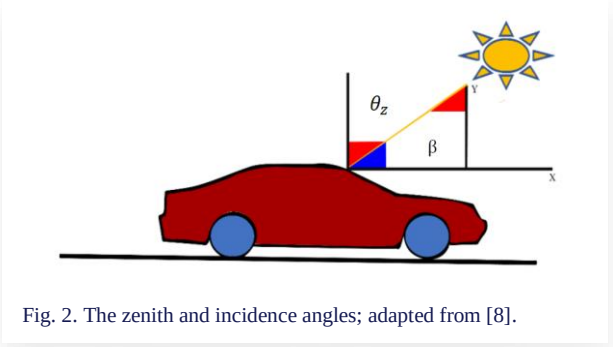

Fig. 2. The zenith and incidence angles; adapted from [8].

$$m_{cab} \cdot c \cdot \frac{dT_{cab}}{dt} = \dot{Q}_{met} + \dot{Q}_{dir} + \dot{Q}_{dif} + \dot{Q}_{ref} + \dot{Q}_{amb} + \dot{Q}_{exa} + \dot{Q}_{mot} + \dot{Q}_{vent} - \dot{Q}_{hvac}, \quad (1)$$

where m_{cab} represents the total mass of the cabin and c denotes its specific heat. However, the temperature of the solid elements inside the cabin differs from the average air temperature. The mass of the solid elements in the cabin and the thermal properties of the materials allow separate balancing of the heating (or cooling) of these elements over time and the calculation of their temperature change, and thus the accumulated heat.

The main simplifications made in the developed model are:

- The cabin mass (m_{cab}) is the sum of the air mass and the mass of seats.
- The specific heat capacity of the cabin (c) is the average between the specific heat capacity of the air and that of the seats.
- The energy exchanged through radiation and convection between the internal components of the cabin, air, and seats is negligible.
- Relative humidity at the evaporator outlet is equal to 0.9.

The calculation results were compared with experimental data.

2.1. Metabolic thermal load

The metabolic thermal load is the thermal load originating from the passengers occupying the automotive cabin. It can be determined based on the height and weight of the occupants as mentioned by Fayazbakhsh and Bahrami [13], but the value per person is around 100 W [10] and this value is adopted in the present model. The total metabolic thermal load is given by:

$$\dot{Q}_{met} = N_p \cdot 100, \quad (2)$$

where N_p represents the number of occupants in the cabin.

2.2. Direct solar radiation thermal load

The direct solar radiation thermal load ($\dot{Q}_{dir}$) is expressed as:

$$\dot{Q}_{dir} = \sum(\dot{I}_{dir} \cdot \tau \cdot A), \quad (3)$$

where A denotes the surface area of the car part described in Table 1, and $\dot{I}_{dir}$ is the direct solar irradiance. The portion of the radiation transmitted to the cabin must take into account the transmissivity (τ) of the material. The transmissivity of the glass was determined according to the instructions provided in the ASHRAE handbook [16], and its methodology has been evaluated in the work of Lee et al. [15]. The direct solar irradiance is calculated based on the apparent solar irradiation ($\dot{I}_{ap}$), the extinction coefficient (B), the zenith angle (θ_z), and the solar angle (β), according to the equation:

$$\dot{I}_{dir} = \dot{I}_{ap} \cdot N_c \cdot e^{(-B \cdot \mathrm{sen}(\beta))}, \quad (4)$$

where β is the solar elevation angle (Fig. 2) measured between the sun's rays and the horizontal at the point of incidence and N_c represents the clarity number. Parameter $\mathrm{sen}(\beta)$ allows the calculation of $\dot{I}_{dir}$ to vary depending on the position of the sun in relation to the angle of incidence. The zenith angle (θ_z) is the angle between the sun's rays and the normal to the surface (Fig. 2). The extinction coefficient (B) and the apparent solar radiation ($\dot{I}_{ap}$) were determined according to ASHRAE [10] for all months of the year 1964 in the USA. The value of the extinction coefficient was researched by Horvath [24] and in this work, a value of 0.15 is considered. The value of apparent solar radiation ($\dot{I}_{ap}$) accepted varies from 1367 W/m² to 1413 W/m² [25]. In this study, a value of 1413 W/m² is used. The clarity number (N_c) was determined in the ASHRAE handbook [26], and it is reasonable to consider it equal to 1.

2.3. Diffused solar radiation thermal load

Diffuse solar radiation is part of the radiation that indirectly strikes the surface of the automobile. It is calculated by multiplying the surface area by the indirect solar irradiance ($\dot{I}_{ind}$):

$$\dot{Q}_{dif} = \sum(\dot{I}_{ind} \cdot \tau \cdot A). \quad (5)$$

Diffuse solar radiation can be broken down into components that strike vertical and non-vertical surfaces. For vertical surfaces, it is necessary to calculate the ratio (Y) of the diffuse sky radiation to the surface radiation [10]:

$$Y = 0.55 + 0.437\cos(\theta_z) + 0.313\cos^2(\theta_z), \quad \text{for } \cos(\theta_z) > -0.2,$$

$$Y = 0.45\alpha, \quad \text{for } \cos(\theta_z) \leq -0.2.$$

Further, $\dot{I}_{ind}$ depends on the solar radiation factor (C) and the angle the surface makes with the horizontal (α). This yields for vertical surfaces:

$$\dot{I}_{ind} = C \cdot Y \cdot \dot{I}_{dir}, \quad (6)$$

and for other surfaces:

$$\dot{I}_{ind} = C \cdot \dot{I}_{dir} \cdot \frac{(1+\cos(\alpha))}{2}. \quad (7)$$

2.4. Reflected solar radiation thermal load

Reflected solar radiation is part of the radiation that strikes the surface of the automobile after being reflected by clouds, the ground, and the surrounding objects and may be expressed as:

$$\dot{Q}_{ref} = \sum(\dot{I}_{ref} \cdot \tau \cdot A), \quad (8)$$

where $\dot{I}_{ref}$ denotes the reflected solar irradiance, which depends on the direct solar irradiance and the ground reflectivity coefficient (ρ):

$$\dot{I}_{ref} = \dot{I}_{dir} \cdot (C + \sin(\beta)) \cdot \rho \cdot \frac{(1-\cos(\alpha))}{2}. \quad (9)$$

The reflectivity coefficient ρ can be considered equal to 0.28 second ASHRAE [10]. Parameter C can be determined according to Table 7 of Chapter 30 of ASHRAE [10].

2.5. Environmental thermal load

The environmental thermal load is calculated based on the temperature difference between the cabin air (T_{cab}) and the ambient air (T_{amb}):

$$\dot{Q}_{amb} = \sum(A \cdot U \cdot (T_{amb} - T_{cab})), \quad (10)$$

where U is the overall heat transfer coefficient, calculated as the inverse of thermal resistance. It considers the heat transfer coefficient by convection of the internal cabin air (H_i), the heat transfer coefficient of the external cabin air (H_e), the thermal conductivity of the surface (k), and its thickness (λ). The external heat transfer coefficient by convection can be determined from [27]:

$$H_e = 1.163 \cdot (4 + 12 \cdot V^{0.5}), \quad (11)$$

where V represents the air velocity if the vehicle is stationary, or the speed of the automobile if it is in motion. The internal heat transfer coefficient can be calculated considering natural convection inside the automotive cabin [28]. According to Creder [29], considering stationary air, the heat transfer coefficient varies from 8.29 to 9.26 W/(m² K). In the present study, an average value of 8.77 W/(m² K) is considered.

2.6. Exhaust thermal load

Due to the temperature difference between the motor exhaust gases and the cabin, part of the energy is transferred to the cabin through the floor. Thus:

$$\dot{Q}_{exa} = A_{exa} \cdot U_{exa} \cdot (T_{exa} - T_{cab}). \quad (12)$$

In the equation above, A_{exa} is the contact area between the cabin surface and the automobile exhaust pipe. The overall heat transfer coefficient U_{exa} can be calculated as the inverse of the thermal resistance between the exhaust pipe surface and the automobile cabin. The internal heat transfer coefficient to the cabin is calculated as described with regard to the calculation of the ambient thermal load (Eq. (10)). Finally, the temperature of the exhaust gases can be estimated as [8]:

$$T_{exa} = 0.138 \cdot n + 63, \quad (13)$$

where n is the car engine's angular speed.

2.7. Internal combustion engine thermal load

The internal combustion engine reaches high temperatures, and as a result, heat transfer occurs to the cabin through the front surface (A_{mot}). The resulting thermal load is expressed by:

$$\dot{Q}_{mot} = A_{mot} \cdot U_{mot} \cdot (T_{mot} - T_{cab}), \quad (14)$$

where U_{mot} represents the heat transfer coefficient from the engine, which can be determined as the inverse of the thermal resistance between the engine and the automotive cabin. The temperature of the engine (T_{mot}) can be estimated as a function of its rotation speed [8]:

$$T_{mot} = -2 \cdot 10^{-6} \cdot n^2 + 0.0355 \cdot n + 77.5. \quad (15)$$

2.8. Ventilation thermal load

When breathing, passengers release CO_2 inside the cabin, therefore air renewal is required. There are different percentages of air renewal relative to the total air mass of the cabin for different automotive vehicles. A minimum of 13% of fresh air relative to the total cabin volume for one passenger and 48% of fresh air for four passengers is recommended [30].

The ventilation thermal load can be calculated as a function of the mass flow rate of ventilation air ($\dot{m}_{air}$) - a mixture of the mass flow rate of fresh air and recirculated air - and the difference in enthalpy between the air at ambient temperature (h_{amb}) and the air at cabin temperature (h_{cab}):

$$\dot{Q}_{vent} = \dot{m}_{air} \cdot (h_{amb} - h_{cab}). \quad (16)$$

The enthalpy of the air in the cabin and also in the environment can be determined based on the temperature (T) and humidity ratio (ω) [13]:

$$h = (1.006 \cdot T + (2501 + 1.770 \cdot T) \cdot \omega) \cdot 10^3, \quad (17)$$

$$\omega = 0.62198 \cdot \frac{\phi \cdot P_s}{P - \phi \cdot P_s}, \quad (18)$$

where P_s is a saturation vapor pressure, P is a pressure and ϕ is a relative humidity. The thermal load of ventilation carries both the latent heat and sensible heat components. The enthalpy of water vapor at temperature T can be evaluated according to Wilhelm [31]:

$$h_w = (2502 + 1.775 \cdot T) \cdot 10^3. \quad (19)$$

Knowing the enthalpies of water vapor at a given environment temperature $(h_{w,amb})$ and the cabin temperature $(h_{w,cab})$, and the mass flow rate of fresh air $(\dot{m}_{ren})$, it is possible to calculate the latent heat and sensible heat that enters the cabin, respectively:

$$\dot{Q}_{lat} = \dot{m}_{ren} \cdot (h_{w,amb} - h_{w,cab}), \quad (20)$$

$$\dot{Q}_{sen} = \dot{Q}_{vent} - \dot{Q}_{lat}. \quad (21)$$

2.9. HVAC thermal load

The evaporator is responsible for discharging the total thermal load coming from the different sources previously mentioned. The heat removed by the evaporator ($\dot{Q}_{hvac}$) can be calculated by considering the mass flow rate of air that passes through it $(\dot{m}_{air})$, the specific heat of the air (c_{air}), and the temperature difference of the air between the inlet (T_{eev}) and outlet (T_{sev}):

$$\dot{Q}_{hvac} = \dot{m}_{air} \cdot c_{air} \cdot (T_{eev} - T_{sev}). \quad (22)$$

The ambient temperature entering the evaporator is the weighted average of the fresh air $(\dot{m}_{ren})$ and recirculated air mass flow rates $(\dot{m}_{rec})$. Therefore:

$$T_{eev} = \frac{(\dot{m}_{ren} \cdot T_{amb} + \dot{m}_{rec} \cdot T_{cab})}{\dot{m}_{air}}. \quad (23)$$

The absolute humidity entering the evaporator can be calculated as a weighted average between the fresh air and recirculated air mass flow rates:

$$\omega_{eev} = \frac{(\dot{m}_{ren} \cdot \omega_{amb} + \dot{m}_{rec} \cdot \omega_{cab})}{\dot{m}_{air}}. \quad (24)$$

Figure 3 shows the schematic representation of the integration of the evaporator, the evaporator fan, and the air inlet and outlet.

To calculate the evaporator outlet temperature and humidity, an energy balance is considered. Combining Eqs. (21), (22), and (24) the following is obtained:

$$T_{sev} = T_{eev} - h_{lv}\left(\frac{(\dot{m}_{ren}\omega_{amb} + \dot{m}_{rec}\omega_{cab})}{\dot{m}e_{air}} - \omega_{sev}\right)\frac{\dot{Q}_{sen}}{c_{air} \cdot \dot{Q}_{lat}}. \quad (25)$$

In this model, the relative humidity at the evaporator outlet (ϕ_{sev}) is considered to be 0.9, and the absolute humidity in the cabin to be the weighted average between the ambient absolute humidity and the one supplied by the evaporator. The evaporator and cabin outlet humidities are given by, respectively:

$$\omega_{sev} = 0.622 \cdot \frac{P_v}{P_{atm} - P_v}, \quad (26)$$

$$\omega_{cab} = \frac{(\omega_{sev} \cdot (\dot{m}_{ren} + \dot{m}_{rec}) + \omega_{amb} \cdot \dot{m}_{ren})}{\dot{m}_{ren} + \dot{m}_{rec}}, \quad (27)$$

where P_v is the vapor pressure and P_{atm} is the atmospheric pressure. The saturation vapor pressure of water, $P_{v,s}$, can be calculated using the classical Antoine equation [32]:

$$P_{v,s} = 133.3 \cdot 10^{8.07131 - \frac{1730.63}{(T + 233.426)}}. \quad (28)$$

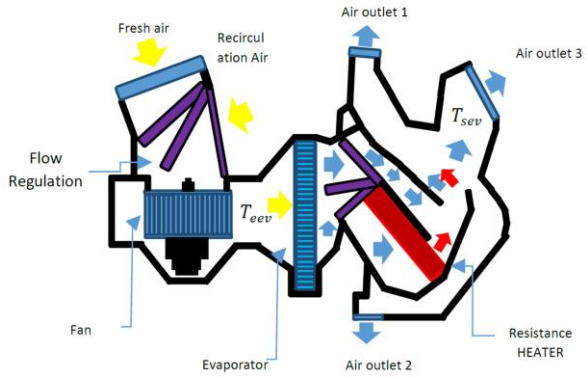

Fig. 3. Evaporator air distribution box.

The relative humidity can be calculated as the ratio between the vapor pressure and the saturation vapor pressure. Therefore:

$$P_v = \phi_{sev} \cdot P_{v,s}. \quad (29)$$

3. Experimentation

The tested vehicle was the 2013 white Volkswagen SpaceFox. It has a motor power of up to 101 horsepower (1.6 l) at 5250 rpm, 4 cylinders with a displacement of 1598 cm^3 and a compression ratio of 12.1:1. Figure 4 shows a photograph of the vehicle along with installed thermocouples and the notebook connected to the data acquisition board.

Sixteen T-type thermocouples with an uncertainty of 0.5ºC were used to measure the temperature at various points inside the automotive cabin for sixteen operating conditions. The National Instruments 9213 board was used for data acquisition, communicating with LabView software to read the thermocouples. Two thermocouples were positioned on the front glass, two on the rear glass, two on the left and right-side glasses, two on the ceiling, two on the floor, one at the air diffuser outlet, two in the cabin interior, and one outside the car recording the ambient temperature.

The thermocouples located inside the cabin were taken as a reference so that the average values between the two could be compared to the temperature predicted by the thermal model. The other thermocouples installed in different regions of the cabin were used to determine which surfaces undergo greater heating compared to the average of the internal thermocouples.

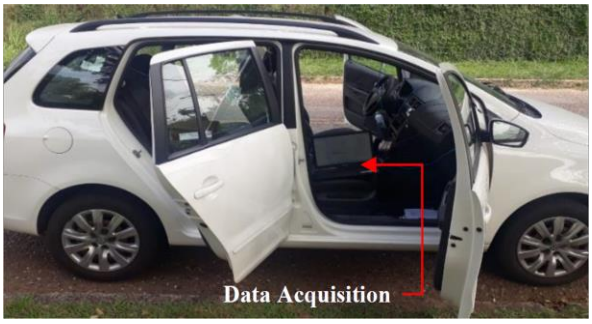

Fig. 4. Experimental vehicle.

The air velocity of the inflow was measured using an anemometer with an uncertainty of ± 0.3 m/s. Subsequently, the values were multiplied by the cross-sectional area of the evaporator (0.057375 m²) and by the density of the air, resulting in the mass inflow rates for the cabin. The expanded uncertainty calculation for the mass flow rate resulted in 0.0209 kg/s. The inflow mass rate values ($\dot{m}_{air}$) are presented in Table 2.

The vehicle was tested when stationary and while moving at a speed of 20 km/h. During the operation, two people were inside the vehicle, one being the driver and the other responsible for data acquisition. Both occupants of the vehicle were seated in the front seats. The fan controller was operated in 4 positions, each corresponding to different evaporator fan speeds and consequently different airflows. In all experiments, the pre-heater was not used, so that the temperature of the evaporator outlet was practically the same as that insufflated into the cabin. The air was blown towards the passengers from the front. The recirculation mode was also tested for each fan speed position.

The experiments were divided into two different days. On day 290 of 2022 (October 17), the experiments with the stationary vehicle were conducted. On day 291 of 2022 (October 18), the experiment was carried out with the vehicle moving at a speed of 20 km/h. For both days, the local relative humidity was 60%. The remaining experimental data, such as the time of the experiment, insufflated air flow rate, initial ambient temperature, initial cabin temperature, and engine rotation, are recorded in Table 2.

4. Results

The data obtained from simulation and experimentation are compared. In addition, the Pearson correlation coefficient (r) and the Mean Absolute Relative Deviation (MARD) are presented, respectively:

$$r = \frac{\Sigma\left(\left(T_{sim}-T_{sim_{mean}}\right)\cdot\left(T_{exp}-T_{exp_{mean}}\right)\right)}{\sqrt{\Sigma\left(\left(T_{sim}-T_{sim_{mean}}\right)^2\cdot\left(T_{exp}-T_{exp_{mean}}\right)^2\right)}}, \quad (30)$$

$$\text{MARD} = \frac{1}{N}\cdot\sum\left|\frac{T_{sim}(i)-T_{exp}(i)}{T_{exp}(i)}\right|, \quad (31)$$

where the subscripts *sim* and *exp* refer to simulated and measured values, respectively, and mean represents the mean difference. Parameter *i* denotes a data point number, and *N* is the total number of the data set points.

The Pearson coefficient *r* varies from –1 to 1, indicating the strength and direction of the correlation between the variables. A value close to 1 indicates a strong positive correlation, meaning that when one variable increases, the other also increases. A value close to –1 indicates a strong negative correlation, meaning that when one variable increases, the other decreases. A value close to 0 indicates a weak or absent correlation between the variables. The MARD parameter is used to evaluate the accuracy of a model or simulation, focusing on the absolute mean difference between the data.

Regarding the comparison between experimental data and simulation, the Pearson correlation coefficient remained in the range between 0.79 and 0.99. The mean absolute relative deviation (MARD) between the experimental data reached its maximum of 17.73% (experiment 8), and its minimum of 1.05% (experiment 1), as can be observed from the results shown in Table 3.

Table 2. Experimental conditions.

Exp.	Day	Hour	T_{cab} [°C]	V [km/h]	$\dot{m}_{air}$ [kg/s]	$\dot{m}_{ren}$ [%]	T_{amb} [°C]	ϕ	n [rpm]
1	290	13:37-13:47	25.2	0	0.154	26	26.0	0.6	1000
2	290	13:59-14:09	23.0	0	0.223	26	25.0	0.6	1000
3	290	14:17-14:27	24.3	0	0.305	26	27.2	0.6	1000
4	290	14:49-14:59	23.2	0	0.389	26	28.8	0.6	1000
5	290	15:09-15:19	23.9	0	0.154	15	25.8	0.6	1000
6	290	15:27-15:37	24.5	0	0.223	10	24.8	0.6	1000
7	290	15:45-15:55	25.2	0	0.305	7	28.2	0.6	1000
8	290	16:01-16:11	25,0	0	0.389	6	26.7	0.6	1000
9	291	13:14-13:24	24.6	20	0.154	26	24.7	0.6	1500
10	291	13:32-13:42	26.9	20	0.223	26	26.5	0.6	1500
11	291	13:52-14:02	25.2	20	0.305	26	25.0	0.6	1500
12	291	14:14-14:24	25.0	20	0.389	26	26.6	0.6	1500
13	291	14:33-14:43	25.5	20	0.154	15	25.3	0.6	1500
14	291	14:53-15:03	26.0	20	0.223	10	26.1	0.6	1500
15	291	15:15-15:25	26.0	20	0.305	7	28.4	0.6	1500
16	291	15:40-15:50	25.8	20	0.389	6	24.5	0.6	1500

Table 3. MARD and Pearson coefficient.

Exp.	Pearson coeff. [%]	MARD [%]
1	99.20	1.05
2	99.21	2.15
3	98.81	4.83
4	90.77	2.71
5	96.03	10.05
6	97.07	7.90
7	98.40	12.60
8	96.79	17.73
9	93.85	6.05
10	81.51	4.12
11	87.78	4.18
12	79.29	5.96
13	95.93	6.68
14	95.16	5.44
15	94.35	7.63
16	81.66	3.65

The comparative graphs between the model and experimental data on the temperature inside the vehicle cabin are presented in Figs. 5–8. Figure 5 refers to the experiments of day 290 with indexes 1 to 4 in Table 3. In these experiments, the vehicle was stationary and exposed to the sun at the same time the HVAC system was activated. Four evaporator fan speeds were tested for the mixed air condition of fresh and recirculated air. Figure 6 also refers to the vehicle at rest and tested at four evaporator fan speed options, however, the air supplied was only the recirculated air with an additional amount of 0.02 kg/s [13] due to air infiltration into the vehicle - naturally, as the cabin due to air infiltration into the vehicle - naturally, as the cabin interior pressure is lower than the exterior pressure.

The vehicle was also tested at a speed of 20 km/h with four different fan speeds for the evaporator. Figure 7 refers to the test where the air supply was a mixture of fresh and recirculated air. Figure 8 shows the results for the case where the air supply was only recirculated air with an additional amount of 0.02 kg/s [13] due to natural air infiltration through the gaps in the cabin.

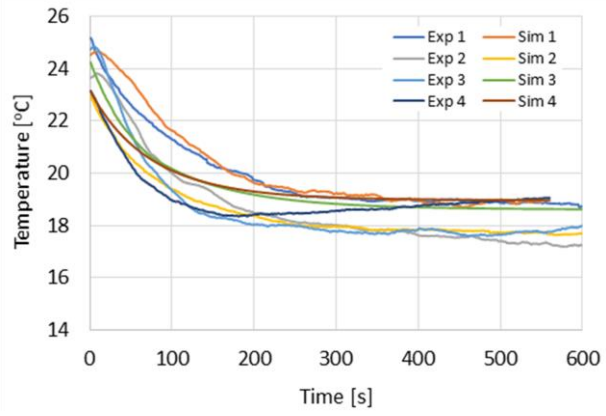

Fig. 5. Change of temperature of the vehicle cabin interior - comparison between model and experimental data: experiments 1 to 4.

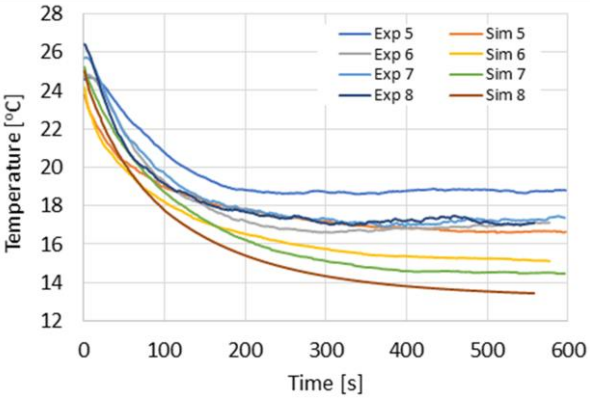

Fig. 6. Change of temperature of the vehicle cabin interior - comparison between model and experimental data: experiments 5 to 8.

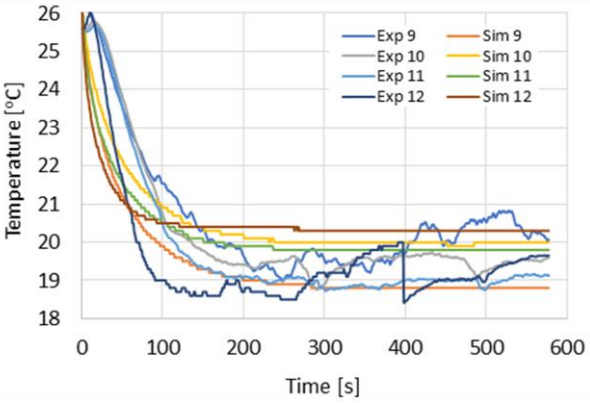

Fig. 7. Change of temperature of the vehicle cabin interior - comparison between model and experimental data: experiments 9 to 12.

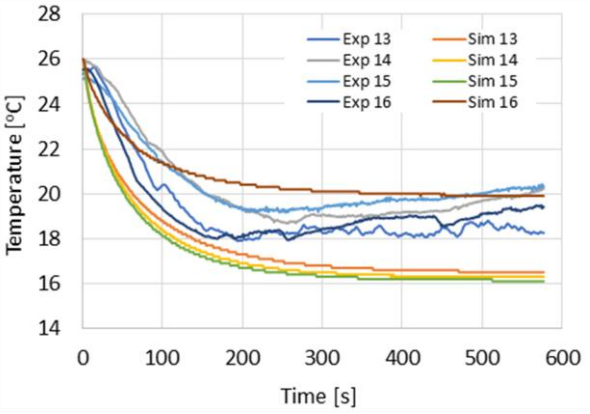

Fig. 8. Change of temperature of the vehicle cabin interior - comparison between model and experimental data: experiments 13 to 16.

As can be seen in the experimental data provided in Figs. 5–8, there is a slight increase in temperature initially after the HVAC is turned on before it starts to decrease. This occurs because the air being blown initially carries thermal energy stored due to the heating of the body and mechanical components of the system. The thermal model is unable to predict this

transient behavior for the initial few seconds of HVAC operation as it does not account for the energy stored in the stationary air within the ducts.

Regarding the transient regime, the time constant of the temperature curve slope is strongly influenced by the mass of the system being conditioned. In this sense, both the mass of the air and the mass of the seats interfere with how the thermal curve slope is constructed in the transient region. Determining the exact mass is a difficult task and varies considerably from vehicle to vehicle. In this work, the internal mass of the cabin was estimated to be 60 kg.

As regards the proposed formulation to calculate the temperature at the evaporator outlet (Eq. (25)), a linear temperature drop was considered based on physical parameters such as temperature, flow rate, pressure, and relative and absolute humidity. However, in real systems, the temperature drop between the inlet and outlet of the evaporator occurs parabolically with temperature curves very similar to the average temperature curves of the air inside the automotive cabin, as shown in the experimental results. This obviously indicates the strong relationship between the temperature of the supplied air and the average temperature of the automotive cabin.

The developed model can predict the thermal variation in the cabin more efficiently when the vehicle is at rest and in the air recirculation mode - as can be observed in Fig. 5. When the air renewal mode is activated and/or the vehicle is in motion, changes in the heat exchange coefficient with the environment interfere with the accuracy of the model.

Regarding the temperatures of the surfaces inside the automotive cabin, they are higher than the temperature of the air inside the cabin. Therefore, it is not possible to use them as a parameter to calculate the average temperature of the air inside the cabin. While the air temperature continues to drop from the start of the HVAC operation to the steady state, the surface temperatures increase and remain at a much higher level than the air temperature inside the cabin. As a result, the average of the temperatures provided by the surfaces or even the radiant temperature does not correspond to the average temperature of the air inside the cabin.

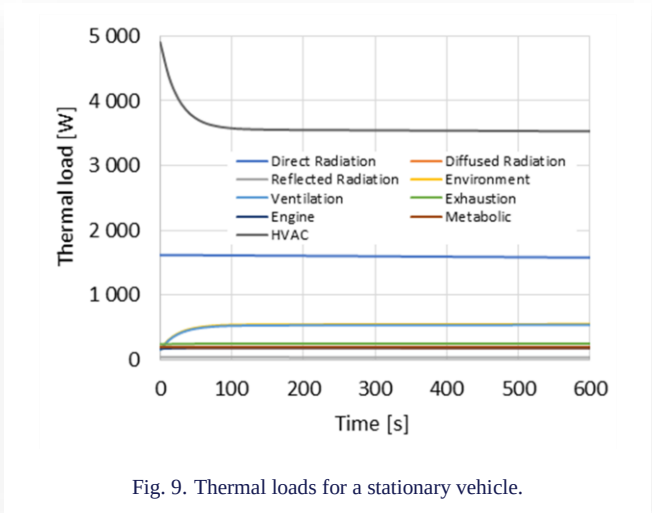

Fig. 9. Thermal loads for a stationary vehicle.

Figures 9 and 10 depict the nine thermal loads inside the cabin related to Eq. (1) for the stationary vehicle and the one moving at 20 km/h, respectively. For the simulation, the same mass flow rate of inflow air and the same percentage of fresh air were considered. It is observed that the car's motion modifies the heat exchange coefficient described by Eq. (11), increasing the percentage of environmental thermal load. The ventilation thermal load varied slightly when changing from 0 to 20 km/h, given that the low-speed variation did not account for changes in the mass flow rate of inflow air. The primary thermal load to be addressed by the HVAC system is the direct radiation thermal load.

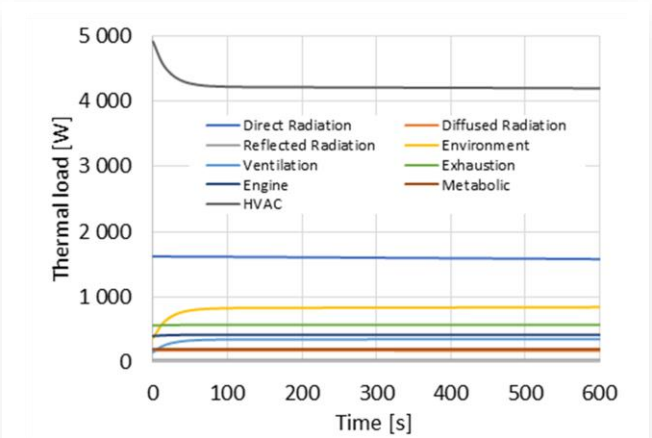

Fig. 10. Thermal loads for vehicle moving with the velocity of 20 m/h.

5. Conclusions

The thermal modeling of automotive cabins is difficult due to the different characteristics of each vehicle and, also, the environment in which it is located. Factors such as internal air mass, and the mass of seats and internal components of the cabin can alter the slope of the temperature curve during the transient period when compared to experimental data. In addition to this, the thicknesses of the bodywork, construction materials, and even the colors of the vehicles can alter the heat transfer coefficients and consequently bring uncertainties to the model. This justifies the trend found in the literature of many authors using modeling via finite volume technique.

Among the results, it was found that increasing the inflow rate and vehicle speed tends to decrease the model's suitability to the experimental data. However, even considering this, the model presented a maximum average relative deviation (MARD) of 17.73%. As for other studies found in the literature regarding thermal modeling of the automotive cabin, no proposal was found for calculating the temperature at the evaporator outlet. In this regard, most authors opted to directly measure this temperature using thermocouples.

Regarding thermal distribution in the cabin, it was noticed that surface temperatures cannot be used to determine the average air temperature inside it. Through experimental observations and simulation, it was found that the highest thermal load acting on the cabin is the direct radiation thermal load. These conclusions are in agreement with other research in the literature, such

as those presented in the works of Fayazbakhsh and Bahrami [13] and Khayyam et al. [8]. It is concluded that the thermal model proposed to determine the average temperature of the air inside the automotive cabin, when used, will present MARD below 20%. However, the characteristics of each vehicle - such as the air mass and seats - can significantly affect the transient state if not correctly determined.

Acknowledgement

This study was financed in part by the Coordenação de Aperfeiçoamento de Pessoal de Nível Superior – Brasil (CAPES) – Finance Code 001.

References

[1] Orofino, L., Amante, F., Mola, S., Rostagno, M., Villosio, G., & Piu, A. (2007). An integrated approach for air conditioning and electrical system impact on vehicle fuel consumption and performances analysis: DrivEM 1.0. *SAE Technical Paper Series*. doi: 10.4271/2007-01-0762

[2] Rugh, J.P., Hovland, V., & Andersen, S.O. (2004). Significant fuel savings and emission reductions by improving vehicle air conditioning. *15th Annual Earth Technologies Forum and Mobile Air Conditioning Summit*, April 13-15, Washington D.C. http://www.nrel.gov/vehiclesandfuels/ancillary_loads/pdfs/fuel_savings_ac.pdf [accessed 9 Oct. 2023].

[3] Moon, J. H., Lee, J. W., Jeong, C. H., & Lee, S. H. (2016). Thermal comfort analysis in a passenger compartment considering the solar radiation effect. *International Journal of Thermal Sciences*, 107, 77–88. doi: 10.1016/j.ijthermalsci. 2016.03.013

[4] Oh, M.S., Ahn, J.H., Kim, D.W., Jang, D.S., & Kim, Y. (2014). Thermal comfort and energy saving in a vehicle compartment using a localized air-conditioning system. *Applied Energy*, 133, 14–21. doi: 10.1016/j.apenergy.2014.07.089

[5] Ahilan, C., Kumanan, S., & Sivakumaran, N. (2010). Design and implementation of an intelligent controller for a split air conditioner with energy saving. *Advances in Modelling and Analysis C*, 65, 21–40.

[6] Shimizu, S., Hara, H., & Asakawa F. (1983). Analysis on air-conditioning heat load of a passenger vehicle. *International Journal of Vehicle Design*, 4(3), 292–311. doi: 10.1504/IJVD.1983.061317

[7] Michalek, D., Gehsat, C., Trapp, R., & Bertram, T. (2005). Hardware-in-the-loop-simulation of a vehicle climate controller with a combined HVAC and passenger compartment model. *IEEE/ASME (AIM) International Conference on Advanced Intelligent Mechatronics*, 24-28 July. 2, Monterey, USA, 1065–1070. doi: 10.1109/aim.2005.1511151

[8] Khayyam, H., Kouzani, A.Z., & Hu, E.J. (2009). Reducing energy consumption of vehicle air conditioning system by an energy management system. *IEEE Intelligent Vehicles Symposium*, 3-5 June, Xi'an, China, 752–757. doi: 10.1109/IVS.2009.5164371

[9] Jha, K.K., Bhanot, V., & Ryali, V. (2013). A simple model for calculating vehicle thermal loads. *SAE Technical Paper*, 2013-01-0855. doi: 10.4271/2013-01-0855.

[10] ASHRAE (2001). *ASHRAE Fundamental Handbook*. Atlanta, p. 30.

[11] Marcos, D., Pino, F.J., Bordons, C., & Guerra, J.J. (2014). The development and validation of a thermal model for the cabin of a vehicle. *Applied Thermal Engineering*, 66, 646–656. doi: 10.1016/j.applthermaleng.2014.02.054

[12] Torregrosa-Jaime, B., Bjurling, F., Corberán, J.M., Di Sciullo, F., & Payá, J. (2015). Transient thermal model of a vehicle's cabin validated under variable ambient conditions. *Applied Thermal Engineering*, 75, 45–53. doi: 10.1016/j.applthermaleng. 2014.05.074

[13] Fayazbakhsh, M.A., & Bahrami, M. (2013). Comprehensive modeling of vehicle air conditioning loads using heat balance method. *SAE Technical Paper*, 2013-01-1507. doi: 10.4271/2013-01-1507

[14] Wilhelm, L. R. (1976). Numerical calculation of psychrometric properties in SI units. *Transactions of the ASABE*, 19(2). doi: 10.13031/2013.36019

[15] Lee, H., Hwang, Y., Song, I., & Jang, K. (2015). Transient thermal model of passenger car's cabin and implementation to saturation cycle with alternative working fluids. *Energy*, 90, 1859–1868. doi: 10.1016/j.energy.2015.07.016

[16] ASHRAE. (2013). *ASHRAE Handbook, Fundamentals*. [chapter 15].

[17] Selow, J., Wallis, M., Zoz, S., & Wiseman, M. (1997). Towards a virtual vehicle for thermal analysis. *SAE Technical Paper Series*. doi: 10.4271/971841

[18] Ramsey, D., Boulon, L., & Bouscayrol, A. (2021). Modeling of an EV air conditioning system for energetic studies in summer. IEEE Vehicle Power and Propulsion Conference (VPPC), 25-28 October, Gijon, Spain. doi: 10.1109/VPPC53923.2021.9699119

[19] Liu, Y., & Zhang, J. (2021). Electric vehicle battery thermal and cabin climate management based on model predictive control. J. Mech. Des. Trans. ASME, 143, 1–8. doi: 10.1115/1.4048816

[20] Delgado, M.L., Jiménez-Hornero, J.E., & Vázquez F. (2023). Design, implementation and validation of a hardware-in-the-loop test bench for heating systems in conventional coaches. *Applied Sciences*, 13(4), 2212. doi: 10.3390/app13042212

[21] Paulke, S., & Ellinger, M. (2007). Air conditioning cabin simulation with local comfort rating of passengers. *2nd European Workshop on Mobile Air Conditioning and Auxiliary Systems – ATA / CRF*, 29-30 November, Torino, Italy.

[22] Singh, S., & Abbassi, H. (2018). 1D/3D transient HVAC thermal modeling of an off-highway machinery cabin using CFD-ANN hybrid method. *Applied Thermal Engineering*, 135, 406–417. doi: 10.1016/j.applthermaleng.2018.02.054

[23] Warey, A., Kaushik, S., Khalighi, B., Cruse, M., & Venkatesan, G. (2020). Data-driven prediction of vehicle cabin thermal comfort: using machine learning and high-fidelity simulation results. *International Journal of Heat and Mass Transfer*, 148, 119083. doi: 10.1016/j.ijheatmasstransfer.2019.119083

[24] Horvath, H. (1991). Spectral extinction coefficients of background aerosols in Europe, North and South America: A comparison. *Atmospheric Environment. Part A, General Topics*, 25, 725–732. doi: 10.1016/0960-1686(91)90071-E

[25] Iqbal, M. (1983). *An Introduction to Solar Radiation*. Academic Press Canada, Ontario. doi: 10.1111/jmp.12384

[26] ASHRAE. (1999). *Handbook Fundamentals*, SI. Atlanta.

[27] Wu, J., Jiang, F., Song, H., Liu, C., & Lu, B. (2017). Analysis and validation of transient thermal model for automobile cabin. *Applied Thermal Engineering*, 22, 91–102. doi: 10.1016/ j.applthermaleng.2017.03.084

[28] Tong, Z., & Liu, H. (2020). Modeling in-vehicle VOCs distribution from cabin interior surfaces under solar radiation. *Sustainability*, 12(14), 5526. doi:10.3390/su12145526

[29] Creder, H. (2004). INSTALAÇÕES DE AR CONDICIONADO. Livros Técnicos e Científicos Editora S.A. (LCT), Rio de Janeiro, 2004. [in Portuguese]

[30] Arndt, M., & Sauer, M. (2004). Spectroscopic carbon dioxide sensor for automotive applications. *Sensors 2004 IEEE*, 1, 24-27 October, Vienna, Austria, pp. 252–255. doi: 10.1109/icsens. 2004.1426149

[31] Singh, A.K., Singh, H., Singh, S.P., & Sawhney, R.L. (2002). Numerical calculation of psychrometric properties. *Building and Environment*, 37(4), 415–419. doi: 10.1016/S0360-1323(01) 00032-4

[32] Thomson, G.W.M. (1946). The Antoine equation for vapor-pressure. Data. *Chemical Reviews*, 38(1), 1–39. doi: 10.1021/cr60119a001

Co-published by
Institute of Fluid-Flow Machinery
Polish Academy of Sciences
Committee on Thermodynamics and Combustion
Polish Academy of Sciences

http://www.imp.gda.pl/archives-of-thermodynamics/

ARCHIVES OF THERMODYNAMICS

Research on optimization of the heating system in buildings in cold regions by energy-saving control

Wanting He[a], Hai Huang[b*]

[a]Chongqing Industry Polytechnic College, Yubei, Chongqing 401120, China
[b]Chongqing Vocational Institute of Engineering JiangJin Chongqing 402260, China
*Corresponding author email: huanglia826@yeah.net

Received: 06.09.2023; revised: 17.10.2023; accepted: 10.01.2024

Abstract

Building heating is an indispensable part of people's winter life in cold regions, but energy conservation and emission reduction should also be taken into account during the heating process. This paper provides a concise overview of the heating system based on air-source heat pump radiant floor and its control strategy. It also optimizes a control system based on thermal comfort and energy efficiency ratio, and analyzes a room in Xining City, Qinghai Province, to test the heating system performance under two control strategies. The final results show that under the traditional control strategy, the cumulative working time of the heating system within a day was 15 hours, the average indoor temperature was 17.36℃, the temperature standard deviation was 2.08℃, and the average power consumption was 189.6 kWh. Under the improved control strategy, the cumulative working time of the heating system within a day was reduced to 10 hours, the average indoor temperature was 18.56℃, the temperature standard deviation was 0.92℃, and the average power consumption was 132.5 kWh.

Keywords: Building heating; Cold region; Energy efficiency control; Radiant floor

Vol. 45(2024), No. 1, 129–135; doi: 10.24425/ather.2024.150445

Cite this manuscript as: He, W.T., & Huang, H. (2024). Research on optimization of the heating system in buildings in cold regions by energy-saving control. *Archives of Thermodynamics*, 45(1), 129–135.

1. Introduction

With the swift progress of the economy and the enhancement of individuals' quality of life, building heating has become an indispensable part of life in cold regions during winter [1]. However, the traditional heating method mainly relies on fossil fuels such as coal and fuel oil, which has a significant negative impact on the environment [2]. The substantial carbon dioxide emissions not only exacerbate global warming but also directly threaten human health. Therefore, optimizing the heating systems in buildings located in cold regions to reduce energy consumption and environmental pollution has become one of the urgent challenges in today's society [3]. Moreover, with the increasing awareness of energy saving and environmental protection, precise control of heating systems and maximizing energy utilization can be achieved through the introduction of intelligent control systems and the utilization of renewable energy sources. Katić et al. [4] introduced a machine learning approach to develop predictive models for managing an individualized heating system. The experiments revealed that the participants experienced consistent comfort levels during the trial, and they expressed contentment with the automated regulation. Gupta et al. [5] proposed a heating controller based on deep reinforcement learning, aiming to enhance occupants' thermal comfort and minimize energy costs in smart buildings. Additionally, Kaminska [6] examined the influence of occupant behaviour on

Nomenclature

c_p – specific heat capacity of the water circulated by the pump between the condenser and the radiant floor, J/(kg K)
C – convective heat transfer between the individual and their surroundings, W/m^2
COP – coefficient of performance
f_{cl} – clothing coefficient of the human body
f_{eff} – correction coefficient of the body movement
G – volumetric flow rate of the circulating water, m^3/s
h_c – convective heat transfer coefficient, W/(m^2 K)
M – heat power emitted at the surface by the body due to metabolism, kW
P – power of the input energy, kW
P_a – partial pressure of steam in the air associated with the relative humidity, Pa
Q_h – output heat of the air source heat pump, kW
R – radiant heat transfer between individual and their surroundings, W/m^2
t_a – average temperature of the air, ^{o}C
t_{cl} – temperature on the surface of the garment, ^{o}C
t_{in} – temperature of the incoming water from the radiant floor flowing back to the condenser, ^{o}C
t_{out} – temperature of the outgoing water from the condenser flowing to the radiant floor, ^{o}C
PMV – average thermal comfort
T_{cl} – absolute temperature at the body surface, K
$\bar{T}_r$ – average absolute temperature in the environment, K
W – heat power emitted at the surface by the body due to work, kW

Greek symbols

ε – human body surface heat transfer rate
ρ – density of the circulating water, kg/m^3
σ – Stefan-Boltzmann constant, W/(m^{2}K^4)

energy usage in existing public buildings in Poland and conducted an experimental evaluation. They found that occupants perceived a broad range of temperature settings as thermally comfortable and a 1°C reduction in the temperature set point could result in energy savings of about 5%. This paper briefly introduced a heating system based on an air-source heat pump radiant floor and its control strategy. It adopted thermal comfort and energy efficiency ratio as the basis for optimizing the control. Furthermore, a case study of a room in Xining City, Qinghai Province, was carried out to test the heating performance of the heating system under two control strategies.

2. Heating system optimization based on energy-saving control

2.1. Heating system based on air-source heat pump floor radiation

A building heating system is a facility and equipment used to provide heat to a building during the cold season. It mainly comprises components such as heating equipment, heat transfer medium, heating pipe network, and a control system [7]. The heating equipment serves as the core component responsible for supplying heat, while the heat transfer medium facilitates the effective transfer of heat energy from the heating equipment to all areas of the building through circulating flow. The heating pipe network forms the network system for transmitting and distributing the heat medium within the building heating system. Finally, the control system assumes a crucial role within the building heating system [8], as it allows for precise regulation of indoor temperature by controlling the heating equipment, heat transfer medium, and heating pipe network. This control system plays a pivotal role in realizing the overall heating system's control strategy.

The heating equipment heat source can be categorized into three types: solar heat source, air heat source and geothermal heat source. Among them, the solar heat source is relatively more energy-saving and environmentally friendly; however, its dependency on sunlight makes it less stable for heating. Although a geothermal heat source is both energy-efficient and environmentally friendly, it requires the installation of heat pumps deep underground, which poses significant construction challenges. On the other hand, the air heat source absorbs heat from the surrounding air [9], providing both stability and ease of installation. In addition to the heat source, there are different kinds of heating ends in the building heating system, including fan coils, radiators and radiant floors. Fan coils achieve heat transfer by forcing indoor air convection through blowing, while radiators transfer heat through natural convection. Radiant floors achieve heat transfer through heat radiation [10]. Compared to the first two heating ends, radiant floor heating is not only quieter but also offers a more uniform heat distribution. Figure 1 presents a schematic diagram of an air-source heat pump radiant floor heating system.

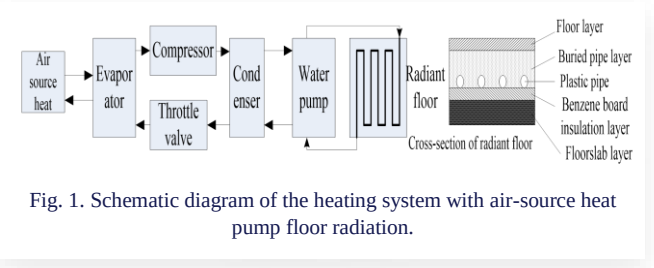

Fig. 1. Schematic diagram of the heating system with air-source heat pump floor radiation.

In this particular system, the evaporator utilizes a liquid medium for heat transfer, which effectively captures thermal energy from the air heat source and undergoes a phase change into a gaseous state [11]. The gaseous medium is then compressed in the compressor, further raising its temperature. Subsequently, the compressed medium condenses back into a liquid form in the condenser. The heat in the medium is transferred to the condensing water in the condenser, and the liquid medium cycles back into the evaporator through a throttle valve to absorb heat again. The process repeats. The condensed water, which absorbs heat in the condenser, is pumped into pipes buried in the radiant floor. The heat within the condensing water is then radiated indoors through the floor and subsequently returned to the condenser for further heat absorption [12].

The structure of the radiant floor is presented in Fig. 1, showcasing a hierarchical composition comprising multiple layers positioned in a top-to-bottom sequence. The first layer is the floor layer, which serves as a decorative structural layer and can be made of materials such as wood or tiles, possessing heat transfer properties. Moreover, the materials have a certain level of heat resistance [13] and do not release harmful substances to the human body when subjected to heat. The second layer is the buried pipe layer, primarily consisting of concrete made from crushed stone. This layer serves as the bed for laying the plastic pipes used for heat transfer. Typically, these plastic pipes are positioned at the lowermost part of the buried pipe layer to optimize the upward conduction of heat. Next, there is the benzene board insulation layer, which provides excellent heat insulation properties, preventing the downward transfer of heat. The final layer is the floor slab layer, acting as the supporting surface of the room.

2.2. Optimization of control strategies for heating systems

To optimize the energy-saving effect of the heating system during operation, in addition to adjusting the structural composition of the heating system [14], energy conservation and emission reduction can also be achieved through the optimization of the system control strategy. The traditional control strategy for an air-source heat pump radiant floor heating system is relatively straightforward in principle. It treats the evaporator, compressor, condenser, throttle valve [15] and water pump as components of a unified air-source heat pump. The control strategy involves maintaining the heat pump workload by monitoring the difference between the return water temperature of the heat pump and the desired temperature. Specifically, when the return water temperature surpasses the maximum set value, measures are taken to decrease the heat pump workload such as reducing the operation of the water pump or compressor and closing off the throttle valve. On the other hand, when the temperature of the returning water drops below the predetermined minimum threshold [16], the heat pump's workload is increased by elevating the workload of the water pump or compressor and opening the throttle valve.

The traditional control strategy, though relatively simple in principle and implementation, may not be suitable for effectively controlling the radiant floor heating system owing to the thermal inertia exhibited by both the floor and the building envelope. The real-time change in indoor temperature cannot be accurately reflected by the variation in return water temperature. Consequently, there may be situations where the indoor temperature is already adequate, yet heat transfer persists due to a lack of corresponding adjustment in the return water temperature. This situation can lead to both heat wastage and discomfort for occupants as indoor temperatures continue to rise [17]. When controlling and regulating the heating system, it is essential to take into account not just the energy-saving effectiveness but also the comfort of the inhabitants. Therefore, in this paper, the control strategy is optimized from two perspectives: the energy efficiency of the heating system and thermal comfort. The optimized control strategy is depicted in Fig. 2.

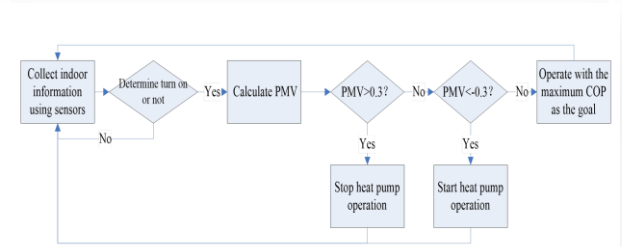

Fig. 2. Optimized heating system control strategy.

According to this:

1. Various sensors installed in the room are utilized to collect information about the room, including room temperature, relative humidity and the number of people in the room.
2. When no one is indoors, the heat provided by the air conditioner is equivalent to waste [18], so first determine whether the heating system is on according to whether there is someone indoors (if there is someone indoors, turn on the system and go to the next step; if there is no one indoors, turn off the system and go back to step 1).
3. The indoor environmental data collected by the sensors are utilized to calculate the indoor thermal comfort [19]. The corresponding formula is:

$$PMV = (0.303e^{-0.036M} + 0.028)((M - W) - 3.05 \times 10^{-3}(5733 - 6.99(M - W) - P_a) + -0.42((M - W) - 58.15) - 1.7 \times 10^{-5}M(5867 - P_a) - 0.0014M(34 - t_a) - R - C \quad (1a)$$

$$R = \varepsilon f_{cl} f_{eff} \sigma (T_{cl}^4 - \bar{T}_r^4), \quad (1b)$$

$$C = f_{cl} h_c (t_{cl} - t_a), \quad (1c)$$

where: PMV represents the average thermal comfort, M represents the heat power emitted at the surface by the body due to metabolism, W represents the heat power emitted at the surface by the body due to work, P_a represents the partial pressure of steam in the air, which is associated with the relative humidity, t_a is the average temperature of the air, R represents the quantity of radiant heat transfer between individual and their surroundings, C represents the quantity of convective heat transfer between the individual and their surroundings, ε is the human body surface heat transfer rate, f_{cl} denotes the clothing coefficient of the human body, f_{eff} is the correction coefficient of the body movement, σ represents the Stefan-Boltzmann constant, T_{cl} is the absolute temperature on the body surface, $\bar{T}_r$ is the average absolute temper

ature in the environment, h_c represents the convective heat transfer coefficient [20], and t_{cl} represents the temperature at the surface of the garment.

4. Whether the indoor thermal comfort is greater than 0.3 is judged. If it is greater than 0.3, it means that the indoor temperature is too hot for the body to feel uncomfortable, then stop the heat pump and return to step 1; otherwise, go to the next step.
5. Whether the indoor thermal comfort is less than −0.3 is judged. If it is less than −0.3, it means that the indoor temperature is low and makes people feel uncomfortable, then turn on the heat pump and go back to step 1; on the contrary, go to the next step.
6. When the thermal comfort is between −0.3 and 0.3, the indoor temperature is in line with the human comfort feeling. At this time, it is necessary to make the heating system operate with the minimum waste of energy. This paper adopts *COP* to measure the energy efficiency ratio of the heating system, which is the ratio of the output heat to the input energy. The larger the value, the less the energy is wasted. The specific formula is:

$$COP = Q_h/P \tag{2a}$$

$$Q_h = \frac{c_p \rho G (t_{out} - t_{in})}{3600} \tag{2b}$$

where: P is the power of the input energy, Q_h is the output heat of the air source heat pump, c_p is the specific heat capacity of the water being circulated by the pump between the condenser and the radiant floor, ρ is the density of the circulating water, G is the volumetric flow rate of the circulating water, t_{out} stands for the temperature of the outgoing water from the condenser flowing to the radiant floor, and t_{in} is the temperature of the incoming water from the radiant floor flowing back to the condenser. The heating system operates at the maximum *COP* as its goal. Finally, it returns to step 1.

3. Example analysis

3.1. Objects of analysis

The room tested is located in Xining City, which is the capital city of Qinghai Province. The climate of Xining City is influenced by the Tibetan Plateau and the Asian monsoon, showing a typical plateau climate. The local summer is relatively short and mild, while the winter is long, from November to March. Winter temperatures are low, usually around 0°C during the day and dropping below −10°C at night, often accompanied by snowfall. Due to the influence of the Tibetan Plateau, Xining City has a large daily difference in temperature and a significant difference between daytime and nighttime temperatures, and can be considered a cold region.

The basic structure of the room used for the test is illustrated in Fig. 3, which is divided into a large and a small area. The large area is 6.0 × 3.5 m, and the small area is 2.0 × 1.5 m. The wall-to-window ratio is 0.3. Walls have a heat transfer coefficient of 0.45 W/(m^2 K). The roof has a heat transfer coefficient of 0.25 W/(m^2 K).

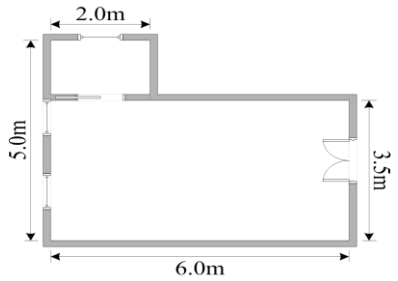

Fig. 3. Basic structure of the test room.

3.2. Equipment parameters

Air-source heat pump related parameters: the rated input power of the compressor was equal to 2.5 kW, with a displacement of 46.5 cm^3 and a refrigerant dosage of 2 kg. The evaporator was of the finned type, and its copper tube had an outer diameter of 9.52 mm, a thickness of 0.5 mm, and a length of 5 m. The rated input power for the fan was 90 W. The expansion valve was an externally balanced valve. The condenser was a pipe heat exchanger, and its outer seamless tube had a diameter of 35 mm and a thickness of 1.5 mm. The inner tube was made of smooth copper and has an outer diameter of 31 mm, a thickness of 0.8 mm, and a length of 4.2 m.

Water pump-related parameters: the water tank was of the pressure-resistant type with a capacity of 0.2 m^3; the water pump was centrifugal with a rated power of 320 W, a maximum flow rate of 9 m^3/h, and a head of 5 m.

Radiant floor: the floor slab layer is 120 mm thick and has a thermal conductivity of 1.75 W/(m K); the benzene board insulation layer is 13 mm thick and has a thermal conductivity of 0.05 W/(m K); the buried pipe layer is 28 mm thick and has a thermal conductivity of 0.94 W/(m K); the floor layer is 18 mm thick and has a thermal conductivity of 0.94 W/(m K); the buried pipe layer contains heat-conducting water pipes composed of crosslinked polyethylene material, with a water pipe diameter measuring 20 mm.

3.3. Test methods

Firstly, temperature and humidity sensors were installed on the walls around the room at intervals of 0.6 m both vertically and horizontally, totalling 45 sensors, and their data were intercommunicated with the data of the heat pump host. The traditional control strategy was also tested in this test to further validate the enhanced control strategy optimization capabilities.

The traditional control strategy is as follows. The outlet water temperature t_{out} of the air-source heat pump was set to 50°C. The inlet water temperature t_{in} was set to 45°C. When t_{in} was higher than 45°C, the heat pump host was turned off gradually, and when t_{in} was lower than 45°C, the heat pump host was turned on gradually.

The improved strategy was as described above. The air-source heat pump was regulated according to the indoor *PMV* as well as the heating system *COP*. The heat pump outlet temperature t_{out} was also set to 50°C.

In conducting the test, the heating system under each control strategy was operated alternately for a time limit of one day (implement a control strategy for a consecutive day, followed by a pause in operation for the next day; then, adopt an alternative control strategy for another consecutive day and again pause operations on a subsequent day). Temperature sensors set up inside and outside of the room were used to collect the average temperature changes indoors and outdoors. The settings of indoor environmental parameters are presented in Table 1. The energy consumption of the heating system during one day was recorded. The experiment was conducted for a total of 12 days, and the results for each day were averaged.

Table 1. Indoor environmental parameters during testing.

Parameters, hours	8:00–20:00	20:00–8:00
Indoor temperature, ℃	20	18
Relative humidity, %	30	30
Number of people indoors (n)	10	2

3.4. Test results

The test recorded the heat pump working status of the heating system every one hour. In the recorded data, a value of "1" indicated that the heat pump was running, while a value of "0" signified that the heat pump was stopped. Figure 4 illustrates the changes in the heat pump operating state in one day under the two control strategies. Table 2 shows the accumulated working time of the heating system within one day under the two control strategies.

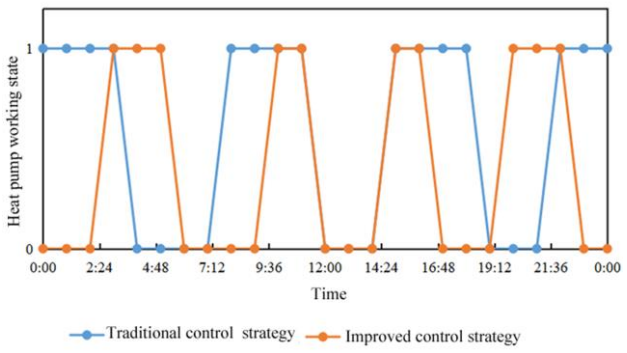

Fig. 4. Heat pump operating state of the heating system in a day under two control strategies.

Table 2. The accumulated working time of the heating system within one day under the two control strategies.

Parameter	Traditional control strategy	Improved control strategy
Accumulated working time within one day, h	15	10

It can be seen from Table 2 and Fig. 4 that both control strategies resulted in intermittent heating, indicating energy-saving characteristics for both approaches. However, the improved control strategy led to a reduced cumulative running time for the heat pump compared to the traditional control strategy.

Figure 5 displays the changes in indoor temperature as well as outdoor temperature in one day under both control strategies. Table 3 presents the statistics of indoor temperature changes under the two control strategies. It is evident from Table 3 and Fig. 5 that, regardless of the control strategies employed, the heating system effectively sustained an indoor temperature considerably above that of the outdoor environment. However, when comparing the indoor temperature under the two strategies, it was observed that while the traditional control strategy resulted in significant fluctuations in indoor temperature, the improved strategy maintained a relatively stable temperature around 18℃, with only slight fluctuations.

Table 3. Statistics of indoor temperatures under the two control strategies.

Parameter	Traditional control strategy	Improved control strategy
Average indoor temperature, ℃	17.36	18.56
Highest indoor temperature, ℃	21.03	20.01
Indoor lowest temperature, ℃	13.01	17.02
Standard deviation of indoor temperature, ℃	2.08	0.92

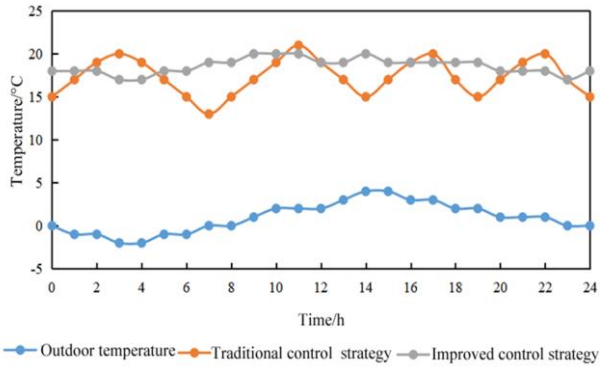

Fig. 5. Variation of indoor temperature as well as outdoor temperature in a day under two control strategies.

The average power consumption of the system in a day under the two control strategies is shown in Fig. 6. The heating system consumed an average of 189.6 kWh per day with the traditional strategy, whereas the improved strategy resulted in an average power consumption of 132.5 kWh for the heating system. It was intuitively seen from Fig. 6 that the heating system under the improved control strategy consumed less power.

The reasons for the above results were analyzed. The traditional strategy gradually adjusted the heat pump host based on variations in the temperature of the returning water. Although there might be shutdown conditions resulting in less than 24 hours of operation time, the heat pump host was regulated step by step while the heat pump continued to run during this process. In contrast, the improved control strategy determined when to switch on/off the heat pump host based on the comfort level, and even within the range of human comfort, it operated with the maximum *COP* as a goal.

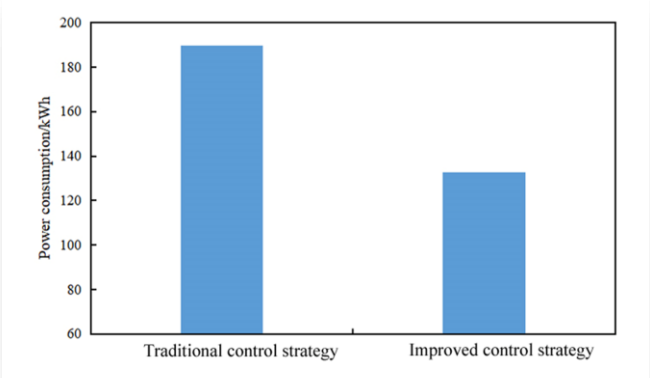

Fig. 6. Average power consumption of the heating system in a day under two control strategies.

Using the comfort level as a regulatory basis considered the thermal inertia of the envelope, which reduced the operating time and naturally resulted in less power consumption.

4. Conclusion

This paper briefly introduced the heating system that utilizes air-source heat pump radiant floor technology and its control strategy and used thermal comfort as well as energy efficiency ratio as the basis to optimize the control. Then, a case study was carried out with a room in Xining City, Qinghai Province, to evaluate the heating efficiency of the heating system under the two control strategies. The results obtained are as follows:

1. The heat pump of the system had intermittent heating under both control strategies, and the cumulative running time of the heat pump under the improved control strategy was less than that under the traditional strategy.
2. The indoor temperature was maintained at a level higher than the outdoor temperature by both control strategies employed for the heating system, but the heating system under the improved strategy provided a more stable indoor temperature.
3. The average power consumption of the heating system in a day was 189.6 kWh under the traditional strategy and 132.5 kWh under the improved strategy.

In conclusion, when using an air-source heat pump radiant floor heating system in cold regions, intermittent heating can be employed with the duration adjusted based on thermal comfort guidelines to achieve energy savings and emission reductions. The future research direction of this study is to further optimize the control strategy of the heating system for better regulation.

References

[1] Wathan, N. (2021). Multi-zone heating control benefits. *Heating Ventilating & Plumbing*, 42(2), 42.

[2] Polyakov, S., Akimov, V., & Polukazakov, A. (2020). Simulation of the heating control system of a smart apartment building. *Modeling of Systems and Processes*, 13(1), 68–76. doi: 10.12737/2219-0767-2020-13-1-68-76

[3] Kim, S.H., Chung, K.S., & Kim, Y.I. (2015). Thermal Comfort Range of Radiant Floor Heating System by Residential Style. *Transactions of the Korea Society of Geothermal Energy Engineers*, 11(1), 7–14. doi: 10.17664/ksgee.2015.11.1.007

[4] Katić, K., Li, R., Verhaart, J., & Zeiler, W. (2018). Neural network based predictive control of personalized heating systems. *Energy & Buildings*, 174, 199–213. doi: 10.1016/ j.enbuild.2018.06.033

[5] Gupta, A., Badr, Y., Negahban, A., & Qiu, RG. (2020). Energy-Efficient Heating Control for Smart Buildings with Deep Reinforcement Learning. *Journal of Building Engineering*, 34(C), 101739. doi: 10.1016/j.jobe.2020.101739

[6] Kaminska, A. (2019). Impact of Heating Control Strategy and Occupant Behavior on the Energy Consumption in a Building with Natural Ventilation in Poland. *Energies*, 12(22), 1–18. doi: 10.3390/en12224304

[7] Du, Y. (2014). Feasibility Analysis of Radiant Floor Cooling and Heating System Applications. *Applied Mechanics and Materials*, 716–717, 428–430. doi: 10.4028/www.scientific.net/AMM.716-717.428

[8] Ma, H., Li, C., Lu, W., Zhang, Z., Yu, S., & Du, N. (2016). Experimenta l study of a multi-energy complementary heating system based on a solar-groundwater heat pump unit. *Applied Thermal Engineering*, 109, 718–726. doi: 10.1016/j.applthermaleng.2016.08.136

[9] Yu, B.H., Seo, B.M., Moon, J.W., & Lee, K.H. (2015). Analysis of the Part Load Ratio Characteristics and Gas Energy Consumption of a Hot Water Boiler in a Residential Building under Korean Climatic Conditions. *Korean Journal of Air Conditioning & Refrigeration Engineering*, 27(9), 455–462. doi: 10.6110/KJACR.2015.27.9.455

[10] Woodson, R. (2015). Radiant Floor Heating, Second Edition. *JAMA: the Journal of the American Medical Association*, 313(1), 93–94.

[11] Yang, E. (2015). Research on Control Property of Low-Temperature Floor Radiant Heating System. *Open Construction & Building Technology Journal*, 9(1), 311–315.

[12] Hong, S.K., & Cho, S.H. (2015). The Experimental Study of the Heat Flux and Energy Consumption on Variable Flow Rate for Secondary Side of DHS. *Korean Journal of Air-Conditioning and Refrigeration Engineering*, 27(5), 247–253. doi: 10.6110/KJACR.2015.27.5.247

[13] Shaw, B.H. (2018). Infection in Mental Hospitals, with Special Reference to Floor Treatment. *Journal of Mental Science*, 69, 24–45. doi: 10.1192/bjp.69.284.24

[14] Kim, S.H., Chung, K.S., & Kim, Y.I. (2015). Thermal Comfort Range of Radiant Floor Heating System by Residential Style. *Transactions of the Korea Society of Geothermal Energy Engineers*, 11(1), 7–14.

[15] Toyoda, S., Fujiwara, T., Uchida, A., & Ishibashi, J. (2016). ESR dating of sea-floor hydrothermal barite: contribution of 228Ra to the accumulated dose. *Nephron Clinical Practice*, 43(1), 201–206. doi: 10.1515/geochr-2015-0042

[16] Kong, Q.X., Feng, J., & Yang, C.L. (2017). Numerical Simulation of a Radiant Floor Cooling Office Based on CFD-BES Coupling and FEM. *Energy Procedia*, 105, 3577–3583.

[17] Barzin, R., Chen, J.J.J., Young, B.R., & Farid, M.M. (2015). Application of PCM underfloor heating in combination with PCM wallboards for space heating using price based control system. *Applied Energy*, 148(1–2), 39–48. doi: 10.1016/j.apenergy.2015.03.027

[18] Bae, W.B., Ko, J.H., Mun, S.H., & Huh, J.H. (2015). An Occupants' Location-Driven Control of Radiant Floor Heating Using Fingerprinting Method in Residential Buildings. *Journal of the Architectural Institute of Korea Planning & Design*, 31(11), 211–219.

[19] Bellos, E., & Tzivanidis, C. (2017). Energetic and financial sustainability of solar assisted heat pump heating systems in Europe. *Sustainable Cities and Society*, 33, 70–84. doi: 10.1016/j.scs.2017.05.020

[20] Singh, S.B., Vummadisetti, S., & Chawla, H. (2017). Influence of Curing on the Mechanical Performance of FRP Laminates. *Journal of Building Engineering*, 16, 1–19. doi: 10.1016/j.jobe.2017.12.002

Co-published by
Institute of Fluid-Flow Machinery
Polish Academy of Sciences
Committee on Thermodynamics and Combustion
Polish Academy of Sciences

http://www.imp.gda.pl/archives-of-thermodynamics/

Experimental study of the potential of concentrated NaCl solutions for use in pressure-retarded osmosis process

Fabian Dietrich[a*], Łukasz Cieślikiewicz[a], Piotr Furmański[a], Piotr Łapka[a]

[a]Warsaw University of Technology, Faculty of Power and Aeronautical Engineering, 21/25 Nowowiejska St., 00-665 Warsaw, Poland
*Corresponding author email: fabian.dietrich.dokt@pw.edu.pl

Received: 17.01.2024; revised: 07.03.2024; accepted: 15.03.2024

Abstract

Pressure retarded osmosis is a process that enables useful work generation from the salinity difference of solutions. The literature most often considers using pressure retarded osmosis with natural sodium chloride (NaCl) solutions, such as seawater, dedicated for open systems. To explore the full potential of this process, however, optimized, highly concentrated solutions of various compounds can be used. The presented research is focused on evaluating the impact of increasing draw solution temperature and concentration on the permeate flow in the osmotic process. The permeate flow is directly related to achievable work in this process, therefore, it is important to find feed and draw solution parameters that maximize it. An experimental setup developed in this study provides full control over the process parameters. Furthermore, the performance characteristics of the membrane over process time were investigated, as it became evident during preliminary experiments that the membrane impact is significant. The studies were conducted without back-pressure, in a configuration typical of the forward osmosis process, with solution circulation on both sides of the membrane. The obtained results show a clear positive impact of both the temperature and concentration increase on the potential output of a pressure retarded osmosis system. The membrane behaviour study allowed for correct interpretation of the results, by establishing the dynamics of the membrane degradation process.

Keywords: Pressure retarded osmosis; Renewable energy; Experimental investigation; High-concentrated solution; Increased temperature effect

Vol. 45(2024), No. 1, 137–143; doi: 10.24425/ather.2024.150446

Cite this manuscript as: Dietrich, F., Cieślikiewicz, Ł., Furmański, P., & Łapka, P. (2024). Experimental study of the potential of concentrated NaCl solutions for use in pressure-retarded osmosis proces. *Archives of Thermodynamics*, 45(1), 137–143.

1. Introduction

World energy use is still largely based on fossil fuels, which are closely linked to emissions of pollutants and carbon dioxide, affecting the state of the ecosystem. As the world's energy demand continues to grow, energy conversion methods previously not used on a large scale are gaining interest. One of these methods is extracting useful power from the difference of concentrations in solutions based on thermodynamic potential (i.e., Gibbs free energy). There are two most promising basic ways of utilization of this potential, i.e., pressure-retarded osmosis (PRO) and reverse electrodialysis (RED), which can be used to generate useful power from salinity difference.

The RED uses membranes for the ions, but not water, transport. Two types of ion-selective cation-exchange membrane (CEM) and anion-exchange membrane (AEM) are used [1]. A number of these membranes are arranged in a variable

pattern between a cathode and an anode. The channels between the membranes are alternately filled with highly concentrated salt solution and diluted salt solution, which flow along the membranes. The difference in electrochemical potential resulting from the difference in salinity causes the transport of ions through the membrane from the concentrated solution to the diluted solution. In a sodium chloride solution, sodium ions permeate through CEMs towards the cathode, and chloride ions permeate through AEMs toward the anode. Electro-neutrality of the solution in the anode cell is maintained by oxidation on the surface of the anode. Electro-neutrality of the solution in the cathode cell is maintained by reduction on the cathode surface. The electric potential difference builds up between two neighboring electrodes. This potential difference allows an electron transfer from the anode to the cathode via an external electrical circuit when the external load is connected to the circuit. The main advantage of using the RED system for obtaining useful energy is that electricity is generated directly from salinity differences between neighboring channel streams. Each pair of membranes generates a voltage of around 0.1–0.2 V from typical river and sea water [1]. It was found that in order to overcome energy losses at the electrodes, at least 20 pairs of membranes are needed. Substantial advances are being made to increase RED power density and energy efficiencies by improving membrane materials, spacing and architecture. The highest power density that was attained for the RED stack with 50 cell pairs was 0.93 W/m^2 at about 3 V, neglecting electrode and pumping losses (based on each type of ion-exchange membrane having a 0.5 m^2 total surface area, or 93 W/m^2 based on the planar cross-sectional area between the electrodes [1]). The main challenge for the commercialization of RED is the cost of ion-exchange membranes, but a global increase in demand leads to a price decrease. Over the past two decades, new materials, improved fabrication methods and increased production of membranes have resulted in a decrease in their costs. But they are still very high, and the RED technology is quite expensive.

The PRO process enables the generation of useful work from the concentration difference of solutions separated by a semipermeable membrane. In the osmosis process, the system tends to equilibrate by equalizing the concentrations on both sides of the membrane. The only way to reach this goal is for the solvent to flow toward the highly concentrated solution, resulting in its dilution. The governing variable of this process is osmotic pressure. It is defined as the minimum pressure needed to stop the osmotic process completely. By applying pressure lower than the osmotic pressure to the concentrated side, one may partially retard the flow of solvent, but in effect, the permeating solvent now has the potential to perform useful work [2], i.e., when passing through the membrane, it increases its pressure to that applied on the concentrated side. There are two other well-known osmotic processes that have elements in common with PRO, i.e., forward osmosis (FO) for wastewater treatment [3] and reverse osmosis (RO) for water purification [4], but these processes are implemented differently and have different objectives than PRO.

The literature most often considers using PRO with natural sodium chloride (NaCl) solutions, such as seawater and river water, or industrial solutions, e.g., seawater desalination concentrate [5]. With the average salinity of seawater in the range of 35 g/kg and the assumption of negligible salinity of clean water, such a system can provide approximately 0.6 kWh of energy per cubic meter of freshwater used. The osmotic pressure of standard seawater is at the level of 0.27 MPa [6]. Moreover, in the vast majority of the papers, only open systems are analyzed depending on the available source of streams feeding the system. The schematic of such a system is shown in Fig. 1a. In these systems, the full potential of PRO as a power generation method cannot be explored due to existing parameter limitations of natural and industrial NaCl solutions.

The second approach, which is less common in scientific publications, is a closed PRO system, shown in Fig. 1b, that allows more extensive manipulation of the parameters of the feed and draw streams, as well as the use of optimized synthetic solutions [7].

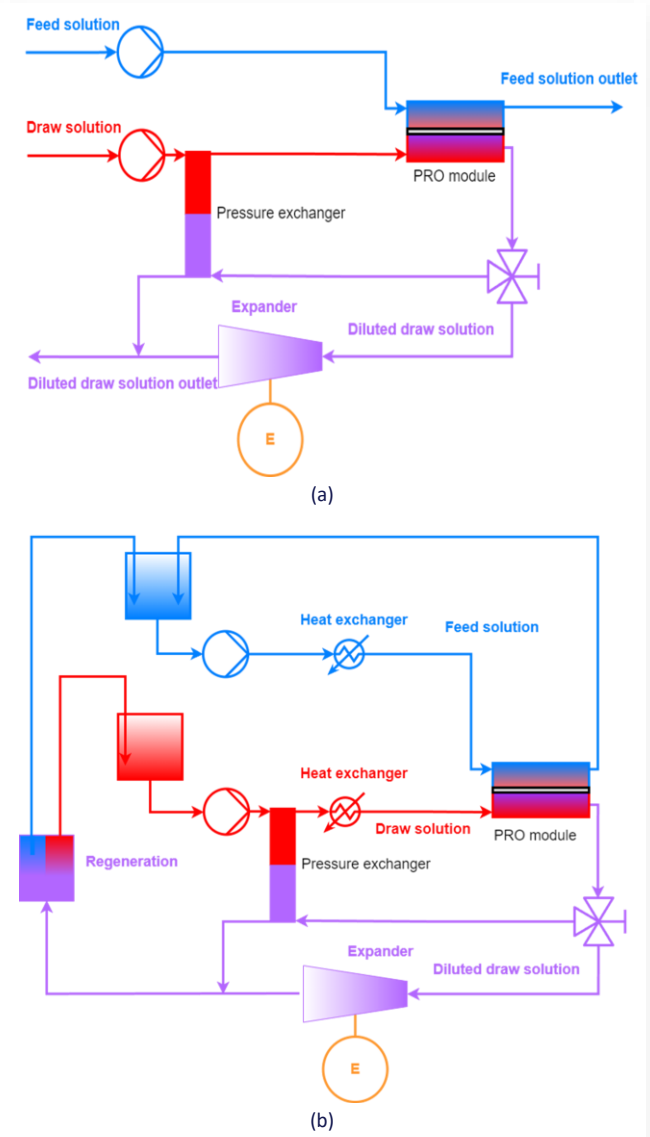

Fig. 1. Schematic of open (a) and closed (b) PRO system.

Alternative engineered solutions have more advantageous properties, such as high solubility and high osmotic pressure, allowing for greater flow of the solvent through the membrane, i.e., producing much higher power densities [8]. To maximize the osmotic pressure, the molecular mass of the solvent should be as low as possible. The selected solutions should also minimize separation energy requirements during the regeneration process, i.e., they should have a high recovery rate using low-grade heat. The considered solutions are, among others, inorganic and organic salts, aqueous solutions of very soluble ammonia salts, diluted ammonia-carbon dioxide solution in water, and aqueous solutions of ammonia hydrocarbons [8–10]. Therefore, the application of a closed PRO system allows optimization of the process depending on the intended applications. Moreover, such systems operate without any inflow of freshwater and require the draw solution regeneration. Methods of regeneration may be divided into thermal and mechanical. Thermal methods use external heat sources to separate components of the solution. A few such methods of solution regeneration have been proposed, e.g., distillation, separation using critical temperatures (over which some liquid vapours become miscible or immiscible), and separation using differences in solubility of dissolved species in a solvent for different temperatures. In essence, the external heat input, required for solution regeneration, can be converted to mechanical energy, resulting in an osmotic heat engine (OHE) [10]. Such an engine may utilize low-grade renewable energy heat sources, such as solar [11] and geothermal energy [12] or waste heat, for solution regeneration and heating of solutions in the PRO cycle, which may also increase the process performance [9]. Additionally, a closed PRO system does not require access to saltwater and freshwater in close proximity, and therefore, its environmental impact and constraints are limited.

The main problem with the PRO and its commercial applications is the low power density per square meter of the membrane when seawater or low-concentrated solutions are used. One of the ways to overcome this problem may be the application of high-concentrated or saturated solutions as working media. Several studies in which hypersaline agents were applied, including the pilot-scale facilities, were described in the work of Bajraktari et al. [13]. Very high power densities per square meter of the membrane are obtained for such working media due to the significant rise in the osmotic pressure and water flux through the membrane with increasing salt concentration. The power density was reported to increase at a higher rate than the draw solution concentration, e.g., by doubling its salinity, power density rises with factors between 2.5 and 3.75 [13]. However, most working media that came from natural resources (i.e., hypersaline lakes, salt domes, hypersaline geothermal water, etc.) and technological processes (industrial brines, e.g., from destination process, brine wastewater, etc.) were considered in the open PRO systems. These media have a NaCl concentration of up to 3 mol/dm^3, which is far below the NaCl saturation point in the water (c.a. 5.36 mol/dm^3 at 20°C) [12].

So far, the studies encountered in the literature are mostly focused on investigating solution concentrations corresponding to the standard seawater concentration in open PRO systems [14]. While some laboratory- and pilot-scale studies were conducted on open PRO systems [15], the studies presented to date regarding closed-loop PRO systems are purely theoretical [16].

To fill the apparent gap in the scope of studies published to date, the studies presented in this paper have been extended to include highly concentrated solutions (i.e., at salt concentrations much higher than those used in the literature), allowing the maximum theoretical potential of the reagent to be determined for future applications in closed PRO systems. The experimental setup designed for the purpose of this study mimics the layout and behaviour of a closed-loop PRO system on a laboratory scale. This enables an investigation of the process in conditions similar to those encountered in future real systems. In addition, determining the effect of solution temperature on process dynamics will allow better prediction of the behavior of such systems under varying operating conditions in order to investigate the possibilities of using low-grade heat to improve the efficiency of PRO systems. The experimental study also makes it possible to detect potential technical problems resulting from increasing the concentration and temperature of working solutions, which are difficult to predict in theoretical analyses. The overall novelty of this study is that it undertakes the development of a methodology for the investigation of closed-loop PRO systems, operating on highly concentrated solutions at elevated temperatures, taking advantage of available heat sources to increase the power density of the setup to the highest possible level.

The research described in this paper focuses on evaluating the effects of the concentration and temperature of NaCl solutions on the flux of the solvent (water) flowing through the semipermeable membrane, which is directly related to the possible useful work generated in the PRO process. The study was conducted without back pressure (i.e., a configuration typical of the FO process), forcing only the flow of the media on both sides of the membrane.

Additionally, the preliminary results of experiments suggested that there is a need to investigate the behavior of the osmotic membrane. A significant decrease in the permeate flow between consecutive measurements led to the conclusion that membrane degradation may play a crucial role in evaluating the PRO process performance. Therefore, the study was extended to incorporate a long-term measurement performed in the reference conditions, designed specifically to investigate the membrane performance itself.

2. Description of the method and materials used

2.1. Test solution

Analytical grade NaCl and deionized water were used to prepare the draw solution. The salt was previously dried in a vacuum dryer. A solution with a concentration of 35 g NaCl/kg of the solution, which corresponds to the standard concentration of seawater, was chosen as the test baseline (reference solution). A concentration twice as high was chosen as the next measurement point, since the increase in osmotic pressure of the solution with its concentration is linear over the assumed measurement range. To determine the maximum potential of the solution,

a concentration of 211 g/kg of solution was investigated, corresponding to 80% of the maximum solubility of NaCl salt in water at 20°C. The saturated solution was not used since crystallization of the salt in the system at points of reduced temperature could lead to the introduction of the solid fraction to the pump and osmotic module, potentially leading to damage to these components. The solution was prepared in batches of 10 kg, and the resulting concentrations were verified by density measurements (METTLER TOLEDO, Densito, accuracy ±0.001 g/cm^3) and compared with literature values.

2.2. Test stand

The bench was mostly made of AISI 316 stainless steel to minimize the risk of component degradation when using highly concentrated salt solutions. The main component of the system was a specially designed and manufactured module consisting of two parts, which, when divided by a semipermeable membrane (Dupont, FilmTec XUS1203) and assembled, form two channels allowing the flow of feed and draw solutions. The parallel flow configuration of the module was used. The working area of the module was 100 × 250 mm^2, and the height of the channels was 2.2 mm. Special support inserts (i.e., spacers) printed using the Fused Deposition Modeling (FDM) method were installed on both sides to avoid membrane deformation and flow restriction. The module with the support insert installed is presented in Fig. 2.

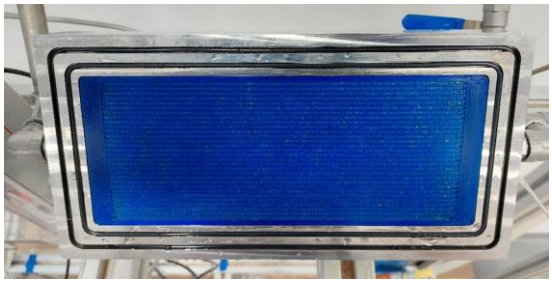

Fig. 2. Half of the membrane module with membrane support insert.

Fluid flow in the system was induced using two FOTTON FTL-222 diaphragm pumps with a maximum flow rate of 4 l/min each, powered by a 24-volt DC power supply and controlled using the method of Pulse Width Modulation (PWM). Keller PAA-33X pressure transmitters with a measurement range of 0.8-1.2 bar and an accuracy of 0.1% of the range were used to measure pressure on both sides of the module, communicating with the system via Modbus RTU RS485 protocol.

The control system, based on pressure measurement at the module outlets, ensures a zero pressure differential on both sides of the membrane (FO configuration operation) by adjusting the flow rate on the draw solution pump. Temperature control in the system was carried out by two complementary elements, i.e., a spiral heat exchanger made of a silicone hose immersed in a water bath connected to a chiller and an electric heater to facilitate the basic control and stabilization of medium temperature, and electric heaters of 300 W each placed in the flow of both media and allowing precise control of the temperature of the solutions using the PWM method. Temperature measurements were carried out using PT100 resistance sensors connected to MAX31865 transmitters communicating with the system using the SPI protocol. The solution temperature was maintained within the range of ± 0.5°C from the set value for the experiment duration.

For medium storage, two 2 l polypropylene vessels were used. Mass changes in the tanks were measured using two RADWAG 3000.X2 precision balances (accuracy ± 7.5 mg, calculated as the sum of max repeatability and linearity errors), communicating over the VISA protocol. The proprietary control and data acquisition system was integrated using a Raspberry Pi 4 8GB single-board computer with a dedicated application written in Python. A diagram of the test stand is shown in Fig. 3.

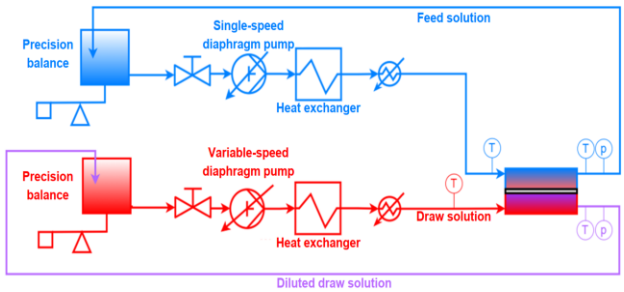

Fig. 3. Test stand schematic.

2.3. Experiment methodology

Nine cases were analyzed during the study, considering different draw solution concentrations and variable temperatures in the PRO system, as shown in Table 1. During testing, the temperature was kept equal for draw and feed solutions. The result obtained for a 35 g/kg NaCl solution at 20°C was used as the reference.

Table 1. Investigated cases.

Solution concentration (g/kg)	35			70			211		
Temperature (°C)	20	40	60	20	40	60	20	40	60

All measurements were carried out in the same configuration, using equal volumes of solutions. Before the experiment was performed, the system temperature was stabilized, and the concentration of the circulated solutions was verified by measuring their densities. Once the temperatures and pressures on both sides of the membrane were stabilized, the measurement was started and stopped automatically after a preset time of 80 minutes, identical for every case. At the end of the experiment, for a given point, the density of the feed solution was measured – to determine any salt backflow – and that of the draw solution – to determine the dilution during the process. Then, by analyzing the data, the mass fluxes of the solutions were determined. To reduce the effect of evaporation and hygroscopicity

of the draw solution, the result was calculated as the average of these fluxes. After taking into account the density of water at the measurement temperature and the membrane active area, the mass flux was converted to unit volume flux.

3. Analysis of preliminary results

Figure 4 shows the obtained data as a function of solution temperature and concentration. The permeate stream gains, however, did not match the theoretical expectations. Despite the fact that doubling the solution concentration doubles the osmotic pressure in a low-concentration range, the flow increases marginally. Strong temperature dependency is evident and reasonably consistent, which would follow in line with the expectation, i.e., the solution temperature variation affected the solution properties, such as the solution viscosity and solute diffusivity, which resulted in the rise in permeate flux with the rising system temperature. The impact of the solution concentration is not as pronounced.

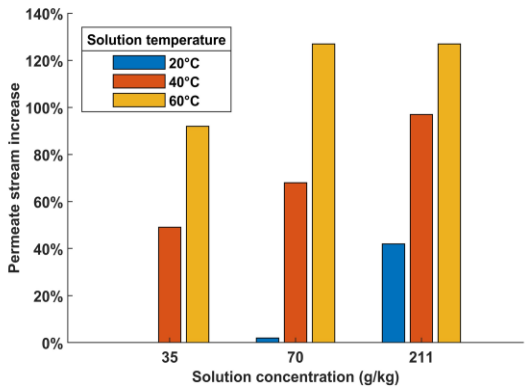

Fig. 4. Obtained flux increments as a function of draw solution concentration and process temperature with respect to the reference case (35 g/kg and 20°C).

The series of measurements was completed with an additional measurement under reference conditions. This measurement showed a significant decrease in the permeate flux compared to the first reference case. Since all the measurements were performed using the same membrane coupon, gradual degradation of the membrane in the process was suspected.

For the preliminary result correction, a linear degradation characteristic was assumed – no data collected at the time suggested a different behavior. The linear character of the degradation and its dependency on process time were checked for a solution concentrated to 35 g/kg at 20°C in a separate series of seven measurements.

The measurements in question were conducted using a single, new membrane coupon. The experiment duration was set to 80 minutes, to mimic the conditions during the actual measurement series – fixed-length runs separated by breaks for solution replenishment. Average hourly permeate flows (i.e., solvent streams through the membrane) were calculated for each experiment and the results in a normalized form (i.e., in relation to the first measurement) are presented in Fig. 5. The measured stream of solvent passing through the membrane was converted to a volumetric rate and divided by the membrane active area, resulting in mass flow rate in liters per square meter of membrane per hour (LMH), which is the standard permeate flow measurement unit in the membrane processes.

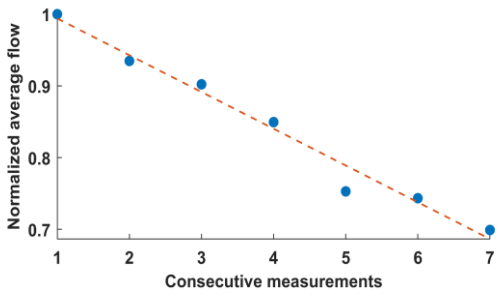

Fig. 5. Normalized hourly permeate flows for consecutive calibration experiments.

The results for each experiment run were then normalized to the flow obtained in the first measurement. It is clear that the mass flow rate is consistently reduced, and its characteristic over time is approximately linear. The average permeate flow reduction was calculated to be in the range of 5% per measurement, and this value was used as a correction factor in the post-processing of preliminary results for other solution concentrations and temperatures, further described in section 5. This reduction rate is consistent with the results of the first and last measurements of the main experiment series, conducted in reference conditions. Thus, an assumption can be made that the rate of flow reduction is constant in the examined case, and the impact of temperature and solution concentration is negligible.

4. Membrane behaviour study

A membrane behaviour study was undertaken to complement the previous step reference measurements and better understand the degradation process. The principal idea was to perform a long-term measurement on a single membrane sample and observe the permeate flux over time. 100 hours was chosen as a reasonable time scale for such an experiment. The solution used was kept at reference conditions – a concentration of 35 g/kg and a temperature of 20°C. Similarly to the first experiment, the draw solution concentration and deionized water purity were assessed at the beginning and end of each experiment step by density measurements. Temperature and pressure stabilizations were achieved before each step.

Naturally, the draw solution dilution is an important factor that is changing the permeate flux. To minimize its impact, the draw solution reservoir was expanded, so that the total mass of the draw solution in the system was kept over 15 kg at any time in a 20 l polypropylene vessel. The mass change was measured only at the feed solution side. Additionally, the measurement was performed in three distinct steps, between which the solution was regenerated by salt addition – bringing its concentration back to the reference values. With these precautions, the dilution did not exceed 7% at the end of each experiment step.

Results of the membrane behaviour study are shown in Fig. 6. The divisions between the steps of measurements are clearly visible. The flow increase at the beginning of each step is believed to be caused by the membrane settling after the test rig was turned off and on again. A diminishing flow trend is evident.

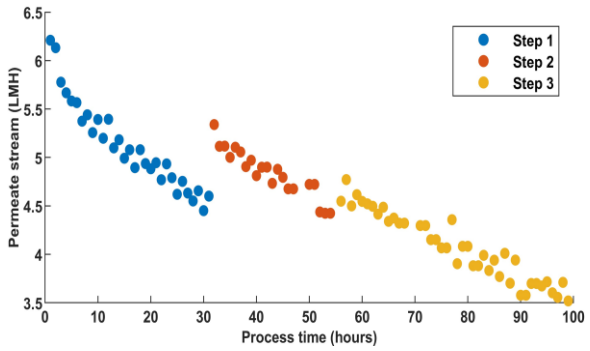

Fig. 6. Hourly average permeate flux values as a function of experiment time, obtained for reference conditions.

In every measurement, after the initial settling, the trend becomes linear. Despite increasing the solution concentration between steps, the general trend is also negative. Significantly longer measurements would have to be carried out to confirm or deny the existence of any plateau, i.e., whether the flow decreases consistently to a complete blockage or settles at an ultimate, stable level. However, in the proposed time scale, one should assume that the characteristic is macroscopically linear.

5. Final results

The linear degradation assumption proposed in section 4 was applied to the preliminary results shown in section 3. The corrected unit volume fluxes flowing through the membrane were compared with the flux obtained under reference conditions. The obtained increments are shown in Fig. 7.

A strong correlation between the solution temperature and the process dynamics is evident and consistent for individual concentrations. The impact of concentration on the obtained flux is less pronounced, but it still seems reasonable to use solutions with the highest practically applicable concentration. The performance characteristics obtained also allow for a conclusion that increasing the temperatures of the working solutions provides measurable performance benefits in osmotic systems, while reducing the risk of crystallization occurring at high concentrations of the draw solution. In order to verify these assumptions, further studies should confirm the independence of membrane degradation characteristics from temperature and solution concentration. In conclusion, the study showed that the low-grade heat source can be used not only for solution regeneration in the closed PRO systems but also for increasing the temperatures of solutions to improve the overall efficiency of the process.

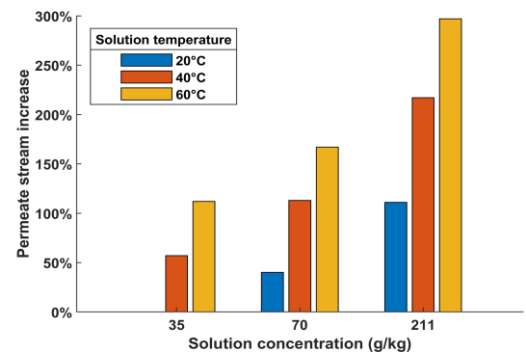

Fig. 7. Flux increments as a function of draw solution concentration and process temperature with respect to the reference case – corrected for membrane degradation

6. Conclusions

The experiments, conducted in a lab-scale osmotic system, allowed for establishing the characteristics of permeate flow as a function of solution concentration and temperature. A highly concentrated NaCl solution was used without any unforeseen problems, providing a noticeable increase in the system performance. Doubling of the permeate stream was achieved with the increased draw solution concentration of 211 g/kg, without increasing its temperature. Thus, a viable potential of highly concentrated solutions in real conditions was confirmed. The rise in temperatures of solutions also positively impacted the membrane water flux, showing the potential for using low-grade heat sources to heat the solutions. The temperature impact is especially prominent, as in the case of the highest solution concentration, the temperature increase by 20°C provided a flow increase of over 200% compared to the reference case, and a further 20°C increase allowed an increase of nearly 300%. Solution heating may be a viable, low-tech and high-impact way of increasing the power output of PRO systems even without increasing the concentrations, provided that suitable waste or low-grade heat sources are available on site. Overall, the results show that the power density of the PRO process can be improved with the introduction of closed-loop systems utilizing highly concentrated solutions. Furthermore, available heat sources can be used to increase the power density further by increasing the solution temperature. This is a promising sign for the development of such systems, as the power density is not dependent only on the available membrane surface and can be maximized within the existing space restrictions. However, the membrane degradation was observed during the measurements and investigated in separate experiments. The results helped estimate the degradation dynamics and thus evaluate data from the first experiment set. The membrane behavior warrants further study to establish the process dynamics in a broader temperature and concentration range and to investigate the possible causes of this phenomenon. So far, the existence and basic characteristics of the effect have been established. Further studies will be conducted to evaluate the osmotic potential of other prospective solutions, i.e., organic salt solutions, using the methodology presented in this work.

Acknowledgements

This work was financially supported by the National Science Centre (Poland) within project no. 2021/43/B/ST8/02968 entitled "Development of the advanced micro-macroscopic model of transport phenomena in the pressure-retarded osmosis (PRO) process", POB Energy of Warsaw University of Technology within the Excellence Initiative: Research University (IDUB) programme within ENERGYTECH-1 project, and the Scientific Council of the Discipline of Environmental Engineering, Mining and Energy of the Warsaw University of Technology.

References

[1] Logan, B.E., & Elimelech, M. (2012). Membrane-based processes for sustainable power generation using water. *Nature*, 488, 313–319. doi: 10.1038/nature11477

[2] Thorsen, T., & Holt, T. (2009) The potential for power production from salinity gradients by pressure retarded osmosis. *Journal of Membrane Science*, 335, 103–110. doi: 10.1016/j.memsci.2009.03.003

[3] Francis, L., Ogunbiyi, O., Saththasivam, J., Lawler, J., & Liu, Z. (2020). A comprehensive review of forward osmosis and niche applications. *Environmental Science: Water Research and Technology*, 6, 1986–2015. doi: 10.1039/D0EW00181C

[4] Qasim, M., Badrelzaman, M., Darwish, N.N., Darwish, N.A., & Hilal, N. (2019). Reverse osmosis desalination: A state-of-the-art review. *Desalination*, 459, 59–104. doi: 10.1016/j.desal.2019.02.008

[5] Kim, Y.C., & Elimelech, M. (2013). Potential of osmotic power generation by pressure retarded osmosis using seawater as feed solution: analysis and experiments. *Journal of Membrane Science*, 429, 330–337. doi: 10.1016/j.memsci.2012.11.039

[6] Helfer, F., Lemckert, C., & Anissimov, YG. (2014). Osmotic power with Pressure Retarded Osmosis: Theory, performance and trends – A review. *Journal of Membrane Science*, 453, 337–358. doi: 10.1016/j.memsci.2013.10.053

[7] Islam, M.S. (2018) Highly effective organic draw solutions for renewable power generation by closed-loop pressure retarded osmosis. *Energy Conversion and Management*, 171, 1226–1236. doi.org/10.1016/j.enconman.2018.06.031

[8] Hickenbottom, K.L., Vanneste, J., & Cath, T.Y. (2016) Assessment of alternative draw solutions for optimized performance of a closed-loop osmotic heat engine. *Journal of Membrane Science*, 504, 162–75. doi: 10.1016/j.memsci.2016.01.001

[9] Adhikary, S., Islam, M.S., Touati, K., Sultana, S., Ramamurthy, A.S., & Rahaman, M.S. (2020). Increased power density with low salt flux using organic draw solutions for pressure-retarded osmosis at elevated temperatures. *Desalination*, 484,114420. doi: 10.1016/j.desal.2020.114420

[10] McGinnis, R.L., McCutcheon, J.R., & Elimelech, M. (2007). A novel ammonia–carbon dioxide osmotic heat engine for power generation. *Journal of Membrane Science*, 305(1–2), 13–19. doi.org/10.1016/j.memsci.2007.08.027

[11] Wang, Q., Cheng, H., Wang, J., Ma, Z., Liu, Z., Sun, Z., Xu, D., Gao, J., & Gao, X. (2021). Temperature-enhanced pressure retarded osmosis powered by solar energy : Experimental validation , economic consideration , and potential implication. *Chemical Engineering Research and Design*, 170, 380–388. doi: 10.1016/j.cherd.2021.04.024

[12] Madsen, H.T., Bruun Hansen, T., Nakao, T., Goda, S., & Søgaard, E.G. (2020). Combined geothermal heat and pressure retarded osmosis as a new green power system. *Energy Conversion and Management*, 226, 113504. doi: 10.1016/j.enconman.2020.113504

[13] Bajraktari, N., Hélix-Nielsen, C., & Madsen, H.T. (2017). Pressure retarded osmosis from hypersaline sources, *Desalination*, 413, 65–85. doi: 10.1016/j.desal.2017.02.017

[14] He, W., Wang, Y., & Shaheed, M.H. (2014). Energy and thermodynamic analysis of power generation using a natural salinity gradient based pressure retarded osmosis process, *Desalination*, 350, 86–94. doi: 10.1016/j.desal.2014.07.015

[15] Jalab, R., Awad, A.M., Nasser, M.S., Minier-Matar, J., & Adham, S. (2020). Pilot-scale investigation of flowrate and temperature influence on the performance of hollow fiber forward osmosis membrane in osmotic concentration process. *Journal of Environmental Chemical Engineering*, 8(6), 104494. doi: 10.1016/j.jece.2020.104494

[16] Han, G., Ge, Q., & Chung, T.S. (2014). Conceptual demonstration of novel closed-loop pressure retarded osmosis process for sustainable osmotic energy generation. *Applied Energy*, 132, 383–393. doi: 10.1016/j.apenergy.2014.07.029

Co-published by
Institute of Fluid-Flow Machinery
Polish Academy of Sciences
Committee on Thermodynamics and Combustion
Polish Academy of Sciences

http://www.imp.gda.pl/archives-of-thermodynamics/

Selected aspects of blood flow simulations in arteries

Ryszard Białecki*[a], Wojciech Adamczyk[a], Ziemowit Ostrowski[a]
[a] Silesian University of Technology, Department of Thermal Technology, Faculty of Energy and Environmental Engineering, Konarskiego 22, 44-100 Gliwice, Poland
*Corresponding author email: ryszard.bialecki@polsl.pl

Received: 17.12.2023; revised: 10.02.2024; accepted: 10.03.2024

Abstract

This article discusses selected aspects of modelling blood flow in the arteries. The method of reproducing the variable-in-time geometry of coronary arteries is given based on a sequence of medical images of different resolutions. Within the defined shapes of the arteries, a technique of generation of numerical meshes of the same topology is described. The boundary conditions and non-Newtonian rheological models used in blood flow are discussed, as well as the description of blood as a multiphase medium. The work also includes a discussion of tests on the phantom of the carotid artery for the accuracy of measurements made using ultrasonography.

Keywords: Blood flow; CFD; Coronary arteries; Boundary conditions; Blood rheology; Blood as a multiphase medium

Vol. 45(2024), No. 1, 145–153; doi: 10.24425/ather.2024.150447

Cite this manuscript as: Białecki, R., Adamczyk, W., & Ostrowski, Z. (2024). Selected aspects of blood flow simulations in arteries. *Archives of Thermodynamics*, 45(1), 145–153.

1. Introduction

Blood flow is fundamental to the functioning of the human body. It is involved in several physiological processes that are necessary for life:

1. Transport of oxygen: Blood is responsible for the transport of oxygen from the lungs to all tissues of the body.
2. Transfer of nutrients and removal of waste products: It also transports nutrients produced as a result of the digestion of food to cells throughout the body and helps to remove metabolic byproducts, including carbon dioxide from cells.
3. Pressure regulation: The heart and blood vessels regulate blood flow and pressure. This is necessary to ensure that blood reaches all parts of the body.
4. Temperature regulation: Blood intensifies the heat exchange between the body and the surroundings.
5. Immune system support: The leukocytes contained in the blood defend the body against infections, viruses, and other pathogens.
6. Distribution of hormones: Hormones, produced by various glands that regulate physiological processes, are transported in the bloodstream to the target organs and tissues.
7. Clotting and wound healing: The healing process is initiated by platelets that initiate clot formation to prevent excessive bleeding.
8. Maintaining the pH and electrolyte balance: Blood contains buffers that can handle changes in pH and electrolytes (such as sodium, potassium, and calcium) that are crucial for different physiological functions.

The paper describes some aspects of modelling blood flow in the arteries that have been developed by the authors of this paper within recent research projects. The article does not de-

Nomenclature

A – cross-sectional area, m^2
D – vessel diameter, mm
E – Young modulus, GPa
f – frictional force
h – wall thickness, mm
k – constant in Quemada viscosity
ΔL – distance between the measurement points, mm
p – pressure, mmHg
Q – volumetric flow, m^3/s
R – tube radius, mm
S – cross-sectional area, m^2
t – time, s
U – cross-sectional averaged velocity, m/s
u – local velocity, m/s
Wo – Womersley number

Greek symbols

γ – shear rate
μ – dynamic viscosity, Pa·s
ν – kinematic viscosity, m^2/s
ρ – blood density, kg/m^3
τ – wall shear stress, Pa
ω – circular frequency of the flow changes

Subscripts and Superscripts

c – critical shear rate
p – plasma
w – wall

Abbreviations and Acronyms

CTA – Computed Tomography Angiography
FSI – Fluid-Structure Interaction
ICA – Invasive Coronary Angiography
MB – Myocardial Bridge
LV – Left heart Ventricle
USG – Ultrasonography
RBC – Red Blood Cells
WSS – Wall Shear Stress

scribe a complete research program but focuses on some important aspects of blood flow that the team encountered during ongoing research projects. Emphasis was placed on the issues that caused the team special difficulties. The article presents ready-made solutions to some problems but also shows possible approaches not yet implemented in the practice of the team. A comprehensive overview of the applications of CFD in hemodynamics can be found in references [1, 2].

The methods and examples discussed in the article concern the arteries of the systemic circulatory system. The walls of the arteries, unlike the walls of the veins, experience significant differences in cyclic pressure caused by heart contractions.

The characteristic features to be considered in flow simulations in the arteries are:

- complex geometry and numerous arterial branches,
- pulsatile, cyclic nature of pressure and flow variability,
- deformation of the vessel walls,
- non-Newtonian rheology,
- nonstandard boundary conditions.

2. Dimensionality of the model

The total length of the arteries in the human body is estimated to be between 100 000 and 160 000 km. The development of a model of geometry of the entire circulatory system is not realistic.

There are models of blood circulation in the human body based on one-dimensional models and the restriction of geometry to larger-diameter vessels. An example of such an approach is the open code STARFiSh developed at NTNU Trondheim [3]. The code is based on a solution of a system of first-order differential equations with partial derivatives:

$$\frac{\partial A}{\partial t} + \frac{\partial Q}{\partial x} = 0, \tag{1}$$

$$\frac{\partial Q}{\partial t} + \frac{\partial\left(\alpha\frac{Q^2}{A}\right)}{\partial x} = -\frac{A}{\rho}\frac{\partial p}{\partial x} + \frac{f}{\rho}. \tag{2}$$

where A is the cross-sectional area, Q is the volumetric flow, p is the pressure assumed constant over the cross-section, ρ is the density of blood, f is the frictional force, α accounts for nonlinearity in the cross-sectional integration of the local velocity u:

$$\alpha(t,x) = \frac{1}{AU^2}\int_S u^2 dS, \tag{3}$$

where U is the cross-sectional averaged velocity.

It has been recognized that the distribution of the shear stresses on the wall of the vessel determines the tendency of deposition of atherosclerotic plaques at the internal layer (endothelium) of the vessel [4]. At the level of histopathology, endothelial cells change their shape from elongated to nearly round and their state from atheroprotective to atherogenic [5].

Equations (1–2) are very useful to simulate the blood flow within the whole body. However, 1D models do not provide details of the blood flow pattern in the vessel, specifically the shear stress at the wall. The latter can be determined only using 2D or 3D models, preferably in time-dependent geometry. 2D models are applied to reduce computational time; in most cases, these papers assume axisymmetry of the geometry [6]. Both 2D and 3D models are based on solutions of the Navier-Stokes equations (mass and momentum conservation). The simplest cases do not account for pulsatile flow using average or extremum flow conditions [7].

More sophisticated approaches use time-dependent boundary conditions (pressure of flow) but neglect the deformation of the walls of the vessels during the cardiac cycle. For most of the major healthy arteries, the vessel diameter changes during the cardiac cycle are approximately 5–10% [8]. Therefore, there are numerous articles in which the walls of the vessels are treated as rigid [9].

The next complexity involves accounting for the periodic deformation of the vessels. 3D simulations where the flexibility of the walls is accounted for are computationally demanding compared to rigid wall modelling. In this case, two techniques are available when:

- the change in geometry is known from medical imaging techniques such as noninvasive coronary CT (CCTA), invasive coronary angiography (ICA), and intravascular ultrasound (IVUS) [10];
- the deformation of the vessels is obtained by applying the fluid-structure interaction where the stress/stress field in the walls is coupled with the blood flow pattern [11].

The remaining portion of the paper is devoted to 3D models.

3. Retrieving the time-dependent geometry. Case of coronary arteries

Coronary arteries are located on the surface of the heart muscle (myocardium). As a result, these arteries are not squeezed at systole and can transport oxygen and nutrients to the heart muscle. Arteries are permanently attached to the myocardium whose volume and shape change during the cardiac cycle causing variations in artery length and curvature. In addition, pressure pulsations generated by the contraction of the left ventricle generate changes in the lumen of the vessel.

The geometry of the coronary artery can even be more complex in the presence of the so-called myocardial bridge (MB) when muscle bands overlay a segment of the coronary artery. This condition is mostly asymptomatic, however, in some cases, it may result in myocardial ischemia, angina, acute coronary syndrome, etc. The presence of MB causes an oscillation in blood flow that results in a deposition of the atherosclerotic plaque proximal (before the inflow) on MB.

The geometry of the vessel can be retrieved by several modalities. The medical images that were used in the paper were acquired at the Silesian Centre of Heart Diseases using angio-computed tomography.

The raw data used to retrieve the geometry of the coronary arteries consisted of a set of ECG-gated angio-CT images recorded every 10% of the time of the cardiac cycle. To reduce the harmful effect of the X-rays on the patient, the radiation dose was not only low but also modulated within the cycle. As a result, the resolution of these packages of images was low. Additional high-resolution images have been taken separately for diastole and systole. The total set consisted thus of images of various resolutions and quality, specifically 10 images of 256 × 256 resolution and 2 images (diastole/systole) of 512 × 512 resolution. The images have been recorded by a 128-slice dual-source computed tomography scanner (SOMATOM Definition Flash, Siemens Healthineers, Forchheim, Germany) using beam collimation 2 × 64 mm × 0.6 mm, slice thickness of 1.5 mm and reconstruction interval of 0.5 mm. Figure 1 shows an example of a raw image.

The set of images requires intensive processing consisting of:

1. segmentation of low-resolution images (extraction of coronary artery shapes from 3D image data);
2. co-registration of the low-resolution images corresponding to subsequent time instants of the cardiac cycle (the process of transforming images into one coordinate system). The result is a set of nonlinear transformations showing the transition between subsequent images;
3. segmentation of the high-resolution data and generation of a 3D surface in STL format;
4. smoothing the obtained in step 3 STL surface;
5. generation of CFD mesh in the smoothed object obtained in step 4;
6. transformation of the mesh obtained in step 5 using the nonlinear transformation resulting from step 2 (co-registration).

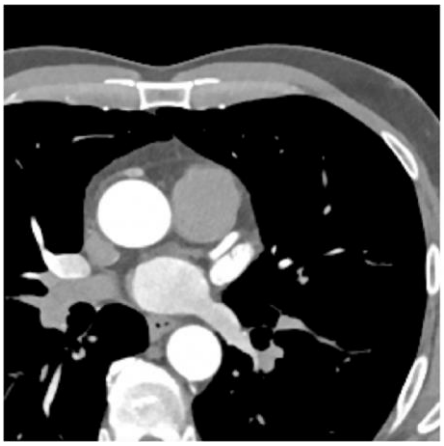

Fig. 1. An example of a raw high-resolution image.

Segmentation of medical images (steps 1 and 3) was carried out using the active contour method with threshold-based pre-segmentation implemented in the ITK SNAP package [12]. The theory behind this method is to find the close contours by solving the equation:

$$\frac{\partial C(u,v,t)}{\partial t} = \vec{F} \cdot \vec{n}\,, \tag{4}$$

where: C – closed contour parametrized by u, v, t with u and v denoting the local coordinates and t – time, $\vec{F}\,\vec{n}$ – the sum of internal and external forces acting on the contour in the normal direction: internal forces associated with the curvature, external with the gradient of the imaged intensity.

The co-registration process consists of three steps: rigid body movement, affine transformation, and nonlinear transformation based on diffeomorphism. These transformations are executed using the ANTs package [13].

The raw 3D surface retrieved from the high resolution data was smoothed using the GeoMagic software [14]. The CFD mesh generation is performed using a standard Fluent Ansys mesher [15]. The nodes of the CFD mesh generated in step 5 are projected using the transformation matrix obtained in step 5 onto every low-resolution object. Based on this surface mesh, the volumetric mesh at each step is generated. The advantage of the proposed method is the generation of a CFD mesh of the same topology at each instant of time. Due to this, the interpolation errors between grids are avoided, the mesh morphing utility can be used directly, and the CFD calculation time is reduced.

The scheme of generation of the geometry of the coronary arteries is shown in Fig. 2. The resulting geometries at 30, 50, 70 and 90% of the cardiac cycle are shown in Fig. 3.

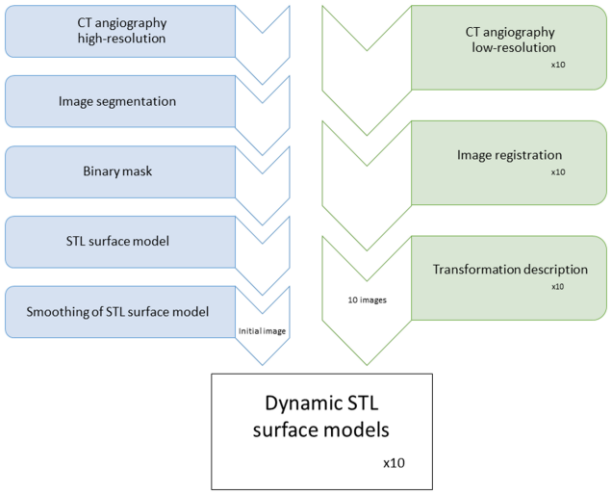

Fig. 2. Scheme of retrieving the time-dependent geometry of the coronary arteries.

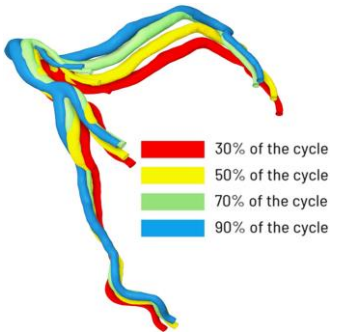

Fig. 3. Geometries of the coronary arteries at 30, 50, 70 and 90% of the cardiac cycle.

4. Measurement of the phantom deformation of the carotid artery

The stiffness of the arteries is a measure of the rigidity of the arterial walls. This property changes with age due to remodeling of the artery wall structure where elastic elastin fibers are replaced by stiffer collagen ones. Increased stiffness is a condition that can have several serious implications for overall well-being. Increased stiffness may result in:

- Hypertension that results from the superposition of the main pressure pulse generated by the systole of the left heart ventricle (LV) and the wave reflected from the bifurcations of the arteries;
- Thickening of the heart muscle (LV hypertrophy) due to the increased workload of the left ventricle resulting from its increased workload contributing to the increased risk of heart failure;
- Reduced blood flow to organs due to the reduced ability of the blood vessels to constrict and dilate;
- Damage of end organs such as kidneys, eyeballs and brain caused by the reduced ability to dump the pulsation of the blood pressure.

The stiffness of the blood vessels is assessed by measuring the pulse wave velocity *PWV* obtained from the time that elapses between pressure peaks in two arteries (usually carotid and femoral). This value is obtained using the Moens-Kortweg equation [16]:

$$PWV = \frac{\Delta L}{\Delta t} = \sqrt{\frac{Eh}{D\rho}}, \tag{5}$$

where: E – Young modulus of the wall, h – wall thickness, D – vessel diameter, ρ – blood density, ΔL – distance between the measurement points along the blood vessel, Δt – time that elapsed between the pressure peaks at measurement points.

Equation (5) gives the mean values of the stiffness of the vessel wall between the pressure measurement points. The project aimed to determine the local stiffness of the carotid artery wall by solving an inverse problem of blood flow in a deforming conduit (solving the fluid-structure interaction (FSI) problem) based on the measured deformation of the walls. The latter was measured using the ultrasound scanner.

The key issue was to determine the precision of the ultrasonography (USG) measurements and the validation of the FSI model based on measurements performed on a phantom undergoing a load similar to the carotid artery. For this purpose, a phantom was built in which pressure pulsations mimicking the work of the heart are produced by a pump, and the deformations of the flexible tube are measured in two perpendicular planes by high-resolution digital cameras. Parallel to these deformation measurements, deformation is measured with a USG scanner. Figure 4 shows the scheme of the experimental rig. The photo of the rig is shown in Fig. 5. The comparison of the camera and USG scanner uncertainties in measured displacements is shown in Fig. 6. As can be seen, the ultrasound-derived displacements exhibit good agreement (mean difference of 0.0113 mm) in comparison with the camera-generated data.

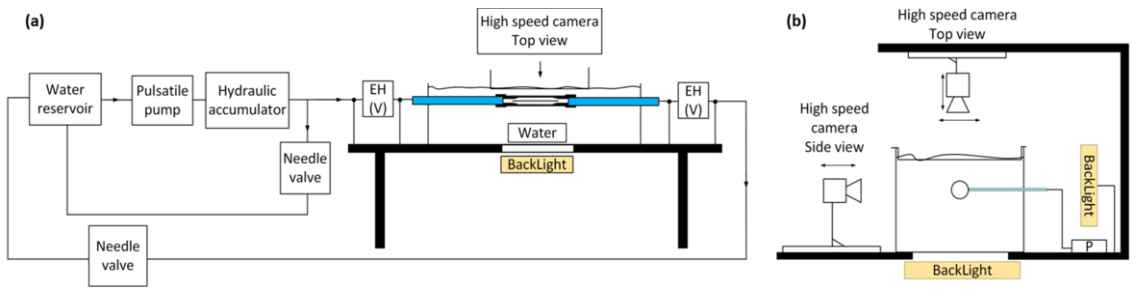

Fig. 4. Scheme of the phantom (a). EH is the Endress Hauser electromagnetic flow meter.
Side view (b). The pressure gauges are installed at the inlet and outlet of the installed elastic tube [17].

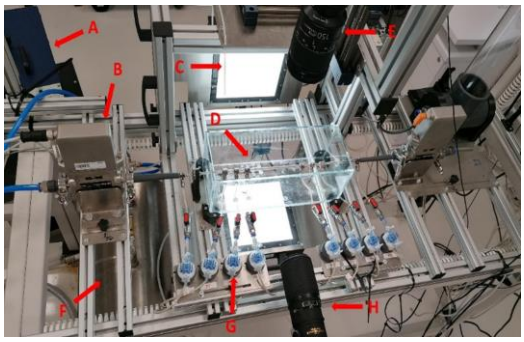

Fig. 5. Photo of the test rig: A – periodic pump, B – flowmeter, C – backlight, D – arterial phantom, E – top camera (MIRO), F – reservoir tank, G – pressure transducers, H – side camera (VEO) [17].

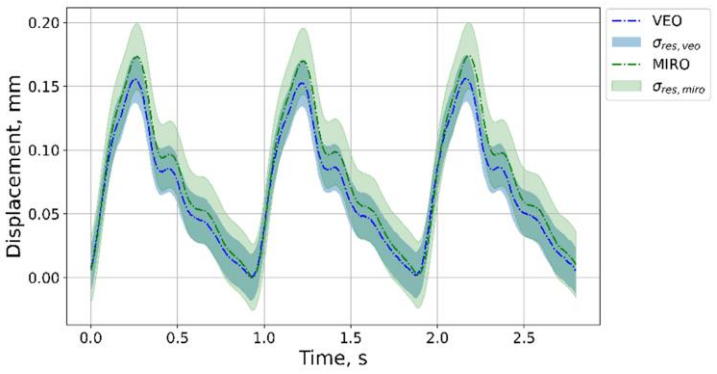

Fig. 6. Comparison of displacements recorded by both cameras with uncertainty represented by overlaid shaded areas. In both cases, uncertainty is characterized as dr el,cam ± σres,cam [17].

5. Boundary conditions

In the case of 3D simulations, simulation of blood flow in the entire cardiovascular system would lead to a prohibitively long calculation time. Therefore, the computational area is limited to a small portion of the circulatory system with at least one inlet and one outlet defined at fictitious surfaces closing the truncated vessel. To obtain the blood flow solution of the Navier-Stokes equations, unambiguous boundary conditions should be specified at these fictitious surfaces. These boundary conditions are formulated in terms of velocity (mass flow), pressure, or a relationship between these two parameters. It should be stressed that the fluid mechanics outflow conditions commonly used cannot be used in blood flow simulations. Such boundary conditions can be applied only in the case of fully developed velocity profiles that correspond to flow in a long, constant cross-section.

Moreover, although the flow in the arteries is, with very few exceptions, laminar, the velocity profile in the arteries is not parabolic. It is the pulsating blood flow generated by the contraction of the left ventricle that distorts the velocity profile. The resulting distribution of the velocity is, for the idealized case of flow in a stiff, constant cross-section tube, governed by the Womersley number defined as:

$$\mathrm{Wo} = R\sqrt{\frac{\omega}{\nu}}, \tag{6}$$

where: R – tube radius, ω – circular frequency of the flow changes, ν – kinematic viscosity. Figure 7 shows the speed profiles for different Womersley numbers.

The boundary conditions can be defined using three approaches:

- measurements (patient-specific data),
- statistics (population data),
- estimates based on physiological assumptions and models.

It is recommended to use, whenever applicable, the first option and define the velocity or pressure. Statistical data cannot be patient-specific and only represent the general population. Inflow and outflow conditions can also be assessed using theories such as Murray's law [19] which defines the link between mass flow rate and vessel diameter, or the theory of constant wall shear stress [20]. Alternatively, the interaction of the computational domain with the remaining part of the cardiovascular system can be addressed using the multi-scale approach. The idea is to couple the 3D model with the 1D [21] or 0D [22] model describing the behaviour of the peripheral vascular system. The latter is usually based on the hydraulic/electric analogy with flow resistance resulting in pressure drop and capacitance describing vascular compliance. The lower-order model is described by an ordinary differential equation whose parameters, describing the behaviour of the vascular system outside of the 3D model, are not easy to determine. Implementation of this type of nonlinear boundary condition leads to an iterative procedure and often requires stabilization.

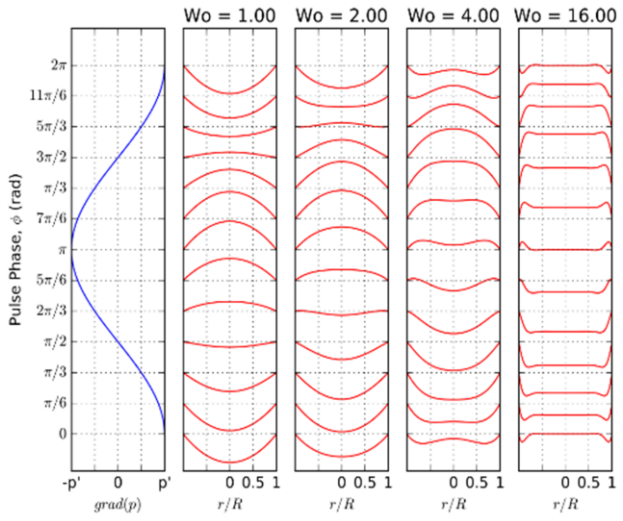

Fig. 7. Four pulsatile flow profiles in a straight tube. The first graph (in blue) shows the pressure gradient as a cosine function, and the other graphs (in red) show dimensionless velocity profiles for different Womersley numbers [18].

5.1. Velocity boundary conditions

In some cases, blood speeds can be measured using non-invasive methods such as the Doppler technique associated with ultrasound, magnetic resonance imaging and computed tomography angiography (CTA) (which requires contrast). Invasive methods

include arterial catheterization, a method that requires the introduction of a catheter into an artery, and rather rarely used electromagnetic flowmetry. The latter consists of measuring the generated voltage induced in coils placed near a blood vessel immersed in a variable. magnetic field.

5.2. Pressure Boundary Conditions

Non-invasive pressure measurement can be carried out at arteries located close to the surface of the body (carotid, radial, femoral) using the applanation tonometer technique [23, 24]. Pressure can be measured by invasive arterial catheterization.

6. Wall shear stress and oscillatory shear stress index

The deposition of atherosclerotic plaque on the walls of arteries depends on the wall shear stress (τ_w, WSS). Typically, the onset of plaque occurs at low τ_w locations while a high WSS prevents plaque deposition [4]. Another parameter that indicates plaque deposition is the oscillatory shear stress index *OSI* defined as [25]:

$$OSI = \frac{1}{2}\left(1 - \frac{|\int_0^T \tau_w dt|}{\int_0^T |\tau_w| dt}\right) \tag{6}$$

Figure 8 shows the distribution of both indices in the left ascending coronary artery. The results have been obtained for the inflow condition: pulsatile pressure, and the outflow condition: mass distribution between outlets based on the Murray law (including accumulation in the volume of the arteries).

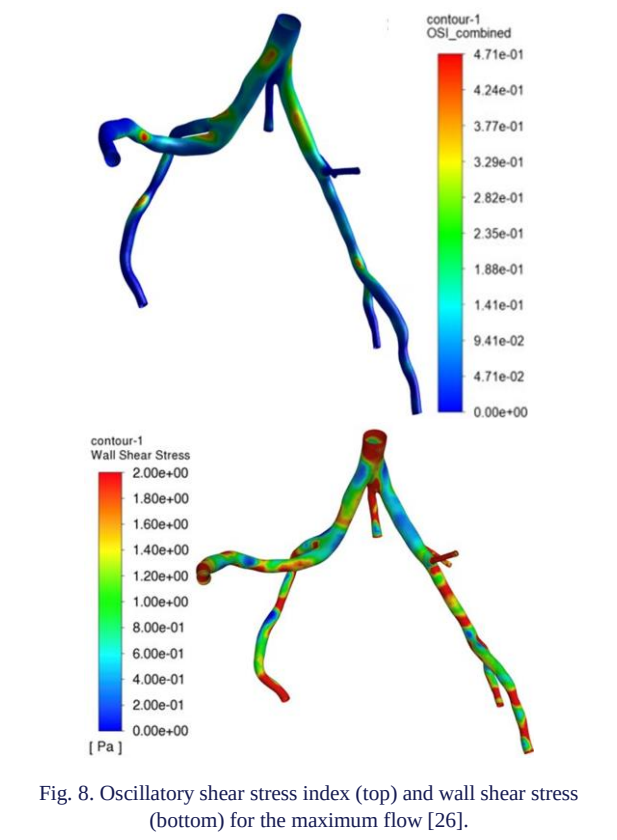

Fig. 8. Oscillatory shear stress index (top) and wall shear stress (bottom) for the maximum flow [26].

7. Rheology of blood

Blood is a non-Newtonian, multiphase fluid with cellular elements: red blood cells (RBC), white blood cells and platelets suspended in plasma. The latter is an aqueous solution containing organic molecules, proteins and salts. Plasma and red blood cells (erythrocytes) play a dominant role in the definition of the viscosity of blood. At low shear rates, the aggregation of RBC occurs accompanied by increased blood viscosity [27].

There are two possible approaches to account for the non-Newtonian properties of blood. The first is the usage of nonlinear constitutive laws for viscosity where the blood is treated as a one phase fluid. The second is to treat blood as a multiphase medium.

The most popular are [28]:

Carreau:

$$\mu = \mu_\infty + (\mu_0 - \mu_\infty[1 + (\lambda\gamma^2]^{\frac{n-1}{2}}), \tag{7}$$

Casson:

$$\mu = \left(\sqrt{\mu_c} + \sqrt{\tau_c/\gamma}\right)^2, \tag{8}$$

Quemada:

$$\mu = \mu_p(1 - \frac{1}{2}\frac{k_0 + k_\infty\sqrt{\frac{|\gamma|}{\gamma_c}}}{1+\sqrt{\frac{|\gamma|}{\gamma_c}}}\phi)^{-2}, \tag{9}$$

where γ is the shear rate and the remaining variables are constants, whose values can be found in [29].

Figure 9 shows the velocity contours corresponding to different instants of the cardiac cycle obtained using various rheological models [30] obtained for one velocity inlet and four pressure outlets, the numerical mesh consisting of 1.3 million cells.

8. Blood as a multiphase medium

When using non-Newtonian constitutive laws, blood is treated as a homogeneous liquid of viscosity that depends on the shear rate. An alternative approach is to take into account the presence of granular phases (blood cells) immersed in a liquid (plasma). The two most popular approaches are known as Euler-Euler and Euler-Lagrange. In the former, the Navier-Stokes equations for plasma are solved in the Eulerian coordinate frame. The granular phases are also modelled as fluids with appropriately defined properties and solved in the Euler coordinate frame. Both plasma and granular phases are then as interpenetrating continua.

In the Euler-Lagrange approach, first the plasma is solved separately in Eulerian coordinates, and then the fate of the granular phase is traced in the Lagrangian coordinates frame. As the volume fraction of the blood cells is high, the interactions (collisions) between the tranced cells should be accounted for. This requires a solution of an additional set of equations based on the kinetic theory of granular flow [31].

Figure 10 shows the results of simulations of blood flow in the aorta with coarctation (congenital narrowing) obtained by the Euler–Euler technique for the inlet pressure conditions and the boundary conditions of the 3-element Windkessel outlet [32].

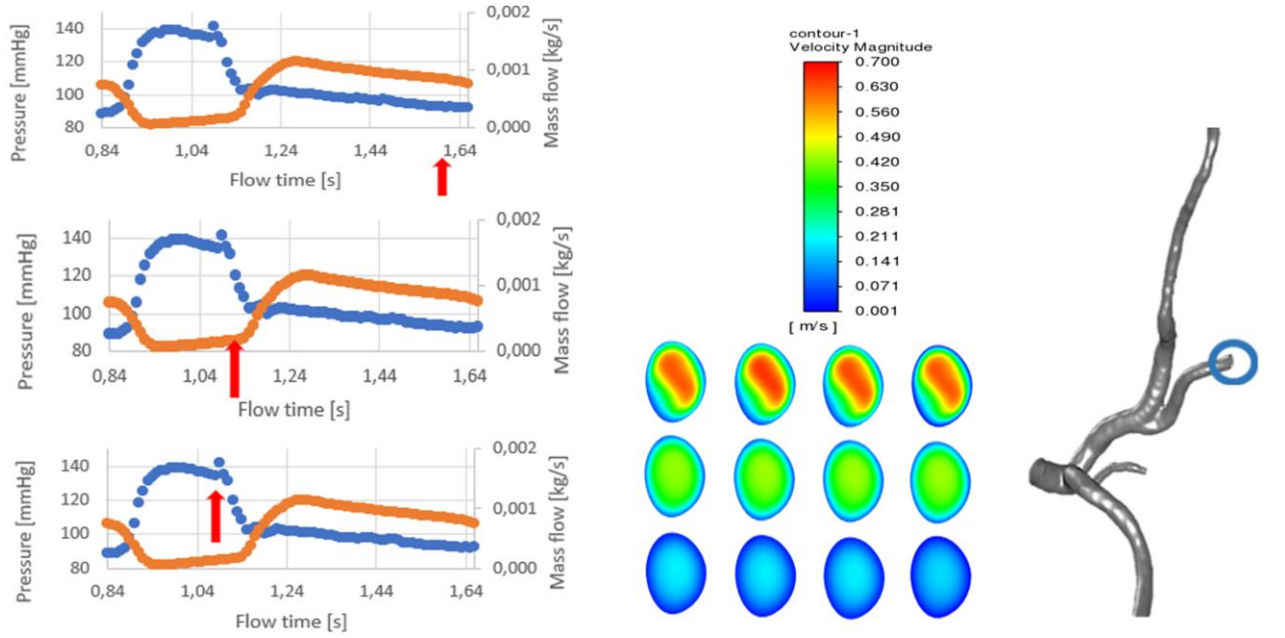

Fig. 9. Times of the cardiac cycle (red arrow) (left). Velocity profiles evaluated using various rheological models (middle). Geometry of the computational domain (bottom). Circle denotes the location of the cross section where the velocity is shown [30].

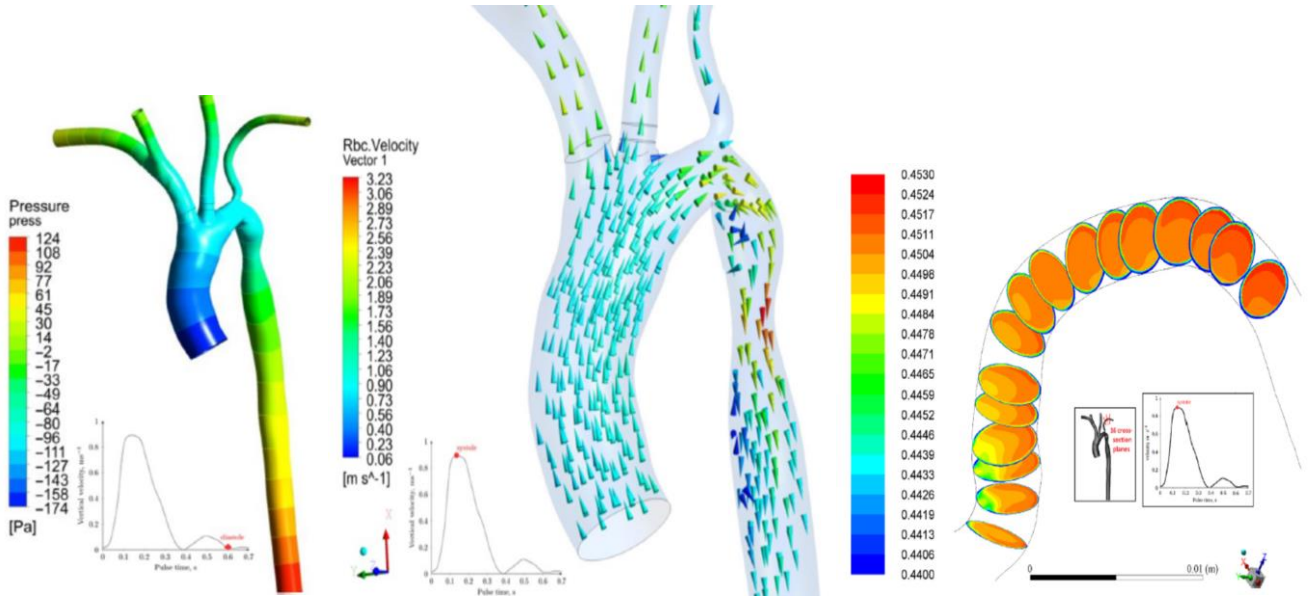

Fig. 10. Pressure distribution in the aorta with systole (left). Velocity of the RBC (middle). Volume fraction of RBC in left subclavian artery [32].

The results (see Fig. 9) confirm the presence of the Fhraeus-Lindqvist effect resulting from the movement of the RBC to the centre of the vessel leaving plasma near the wall [33].

9. Conclusions

CFD can be used successfully to simulate blood flow in the arteries. Reliable simulation results are based on the restoration of vessel geometry, which requires the processing of medical images obtained using tomographic modalities. The difficulties encountered in these activities result from the variability of images over time. The article shows a method that allows not only to reproduce such shapes but also to generate numerical grids with the same topology in subsequent time steps. Difficulties in blood flow simulations are also caused by the proper definition of boundary conditions and non-Newtonian blood rheology. An overview of the types of boundary conditions and rheological models encountered and examples of their application are given.

Acknowledgements

The research leading to these results is funded by the Norwegian Financial Mechanism 2014-2021 operated by the National Science Center, PL (NCN) within GRIEG program under grant

#UMO2019/34/H/ST8/00624, project (ENTHRAL), and by the National Science Center within OPUS scheme under contract 2017/27/B/ST8/01046, and by Ministry of Education and Science (Poland) under statutory research funds of the Faculty of Energy and Environmental Engineering of SUT under contract BK-252/RIE6/2023 08/060/BK_23/1096.

References

[1] Morris, P.D., Narracott, A., von Tengg-Kobligk, H., Silva Soto, D.A., Hsiao, S., Lungu, A., Evans, P., Bressloff, N.W., Lawford, P.V., Hose, D.R., & Gunn, J. P. (2016). Computational fluid dynamics modelling in cardiovascular medicine. *Heart (British Cardiac Society)*, 102(1), 18–28. doi: 10.1136/heartjnl-2015-308044

[2] Gijsen, F., Katagiri, Y., Barlis, P., Bourantas, C., Collet, C., Coskun, U., Daemen, J., Dijkstra, J., Edelman, E., Evans, P., van der Heiden, K., Hose, R., Koo, B.-K., Krams, R., Marsden, A., Migliavacca, F., Onuma, Y., Ooi, A., Poon, E., & Serruys, P. (2019). Expert recommendations on the assessment of wall shear stress in human coronary arteries: existing methodologies, technical considerations, and clinical applications. *European Heart Journal*, 40(41), 3421–3433. doi: 10.1093/eurheartj/ehz551

[3] Hellevik L.R., & Sturdy J. https://www.ntnu.no/starfish [accessed 20 Nov. 2023].

[4] Zhou, M., Yu, Y., Chen, R., Liu, X., Hu, Y., Ma, Z., Gao, L., Jian, W., & Wang, L. (2023). Wall shear stress and its role in atherosclerosis. *Frontiers in Cardiovascular Medicine*, 10, 1083547. doi: 10.3389/ fcvm.2023.1083547

[5] Malek, A.M. (1999). Hemodynamic shear stress and its role in atherosclerosis. *JAMA: The Journal of the American Medical Association*, 282(21), 2035. doi: 10.1001/jama.282.21.2035

[6] Katz, S., Caiazzo, A., Moreau, B., Wilbrandt, U., Brüning, J., Goubergrits, L., & John, V. (2023). Impact of turbulence modeling on the simulation of blood flow in aortic coarctation. *International Journal for Numerical Methods in Biomedical Engineering*, 39(5), 3695. doi: 10.1002/cnm.3695

[7] Bordones, A.D., Leroux, M., Kheyfets, V.O., Wu, Y.A., Chen, C.Y., & Finol, E.A. (2018). Computational fluid dynamics modeling of the human pulmonary arteries with experimental validation. *Annals of Biomedical Engineering*, 46(9), 1309–1324. doi: 10.1007/s10439-018-2047-1

[8] Taylor, C.A., Hughes, T.J.R., & Zarins, C.K. (1998). Finite element modeling of blood flow in arteries. *Computer Methods in Applied Mechanics and Engineering*, 158(1–2), 155–196. doi: 10.1016/s0045-7825(98)80008-x

[9] Gharahi, H., Zambrano, B.A., Zhu, D.C., DeMarco, J.K., & Baek, S. (2016). Computational fluid dynamic simulation of human carotid artery bifurcation based on anatomy and volumetric blood flow rate measured with magnetic resonance imaging. *International Journal of Advances in Engineering Sciences and Applied Mathematics*, 8(1), 46–60. doi: 10.1007/s12572-016-0161-6

[10] Decroocq, M., Frindel, C., Rougé, P., Ohta, M., & Lavoué, G. (2023). Modeling and hexahedral meshing of cerebral arterial networks from centerlines. *Medical Image Analysis*, 89, 102912. doi: 10.1016/j.media.2023.102912

[11] Athani, A., Ghazali, N.N.N., Badruddin, I.A., Kamangar, S., Anqi, A.E., & Algahtani, A. (2022). Investigation of two-way fluid-structure interaction of blood flow in a patient-specific left coronary artery. *Bio-Medical Materials and Engineering*, 33(1), 13–30. doi: 10.3233/bme-201171

[12] Yushkevich, P.A., Piven, J., Hazlett, H.C., Smith, R.G., Ho, S., Gee, J.C., & Gerig, G. (2006). User-guided 3D active contour segmentation of anatomical structures: Significantly improved efficiency and reliability. *NeuroImage*, 31(3), 1116–1128. doi: 10.1016/j.neuroimage.2006.01.015

[13] Avants, B.B., Tustison, N.J., Song, G., Cook, P.A., Klein, A., & Gee, J.C. (2011). A reproducible evaluation of ANTs similarity metric performance in brain image registration. NeuroImage, 54(3), 2033–2044. doi: 10.1016/j.neuroimage.2010.09.025

[14] Systems 3D. http://www.geomagic.com/en/products/design/overview [accessed 25 Nov. 2023].

[15] Ansys.com. *Academic Research Fluent, Release 2021R2*. 2021.

[16] Korteweg, D.J. (1878). Ueber die Fortpflanzungsgeschwindigkeit des Schalles in elastischen Röhren. *Annalen Der Physik*, 241(12), 525–542. doi:10.1002/andp.18782411206

[17] Sinek, A., Mesek, M., Rojczyk, M., Juszczyk, J., Adamczyk, W. P., Sturdy, J., Melka, B., Golda, A., Nowok, M., Ostrowski, Z., & Białecki, R. (2023). Evaluating the precision and reproducibility of non-invasive deformation measurements in an arterial phantom. *Measurement: Journal of the International Measurement Confederation*, 216(112904), 112904. doi: 10.1016/j.measurement.2023.112904

[18] Hellmuth R. https://commons.wikimedia.org/w/index.php?curid=54810155 [accessed 25 Nov. 2023].

[19] Painter, P.R., Edén, P., & Bengtsson, H.U. (2006). Pulsatile blood flow, shear force, energy dissipation and Murray's Law. *Theoretical Biology & Medical Modelling*, 3, 31. doi: 10.1186/1742-4682-3-31

[20] Zarins, C.K., Zatina, M.A., Giddens, D.P., Ku, D.N., & Glagov, S. (1987). Shear stress regulation of artery lumen diameter in experimental atherogenesis. *Journal of Vascular Surgery*, 5(3), 413–420. https://pubmed.ncbi.nlm.nih.gov/3509594

[21] Olufsen, M.S., Peskin, C.S., Kim, W.Y., Pedersen, E.M., Nadim, A., & Larsen, J. (2000). Numerical simulation and experimental validation of blood flow in arteries with structured-tree outflow conditions. *Annals of Biomedical Engineering*, 28(11), 1281−1299. doi: 10.1114/1.1326031

[22] Vignon-Clementel, I.E., Figueroa, C.A., Jansen, K.E., & Taylor, C.A. (2006). Outflow boundary conditions for three-dimensional finite element modeling of blood flow and pressure in arteries. *Computer Methods in Applied Mechanics and Engineering*, 195(29–32), 3776–3796. doi: 10.1016/j.cma.2005.04.014

[23] Adji, A., Hirata, K., & O'Rourke, M.F. (2006). Clinical use of indices determined non-invasively from the radial and carotid pressure waveforms. *Blood Pressure Monitoring*, 11(4), 215–221. doi: 10.1097/01.mbp.0000218001.50333.b7

[24] Nelson, M.R., Stepanek, J., Cevette, M., Covalciuc, M., Hurst, R.T., & Tajik, A.J. (2010). Noninvasive measurement of central vascular pressures with arterial tonometry: Clinical revival of the pulse pressure waveform? *Mayo Clinic Proceedings. Mayo Clinic*, 85(5), 460–472. doi: 10.4065/mcp.2009.0336

[25] Ku, D.N., Giddens, D.P., Zarins, C.K., & Glagov, S. (1985). Pulsatile flow and atherosclerosis in the human carotid bifurcation. Positive correlation between plaque location and low oscillating shear stress. *Arteriosclerosis (Dallas, Texas)*, 5(3), 293–302. doi: 10.1161/01.atv.5.3.293

[26] Melka, B., Psiuk-Maksymowicz, K, Borys, D., Ostrowski, Z., Rojczyk, M., Gracka, M., Adamczyk, W.P., & Białecki, R.A. (2023). Numerical modelling of myocardial bridge covering dynamic shape of the human coronary artery (Book of Abstracts, pp. 87). *XXVII Polish Conference on Biocybernetics and Biomedical Engineering*, 27–29 September, Lodz, Poland.

[27] Nader, E., Skinner, S., Romana, M., Fort, R., Lemonne, N., Guillot, N., Gauthier, A., Antoine-Jonville, S., Renoux, C., Hardy-Dessources, M.D., Stauffer, E., Joly, P., Bertrand, Y., & Connes, P. (2019). Blood rheology: Key parameters, impact on blood

flow, role in sickle cell disease and effects of exercise. *Frontiers in Physiology*, 10, . doi: 10.3389/fphys.2019.01329

[28] Wajihah, S.A., & Sankar, D.S. (2023). A review on non-Newtonian fluid models for multi-layered blood rheology in constricted arteries. *Archive of Applied Mechanics*, 93(5), 1771–1796. doi: 10.1007/s00419-023-02368-6

[29] Abbasian, M., Shams, M., Valizadeh, Z., Moshfegh, A., Javadzadegan, A., & Cheng, S. (2020). Effects of different non-Newtonian models on unsteady blood flow hemodynamics in patient-specific arterial models with in-vivo validation. *Computer Methods and Programs in Biomedicine*, 186(105185), 105185. doi: 10.1016/j.cmpb.2019.105185

[30] Bigaj, K., Rojczyk, M., Wasilewski, J., Melka, B., Ostrowski, Z., Gracka, M., Adamczyk, W., & Białecki, R. (2023). CFD assessment of hemodynamics in coronary arteries using three rheological models (in Polish). *Proceedings of the Polish Congress of Rheology*, 18–20 September, Kraków-Wieliczka, Poland.

[31] Liu, J., Yu, F., & Zhang, Y. (2020). MP-PIC simulation of blood cell movement through a LAD with high stenosis. *Powder Technology*, 361, 448–454. doi: 10.1016/j.powtec.2019.05.076

[32] Melka, B., Adamczyk, W.P., Rojczyk, M., Nowak, M.L., Gracka, M., Nowak, A.J., Golda, A., Bialecki, R.A., & Ostrowski, Z. (2019). Numerical investigation of multiphase blood flow coupled with lumped parameter model of outflow. *International Journal of Numerical Methods for Heat and Fluid Flow*, 30(1), 228–244. doi: 10.1108/hff-04-2019-0279

[33] Farina, A., Fasano, A., & Rosso, F. (2023). A theoretical model for the Fåhræus effect in medium–large microvessels. *Journal of Theoretical Biology*, 558, 111355. doi: 10.1016/j.jtbi.2022.111355

Co-published by
Institute of Fluid-Flow Machinery
Polish Academy of Sciences
Committee on Thermodynamics and Combustion
Polish Academy of Sciences

http://www.imp.gda.pl/archives-of-thermodynamics/

Numerical study on effect of operating pressures on CRKEC-based two-stage ejector

Virendra Kumar[a], Surendra Kumar Yadav[b*], Anil Kumar[c], Nishant Kumar Singh[a], Lalta Prasad[d]

[a]Department of Mechanical Engineering. Harcourt Butler technical University, Kanpur 208002, India
[b]Department of Mechanical Engineering. K R Mangalam University, Gurugram 122001, India
[c]Department of Mechanical Engineeringg. KNIT, Sultanpur 228118, India
[d]Department of Mechanical Engg. NIT, Uttrakhand 246174, India
*Corresponding author email: surendra.yadav@krmangalam.edu.in

Received: 14.04.2023; revised: 17.05.2023; accepted: 06.12.2023

Abstract

The two-stage ejector mixing-diffuser section in this study was computed using the Redlich-Kwong equation of state. The ejector was designed based on the constant rate of kinetic energy change (CRKEC) approach. The water vapor mixing diffuser profile and flow properties were calculated using a one-dimensional gas dynamic model. For the numerical investigation, the estimated geometrical profile based on the input design and operating conditions was utilized. ANSYS-Fluent 14.0 was employed for the numerical study. The analysis was conducted under both on-design and off-design scenarios using the standard k-ε turbulence model. The impact of operating factors on flow behavior and entrainment ratios was investigated at off-design conditions. The findings demonstrated that the operational total pressures of the primary, secondary, and exit flows are a function of the two-stage ejector (TSE) entrainment ratio. With a higher exit pressure and more secondary/entrained flows, the entrainment ratio increases. However, altering the primary flow pressure in ways other than for the design conditions reduces the entrainment ratio.

Keywords: Ejector; Constant rate of kinetic energy change (CRKEC); Two-stage ejector (TSE); Jet-pump; Mixing-diffuser

Vol. 45(2024), No. 1, 155–164; doi: 10.24425/ather.2024.150448

Cite this manuscript as: Kumar, V., Yadav, S. K., Kumar, A., Singh, N. K., & Prasad, L. (2024). Numerical study on effect of operating pressures on CRKEC-based two-stage ejector. *Archives of Thermodynamics*, 45(1), 155–164.

1. Introduction

The ejector is a simple mechanical device and is essential for industries and society because of environmental concerns, as it has no moving parts and working fluid restrictions. It can also operate with low-pressure temperature steams produced by industrial waste or solar energy. Ejectors enable pumping the fluid, vacuum creation, and compression of gases from lower pressure to higher pressure. The ejector systems can be utilized in heating as a heat pump [1], refrigeration systems [2, 3], rocket engines [4–6], hydrogen refueling systems [7, 8], geothermal power plants [9], vacuum generator [10], gas mixing [11], augmentation of thrust and suppression of noise [12]. The system performances are highly dependable on the performance of the ejector, which is generally low. The ejector performance is generally measured based on the ratio of entrainment capability. The entrainment ratio is the ratio of the entrained fluid mass flow rate to the primary or motive fluid mass flow rate. The ejector entrainment ratio is affected by geometrical parameters, operating parameters, and the working fluid used.

Nomenclature

a, b – Redlich-Kwong constants
A – cross-section area, m^2
c, C – velocity, m/s
C_1, C_2 – Sutherland constants
D – diameter, m
f – Fanning friction factor
G – constant
KE – kinetic energy
K – wall roughness, μm
L_n – nozzle section length, m
$\dot{m}_p$ – primary mass flow rate, kg/s
$\dot{m}_{s1}$ – first entrain mass flow rate, kg/s
$\dot{m}_{s2}$ – second entrain mass flow rate, kg/s
M – Mach number
p, P – pressure, Pa
r – radius, m
R – individual gas constant, kJ/K
Re – Renolds Number
T – temperature, K
v, V – specific volume, m^3/s
x, X – axial distance, m
y, Y – cross-section distance, m

Greek symbols

γ – specific heat ratio
μ – dynamic viscosity, Pa·s
ρ – density, kg/m^3
ϕ – rate of kinetic energy change, kg·m/s^3
ω – entrainment ratio

Subscripts and Superscripts

d – diffuser
i, j, k – space component
n – nozzle
m – mixing
o – stagnation condition
p – primary flow
s – secondary flow
x, y – direction

Numerical tools are widely used to optimize the geometrical and operating parameters. The profile of a single-stage ejector is dependent mainly on the design approaches. Constant pressure mixing (CPM) and constant area mixing (CAM) are the traditional ejector design methodologies [13]. Constant rate of momentum change (CRMC) and constant rate of kinetic energy change (CRKEC) are two methods for designing ejectors that are based on physics [14, 15]. The profile of a typical single-stage conventional ejector is shown in Fig. 1. The parameters optimized by researchers are the area ratio [16], multi ejector refrigerating system [17], convergence angle of the suction chamber [18], diameter of the nozzle throat and mixing section [19]. The entrainment ratio and critical back pressure of the ejectors are influenced by the position of the nozzle exit. According to the CAM and CPM-based ejectors study [20], increased boiler temperature ratios result in increased critical back pressure. By raising the evaporator temperature, the entrainment ratio and critical back pressure rise. The operating parameters optimized by researchers are primary flow total pressures and temperatures [21], secondary flow pressures and temperatures [22], and exit flow total pressures [20].

Recent studies focus on developing physics-based design approaches such as CRMC and CRKEC to improve performance by mitigating loss due to thermodynamic shocks in conventional (CAM and CPM) single-stage ejectors [13]. To further boost the performance, a two-stage ejector is a useful substitution [23–25]. The second entrained stream is driven into the second stage of the ejector using the excess momentum of the discharged flow at the mixing section exit [26]. The physics-based CRMC single-stage ejector performance is further improved by modifying single-stage to two-stage ejectors [27] and others [28–29]. The typical two-stage ejector is shown in Fig. 2.

The literature review shows a gap in using the physics-based CRKEC approach for real fluids in designing a two-stage ejector. This work addresses this gap by modifying the physics-based 1D gas dynamic CRKEC model [15] for single-stage ejector design with the Redlich-Kwong equation of state, to create a model for two-stage ejectors. This modified model, called the 1D gas dynamic TSE model, is used to calculate profiles and flow properties in the mixing-diffuser section. The TSE is further analyzed using ANSYS-Fluent 14.0 at design and operating conditions.

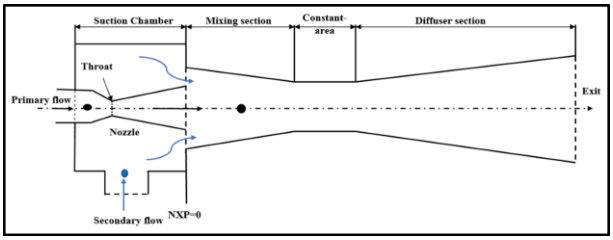

Fig. 1. A schematic diagram of the conventional ejector [27].

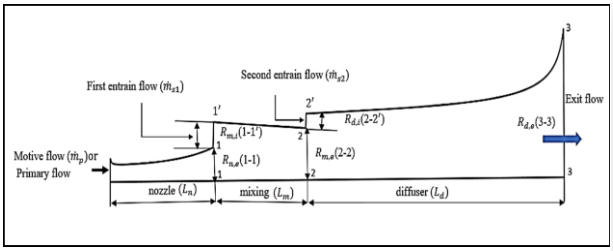

Fig. 2. Two-stage ejector.

2. 1D gas dynamic mixing-diffuser design

The 1D gas dynamic CRKEC design approach [15] was considered a reference to further model the mixing-diffuser two-stage ejector for water vapour. The geometry was considered axisymmetric. The 1D gas dynamic compressible flow mixing-diffuser design model was derived considering the steady-state flow and adiabatic conditions using mass, momentum, and energy equations. The following section lists the equations and their differential forms used to calculate the incremental change in area, pressure, and temperature.

The Mach number and its differential form are given by

$$M^2 = \frac{C^2}{\gamma RT},\ \frac{dM}{M} - \frac{dC}{C} + \frac{dT}{2T} = 0. \tag{1}$$

The equation of state (Redlich Kwong) and its differential form are given by

$$P = \frac{RT}{\frac{V}{n}-b} - \frac{a}{\sqrt{T}\frac{V}{n}\left(\frac{V}{n}+b\right)},\quad dP = [(X)dT + (Y)d\rho], \tag{2}$$

where

$$X = \left[\frac{\rho\,.\,R}{(G-\rho b)} + \frac{1}{2}\left\{\frac{\rho^2.\,a}{T^{1.5}.\,G(G+\rho\,.\,b)}\right\}\right], \tag{2a}$$

$$Y = \left[\frac{RT(G-\rho b)+b\rho RT}{(G-\rho b)^2} - \frac{a}{\sqrt{T}}\left\{\frac{2\rho(G+\rho b)-\rho^2 b}{G(G+\rho b)^2}\right\}\right], \tag{2b}$$

where the Redlich Kwong constants are

$$a = \frac{0.4275R^2T_C^{2.5}}{P_C}, b = \frac{0.0866RT_C}{P_C}. \tag{2c}$$

The conservation of mass has the form:

$$\dot{m} = \rho AC,\quad \frac{d\rho}{\rho} + \frac{dA}{A} + \frac{dC}{C} = 0. \tag{3}$$

The conservation of energy and its differential form for passive adiabatic conditions are as follows

$$T_0 = T + \frac{C^2}{2C_P},\quad dT + \frac{CdC}{C_P} = 0. \tag{4}$$

The conservation of momentum including friction writes as

$$\frac{dP}{P} + \frac{\gamma}{2}M^2\frac{4fdx}{D} + \gamma M^2\frac{dC}{C} = 0, \tag{5}$$

where the local Fanning friction factor f is defined as [15]:

$$f = \frac{0.0625}{\left[log_{10}\left(\frac{K}{3.7D}+\frac{5.74}{R_e^{0.9}}\right)\right]^2}, \tag{5a}$$

where the local Reynolds number is $\mathrm{Re} = \frac{\rho CD}{\mu}$, and $\mu = \frac{C_1T^{1.5}}{T+C_2}$, according to Sutherland's law of viscosity, where C_1 and C_2 are Sutherland's constants.

The following assumptions were made to develop a 1D gas dynamic mathematical model to compute the profile of two-stage ejector mixing-diffuser design and flow properties.

- The working fluid is water vapour. In addition, due to the low operating pressure, the kinetic energy of gas molecules becomes more significant than intermolecular forces and molecular size. Consequently, water vapour can be approximated as an ideal gas in this particular behaviour [30];
- The expected entrainment ratio (ω) is considered;
- At the ejector inlet, the combined pressure and temperature of the primary and secondary flows are known;
- The secondary flow velocity is known;
- Locally, the Fanning friction factor is used to specify the influence of friction.

The baseline equation for CRKEC two-stage ejector mixing-diffuser section design is given by Eq. (6)

$$\frac{d(\dot{K}E)}{dx} = \dot{m}_p(1+\omega)\cdot C_{i,x}\frac{dC}{dx} = \phi, \tag{6}$$

where ϕ is the rate of kinetic energy change, which is considered constant.

The velocity gradient can be calculated using Eq. (7), which is derived from Eq. (1), for a chosen value of ϕ and dx

$$\frac{dC}{C_{i,x}} = \frac{\phi\,dx}{\dot{m}_p(1+\omega){C_{i,x}}^2}. \tag{7}$$

The change in local cross-sectional area of the diffuser at the i^{th} location is given by

$$\frac{dA}{A_{i,x}} = \frac{\gamma}{2}M_{i,x}^2\frac{P_{i,x}}{\rho_{i,x}Y}\frac{4f_{i,x}dx}{D_{i,x}} + \\ + \frac{1}{\rho_{i,x}Y}\left(\gamma M_{i,x}^2\rho_{i,x} - XM_{i,x}^2(\gamma-1)T_{i,x} - \rho_{i,x}Y\right)\frac{\phi\,dx}{\dot{m}_p(1+\omega)C_{i,x}^2}. \tag{8}$$

The change in local pressure of the diffuser at the i^{th} location is given by

$$\frac{dP}{P_{i,x}} = -\rho_{i,x}Y\frac{dA}{A_{i,x}} + \left[XM_{i,x}^2(1-\gamma)T_{i,x} - \rho_{i,x}Y\right]\frac{\phi\,dx}{\dot{m}_p(1+\omega)C_{i,x}^2}. \tag{9}$$

The mixing section produces the most entropy when compared to the nozzle and diffuser of the ejector because it experiences extensive interactions between supersonic primary/motive flow and subsonic (incompressible) entrain/secondary flows. Compounding the mixing section profile is considered crucial compared to other components of ejector design. Further, to model this section, it was considered that mixing takes place at a constant rate, and during mixing, the pressure remains constant (dp=0) [14].

The following equation (10) provides the change in the mixing-diffuser local cross-sectional area at the i^{th} place

$$\frac{dA}{A_{i,x}} = -\frac{1}{\rho Y}\left[XM_{i,x}^2(\gamma-1) + \rho Y\right]\frac{\phi\,dx}{\dot{m}_p(1+\omega){C_{i,x}}^2}. \tag{10}$$

The change in local pressure of the mixing section at the i^{th} location is given by

$$dp = 0. \tag{11}$$

The change in local temperature of the mixing-diffuser at the i^{th} location is given by

$$\frac{dT}{T_{i,x}} = \left[(1-\gamma)M_{i,x}^2\right]\frac{\phi\,dx}{\dot{m}_p(1+\omega){C_{i,x}}^2}. \tag{12}$$

The change in local Mach number of the mixing-diffuser at the i^{th} location can be found from

$$\frac{dM}{M_{i,x}} = \left[1 + \frac{\gamma-1}{2} M_{i,x}^2\right] \frac{\phi\, dx}{\dot{m}_p(1+\omega) c_{i,x}{}^2}. \quad (13)$$

Equations (14) and (15) can be used to calculate the total pressure and temperature at the i^{th} position of the mixing-diffuser section, respectively

$$P_{o,i,x} = P_{i,x}\left[1 + \frac{(\gamma-1)}{2} M_{i,x}^2\right]^{\gamma/\gamma-1}, \quad (14)$$

$$T_{o,i,x} = T_{i,x}\left[1 + \frac{(\gamma-1)}{2} M_{i,x}^2\right]. \quad (15)$$

By adding up variations in parameters (*dA*, *dP*, *dM and dT*) for *dx* with parameter's (*A*, *P*, *M*, and *T*) value of its i^{th} location provides the parameter's value at its i+1 location in the flow domain.

3. Computation of geometrical profile and flow parameters

On the basis of Euler's technique, a separate MATLAB programmed was created for each section of the TSE system. The program was used to calculate the geometric coordinates and the attributes of the flow. The input design data which were utilized are shown in Table 1. At each small step (dx=0.5 mm), the variation in radius and the fluid flow characteristics were locally calculated. At the end of the mixing section (2–2) [see Fig. 2] and at the diffuser inlet section (2–2'), equilibrium properties of the incoming primary/motive flow and entrained/secondary flows were first calculated. Appendix A [17] shows the calculations for the equilibrium properties in sections (2–2) and (2–2'). The mixing section was computed by moving from the exit section (2–2) to the inlet section (1–1'), while the diffuser section was calculated by moving from the inlet section (2–2') to the exit section (3–3). The computational process is shown in the flow chart in Fig. 3.

Table 1. Input design and operating parameters of the two-stage ejector.

Parameter	Unit	Value
Motive/primary flow inlet total pressure $P_{o,p}$	Pa	1.91×10^5
Motive/primary flow inlet total temperature $T_{o,p}$	K	396
Motive/primary flow mass flow rate $(\dot{m}_p)$	kg/s	0.001
Entrain/secondary flow inlet total pressure $P_{o,s}$	Pa	872
Entrain/secondary flow inlet total temperature $T_{o,s}$	K	278
Entrain/secondary flow inlet velocity V_s	m/s	50
Individual gas constant (R)	J/kg.K	462
Entrainment ratio(ω)	-	0.42
Wall roughness (K)	m	1.5×10^{-6}
Specific heat ratio (γ)	-	1.3
Working fluid: water vapour		

The value of the CRKEC constant (ϕ) was selected for each section based on no flow separation and no null parameter at its inlet/exit section. The positive value of ϕ was selected because flow accelerates for the nozzle and mixing section while computing from throat to exit of the nozzle and from exit to inlet of mixing. The negative value of ϕ was selected for the diffuser section as the flow decelerated from the inlet to the exit. For the specified design conditions listed in Table 1, the nozzle section was also estimated using the CRKEC technique. Table 2 displays the computed dimensional parameters for the chosen sections of the nozzle, mixing, and diffuser at critical places. Figure 4 and 5 demonstrate, respectively, the variation in the cross- sectional radius of the computed profile of the mixing and diffuser section, and flow characteristics along the mixing diffuser.

4. CFD analysis

The commercial CFD software ANSYS-Fluent is a powerful tool for simulating the problem. The control volume-based technique was used to discretize and solve the governing equations. Numerical equations were solved in space using the second-order upwind approach. The coupled solver with the implicit scheme was used and pressure was linked directly to density to obtain the real physical relations for compressible flow and to capture shock waves.

The computational domain of the TSE system for the CFD simulation was prepared using ANSYS-Workbench. The coordinates of the cross-sectional profile of mixing-diffuser sections were utilized to develop the ejector profile. The computational domain was meshed with a structured quadrilateral. For this kind of mesh, the cell aspect ratio and alignment with the flow domain are easy to control. A relatively higher number of cells were used in the region with higher entropy generation. Fig. 6 displays the created computational domain and its mesh. At the ejector entry and exit, the pressure boundary condition was used, as shown in Table 3. The grid dependency test was run using the standard k-ε turbulence model to determine the best grid size. For testing the ideal grid size under on-design circumstances, the global performance parameter "entrainment ratio" was taken into account. After employing the various mesh sizes (30 000–80 000), it was found that approx. 45 000 cells are suitable for the sake of computational time, accuracy, and cost. The employment of gradient mesh near and inside the mixing region helped predict the boundary layer near the wall and the mixing phenomenon inside the mixing section.

5. Results and discussion

The ANSYS-Fluent simulation results of the computed geometrical profile of TSE are discussed in this section. The complete CFD simulation was performed at zero nozzle exit position (on-design). This section talks about how operating parameters affect flow characteristics and entrainment ratio. The on-design ejector system impacts were predicted by changing one operating parameter at a time.

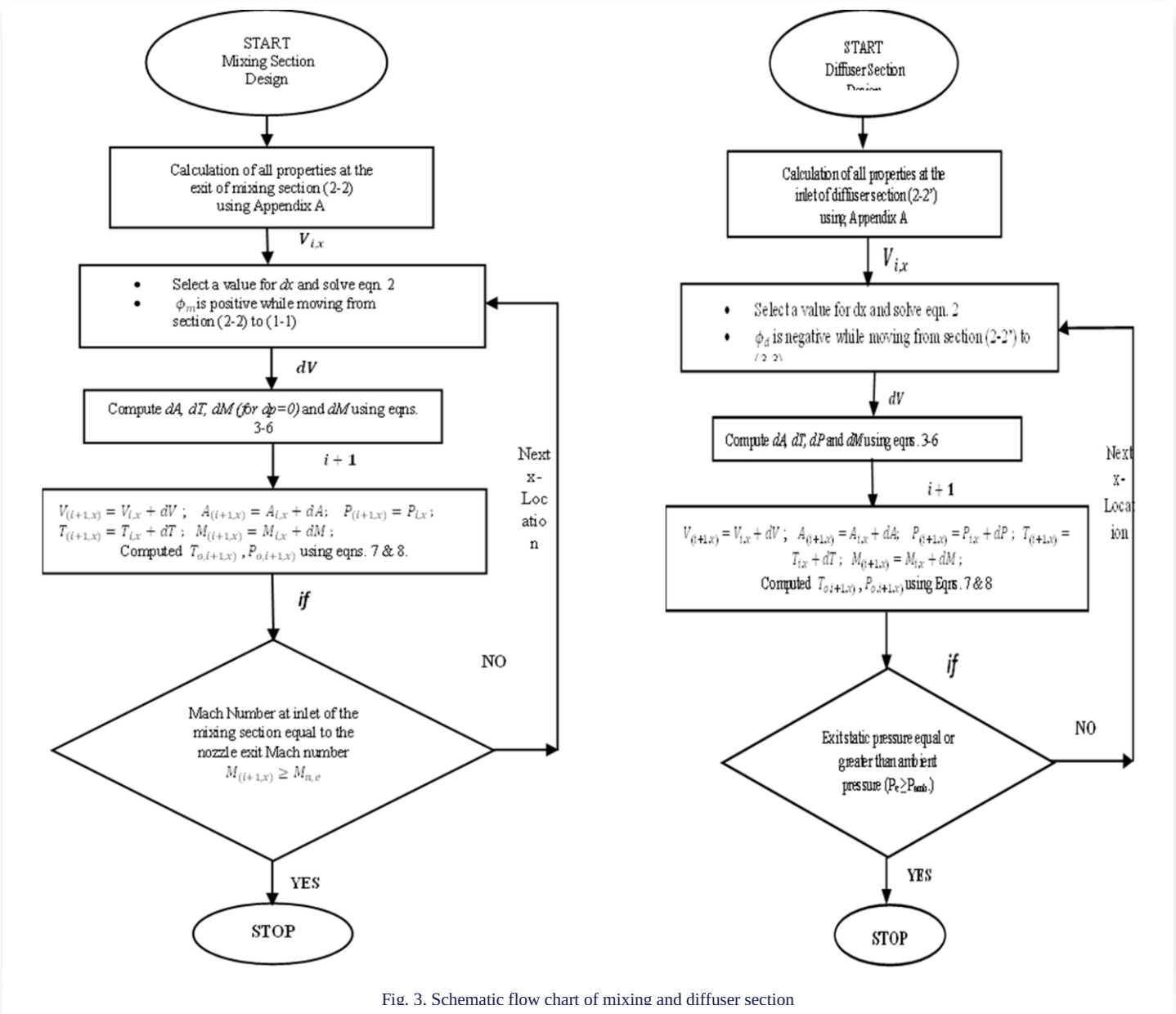

Fig. 3. Schematic flow chart of mixing and diffuser section

Table 2. The dimensional specifications of different sections

Sections	Dimension (mm)
Nozzle	
Inlet radius	2.28
Throat radius	1.01
Exit radius	5.30
Length	100.00
Mixing section	
Inlet radius	11.54
Exit radius	10.06
Length	90.00
Diffuser section	
Inlet radius	13.64
Exit radius	34.66
Length	250

5.1. Effect of exit pressure

The effect of exit pressure has been studied and predicted variations in flow properties and over the entrainment ratio are shown in Figures 7, 8, and 9, respectively. The total pressure at the nozzle intake and the entrained flow (primary and secondary) total pressure at the inlets of the first and second stages were held constant to analyse the impact of exit pressure. Figure 7 depicts the change in centreline static pressure along the mixing-diffuser segment.

The exit pressure directly affects the amount of entrained flow. The pressure and Mach number intense oscillations due to supersonic and subsonic flow mixing inside the mixing chamber are visible but the effect of exit pressure variation on oscillations inside the mixing region is insignificant. However, increasing the exit pressure reduces the Mach number at the exit of the diffuser and helps in pressure recovery at the exit of the diffuser.

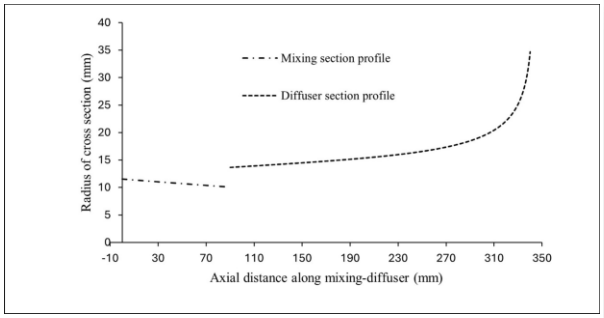

Fig. 4. Variation of cross-section radius along mixing-diffuser section [$\phi_m = -2600\ \mathrm{kgm/s^3}$ and $\phi_d = -550\ \mathrm{kgm/s^3}$].

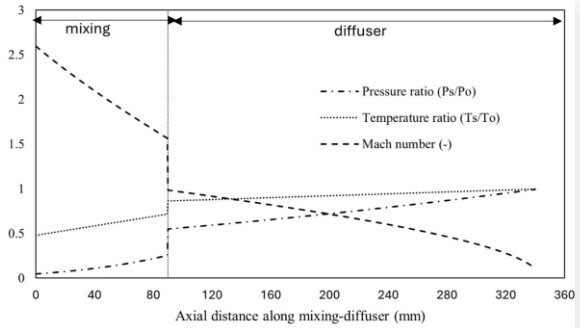

Fig. 5. Variation of flow properties along the mixing-diffuser section [$\phi_m = -2600\ \mathrm{kgm/s^3}$ and $\phi_d = -550\ \mathrm{kgm/s^3}$]

As seen in Figure 9, as the total exit pressure rises and the entrainment ratio falls, the pressure difference between the suction and entrain flow also reduces, which lowers the mass of the entrained flow.

5.2. Effect of entrained flow total pressure

The exit pressure and primary flow total pressure were held constant at on-design conditions in order to analyse the impact of secondary flow total pressure. Figure 10 depicts the change

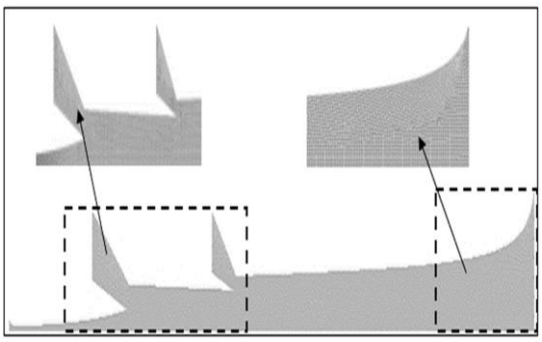

Fig. 6. Computational domain of two-stage ejector

Table 3. Boundary conditions for CFD study.

Section	Boundary Condition	Values
Wall	Adiabatic with no slip	–
Exit	Pressure outlet	$P_{o,e}$=1240 Pa, $T_{o,e}$= 350K
Inlet	Pressure inlet: Primary flow	$P_{o,p}$=191000 Pa, $T_{o,p}$=396K
	Pressure inlet: Secondary flow, stage I and II	$P_{o,s}$=872 Pa, $T_{o,s}$= 278K

in centreline static pressure together with an increase in entrained flow total pressure. With the higher entrained flow total pressure, the amplitude of pressure oscillations in the mixing region is lower compared to lower entrained flow total pressure. The secondary flow total pressure does not allow enough space to expand the primary jet inside the mixing region. In other words, the expansion of the combined jet decreases with an increase in secondary flow total pressure. It is also observed that after the intense interactions of primary and entrain flows, the static pressure gradually increases in the diffuser section.

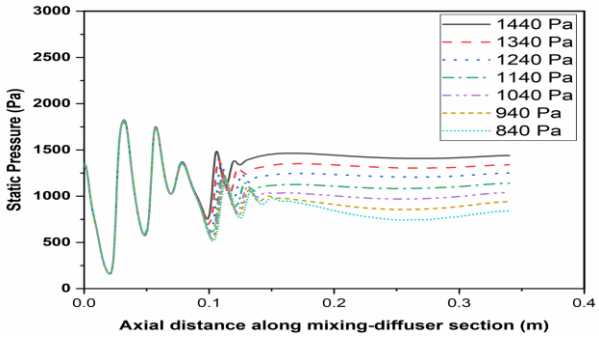

Fig. 7. Variation in static pressure with exit pressure.

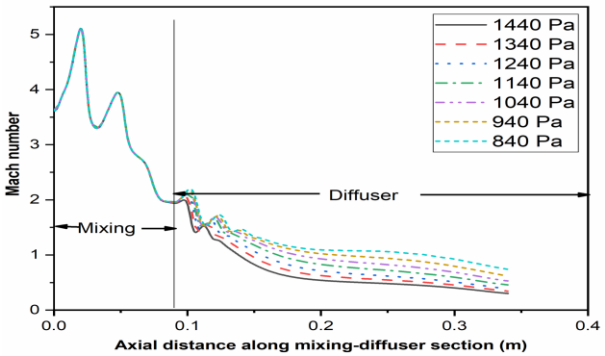

Fig. 8. Variation in Mach number with exit pressure.

With various entrain flow total pressures along the mixing-diffuser, the fluctuation in centreline Mach number is depicted in Figure 11. In the supersonic range, the compression and expansion waves are visible. Additionally, the combined Mach

number grows as the entrain total flow pressure increases. However, the Mach number drops along the mixing-diffuser segment.

Figure 12 illustrates how the two-stage ejector entrainment ratio grows with an increase in entrain flow total pressure. Lower entrainment ratios are produced as a result of the expansion of the primary/motive jet flow expansion wave in the mixing area, which is made possible by the lower entrain total flow pressure.

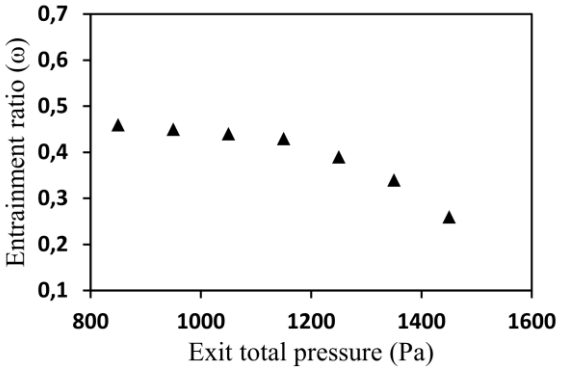

Fig. 9. Variation in entrainment ratio with exit pressures.

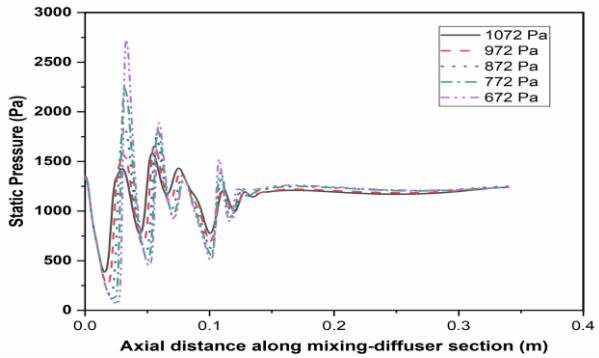

Fig. 10. Variation in static pressure with entrain flow total pressure.

5.3. Effect of primary flow total pressure

Figure 13 depicts the projected centerline static pressure variation along the mixing diffuser for various primary flow total pressures. With an increase in primary flow total pressure, the flow momentum rises. Due to the intensive flow interaction between the high-speed (supersonic) primary flow and the low-speed (subsonic) entrain flows, pressure oscillations are seen inside the mixing region. For larger primary flow total pressures, the pressure oscillation in the mixing region is higher.

The primary flow overall pressure is what causes the momentum to grow. With a sizable expansion angle, it quickens the primary flow at the nozzle exit. Figure 14 demonstrates how the increasing total pressure causes a higher Mach number as the primary flow increases. Figure 15 depicts how the primary flow total pressure affects the entrainment ratio. When the entrainment ratio varies with decreasing primary flow total pressure values, the system is operating at sub-critical conditions because

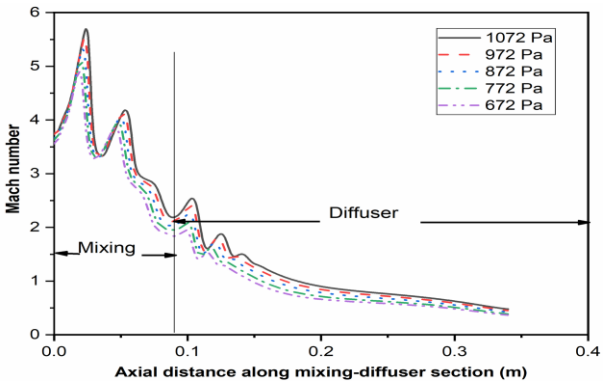

Fig. 11. Variation in Mach number with entrain flow total pressure.

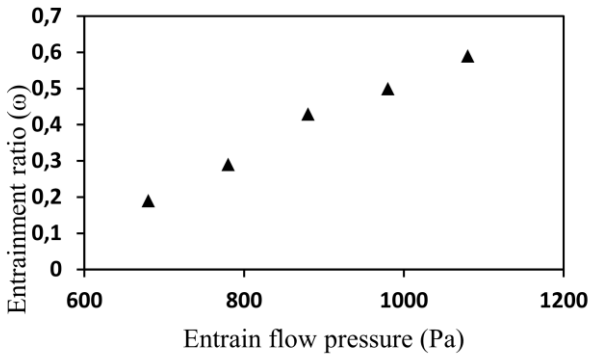

Fig. 12. Variation in entrainment ratio with entrain total flow pressure.

the ejector system operates with a low-pressure differential (below on-design). Entrain flows are proportionately and extremely sensitive to primary flow total pressures in this scenario. When the system enters its critical mode of operation, which in this case is on-design, the optimum entrainment ratio occurs. The pressure difference between the primary flow and ejector output indicates that the system operates above critical conditions when the primary flow pressure is higher (above on-design). In these circumstances, entrainment is reduced because the secondary flow is less sensitive to the total pressure of the primary flow.

6. Conclusions

To create a two-stage ejector, the 1D gas dynamic CRKEC method for water vapour was developed. Based on the CRKEC technique at design operating conditions, the variations in radius and flow characteristics along the mixing-diffuser section of the two-stage ejector are computed. Utilizing ANSYS-Fluent software, the computed geometrical profile of the ejector is numerically analysed. A two-stage ejector response to operating circumstances has been discussed. Due to compression and expansion in the mixing zone, strong interactions have been seen in the entrainment region. After a period of intensive interaction, equilibrium is reached in the mixing section flow. After achieving equilibrium, the diffuser centerline pressure and Mach number progressively change. The primary, entrained and exit flow

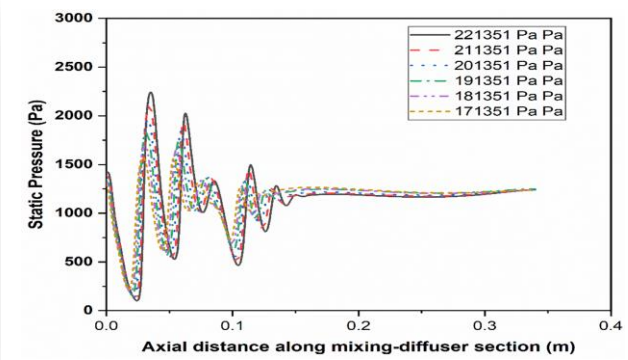

Fig. 13. Variation in static pressure with primary flow total pressure.

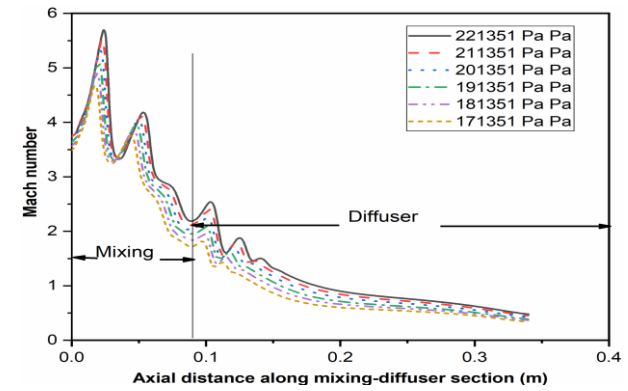

Fig. 14. Variation in Mach number with primary flow total pressure.

pressures of the two-stage ejector are related to the global performance metric "entrainment ratio". It rises when the entrain flow total pressure is raised and falls when the exit flow total pressure is raised. The entrainment ratio of TSE is maximum at on-design (1.91 bar) flow primary flow total pressure. Running the system in other than the on-design primary flow total pressure reduces its performance. However, before the actual field application, a detailed experimental study at on and off-design conditions is needed on the CRKEC-based TSE system. The CRKEC approach has limitations, such as assuming that fluid properties remain constant throughout the system. It may not accurately predict fluid behaviour in systems with complex geometries or strong non-ideal effects, like heat transfer and compression. Thus, further experimental validation is required to support this approach.

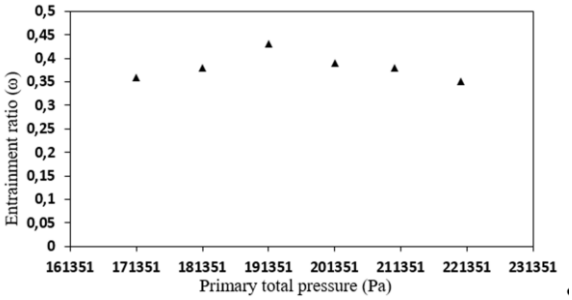

Fig. 15 Variation in entrainment ratio with primary flow total pressure.

Acknowledgements

The authors want to show their gratitude and acknowledge the use of computational facilities in the CFD lab of the Mechanical Engineering Department of Kamla Nehru Institute of Technology, Sultanpur, Uttar Pradesh, India.

Appendix A [15]

Calculation of flow properties at the mixing section exit (2–2).

The essential thermodynamic flow properties at the exit of the mixing section (2–2) as in Fig. 2 were computed based on the following considerations:

- The exit velocity ia an equal-weighted average of the motive/primary and entrain/secondary fluid velocities;
- The combined fluid total temperature at the exit of the adiabatic mixing section is the same as the weighted average of the primary and entrain flows.

The mixed flow velocity is given by

$$C_{2-2} = \frac{C_{n,e}+\omega\, C_S}{1+\omega}. \quad \text{(A.1)}$$

The mixed flow total temperature is given by

$$T_{o,2-2} = \frac{T_{o,p}+\omega T_{o,S}}{1+\omega}. \quad \text{(A.2)}$$

The mixed flow static temperature is given by

$$T_{2-2} = T_{o,2-2} - \frac{c_{2-2}^2}{2c_p}. \quad \text{(A.3)}$$

The mixed fluid total pressure is given by

$$P_{o,2-2} = P_{2-2}\left(\frac{T_{o,2-2}}{T_{2-2}}\right)^{(\gamma/(\gamma-1))}. \quad \text{(A.4)}$$

The mixed flow Mach number is given by

$$M_{2-2} = \frac{C_{2-2}}{\sqrt{\gamma R T_{2-2}}}. \quad \text{(A.5)}$$

The diameter at the exit of the mixing section is given by

$$D_{2-2} = \sqrt[2]{\frac{\dot{m_p}\,(1+\omega)RT_{2-2}}{\pi P_{2-2} C_{2-2}}}. \quad \text{(A.6)}$$

Calculation of flow properties at the inlet of the diffuser (2–2')

The essential flow properties at the inlet of the diffuser section (2–2') as in Fig. 2 were computed by making the following modifications in the formulation for sections (2–2).

$$C_{n,e} \rightarrow C_{m,e},$$

$$\omega_1 \rightarrow \omega_2 = \frac{\dot{m}_{s2}}{\dot{m}_{m,e}},$$

where

$$\dot{m}_{m,e} = \dot{m}_p + \dot{m}_{s2},$$

$$T_{0,p} \rightarrow T_{0,m},$$

$$T_{0,s1} \rightarrow T_{0,s2},$$

$$P_{0,s1} \rightarrow P_{0,s2}$$

and

$$\rho_{0,s1} \rightarrow \rho_{0,s2,}.$$

References

[1] Zhang, B., Wang, Y., Kang, L., & Lv, J. (2013). Study of an innovative ejector heat pump boosted district heating system. *Applied Thermal Engineering*, 58, 98–110. doi: 10.1016/j.applthermaleng.2013.04.021

[2] Jeon, Y., Lee, D., & Cho, H. (2022). Optimisation of motive nozzle position in a modified two-phase ejector expansion household refrigeration cycle using an artificial neural network. *Energy Reports*, 8, 1114–1123. doi: 10.1016/j.egyr.2021.12.033

[3] Cheng, Y., Wang, M., & Yu, J. (2021). Thermodynamic analysis of a novel solar-driven booster-assisted ejector refrigeration cycle. *Solar Energy*, 218, 85–94. doi:10.1016/j.solener.2021.02.031

[4] Yang, Q., Shi, W., Chang, J., & Bao, W. (2015). Maximum thrust for the rocket-ejector mode of the hydrogen fueled rocket-based combined cycle engine. *International Journal of Hydrogen Energy*, 40(9), 3771–3776. doi: 10.1016/j.ijhydene.2015.01.033

[5] Gu, R., Sun, M., Cai, Z., Li, P., & Huang, Y. (2021). Numerical modeling and experimental investigation on the rocket-ejector system with limited mixer length. *Acta Astronautica*, 182, 13–20. doi: 10.1016/j.actaastro.2021.01.055

[6] Gu, R., Sun, M., Cai, Z., Chen, J., Li, P., Dong, Z., Wang, T., Yao, Y., & Huang, Y. (2021). Experimental study on the rocket-ejector system with a throat in the secondary stream. *Aerospace Science and Technology*, 113, 106697. doi: 10.1016/j.ast.2021.106697

[7] Rogie, B., Wen, C., Kaern, M. R., & Rothuizen, E. (2021). Optimisation of the fuelling of hydrogen vehicles using cascade systems and ejectors. *International Journal of Hydrogen Energy*, 46(14), 9567–9579. doi:10.1016/j.ijhydene.2020.12.098

[8] Rogie, B., Kaern, M. R., Wen, C., & Rothuizen, E. (2021). Numerical optimisation of a novel gas-gas ejector for fuelling of hydrogen vehicles. *International Journal of Hydrogen Energy*, 45(41), 21905–21919. doi:10.1016/j.ijhydene.2020.05.169

[9] Mondal, S., Sahana, C., & De, S. (2022). Optimum operation of a novel ejector assisted flash steam cycle for better utilisation of geothermal heat. *Energy Conversion and Management*, 253, 115–164. doi: 10.1016/j.enconman.2021.115164

[10] Xue, H., Wang, L., Jia, L., Xie, C., & Lv, Q. (2020). Design and investigation of a two-stage vacuum ejector for MED-TVC system. *Applied Thermal Engineering*, 167, 114–713. doi: 10.1016/j.applthermaleng.2019.114713

[11] Hailun, Z., Sun, W., Xue, H., Wang, L., & Jia, L. (2021). Performance analysis and prediction of ejector-based hydrogen recycle system under variable proton exchange membrane fuel cell working conditions. *Applied Thermal Engineering*, 197, 117–302. doi: 10.1016/j.applthermaleng.2021.117302

[12] Ye, W., Zhang, J., Xu, W., & Zhang, Z. (2020). Numerical investigation on the flow structures of the multi-strut mixing enhancement ejector. *Applied Thermal Engineering*, 179, 115–653. doi: 10.1016/j.applthermaleng.2020.115653

[13] Keenan, J. H., & Neumann, E. P. (1942). A simple air ejector. *Journal of Applied Mechanics*, 9(2), A75-A8. doi: 10.1115/1.4009187

[14] Kumar, V., Singhal, G., & Subbarao, P. M. V. (2013). Study of supersonic flow in a constant rate of momentum change (CRMC) ejector with frictional effects. *Applied Thermal Engineering*, 60(1-2), 61–71. doi: 10.1016/j.applthermaleng.2013.06.045

[15] Kumar, V., Singhal, G., & Subbarao, P. M. V. (2018). Realisation of novel constant rate of kinetic energy change (CRKEC) supersonic ejector. *Energy*, 164, 694–706. doi: 10.1016/j.energy.2018.08.184

[16] Gu, W., Wang, X., Wang, L., Yin, X., & Liu, H. (2019). Performance investigation of an auto-tuning area ratio ejector for MED-TVC desalination system. *Applied Thermal Engineering*, 155, 470–479. doi: 10.1016/j.applthermaleng.2019.04.018

[17] Aligolzadeh, F., & Hakkaki-Fard, A. (2019). A novel methodology for designing a multi-ejector refrigeration system. *Applied Thermal Engineering*, 151, 26–37. doi: 10.1016/j.applthermaleng.2019.01.112

[18] Ramesh, A. S., & Sekhar, S. J. (2018). Experimental and numerical investigations on the effect of suction chamber angle and nozzle exit position of a steam-jet ejector. *Energy*, 164, 1097–1113. doi: 10.1016/j.energy.2018.09.010

[19] Mohammadi, A. (2019). An investigation of geometrical factors of multi-stage steam ejectors for air suction. *Energy*, 186, 115–808. doi: 10.1016/j.energy.2019.07.138

[20] Aidoun, Z., & Ouzzane, M. (2004). The effect of operating conditions on the performance of a supersonic ejector for refrigeration. *International Journal of Refrigeration*, 27(8), 974–984. doi: 10.1016/j.ijrefrig.2004.05.006

[21] Kuo, J. K., & Hsieh, C. Y. (2021). Numerical investigation into effects of ejector geometry and operating conditions on hydrogen recirculation ratio in 80 kW PEM fuel cell system. *Energy*, 233, 121100. doi: 10.1016/j.energy.2021.121100

[22] Poirier, M. (2022). Influence of Operating Conditions on the Optimal Nozzle Exit Position for Vapor Ejector. *Applied Thermal Engineering*, 210, 118377. doi: 10.1016/j.applthermaleng.2022.118377

[23] Ghorbani, B., Ebrahimi, A., Moradi, M., & Ziabasharhagh, M. (2021). Continuous production of cryogenic energy at low-temperature using two-stage ejector cooling system, Kalina power cycle, cold energy storage unit, and photovoltaic system. *Energy Conversion and Management*, 227, 11354. doi: 10.1016/j.enconman.2020.113541

[24] Wang, P., Ma, H., Spitzenberger, J., Abu-Heiba, A., & Nawaz, K. (2021). Thermal performance of an absorption-assisted two-stage ejector air-to-water heat pump. *Energy Conversion and Management*, 230, 113761. doi: 10.1016/j.enconman.2020.113761

[25] Yan, J., Wen, N., Wang, L., Li, X., Liu, Z., & Li, S. (2018). Optimisation on ejector key geometries of a two-stage ejector-based multi-evaporator refrigeration system. *Energy Conversion and Management*, 175, 142–150. doi: 10.1016/j.enconman.2018.08.110

[26] Kong, F., & Kim, H. D. (2016). Optimisation study of a two-stage ejector–diffuser system. *International Journal of Heat and Mass Transfer*, 101, 1151–1162. doi: 10.1016/j.enconman.2018.08.110

[27] Yadav, S. K., Pandey, K. M., Kumar, V., & Gupta, R. (2021). Computational analysis of a supersonic two-stage ejector. *Materials Today: Proceedings*, 38, 2700–2705. doi: 10.1016/j.matpr.2020.08.483

[28] Domairry, G., & Aziz, A. (2009). Approximate Analysis of MHD squeeze flow between two parallel disks with suction or injection by homotopy perturbation method. *Mathematical Problems in Engineering*. doi: 10.1155/2009/603916

[29] Izadi, M., Yüzbaşı, Ş., & Adel, W. (2021). Two novel Bessel matrix techniques to solve the squeezing flow problem between infinite parallel plates. *Computational Mathematics and Mathematical Physics*, 61(12), 2034–2053. doi: 10.1134/s096554252131002x

[30] Dong, J., Hu, Q., Yu, M., Han, Z., Cui, W., Liang, D., Ma, H., & Pan, X. (Year). Numerical investigation on the influence of mixing chamber length on steam ejector performance. *Applied Thermal Engineering*, 174, 115204. doi.org/10.1016/j.applthermaleng.2020.115204

Co-published by
Institute of Fluid-Flow Machinery
Polish Academy of Sciences
Committee on Thermodynamics and Combustion
Polish Academy of Sciences

http://www.imp.gda.pl/archives-of-thermodynamics/

ARCHIVES OF THERMODYNAMICS

Unsteady magnetohydrodynamic free convection and heat transfer flow of Al_2O_3–Cu/water nanofluid over a non-linear stretching sheet in a porous medium

Joel Mathews[a*], Talla Hymavathi[b]

[a]Dept. of Mathematics, Krishna University, Machilipatnam, 521 004, A.P, India.
[b]Dept. of Mathematics, University College of Science and Technology, Adikavi Nannaya University, Rajamahendravaram, 533 296, A.P, India.
*Corresponding author email: lollajoel.mathews765@gmail.com

Received: 14.05.2023; revised: 29.07.2023; accepted: 01.08.2023

Abstract

This article investigates the impact of time-dependent magnetohydrodynamics free convection flow of a nanofluid over a non-linear stretching sheet immersed in a porous medium. The combination of water as a base fluid and two different types of nanoparticles, namely aluminum oxide (Al_2O_3) and copper (Cu) is taken into account. The impacts of thermal radiation, viscous dissipation and heat source/sink are examined. The governing coupled non-linear partial differential equations are reduced to ordinary differential equations using suitable similarity transformations. The solutions of the principal equations are computed in closed form by applying the MATLAB bvp4c method. The velocity and temperature profiles, as well as the skin friction coefficient and Nusselt number, are discussed through graphs and tables for various flow parameters. The current simulations are suitable for the thermal flow processing of magnetic nanomaterials in the chemical engineering and metallurgy industries. From the results, it is noticed that the results of copper nanofluid have a better impact than those of aluminium nanofluid.

Keywords: Non-linear stretching; Magnetohydrodynamics; Viscous dissipation; Heat source/sink; Porous medium

Vol. 45(2024), No. 1, 165–173; doi: 10.24425/ather.2024.150449

Cite this manuscript as: Mathews, J., & Hymavathi , T. (2024). unsteady magnetohydrodynamic free convection and heat transfer flow of Al_2O_3–Cu/water nanofluid over a non-linear stretching sheet in a porous medium. A*rchives of Thermodynamics*, 45(1), 165–173.

1. Introduction

Prandtl observed that the boundary layer is crucial in accurately predicting the flow of some fluids about a century ago. He demonstrated that viscosity is minimal in the middle of the flow but becomes critical near the boundaries. The asymptotic method, invented by Prandtl, drastically modified the mathematical characteristics of the original Navier-Stokes equations. The boundary layer equations are parabolic in character, whereas these equations (Navier-Stokes equations) are elliptic in nature. In order to achieve numerical solutions for practical problems, the mathematical treatment of boundary layer equations of the parabolic type is significantly simplified. Because of its applications in various engineering disciplines, boundary layer flow past a stretching surface has received a lot of attention. This kind of flow can occur during the cooling or drying of papers and textiles, the manufacturing of glass fibre, the boundary layer along a material-handling conveyor, the boundary layer along liquid film and condensation processes, etc. With this motivation, the investigation of boundary layer flow over a stretched sheet was started by Sakiadis [1]. Crane [2] examined the steady flow of a viscous incompressible fluid over an elastic sheet with

Nomenclature

B_0 – uniform magnetic field
T – fluid temperature
ρ – fluid density
Gr – local Grashof number
k – thermal conductivity
M – magnetic parameter
Pr – Prandtl number
Q_0 – dimensional heat generation / absorption coefficient
R – radiation parameter
g – gravitational acceleration
n – non-linear expanding parameter
q_r – radiative heat flux
A – unsteadiness parameter
K^1 – porous permeability
K_0 – permeability constant
K – permeability parameter
q_w – heat flux
k^* – mean absorption coefficient
Re_x – local Reynolds number
u, v – velocity components along x and y directions.
t – time
f – dimensionless stream function
a, b – constants

Greek symbols

ψ – stream function
η – coordinate transformation variable
σ – electrical conductivity
θ – dimensionless temperature
ϕ – nanoparticle volume fraction
τ – shear stress
σ^* – Stefan-Boltzman constant
α – thermal diffusivity
λ – parameter
μ – fluid dynamic viscosity
ν – kinematic viscosity

Subscripts and Superscripts

w – condition on the wall
∞ – ambient condition
nf – nanofluid
f – base fluid
$'$ – differentiation with respect to η

a velocity that varied linearly with distance from a fixed point, with the flow being purely produced by the stretching of the sheet in its plane. Many researchers have extended Crane's [2] problem in recent years by incorporating various aspects of flow and heat transfer features. Following this pioneering work, many investigations on this work [3–6] are generated. Kumaran and Ramanaiah [7] examined the viscous incompressible flow over a flat stretching sheet issuing from a long thin slit. In this study, the authors considered the velocity of a sheet as a quadratic polynomial of the distance function. All of these investigations are limited to linear stretching surface. It is worth noting that the stretching is not always linear, as in the case of polymer extrusion. The following authors considered the problem of a non-linear stretching sheet. The flow and heat transfer properties of a viscous fluid across a non-linear stretching surface were examined by Vajravelu [8]. Later, Cortell [9] discussed the viscous flow in two cases namely; constant surface temperature (CST) and prescribed surface temperature (PST) over a non-linear stretching sheet. Raptis and Perdikis [10] illustrated the magnetohydrodynamics (MHD) flow over a non-linear stretching sheet in the presence of chemical reactions. An approximate solution of viscous flow past a non-linear sheet under the influence of a magnetic field and chemical reaction was noticed by Kechil and Hashim [11]. Flows over non-linear sheets on more complex geometries and conditions are presented in [12–16].

Nanotechnology has recently become a highly debated topic of study. Every day, nanotechnology is interested in verifiable issues. It is important in processes including industry, biomedicine, medicine and technology. The primary role of nanotechnology is to improve the heat transfer mechanism in a variety of electronic devices to increase their performance. Further, industrial applications include micro-manufacturing, power production, chemical and metallurgical processing, transportation, ventilation, cooling, air conditioning, and drive up the demand for fluids with improved thermal conductivity and heat transfer properties. It is vital to develop advanced heat transfer fluids since the heat transfer rates reached by frequently used cooling media like water and air are unsuitable for other industrial applications. High thermal conductivity fluids can be engineered by suspending nanoparticles in conventional heat transfer fluids such as motor oil, water, ethylene glycol, and so on. The mixture of the nanoparticles and the base fluid results in a new innovative fluid, coined a nanofluid by Choi and Eastman [17]. Buongiorno [18] conducted an extensive survey of convective transport in nanofluids. In particular, nanofluids are a revolutionary type of nanotechnology-based heat transfer fluids that have been developed by stabilizing the suspension of minute amounts (1% volume) of nanoparticles with dimensions comparable to those of conventional heat transfer fluids. The properties of nanofluid under the influence of magnetic fields make it the most appealing method in this procedure due to its ease of use as well as its uniqueness and nature. The impact of nanoparticle size, shape and type on the magnetohydrodynamic convection flow of nanoparticles was observed by Reddy and Chamkha [19]. The authors [19] discovered that increasing thermal conductivity raises the temperature of the coolant fluid. The impact of the MHD flow of a nanofluid past a stretching surface was investigated by Ali et al. [20]. Mjankwi et al. [21] examined the time-dependent conductive flow of a nanofluid across an inclined stretching surface with heat and mass transfer effects. The study of nanofluid flows over a nonlinear stretching/shrinking sheet is important in heat transfer analysis for natural and engineering applications such as electronic cooling, nuclear reactor technology and nanotechnology industries. The stagnation point flow over a non-linear stretching sheet embedded in Carbon nanotubes under the influence of a magnetic field was explored by Anuar et al. [22]. The influence of a magnetic field over a non-linear stretching surface with viscous dissipation, thermo-

phoresis and Brownian motion was analysed by Mabood et al. [23]. The impact of thermal radiation, heat source and viscous dissipation effects on conducting nanofluid past a non-linear stretching surface was considered by Jafar et al. [24]. Triveni et al. [25] investigated the MHD Casson nanofluid flow past a non-linear stretching sheet under the impact of a non-uniform heat source and viscous dissipation effects. The importance of radiation and viscous dissipation effects on magnetic Casson nanoliquid over a nonlinear stretching sheet was investigated by Reddy et al. [26]. The authors, Rasool et al. [27], discussed the non-Newtonian type Cason nanofluid flow across a non-linear stretching surface immersed in a porous medium. In their study, the porous medium is developed by the Darcy-Forchheimer relation. Jagan et al. [28] present the MHD unsteady flow of a nanofluid across a non-linear stretched sheet with thermal radiation. Vinod Kumar et al. [29] investigated the unsteady stagnation point flow of a nanofluid using the Buongiorno's model in the presence of viscous dissipation and thermal radiation. Recently, the authors Rajputa et al. [30] studied the unsteady flow of a nanofluid generated by the non-linear expansion of a stretching sheet. In their study, the flow of nanofluid is modelled by using two-phase Buongiorno's model. However, earlier works on unsteady non-linear stretching surface were discussed in [31–35]. The recent investigations on nanofluids by considering the effects of magnetic field, porous media, radiation and heat source/sink, are investigated in [36–39].

Heat transfer issues involving nanofluids have become more important in biomedical activities such as drug targeting systems, cancer therapy, biotherapy, blood testing and coagulation systems, and many more. With this in mind, the current attempt aims to analyze the characteristics of radiation, viscous dissipation, and heat source/sink in hydromagnetic nanofluid flow over a non-linear stretchable surface. Moreover, the investigations on unsteady nanofluid free convection flows caused by non-linear stretching sheets have gained less attention.

2. Problem formulation

A two-dimensional laminar incompressible free convection creeping flow of an unsteady water-based nanofluid over a non-linear sheet immersed in a porous medium is considered. The mathematical model of Tiwary and Das [40] is used for developing the boundary layer equations. Two types of distinct nanoparticles namely; aluminum oxide (Al_2O_3) and copper (Cu) are added to the water. The sheet is stretched with the velocity u_w. The sheet velocity is assumed in the form $u_w(x) = \frac{ax^n}{(1-\lambda t)}$. The magnetic field strength B_0 is applied normal to the flow direction. The flow is confined to y > 0. The induced magnetic field is ignored because of the low magnetic Reynolds number. The electric dissipation is ignored, so that Joule heating is negligible [41]. In most situations, the Hall and ion slip factors were neglected because they have no discernible influence on small and moderate magnetic field values. However, the authors can refer to the impact of ion and Hall effects on fluid flow in [42–43]. The porous medium is modelled with Darcy's law [44] to describe slow flows. The flow is produced by the stretching of the sheet caused by the simultaneous application of two equal and opposite forces along the x −axis as illustrated in Fig.1. The effects of heat source/sink and viscous dissipation are considered in the energy equation. The magnetic field, permeability, heat source and thermal Grashof (Gr) number coefficient terms are taken in the following forms:

$$B(x,t) = \frac{B_0 x^{\frac{n-1}{2}}}{\sqrt{(1-\lambda t)}}, \qquad K'(x,t) = K_0 x^{1-n}(1-\lambda t)$$

$$Q^* = \frac{Q_0 x^{n-1}}{(1-\lambda t)}, \qquad g^* = \frac{g}{(1-\lambda t)^{\frac{3}{2}}}$$

where λ is a parameter. The nanoparticles thermo-physical properties and their physical values are presented in Tables 1 and 2.

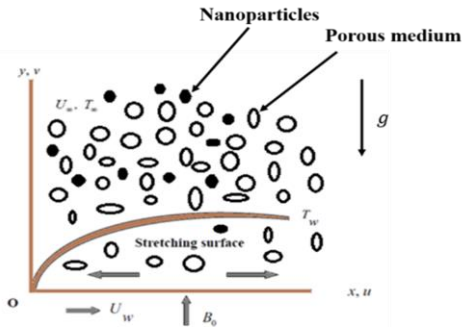

Fig. 1. Flow configuration.

Table 1. The nanofluid's thermo-physical characteristics [45 & 46].

Physical property	Nanofluid
Viscosity (μ)	$\frac{\mu_f}{(1-\phi)^{2.5}}$
Density (ρ)	$(1-\phi)\rho_f + \phi\rho_s$
Heat capacity (ρC_p)	$(1-\phi)(\rho C_p)_f + \phi(\rho C_p)_s$
Thermal conductivity (k)	$\frac{(2k_f + k_s) + 2\phi(k_s - k_f)}{(2k_f + k_s) + \phi(k_f - k_s)}(k_f)$
Electrical conductivity (σ)	$\sigma_{nf} = \frac{(2\sigma_f + \sigma_{s_1}) + 2\phi(\sigma_s - \sigma_f)}{(2\sigma_f + \sigma_s) + \phi(\sigma_f - \sigma_s)}\sigma_f$
Diffusivity (α)	$\frac{k_{nf}}{(\rho C_p)_{nf}}$
Thermal expansion ($\rho\beta$)	$[(1-\phi)(\rho\beta)_f + \phi(\rho\beta)_s]$

Table 2. The base fluid and nanoparticle's thermo-physical properties for copper (Cu), aluminium oxide (Al_2O_3) and water (H_2O) [47].

Property	Cu	Al_2O_3	H_2O
Density (ρ)	8,933	3,970	997.1
Specific heat (C_p)	385	765	4,179
Thermal conductivity (k)	401	40	0.613
Electrical conductivity (σ)	5.96×10^{7}	3.69×10^{7}	5.5×10^{-6}
Thermal expansion coefficient (β)	1.67×10^{-5}	0.85×10^{-5}	21×10^{-5}

The time-dependent boundary layer dimensional governing equations are provided by under the aforementioned presumptions (Jafar et al. [24]):

$$u_x + v_y = 0, \tag{1}$$

$$u_t + uu_x + vu_y = \nu_{nf} u_{yy} - \frac{\sigma_{nf}}{\rho_{nf}} B^2 u - \frac{\nu_{nf}}{K'} u + g^* \frac{(\rho\beta)_{nf}}{\rho_{nf}} (T - T_\infty), \tag{2}$$

$$T_t + uT_x + vT_y = \alpha_{nf} T_{yy} + \frac{\mu_{nf}}{(\rho c_p)_{nf}} (u_y)^2 - \frac{1}{(\rho c_p)_{nf}} \frac{\partial q_r}{\partial y} + \frac{Q^*}{(\rho c_p)_{nf}} (T - T_\infty), \tag{3}$$

assisted by the boundary conditions of:

– at $y = 0$

$$u = u_w(x,t) = \frac{ax^n}{1-\lambda t}, \qquad v = 0, \qquad T = T_w(x,t) = T_\infty + \frac{bx^{2n-1}}{\sqrt{1-\lambda t}}, \tag{4a}$$

– as $y \to \infty$

$$u \to 0, \qquad T = T_\infty . \tag{4b}$$

Roseland's approximation is considered as:

$$q_r = -\frac{4\sigma^*}{3k^*} \frac{\partial T^4}{\partial y} . \tag{5}$$

The temperature T^4 can be expanded using the Taylor series in powers of T_∞ as $T^4 = 4T_\infty{}^3 T - 3T_\infty{}^4$. In view of approximation (5), Eq. (3) can be transformed as:

$$T_t + uT_x + vT_y = \alpha_{nf} T_{yy} + \frac{\mu_{nf}}{(\rho c_p)_{nf}} (u_y)^2 + \frac{1}{(\rho c_p)_{nf}} \frac{16 T_\infty{}^3 \sigma^*}{3k^*} \frac{\partial^2 T}{\partial y^2} + \frac{Q^*}{(\rho c_p)_{nf}} (T - T_\infty). \tag{6}$$

2. Solution of the problem

The suitable similarity transformations are defined as:

$$\psi = \sqrt{\frac{2\nu a}{(n+1)(1-\lambda t)}} x^{\frac{n+1}{2}} f(\eta) ,$$

$$\eta = \sqrt{\frac{(n+1)a}{2\nu(1-\lambda t)}} x^{\frac{n-1}{2}} y ,$$

$$u = \frac{\partial \psi}{\partial y} = \frac{ax^n f'(\eta)}{(1-\lambda t)} ,$$

$$v = -\frac{\partial \psi}{\partial x} = -\left[\sqrt{\frac{2\nu a}{(n+1)(1-\lambda t)}} \frac{n+1}{2} x^{\frac{n-1}{2}} f(\eta) + \frac{a}{(1-\lambda t)} \frac{n-1}{2} f'(\eta) y x^{n-1} \right],$$

$$\theta(\eta) = \frac{(T - T_\infty)}{(T_w - T_\infty)} . \tag{7}$$

The wall temperature is defined as $T_w = T_\infty + \frac{bx^{2n-1}}{\sqrt{1-\lambda t}}$.

In view of the above transformations the governing equations (2) and (6) are reduced as:

$$f''' + (1-\phi)^{2.5} D_1 f f'' - \left[\frac{2n}{n+1}\right] (1-\phi)^{2.5} D_1 (f')^2 - M(1-\phi)^{2.5} D_3 f' - Kf' + \mathrm{Gr}(1-\phi)^{2.5} D_2 \theta - \frac{2A}{(n+1)} (1-\phi)^{2.5} D_1 \left[\frac{\eta}{2} f'' + f'\right] = 0, \tag{8}$$

$$\frac{1}{D_4} \left[\frac{1}{\mathrm{Pr}} \left(D_5 + \frac{4R}{3} \right) \theta'' + \frac{\mathrm{Ec}(f'')^2}{(1-\phi)^{2.5}} + Q\theta \right] - \frac{A}{(n+1)} (\theta + \eta\theta') - \frac{(2n-1)}{(n+1)} \theta f' + \theta' f = 0, \tag{9}$$

where functions D_1–D_5 are explained in Appendix.

The changed non-dimensional boundary conditions are:

– at $\eta = 0$

$$f = 0, \qquad f' = 1, \qquad \theta = 1, \tag{10a}$$

– as $\eta \to \infty$

$$f' \to 0, \qquad \theta \to 0, \tag{10b}$$

In Eqs. (8) and (9): $K = \frac{2\nu}{K_0 a(n+1)}$; $M = \frac{2\sigma_f B_0^2}{a(n+1)\rho_f}$; $A = \frac{\lambda}{a} x^{n-1}$; $\mathrm{Gr} = \frac{2gb\beta_f}{a^2(n+1)}$; $\mathrm{Pr} = \frac{(\mu C_p)_f}{k_f}$; $R = \frac{4\sigma^* T_\infty^3}{k_f k^*}$; $Q = \frac{Q_0}{a(\rho C_p)_f (n+1)}$; $\mathrm{Ec} = \frac{a^2 x}{b(1-\lambda t)^{\frac{3}{2}} C_{Pf}}$,

where Q_0 is a dimensional heat generation/absorption coefficient, K_0 is the porous permeability constant, and a, b are constants.

3. Physical quantities

The coefficient of skin friction and Nusselt number are expressed as follows:

$$C_f = \frac{\tau_w}{\rho_f u_w^2} , \tag{11a}$$

$$\mathrm{Nu_x} = \frac{x q_w}{k_f (T_w - T_\infty)} , \tag{11b}$$

where the shear stress $\tau_w = \mu_{nf} \left(\frac{\partial u}{\partial y}\right)_{y=0}$ and the heat flux $q_w = -k_{nf} \left(\frac{\partial T}{\partial y}\right)_{y=0}$ can be expressed as:

$$C_f \sqrt{\mathrm{Re_x}} = \frac{f''(0)}{(1-\phi)^{2.5}} \sqrt{\frac{n+1}{2}} , \tag{12}$$

$$(\mathrm{Re}_x)^{-1/2} \mathrm{Nu}_x = -\theta'(0) \times \frac{k_{nf}}{k_f} \sqrt{\frac{n+1}{2}}, \tag{13}$$

where the local Reynolds number $\mathrm{Re}_x = \frac{u_w x}{\nu_f}$.

4. Results and discussion

The set of dimensionless equations (8)–(9) with the related conditions (10) is simplified by utilizing the MATLAB bvp4c function [48]. The obtained results are plotted in Table 3 and Figs. 2–13. The current numerical results (see Table 4) are compared with the existing results of Vinod Kumar et al. [32], Ranaand Bhargava [49] and Kalidas Das [50]. The following parameters have been fixed throughout our analysis: the Prandtl number taken as: Pr = 6.2 and Ec = 0.5, $\eta = 0.1$, $A = 0.5$, Gr = 10, $M = 0.5$, $R = 0.5$, $K = 0.5$, $Q = 0.5$, $n = 0.1$. The range of volume fraction parameterϕ is considered as $0 < \phi \leq 0.1$.

Table 3. Numerical values of $Re_x^{1/2} C_f$, and $Re_x^{-1/2}$ Nu for various values of flow parameters when $\phi_1 = 0.1$, $\phi_2 = 0.1$, $\eta = 0.5$, $c = 0.5$, $M = 0.5$, Pr = 6.2, $A = 0.5$, Gr = 0,5, $K = R = Q = 0.5$.

M	*K*	*A*	Gr	*n*	*R*	*Q*	$Re_x^{1/2}\,Cf$		$Re_x^{-1/2}\,Nu_x$	
							Cu + H_2O	Al_2O_3 + H_2O	Cu + H_2O	Al_2O_3 + H_2O
0.1							1.774433	1.790626	-0.493296	-0.516242
0.2							1.718406	1.732834	-0.459773	-0.479898
0.3							1.664387	1.677254	-0.428849	-0.446479
	0.1						0.710402	0.751428	-0.005428	0.007241
	0.2						0.671865	0.711406	-0.000381	0.013399
	0.3						0.633842	0.672048	0.004200	0.018748
		1					0.348103	0.478336	-0.326767	-0.310067
		2					0.061212	0.364972	-1.189281	-1.221245
		3					0.022868	0.560151	-2.498586	-2.859526
			0				-1.971437	-1.833754	-0.745983	-0.639561
			5				-0.761404	-0.677244	-0.161698	-0.112582
			10				0.559381	0.594962	0.011729	0.027959
				0			0.802446	0.809084	-0.219926	-0.204617
				0.5			0.318425	0.381278	0.331944	0.345007
				1			0.056470	0.149524	0.782100	0.786824
					1		0.365539	0.405030	0.198145	0.218041
					2		0.175535	0.221788	0.406026	0.422812
					3		0.082008	0.132436	0.520088	0.532815
						0.1	0.844363	0.876468	-0.508353	-0.504293
						0.2	0.763414	0.796337	-0.362504	-0.354822
						0.3	0.689568	0.723333	-0.228261	-0.217334

Table 4. Comparison values of $\theta'(0)$ for various values of *n*.

Pr	*n*	Rana and Bhargava [49]	Das K. [50]	Kumar G.V. et al. [32]	Present results
1	0.2	0.6113	0.610571	0.610266	0.610400
	0.5	0.5967	0.595719	0.595298	0.596688
	1.5	0.5768	0.574525	0.574894	0.576870
5	0.2	1.5910	1.60713	1.607787	1.605107
	0.5	1.5839	1.58619	1.586774	1.586586
	1.5	1.5496	1.55719	1.557686	1.557521

The Fig. 2 illustrates the impact of the magnetic field parameter (*M*) over the velocity field $f'(\eta)$. The profiles are drawn for copper and aluminium oxide nanofluids. It follows from this figure that the fluid velocity declines with the rising values of *M*.

This is because the Lorentz force generates resistance to the fluid flow and hence slows down the fluid velocity. Moreover, significant behaviour is observed for copper water nanofluid. The influence of the porous permeability parameter (*K*) on fluid velocity is shown in Fig. 3. It is seen that the fluid velocity decreases with the rising values of *K* for both copper-water and aluminium oxide nanofluids. Physically, an increase in *K* strengthens the porous layer and hence reduces fluid velocity. Also, a decrement in the momentum boundary layer is noticed.

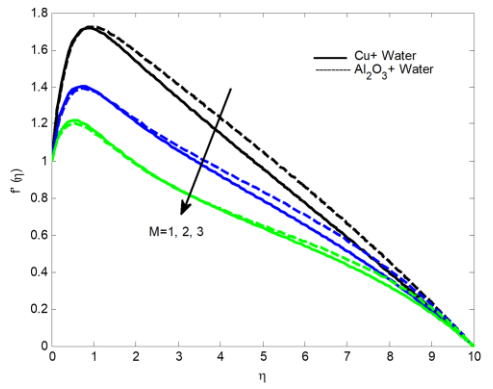

Fig. 2. Effect of *M* on $f'(\eta)$.

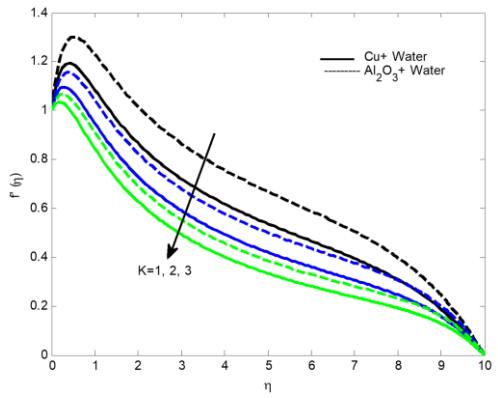

Fig. 3. Effect of K on $f'(\eta)$.

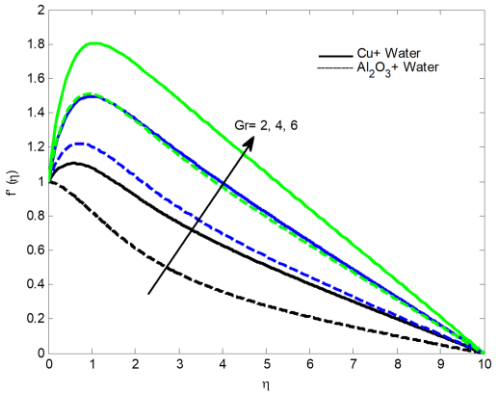

Fig. 4. Effect of Gr on $f'(\eta)$.

The effect of the thermal Grashof number (Gr) on velocity distribution is illustrated in Fig.4. It has been seen that the velocity of the fluid is enhanced with the rising values of Gr. The Grashoff number accelerates fluid velocity and hence increases boundary layer thickness because the equations of the governing boundary layer are coupled to the convection parameter. Figure 5 displays the influence of the non-linear stretching sheet parameter (n) on fluid velocity.

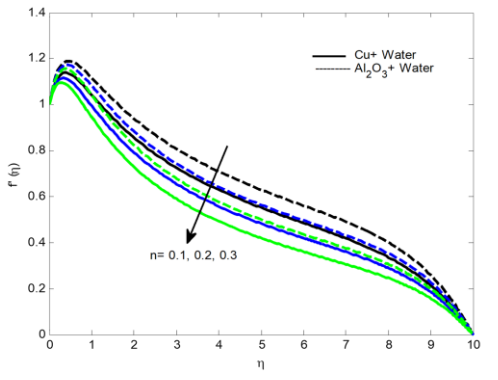

Fig. 5. Effect of n on $f'(\eta)$.

It may be seen that the velocity decreases almost exponentially with constant values of$n$for both cases. Figs. 6 and 7 explain the influence of nanoparticle volume fraction parameter (ϕ) on$f'(\eta)$ and $\theta(\eta)$. It is observed that the fluid velocity reduces with the growing values of ϕ. Additionally, pure fluid has a larger momentum boundary layer than nanofluid. Moreover, on the temperature field, the opposite pattern is noticed. This is because the higher value of ϕ produces more thermal conductivity of the nanofluid, and this causes the fluid temperature to

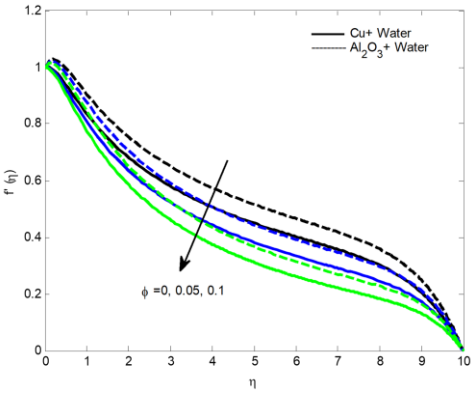

Fig. 6. Effect of ϕ on $f'(\eta)$.

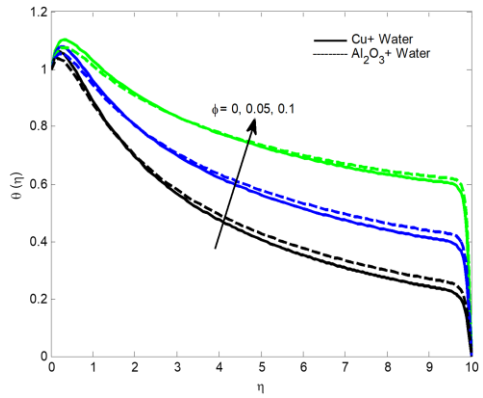

Fig. 7. Effect of ϕ on $\theta(\eta)$.

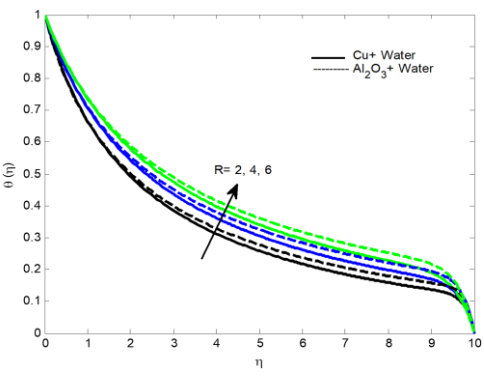

Fig. 8. Effect of R on $\theta(\eta)$.

increase (see Fig. 7). The effects of thermal radiation variations (R) on the temperature field are depicted in Fig. 8.

From the figure, it is noticed that thermal radiation significantly increases the fluid temperature for both the cases since thermal radiation enhances thermal diffusion. Moreover, a thicker thermal boundary layer is observed for aluminium oxide nanofluid than for copper-water nanofluid. The effect of viscous dissipation (Ec) on fluid velocity and temperature fields is depicted in Figs. 9–10. The fluid velocity and temperature were increased with the increasing viscous dissipation parameter. This is because the viscous dissipation parameter allows energy to be stored in the fluid region as a result of viscosity and elastic deformation, which produces heat due to fractional heating. This physically explains why the fluid's velocity and temperature increase. The nanofluid velocity and temperature is a decreasing function of an unsteady parameter (A) for both cases (see Figs. 11–12). Generally, increasing A can be associated with reducing the nanofluid temperature. This effect causes a reduction in the fluid velocity and temperature.

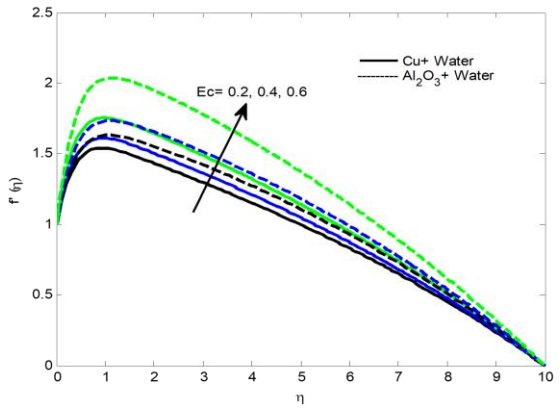

Fig. 9. Effect of Ec on $f'(\eta)$.

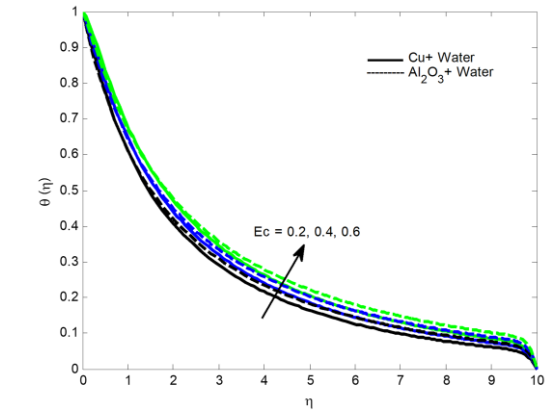

Fig. 10. Effect of Ec on $\theta(\eta)$.

From Fig. 13, it is noted that the fluid temperature rises as the heat generation parameter Q increases for both nanofluids. The huge amount of heat produced in the fluid causes an enhancement of the thermal energy of the nanofluid. This process increases the thickness of the thermal boundary layer, implying that heat energy is released and, as a result, the fluid's temperature rises. Further, it has been observed that the temperature of the aluminium oxide nanofluid is considerably lower than that of the copper water nanofluid.

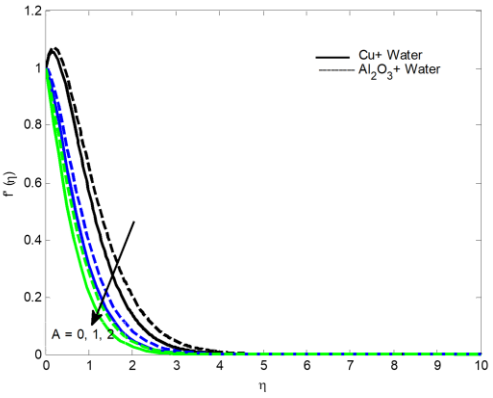

Fig. 11. Effect of A on $f'(\eta)$.

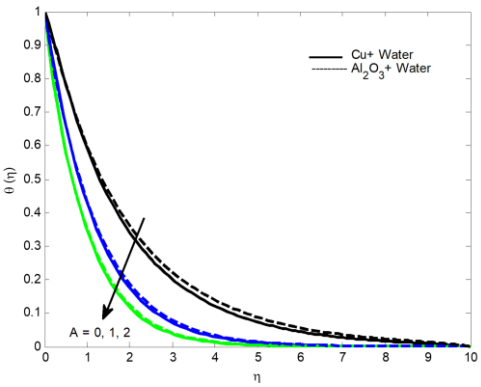

Fig. 12. Effect of A on $\theta(\eta)$.

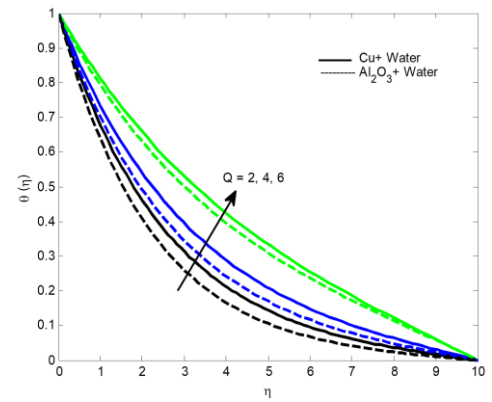

Fig. 13. Effect of Q on $\theta(\eta)$.

The numerical results of the skin-friction coefficient ($Re_x^{1/2} C_f$) and Nusselt number ($Re_x^{-1/2}$ Nu) for various flows of copper-water and aluminium oxide nanofluids are presented in Table 3. From this table, it is noticed that the skin friction at the

wall decreases with increasing values of *M*, *K*, *A*, *n*, *R* and *Q*, while it rises with the increasing values of Gr. However, the heat transfer rate significantly increases with the increasing values of *M*, *K*, Gr, *n*, *R* and *Q*. The opposite pattern is observed for *A*.

5. Conclusions

The effects of an unsteady nanofluid across a non-linear porous stretching sheet in the presence of thermal radiation and heat generation caused by a uniform magnetic field are investigated. The set of non-linear ordinary differential equations are solved by using the MATLAB bvp4c package. The outcomes are presented and analyzed through figures and tables. The primary findings of the current investigation are:

1) The volume fraction parameter shows a significant impact on fluid temperature.
2) The Cu-water nanofluid has much greater friction at the wall than the Al_2O_3-water nanofluid.
3) A thicker thermal boundary layer is noticed for the aluminium oxide nanofluid than for the copper-water nanofluid with the rising values of *R*.
4) The momentum boundary layer is thicker for pure fluid than for the nanofluid.
5) With increasing values of A, the heat transfer rate coefficient drops.

Appendix

Functions D_1-D_5 that appear in Eqs. (8), (9) are explained below

$$D_1 = \left[(1-\phi) + \phi\frac{\rho_s}{\rho_f}\right], \tag{A.1}$$

$$D_2 = \left[(1-\phi) + \phi\frac{(\rho\beta)_s}{(\rho\beta)_f}\right], \tag{A.2}$$

$$D_3 = \left[(1-\phi) + \phi\frac{\sigma_s}{\sigma_f}\right], \tag{A.3}$$

$$D_4 = \left[(1-\phi) + \phi\frac{(\rho Cp)_s}{(\rho Cp)_f}\right], \tag{A.4}$$

$$D_5 = \frac{K_{nf}}{K_f} = \frac{(2K_f+K_s)-2\phi(K_f-K_s)}{(2K_f+K_s)+\phi(K_f-K_s)}. \tag{A.5}$$

References

[1] Sakiadis, B.C. (1961). Boundary layer behaviours on continuous solid surface. *AIChE Journal*, 7(2), 221–225. doi: 10.1002/aic.690070211

[2] Crane, L.J. (1970). Flow past a stretching plate. *Zeitschrift für Angewandte Mathematik und Physik (ZAMP)*, 21, 645–647. doi: 10.1007/bf01587695

[3] Schlichting, H. (1955). *Boundary-layer Theory*. New York. McGraw-Hill.

[4] Soundalgekar, V.M., & Ramanamurthy, T.V. (1980). Heat transfer past a continuous moving plate with variable temperature. *Wärme- und Stoffübertragung*, 14, 91–93. doi: 10.1007/BF01806474

[5] Grubka, L.G., & Bobba, K.M. (1985). Heat transfer characteristics of a continuous stretching surface with variable temperature. *ASME Journal of Heat and Mass Transfer*, 107(1), 248–250. doi: 10.1115/1.3247387

[6] Ishak, A., Nazar, R., & Pop, I. (2009). Boundary layer flow and heat transfer over an unsteady stretching vertical surface. *Meccanica*, 44, 369–375. doi:10.1007/s11012-008-9176-9

[7] Kumaran, V., & Ramanaiah, G. (1996). A note on the flow over a stretching sheet. *Acta Mechanica*, 116, 229–233. doi: 10.1007/BF01171433

[8] Vajravelu, K. (2001). Viscous flow over a nonlinearly stretching sheet. *Applied Mathematics and Computation*, 124, 281–288. doi: 10.1016/S0096-3003(00)00062-X

[9] Cortell, R. (2007). Viscous flow and heat transfer over a nonlinear stretching sheet. *Applied Mathematics and Computation*, 184, 864–873. doi: 10.1016/j.amc.2006.06.077

[10] Raptis, A., & Perdikis, C. (2006). Viscous flow over a non-linearly stretching sheet in the presence of a chemical reaction and magnetic field. *International Journal of Non-Linear Mechanics*, 41(4), 527–529. doi: 10.1016/j.ijnonlinmec.2005.12.003

[11] Kechil, S.A., & Hashim, I. (2008). Series solution of flow over non-linearly stretching sheet with chemical reaction and magnetic field. *Physics Letters, Section A*, 372(13), 2258–2263. doi: 10.1016/j.physleta.2007.11.027

[12] Sanni, K.M., Hussain, Q., & Asghar, S. (2020). Heat Transfer Analysis for Non-linear boundary driven flow over a curved stretching sheet with variable magnetic field. *Frontiers in Physics*, 8,113. doi: 10.3389/fphy.2020.00113

[13] Alinejad., J, & Samarbakhsh., S. (2012). Viscous flow over nonlinearly stretching sheet with effects of viscous dissipation. *Journal of Applied Mathematics*, 2012, 1–10. doi: 10.1155/2012/587834

[14] Jabeen, K., Mushtaq, M., & Akram, R.M. (2020). Analysis of the MHD boundary layer flow over a nonlinear stretching sheet in a porous medium using semi-analytical approaches. *Mathematical Problems in Engineering*, 2020, 1–9. doi: 10.1155/2020/3012854

[15] Mahantesh M., Nandeppanavar., Vajravelu, K., Subhas Abel, M., & Chiu-On Ng. (2011). Heat transfer over a nonlinearly stretching sheet with non-uniform heat source and variable wall temperature. *International Journal of Heat and Mass Transfer*, 54, 4960–4965. doi: 10.1016/j.ijheatmasstransfer.2011.07.009

[16] Sanni, K.M., Asghar, S., Jalil, M., & Okechi., N.F. (2017). Flow of viscous fluid, along a nonlinearly stretching curved surface. *Results in Physics*, 7, 1–4. doi: 10.1016/j.rinp.2016.11.058

[17] Choi, S.U.S., & Eastman, J A. (1995). Enhancing Thermal Conductivity of Fluids with Nanoparticles. *ASME International Mechanical Engineering Congress &Exposition*, 12–17 November, San Francisko, USA.

[18] Buongiorno, J. (2006). Convective transport in nanofluids. *ASME Journal of Heat and Mass Transfer*, 128(3), 240–250. doi: 10.1115/1.2150834

[19] Sudarsana Reddy, P., & Chamkha, A.J. (2016). Influence of size, shape, type of nanoparticles, type and temperature of the base fluid on natural convection MHD of nanofluids. *Alexandria Engineering Journal*, 55(1), 331–341. doi: 10.1016/j.aej.2016.01.027

[20] Ali, L, Liu, X., & Ali, B. (2020). Finite element analysis of variable viscosity impact on MHD flow and heat transfer of nanofluid using the Cattaneo–Christov model. *Coatings*, 10, 395. doi: 10.3390/coatings10040395

[21] Mjankwi, M.A., Masanja, V.G., Mureithi, E.W., & James, M.N. (2019). Unsteady MHD flow of nanofluid with variable properties over a stretching sheet in the presence of thermal radiation and chemical reaction. *International Journal of Mathematics and Mathematical Sciences*, 2019, 1–14. doi: 10.1155/2019/7392459

[22] Anuar, N.S., Bachok., N, Arifin, N.M., & Rosali, H. (2020). MHD flow past a nonlinear stretching/shrinking sheet in carbon nanotubes: Stability analysis. *Chinese Journal of Physics*, 65, 436–446, doi: 10.1016/j.cjph.2020.03.003

[23] Mabood, F., Khan, W.A., & Ismail, A.I.M. (2015). MHD boundary layer flow and heat transfer of nanofluids over a nonlinear stretching sheet: A numerical study. *Journal of Magnetism and Magnetic Materials*, 374, 569–576. doi: 10.1016/j.jmmm.2014.09.013

[24] Jafar, A.B., Shafie, S., & Ullah, I. (2020). MHD radiative nanofluid flow induced by a nonlinear stretching sheet in a porous medium. *Heliyon*, 6(6), doi: 10.1016/j.heliyon.2020.e04201

[25] Triveni, B., Subba Rao, M.V., Gangadhar, K., & Chamkha, A.J. (2023). Heat transfer analysis of MHD Casson nanofluid flow over a nonlinear stretching sheet in the presence of non-uniform heat source. *Numerical Heat Transfer, Part A: Applications*. doi: 10.1080/10407782.2023.2219831

[26] Reddy, Y.D., Goud, B.S., Chamkha, A.J., & Kumar, M.A. (2022). Influence of radiation and viscous dissipation on MHD heat transfer Casson nanofluid flow along a nonlinear stretching surface with chemical reaction. *Heat Transfer*, 51(4), 3495–3511. doi: 10.1002/htj.22460

[27] Rasool, G., Chamkha, A.J., Muhammad, T., Shafiq, A., & Khan, I. (2020). Darcy-Forchheimer relation in Casson type MHD nanofluid flow over non-linear stretching surface. *Propulsion and Power Research*, 9(2), 159–168. doi: 10.1016/j.jppr.2020.04.003

[28] Jagan, K., Sivasankaran, S., Bhuvaneswari, M., & Rajan, S. (2018). Effect of thermal radiation and slip on unsteady 3D MHD nanofluid flow over a non-linear stretching sheet in a porous medium with convective boundary condition. *Journal of Physics: Conference Series*, 1139. doi: 10.1088/1742-6596/1139/1/012027

[29] Kumar, V.G., Kiran Kumar, R.V.M.S.S., & Varma, S.V.K. (2018). Unsteady magnetohydrodynamic stagnation point flow of a nanofluid over a slendering stretching sheet using Buongiorno's odel. *International Journal of Research in Industrial Engineering*, 7(1), 84–105. doi: 10.22105/riej.2018. 102367.1028

[30] Rajputa, S., Bhattacharyyaa, K., Pandeya, A.K., & Chamkha, A.J. (2022). Unsteady axi-symmetric flow of nanofluid on non-linearly expanding surface with variable fluid properties. *JCIS Open*, 8(100064). doi: 10.1016/j.jciso.2022.100064

[31] Ramana Reddy, J.V., Sugunamma, V., & Sandeep, N. (2018). Thermophoresis and Brownian motion effects on unsteady MHD nanofluid flow over a slandering stretching surface with slip effects. *Alexandria Engineering Journal*, 57, 2465–2473. doi: 10.1016/j.aej.2017.02.014

[32] Kumar, V.G., Varma, S.V.K., & Kiran Kumar, R.V.M.S.S. (2019). Slip effects on magnetohydrodynamic boundary layer flow of a radiative nanofluid over an unsteady non-linear stretching sheet with non-uniform heat source/sink. *Journal of Nanofluids*, 8, 500–508. doi: 10.1166/jon.2019.1617

[33] Kumar, V.G., Varma, S.V.K., & Kiran Kumar, R.V.M.S.S. (2019). Unsteady three-dimensional MHD nanofluid flow over a stretching sheet with variable wall thickness and slip effects. *International Journal of Applied Mechanics and Engineering*, 24, 709–724. doi: 10.2478/ijame-2019-0044

[34] Dinarvand, S., Yousefi, M., & Chamkha, A.J. (2022). Numerical simulation of unsteady flow toward a stretching/shrinking sheet in porous medium filled with a hybrid nanofluid. *Journal of Applied and Computational Mechanics*, 8(1), 11-20. doi: 10.22055/jacm.2019.29407.1595

[35] Kumar, V.G., Ur Rehman, K., Kiran Kumar, R.V.M.S.S., & Shatanawi, W. (2022). Unsteady magnetohydrodynamic nanofluid flow over a permeable exponentially surface manifested with non-uniform heat source/sink effects. *Waves in Random and Complex Media*, 1–19. doi: 10.1080/17455030.2022.2072531

[36] Madhu, M., Kishan, N., & Chamkha, A.J. (2017). Unsteady flow of a Maxwell nanofluid over a stretching surface in the presence of magnetohydrodynamic and thermal radiation effects. *Propulsion and Power Research*, 6, 31–40. doi: 10.1016/j.jppr.2017.01.002

[37] Veera Krishna, M., & Chamkha, A.J. (2019). Hall and ion slip effects on MHD rotating boundary layer flow of nanofluid past an infinite vertical plate embedded in a porous medium. *Results in Physics*, 15. doi: 10.1016/j.rinp.2019.102652

[38] Veera Krishna, M., Ahammad, N.A., & Chamkha, A.J. (2021). Radiative MHD flow of Casson hybrid nanofluid over an infinite exponentially accelerated vertical porous surface. *Case Studies in Thermal Engineering*, 27(101229). doi: 10.1016/j.csite.2021.101229

[39] Sreedevi, P., Sudarsana Reddy, P., & Chamkha, AJ. (2022). Heat and mass transfer analysis of unsteady hybrid nanofluid flow over a stretching sheet with thermal radiation. *SN Applied Sciences*, 2(7), 1222. doi: 10.1007/s42452-020-3011-x

[40] Tiwari, R.J., & Das, M.K. (2007). Heat transfer augmentation in a two-sided lid-driven differentially heated square cavity utilizing nanofluids. *International Journal of Heat and Mass Transfer*, 50(9–10), 2002–2018. doi: 10.1016/j.ijheatmasstransfer.2006.09.034

[41] Veera Krishna, M., Ameer Ahamad, N., & Aljohani, A.F. (2021). Thermal radiation, chemical reaction, Hall and ion slip effects on MHD oscillatory rotating flow of micro-polar liquid. *Alexandria Engineering Journal*, 60, 3467–3484. doi: 10.1016/j.aej.2021.02.013

[42] Veera Krishna, M., & Chamkha, A.J. (2018). Hall effects on unsteady MHD flow of second grade fluid through porous medium with ramped wall temperature and ramped surface concentration. *Physics of Fluids*, 30(5). doi: 10.1063/1.5025542

[43] Veera Krishna, M., & Chamkha, A.J. (2020). Hall and ion slip effects on MHD rotating flow of elastic-viscous fluid through porous medium. *International Communications in Heat and Mass Transfer*, 113. doi.: 10.1016/j.icheatmasstransfer.2020.104494

[44] Darcy, H.P. (1856). *Les fontaines publiques de la ville de Dijon*. Paris. Dalmont.

[45] Gupta, S., Kumar, D., & Singh, J. (2019). Magnetohydrodynamic three-dimensional boundary layer Flow and heat transfer of water-driven copper and alumina nanoparticles induced by convective conditions. *International Journal of Modern Physics B*, 33(26), 1950307. doi: 10.1142/S0217979219503077

[46] Das, K., Sarkar, A., & Prabir Kumar, K. (2017). Cu-water nanofluid flow induced by a vertical stretching sheet in presence of a magnetic field with convective heat transfer. *Propulsion and Power Research*, 6(3), 206–213. doi: 10.1016/j.jppr.2017.07.001

[47] Oztop, H.F., & Abu-Nada, E. (2008). Numerical study of natural convection in partially heated rectangular enclosures filled with nanofluids. *International Journal of Heat and Fluid Flow*, 29(5), 1326–1336. doi: 10.1016/j.ijheatfluidflow.2008.04.009

[48] Shampine, L.F., Kierzenka, J., & Reichelt, M.W. (2000). Solving boundary value problems for ordinary differential equations in MATLAB with bvp4c. http://users.math.uoc.gr/~marina/BVP_tutorial.pdf [accessed 20 Nov. 2023].

[49] Rana, P., & Bhargava, R. (2012). Flow and heat transfer of a nanofluid over a non-linearly stretching sheet: a numerical study. *Communications in Nonlinear Science and Numerical Simulation*, 17(1), 212–226. doi: 10.1016/j.cnsns.2011.05.009

[50] Das, K. (2015). Nanofluid flow over a non-linear permeable stretching sheet with partial slip. *Journal of the Egyptian Mathematical Society*, 23, 451–456. doi: 10.1016/j.joems.2014.06.014